TESIS DE LA UNIVERSIDAD DE ZARAGOZA

2016

153

Noelia Garijo Millán

Bone remodeling simulations: challenges, problems and applications

Departamento
Ingeniería Mecánica

Director/es
Pérez Ansón, María Ángeles
García Aznar, José Manuel

ISSN 2254-7606

Prensas de la Universidad
Universidad Zaragoza

ISSN 2254-7606

Universidad Zaragoza
1542

Tesis Doctoral

BONE REMODELING SIMULATIONS: CHALLENGES, PROBLEMS AND APPLICATIONS

Autor

Noelia Garijo Millán

Director/es

Pérez Ansón, María Ángeles
García Aznar, José Manuel

UNIVERSIDAD DE ZARAGOZA

Ingeniería Mecánica

2016

Escuela de
Ingeniería y Arquitectura
Universidad Zaragoza

Departamento de
Ingeniería Mecánica
Universidad Zaragoza

DISSERTATION

Bone remodeling simulations: challenges, problems and applications.

Noelia Garijo Millán

Doctoral degree in *Computational Mechanics*

Faculty Advisors:

Dra. Mª Ángeles Pérez Ansón

and

Dr. José Manuel García Aznar

Departamento de Ingeniería Mecánica
Escuela de Ingeniería y Arquitectura (EINA)
Universidad de Zaragoza. December 2015

SINOPSIS

La remodelación ósea es el mecanismo que regula la relación entre la morfología del hueso y sus cargas mecánicas externas. Se basa en el hecho de que el hueso se adapta a las condiciones mecánicas a las que está expuesto. Varios factores mecánicos y bioquímicos pueden regular la respuesta final de la remodelación ósea. De hecho, la remodelación ósea intenta alcanzar varios objetivos mecánicos: reparar el daño para reducir el riesgo de fractura y optimizar la rigidez y resistencia con el mínimo peso. Durante las últimas décadas, se han propuesto un gran número de leyes matemáticas implementadas numéricamente, pero la mayoría de ellas presentan diferentes problemas como la estabilidad, la convergencia o la dependencia de las condiciones iniciales. Por tanto, el objetivo principal de esta tesis es estudiar los modelos de remodelación ósea, mostrando sus retos, su problemática en la actualidad y su aplicación en el ámbito clínico.

En primer lugar, se han revisado de dos teorías clásicas de la remodelación ósea (modelo de Stanford y el modelo de Doblaré y García). En ambos, se planteó que el estímulo homeostático de referencia no es constante, sino que depende localmente de la historia de carga que cada punto local está soportando. Como consecuencia directa de esta hipótesis, se demuestra que las inestabilidades numéricas que normalmente presentan estos algoritmos pueden ser resueltas, mejorando claramente los resultados finales. Por esta razón, se aplicó esta metodología a un modelo de elementos finitos 2D/3D. Esta contribución mejora la convergencia de la solución, asegurando su estabilidad numérica a largo plazo.

Por otra parte, en un intento de dilucidar las características de adaptación del hueso en diferentes escalas, se plantea una relación a nivel órgano y a nivel de tejido que dependa de un cambio en el estímulo homeostático de referencia acorde con la densidad, mientras la energía de tejido permanece invariante. Esta hipotesis mejora la unicidad de la solución y la hace independientemente de las condiciones iniciales seleccionados ayudando también a su estabilidad numérica.

Además, el modelado de paciente específico está adquiriendo cada vez más importancia. Una de las principales dificultades en la creación de modelos de paciente específico, es la determinación de la carga que el hueso está realmente soportando. Los datos relativos a pacientes específicos, como la geometría ósea y la distribución de la densidad ósea, puede ser utilizados para determinar estas cargas. Por lo tanto, se ha estudiado la estimación de la cargas con tres diferentes técnicas matemáticas: regresión lineal, redes neuronales artificiales y máquinas de soporte vector. Estas técnicas han sido aplicadas a un ejemplo teórico para obtener las cargas a través de la densidad que se predice con los modelos de remodelación ósea.

Para concluir, la metodología desarrollada que combina modelos de remodelación ósea con redes neuronales se ha aplicado a la predicción de las cargas de

cinco tibias de pacientes. Para ello, se han determinado la geometría y la distribución de la densidad a partir de un TAC y se han introducido los valores de densidad en el modelo previamente desarrollado, obteniendo así, las cargas específicas de las tibias de los pacientes. Con el fin de validar la capacidad de esta novedosa técnica, se han comparado las cargas obtenidas de la técnica propuesta con las cargas obtenidas en un análisis de marcha de dichos pacientes. Los errores obtenidos en las predicciones han sido menores de un 6%. Por lo tanto, la metodología propuesta se ha dado por validada.

Palabras clave: Remodelación ósea, Predición de densidad ósea, Estimaciones de error, Adaptación ósea, Análisis de elementos finitos, Estabilidad, Simulación numérica/ convergencia, Zona muerta, Multiescala, Red neuronal artificial, Máquina de soporte vector, Regresión lineal, Condiciones de carga, Problema remodelación ósea inverso, Simulación de paciente específico, Modelos musculoesqueléticos, Análisis de marcha.

Abstract

Bone remodeling is the mechanism that regulates the relationship between bone morphology and its external mechanical loads. It is based on the fact that bone adapts itself to the mechanical conditions to which it is exposed. Several mechanical and biochemical factors may regulate the final bone remodeling response. In fact, bone remodeling is hypothesized to achieve several mechanical objectives: repair damage to reduce the risk of fracture and optimize stiffness and strength with minimum weight. During recent decades, a great number of numerically implemented mathematical laws have been proposed, but most of them present different problems as stability, convergence or dependence of the initial conditions. Thus, the main scope of this Thesis is to study bone remodeling models, showing their challenges, their problematic and their applicability in the clinical setting.

Firstly, we revisit two classical bone remodeling theories (Stanford model and Doblaré and García model). In both of them, the reference homeostatic stimulus is hypothesized that is not constant, but it is locally dependent on the loading history that each local point is effectively supporting. As a direct consequence of this assumption, we demonstrate that the numerical instabilities that all these algorithms normally present can be solved, clearly improving the final results. For this reason, we applied this methodology to 2D/3D finite element models. This contribution improves the convergence of the solution, leading to its numerical stability in the long-term.

In an attempt to elucidate the features of bone adaptation at the different scales, we hypothesize that the relationship between the organ level and tissue level depends on the reference homeostatic stimulus changes according to the density and the tissue effective energy remains unchanged. This assumption improves the uniqueness of the solution, independently of the initial conditions selected and clearly helps in its numerical stability.

In addition, patient-specific modeling is becoming increasingly important. One of the most challenging difficulties in creating patient-specific models is the determination of the specific load that the bone is really supporting. Real information related to specific patients, such as bone geometry and bone density distribution, can be used to determine patient loads. Therefore, we studied three different mathematical techniques: linear regression, artificial neural networks (ANN) and support vector machines (SVM). These techniques have been applied to a theoretical femur to obtain the load through the density that came from many bone remodeling simulations.

Finally, the application of this novel methodology has been applied for the loading prediction of five real tibias. We are able to determine the subject-specific forces from CT data, from which we obtain bone geometry and density distribu-

tion of the five tibias. Then, the density values at certain bone regions have been introduced in the methodology developed that combines bone remodeling models and artificial neuronal networks (ANN) for obtaining the predicted subject-specific loads. Finally, in order to validate this novel technique for tibia loading predictions, we compare predicted loads with the loads obtained from the patient-specific musculoskeletal model. The errors between both loads were lower than 6%. Therefore, the methodology proposed has been validated

Keywords: Bone remodeling, Bone density prediction, Error estimates, Bone adaptation, Finite element analysis, Stability, Numerical simulations/convergence, Dead zone, Multiscale, Artificial neuronal network, Support vector machine, Linear regression, Loading conditions, Inverse bone remodeling problem, Subject-specific simulation, Musculoskeletal modeling, Gait analysis.

Indice general - Table of contents

List of figures

List of tables

List of Symbols and Acronyms - Notation

Bone remodeling models

$\mathbb{S}^d$	space of second order symmetric tensors
$\mathbb{R}^d$	space of symmetric matrices of order d
d	order of vector space
Ω	open bounded domain
Γ	boundary
Γ_D	disjoint part of the boundary (Lipschitz continuous)
Γ_N	disjoint par of the boundary (Lipschitz continuous)
$\boldsymbol{x}$	a generic point
$\boldsymbol{\nu}(\boldsymbol{x})$	outward unit normal vector
$\overline{\Omega}$	closure of set Ω
$\boldsymbol{f}$	volume force of density it is clamped on Γ_D
$\boldsymbol{g}$	surface traction with density act on Γ_N
T	time interval
$\boldsymbol{u}$	displacement field
$\boldsymbol{\sigma}$	stress tensor
$\boldsymbol{\varepsilon}$	strain tensor
U	internal strain energy
$\overline{\sigma}_t$	effective stress at the tissue level
$\mu(\rho)$	Lame's coefficients (shear modulus)
$\lambda(\rho)$	Lame's first parameter
ρ	apparent density
$E(\rho)$	Young's modulus
$\kappa(\rho)$	Poisson's ratio
M	positive constant which characterize the Young's modulus
γ	exponent which characterize the Young's modulus
ψ_t	daily tissue stress level
N	number of different load cases
n	average number of load cycles per time step
i	load case
m	an experimental parameter for each load case
α	constant which characterize the bone properties
β	constant which characterize the bone properties

L	truncation value
$2w$	width of the dead zone
c	constant remodeling velocity
e	remodeling error ψ_t-ψ_t^*
$f(z)$	function of the remodeling
$\dot{r}$	bone remodeling rate
ψ_t^*	the reference value of the tissue stress level
k	ratio between the available surface for remodeling and the total surface
$S_v(\rho)$	the specific surface (internal surface per unit volume)
$\overline{\rho}$	maximal density of cortical bone
$\underline{\rho}$	minimal density of the bone
ρ_0	initial apparent density
$(\psi_t^*)_0$	initial reference value of the tissue stress level
$\mathbf{D}$	damage tensor
$O(\rho)$	parameter that is obtained by particularising the general anisotropic model to the isotropic case
$\mathbf{H}$	remodeling tensor
$\hat{\mathbf{H}}$	fabric tensor
$\mathbf{Y}$	variable thermodynamically conjugated to $\mathbf{H}$ as independent variable of strain
$\mathbf{Y}^\sigma$	variable thermodynamically conjugated to $\mathbf{H}$ as independent variable of stress
Ψ	free energy function
$\boldsymbol{g}^r$	hardening the damage criteria of resorption
$\boldsymbol{g}^f$	hardening the damage criteria of formation
$\mathbf{J}$	a tensor that quantifies the relative influence of the stimulus in the damage criterion
ω	a scalar parameter that defines the anisotropy level of the damage criteria
μ^r	consistency parameter associated with the damage criteria of resorption
μ^f	consistency parameter associated with the damage criteria of formation
$\hat{\omega}$	fourth-order tensor assigned to the damage criterion
c_r	resorption velocity per unit stress
c_f	formation velocity per unit stress
a	constant exponent that regulates the adaptivity of the reference stimulus
A	constant that regulates the adaptivity of the reference stimulus
F	relation between the tissue-level and the continuum-level
Y	Sobolev spaces of $L^2(\Omega)$
H	Sobolev spaces of $[L^2(\Omega)]^d$
V	variational subspaces of $[H^1(\Omega)]^d$

Q	variational subspaces of $[L^2(\Omega)]^{d\times d}$
$\boldsymbol{v}$	vector of dimension d
$\boldsymbol{\tau}$	matrix of dimension $d \times d$
C	space of continuum function
Φ	function of $Y \times Y$
$I_{[\underline{\rho},\overline{\rho}]}$	the indicator function of the interval $[\underline{\rho}, \overline{\rho}]$
K	a convex set
ξ	element of K
V^h	finite element subspace $\subset V$
Q^h	finite element subspace $\subset Q$
B^h	finite element subspace $\subset Y$
$\mathcal{T}^h$	a triangulation of $\overline{\Omega}$
q	variable in T
P_q	the space of polynomials of global degree less or equal to q
h	spatial discretization parameter
k	independent of the discretization parameters
K^h	a discrete convex set $K \cap B^h$
$g(t)$	continuous function
z	vector of dimension d
p	constant
ϵ	positive constant
$\mathcal{P}^h$	projection operator
$\mathcal{I}$	denotes the identity operator in $\mathbb{S}^d$

Operators

$\mathbf{1}$	the identity second order tensor
Div	the divergence operator
Tr	trace operator
:	inner product
$\dot{\bullet}$	derivative of $\bullet$ with respect to time
$\bullet \cdot \bullet$	inner product of vectors
$\bullet : \bullet$	double inner product or tensor contraction
$\bullet \times \bullet$	tensor product
$\| \bullet \|$	norm of $\bullet$
$\partial_\bullet \circ$	the derivative of $\circ$ with respect to $\bullet$

Artificial Neural Network (ANN)

$\mathbf{w}^t$	weights vector
$\mathbf{x}$	input signals vector
n	input space dimension
k	output space dimension
$\mathcal{U}$	hidden variables space subspace $\mathbf{x}$
ψ	hidden layer activation function
w_j	parameter vector of the hidden layer
w_{j0}	threshold value
φ	output layer activation function
c_j	weights
c_{j0}	threshold value
$\mathbf{u}$	learning vector
μ_P	index of actual learning patterns
P	number of learning patterns
$\mathbf{u}_j^{m\mu_P}$	output values of each element for all layers using the formula
m	index of actual layer
M	number of layers without including the input layer
j	index of actual element
f	activation function
π	learning error
$\widehat{y}$	expected network output value
y	actual network output value
ε	sum of squares errors
Δw	change of given weight for pattern
η	coefficient

Support Vector Machine (SVM)

f	a function
$\mathcal{X}$	subspace of $\mathbb{R}^n$
$\mathcal{Z}$	subspace of $\mathbb{R}^g$
g	output space dimension
$\mathbf{x}$	point
$\mathbf{y}$	point
$\mathbf{w}$	normal vector to the hyperplane
τ_m	a margin

β_0	threshold value O the vector
$\phi(\mathbf{x})$	a non-linear product of base functions
β_i	training vectors
$K(\mathbf{x}_i, \mathbf{x})$	inner product kernel
$\phi(\mathbf{x})$	base functions
ξ_i	slack variables
$\xi_i^{'}$	slack variables
ϵ	radius band
C	cost parameter
ν_{SVM}	the function of margin errors in the training set

Errors

$\hat{\theta}$	predicted data
θ	real data
$\sigma_{\hat{\theta}\theta}$	covariance
$\sigma_{\hat{\theta}}$	standard deviation of $\hat{\theta}$
σ_{θ}	standard deviation of θ

Acronyms

2D	Two dimensional
3D	Three dimensional
FE	Finite Element
MLP	Multi Layer Perceptron
MLT	Machine Learning Techniques
ANN	Artificial Neuronal Network
SVM	Support Vector Machine
LR	Linear Regression
RE	absolute of relative error
RSQ	correlation coefficient
CT	Computed Tomography
HU	Hounsfield Units
BMU	Basic Multicellular Unit
PTH	Parathyroid Hormone
RANKL	Receptor Activator of Nuclear κB Ligand
RANK	Receptor Activator of Nuclear κB
BMP	Bone Morphogenetic Protein

FGF	Fibroblast Growth Factor
TGFβ	Transforming Growth Factor β
DEXA	Dual-Energy X-ray Absorptiometry

Capítulo I

Resumen

I.1 Introducción

Los huesos son organismos vivos que están en constante cambio. La regeneración o sustitución de material óseo es continuo en el hueso y se conoce con el nombre de remodelación ósea. En general, el hueso adapta su masa y estructura a las cargas mecánicas a las que está sometido. En situaciones normales, este proceso adaptativo asegura un buen balance entre masa ósea y resistencia.

La biomecánica es la ciencia que estudia el comportamiento de los organismos ante respuestas mecánicas. Gracias a ella, se pueden crear modelos computacionales capaces de describir la reacción de los mismos en la vida cotidiana, y así, saber cómo van a evolucionar. Estos modelos pueden revolucionar la forma en que los médicos puedan diagnosticar y tratar determinadas patologías, pudiéndose crear modelos para ayudar a desarrollar tratamientos preventivos para cada persona. Gracias a la tecnología, se es capaz de simular el comportamiento de nuestros huesos. La imagen médica puede estar contribuyendo también a este fin. Con una tomografía axial computarizada (TAC) se puede obtener una reconstrucción tridimensional de hueso y al mismo tiempo, obtener una distribución de la densidad ósea. Esto permite evaluar la calidad del hueso y estudiar comportamiento bajo diferentes acciones fisiológicas.

I.2 Modelos de remodelación ósea

Desde hace tiempo, muchos investigadores han venido estudiando la relación existente entre la estructura del hueso y las cargas a las que se encuentra sometido. En el siglo diecinueve, varios autores describieron la relación entre la forma y la función del hueso con gran detalle, siendo Wolff (Wolff, 1982) quien hizo la observación de que no sólo existe una clara relación entre la estructura ósea y la

carga, sino que el hueso como tejido vivo es capaz de adaptarse a las alteraciones de cargas que sufre de acuerdo con leyes matemáticas (Carter, 1987; Beaupré et al., 1990). Este proceso se ha venido a llamar remodelación ósea. Estudios experimentales han verificado las observaciones de la ley de Wolff mostrando que, como consecuencia de la remodelación ósea, el hueso puede adaptarse a las variaciones en las cargas, incluso en estado adulto (Huiskes et al., 1987; Beaupré et al., 1990; Doblaré and García, 2001; Prendergast and Taylor, 1994; Monnier and Trabucho, 1998).

Muchas teorías y modelos matemáticos se han desarrollado para analizar la evolución de la microestructura del hueso y sus propiedades mecánicas en función de un cierto patrón de carga. Normalmente, estos modelos han sido implementados en programas de elementos finitos (EF), y estos modelos computacionales han demostrado ser herramientas muy útiles para predecir la respuesta del hueso después de la implantación de prótesis (Doblaré and García, 2001; Folgado et al., 2008; Pérez et al., 2010; Caouette et al., 2012; Christen et al., 2012a; Webster et al., 2012; Fernández et al., 2010). Sin embargo, estos modelos se han desarrollado con carácter general, sin considerar que cada hueso o paciente son diferentes.

A pesar de la gran utilidad de estos modelos de remodelación ósea, siguen siendo unos modelos en evolución. Uno de los mayores problemas que tienen, es la falta de convergencia y estabilidad a largo plazo, lo que impide poder estudiar la evolución de estos modelos en el tiempo.

Hoy en día, el desarrollo de modelos específicos para cada paciente es cada vez más importante (Galibarov et al., 2010). Un ejemplo de esta importancia radica en la necesidad de determinar las cargas específicas que causan la distribución de la densidad del hueso del paciente, con el fin de utilizar estas cargas en el diseño de un tratamiento específico para él. Uno de los tratamientos específicos con mayor demanda en la actualidad, es la posibilidad de personalizar la colocación de una protesis para un tipo de lesión ósea determinada. Este análisis es extremadamente complejo debido a la gran cantidad de factores que en él influyen, entre ellos, relacionadas con el hueso: densidad, forma y cargas a las que está sometido Galibarov et al. (2010); y relacionadas con el paciente: edad, sexo, balance hormonal y actividad. Por ello, es necesario estudiar y mejorar los modelos de remodelación ósea, para que permitan caracterizar el comportamiento del tejido óseo y su capacidad de adaptación en función del estado mecánico o de solicitaciones al que se encuentra sometido, y de forma particular para cada paciente. Para ello, se utilizarán estos modelos validándolos con resultados experimentales, con el propósito de utilizarlos como herramienta de trabajo a la hora de predecir las alteraciones que va a sufrir el hueso cuando se incorpora una prótesis, una fijación, cargas no habituales, etc; y con ello abordar la mejora del diseño de implantes (mejor ubicación, forma, rugosidad de la superficie, material, restriciones, etc) (Pérez et al., 2006, 2010). Por ello, es necesario desarrollar modelos de remode-

lación ósea que incorporan la variación de las propiedades mecánicas internas del tejido (remodelación ósea interna).

Tradicionalmente, las cargas a las que está sometido el hueso se han obtenido mediante plataformas de carga, determinando por ejemplo las cargas que soporta el fémur durante el proceso de caminar (Vahdati et al., 2014). Este proceso de obtención de cargas, es muy costoso y laborioso; y además, las cargas que utiliza cada individuo presentan una gran variabilidad. Un gran avance sería a partir las densidades que tienen nuestros huesos, determinar las cargas que las han generado (Fischer et al., 1995, 2003; Bona et al., 2003, 2006). Es por ello de vital importancia, desarrollar herramientas capaces de determinar las cargas a las que está sometido el hueso de cada paciente.

Existen diferentes estrategias numéricas basadas en modelos inversos que son capaces de estimar las cargas. Este problema inverso se ha resuelto con anterioridad por diversos autores con diferentes enfoques numéricos. De hecho, Fischer et al. (1995) desarrollaron un procedimiento de optimización que ajusta la magnitud de cada carga básica para lograr la densidad ósea deseada. Este enfoque se aplicó a la sección proximal del fémur en 2D para determinar las cargas utilizando datos del TAC (Fischer et al., 1998, 1999). Bona et al. (2006) propusieron un algoritmo de contacto para la estimación de cargas basado en la densidad y utilizaron el método para distinguir entre las diferentes maneras de locomoción de los animales. Más recientemente, Christen et al. (2012a) han desarrollado un algoritmo de estimación de cargas en el hueso para predecir condiciones de carga basadas en la historia de carga que produce la energía de deformación en el tejido óseo.

Todos estos enfoques anteriores se basaban en técnicas iterativas de predicción de carga, lo que implica un coste computacional significativo. A fin de acortar el tiempo de cálculo computacional, se han desarrollado diferentes técnicas matemáticas. Muchos investigadores han estado tratando de resolver los diferentes problemas inversos en biomecánica mediante el desarrollo de controladores que emplean métodos de computación inteligentes, como las redes neuronales artificiales (ANN), redes neuronales difusas (NF), máquinas de regresión por medio de Vectores de Soporte, (SVR), algoritmos genéticos o redes de ondas (Goulermas et al., 2005; Liu et al., 2009; Favre et al., 2012; Cilla et al., 2012; Behrens et al., 2009). Hambli et al. (2011) (Hambli, 2011b,a), desarrollaron una metodología multiescala para la simulación de la remodelación ósea utilizando elementos finitos y combinándolo con ANN. Sin embargo, Campoli et al. (2012) fueron de los primeros en utilizar las ANN para la predicción de cargas del fémur mediante la distribución de la densidad ósea. Combinaron una técnica de descomposición de ondas con una red neuronal artificial (ANN) para la estimación de los parámetros de carga del fémur.

I.3 Motivación, objetivos y organización de la Tesis

Motivación

La principal motivación de esta tesis es desarrollar modelos de remodelación ósea capaz de ayudar en un entorno clínico. Existen varios modelos teóricos que describen con precisión el comportamiento del hueso, aunque no todos ellos, satisfacen las demandas de los pacientes. El reto de los modelos de remodelación es proporcionar información útil para el investigador y, en consecuencia, para el paciente. Por ello, estas nuevas y prometedoras técnicas pueden proporcionarnos información útil, como la calidad del hueso, su comportamiento, predecir el riesgo de fractura y en caso de tener una prótesis, su vida útil.

Por eso, es necesario avanzar hacia una metodología numérica para el modelado óseo, ayudando a entender el comportamiento de los huesos. Actualmente, hay varios modelos de remodelación ósea que presentan problemas con el estudio de la evolución de la distribución ´ósea en pacientes concretos. Ádemas, estos modelos támbien plantean problemas de estabilidad y convergencia a largo plazo. Para ello, la creación de modelos remodelación ósea de paciente específico sería muy interesante.

Resumiendo, estas metodologías deben ayudar en un ambiente clínico. Nos puede dar información sobre qué prótesis va a ser la más apropiada para un paciente a lo largo plazo y cuál va a producir la mejor distribución de las cargas a través de esta prótesis para aumentar la vida de hueso, la vida útil de la prótesis y, finalmente, una mejor calidad de vida para el paciente. Todas estas características pueden proporcionar un ahorro de costes y una mejora de la salud. En consecuencia, estas metodologías pueden ser útiles en cirugía virtual y proporcionarnos toda la información sobre el tratamiento y la evolución ósea un paciente.

Esta tesis doctoral ha estado involucrada en el proyecto europeo CAD-BONE: Patient-specific predictions for bone treatments (Marie Curie Industry-Academia Partnerships and Pathways / FP7-PEOPLE-2011-IAPP) (http://cadbone.unizar.es/) cuyo principal objetivo es desarrollar una investigación multidisciplinar que se traducirá en tecnologías que van a mejorar radicalmente el desarrollo de modelos computacionales de paciente específico para modelar de la adaptación/curación del hueso después de la implantación de prótesis en las aplicaciones musculoesqueléticas. El principal propósito the CADBONE es demostrar la viabilidad de la integración de modelado de paciente específico, cargas musculoesqueléticas y análisis adaptativo de remodelación ósea para simular el resultado funcional de los tratamientos de los pacientes. Además, esta investigación estuvo involucrada en el Proyecto Nacional titulado “Design and development of a computational tool for the personalised risk fracture prediction in Osteoporotic patient” y subvencionado por el Ministerio Español de Economía y Competitividad (DPI 2011-22413).

Objetivos

El objetivo principal de esta Tesis es el estudio de los modelos de remodelación ósea, mostrando sus retos, su problemática, así como, su aplicación en el ámbito clínico.

Con el fin de conseguir este objetivo, un modelo computacional que permita predecir la distribución de la densidad ósea ha sido desarrollado, mejorando así, los modelos previos. Posteriormente, estos modelos de remodelación se han utilizado en el proceso inverso para obtener diferentes metodologías que pueden predecir las cargas que el hueso está realmente soportando. Por ello, el objetivo final es aplicar esta metodología en casos clínicos y la información obtenida puede ayudar en futuros tratamientos del hueso. Para lograr esto, diversos objetivos secundarios han sido definidos:

- Estudiar las diferentes teorías de remodelación ósea, su problemática y sus limitaciones. Para ello, desarrollamos un modelo de remodelación ósea capaz de simular la evolución de la distribución de la densidad ósea en un modelo paciente específico. En particular, modificamos el algoritmo de Stanford (Jacobs, 1994) y el modelo anisotrópo de remodelación ósea (Doblaré and García, 2002; Mengoni and Ponthot, 2015), basándonos en que el estímulo homeostático de referencia dependerá ahora de la historia de carga que cada punto está soportando. Se pretende mejorar la estabilidad de los resultados numéricos correspondientes a la distribución de la densidad y en consecuencia, la convergencia del algoritmo. Además, realizar un análisis teórico para demostrar la convergencia lineal del algoritmo de remodelación ósea, incorporando que el estímulo homeostático de referencia no es constante. Y finalmente, se va a estudiar la fuerte dependencia de las condiciones iniciales en los modelos de remodelación ósea y se desarrollará un método capaz de disminuir esta dependencia.

- Desarrollar una metodología para la obtención de las cargas que el hueso de un paciente concreto soporta. Para ello, desarrollamos, evaluamos y comparamos tres enfoques numéricos existentes para estimar las cargas musculoesqueléticas en el fémur, con el fin de resolver adecuadamente el problema de remodelación ósea inverso. Específicamente, nos centramos en dos diferentes técnicas de aprendizaje automáticas (MLT): perceptrón multicapa (MLP) incluido en las redes neuronales artificiales (ANN) y las máquinas de vector soporte (SVM), comparando estos resultados con una técnica clásica: la regresión lineal (LR).

- Demostrar la importancia de los modelos de remodelación ósea en un caso clínico. Para ello, aplicamos todas las metodologías desarrolladas previa-

mente en cinco tibias específicas de las que conocemos su geometría ósea y su distribución de densidad gracias a los datos del TAC. Con todo esto, se va a predecir la condiciones de cargas específicas de la tibia. Finalmente, para evaluar cuantitativamente la capacidad predictiva de esta novedosa metodología, se comparan estas cargas con las cargas obtenidas para cada paciente a partir de un análisis de la marcha individual.

Estructura

Esta tesis está organizada en siete capítulos de la siguiente manera:

Las principales características del modelo de remodelación ósea se presentan en el Capítulo 2. Una revisión de los modelos de remodelación ósea se proporciona, con especial énfasis, en los modelos fenomenológicos como el de Stanford (Jacobs, 1994) y el modelo anisotropo de Doblaré and García (2002), así como en su formulación.

En el Capítulo 3, presentamos un novedoso modelo de remodelación ósea que considera que el estímulo de referencia es dependiente de la historia de carga. Por ello, realizamos un análisis teórico para demostrar la convergencia lineal del algoritmo de remodelación ósea. Y finalmente, se realiza una evaluación cuantitativa y cualitativa del modelo comparándolo con el modelo original de Stanford y el modelo anisótropo (Mengoni and Ponthot, 2015).

Además, en el Capítulo 4 continuamos con las limitaciones de los modelos de remodelación ósea. Por ello, evalúamos la dependencia de las condiciones iniciales y se presenta otro novedoso modelo de remodelación ósea que supera esta problemática. Mostramos la importancia de la relación entre las escalas micro-macro, relacionando los estímulos mecánicos macroscópicos con estímulo local o celular.

El Capítulo 5 contiene una revisión de las herramientas matemáticas basadas en MLT, como ANN y SVM. Estas herramientas matemáticas han sido utilizados para la creación de una metodología que permite la estimación de las cargas que soporta cada hueso específico. Asimismo, una comparación del rendimiento de estas técnicas (SVM y ANN) con la regresión lineal clásica se muestra, con el fin de resolver el problema inverso. Además, explicamos todas las metodologías para la obtención de los datos para realizar la metodología inversa. Esta herramienta computacional ha sido entrenada con los resultados obtenidos en un modelo 2D y 3D de Elementos Finitos de un fémur.

Posteriormente, en el Capítulo 6 aplicamos todas las metodologías anteriores en diferentes casos clínicos. Para ello, seleccionamos cinco tibias de paciente específico, en colaboración con el Laboratorio de Investigación Ortopédica (ORL) en Nijmegen y Laboratorio de Ingeniería Biomecánica de la Universidad de Twente (Países Bajos). A partir de datos individuales del TAC, obten-

emos su geometría y su distribución ósea. Los modelos de elementos finitos son construidos y se usados para la obtención de la distribución de densidad con múltiples condiciones de cargas a través de diferentes modelos de remodelación ósea. A continuación, estos datos se utilizan como entradas para las herramientas numéricas. Por último, con el fin de validar el rendimiento de las redes neuronales (ANN) para la predicción de las cargas en la tibia, comparamos las cargas predichas de paciente específico con las cargas obtenidas a partir del modelo musculoesquelético del paciente específico de un análisis de la marcha.

Por último, las principales conclusiones de este trabajo, junto con un breve resumen con las aportaciones originales presentadas a lo largo de esta tesis y las futuras líneas de trabajo, se recogen en el Capítulo 7.

Además, en este Capítulo, de acuerdo con las directrices de la Universidad de Zaragoza, para obtener el graduado de Doctor Europeo (art. 15 RD 99/2011), se presenta un resumen en español de la Tesis. Este resumen contiene la motivación, estructura, objetivos y metodología de la Thesis, así como las principales conclusiones, contribuciones originales y futuras líneas de este trabajo.

I.4 Resumen del trabajo realizado

El objetivo principal de esta tesis ha sido el estudio del comportamiento del hueso durante el proceso de remodelación a través de modelos computacionales, teniendo en cuenta su problemática, sus retos y sus aplicaciones. Con este propósito, se ha desarrollado una metodología computacional ha sido desarrollada, capaz de evaluar la densidad ósea de un paciente específico y predecir las cargas que este hueso está soportando.

Primero, se ha estudiado dos modelos de remodelación ósea clásicos, uno isótropo (modelo de Stanford) y otro anisótropo (modelo de Doblaré y García). En ambos casos, se muestra un análisis matemático completo mostrando sus resultados. Después, se ha presentado algunos problemas matemáticos del modelo anisótropo y se expone una extensión de la ley previa con mejoras en el proceso de reabsorción (Mengoni and Ponthot, 2015).

Posteriormente, en el Capítulo 3 y 4, se ha justificado que los modelos de remodelación ósea actuales presentan algunas limitaciones numéricas. Muchos investigadores han tratado de encontrar las leyes matemáticas más adecuadas para describir el comportamiento del hueso, sin que ninguno realizará un análisis completo. En esta tesis, se han propuesto dos hipótesis novedosas que mejoran los modelos de remodelación. Actualmente, en el Capítulo 3, se ha modificado el modelo de Stanford (Jacobs, 1994) y el modelo de Doblaré y García (Doblaré and García, 2002), basándonos en que el estímulo homeostático de referencia depende actualmente, de la historia de cargas que cada punto está soportando. Para ello, se

ha considerado que el estímulo de referencia no es constante y va cambiando con la densidad aparente. Esta modificación mejora la estabilidad de los resultados numéricos correspondientes a la distribución de la densidad y en consecuencia, la convergencia del algoritmo. Este algoritmo ha sido probado en modelos 2D y 3D de Elementos Finitos donde se demuestra que la densidad alcanza un equilibrio espacio-temporal.

Además, se ha planteado un análisis matemático para demostrar la convergencia lineal del algoritmo isótropo de la remodelación ósea, incorporando el supuesto anterior donde el estímulo homeostático de referencia es no constante. Por último, en los resultados se ha demostrado claramente que esta modificación mejora ambos modelos de remodelación ósea. Además, puede ayudar al estudio de la evolución de la densidad a largo plazo.

Otra modificación ha sido propuesta en el Capítulo 4 donde se ha estudiado la fuerte dependencia de las condiciones iniciales en los modelos de remodelación ósea y se ha desarrollado un método capaz disminuir esta dependencia. Para ello, se ha modificado la relación entre el nivel de órgano y el nivel de tejido a través de una nueva ecuación, donde el estímulo homeostáticos de referencia cambia acorde con la densidad; y la energía efectiva de tejido permanece invariable. Esta modificación mejora la unicidad de la solución, la independencia de las condiciones iniciales selecionadas y claramente, ayuda a su estabilidad numérica.

Por otro lado, se ha mostrado como estos modelos pueden ser aplicados a pacientes concretos. En primer lugar, se ha desarrollado una metodología general para la obtención de las cargas que el hueso soporta. Con este propósito, se ha desarrollado tres diferentes técnicas matemáticos para la predicción de las cargas: las redes neuronales artificiales (ANN), las máquinas de soporte vector (SVM) y la regresión lineal. Estas técnicas permiten obtener los casos de carga que el hueso soporta en un breve periodo de tiempo. Para ello, los tres modelos matemáticos han resuelto el problema inverso a través de una alta cantidad de datos obtenidos de diferentes modelos de remodelación ósea. Después de un proceso iterativo, las redes neuronales (ANN) y la regresión lineal han demostrado una buena predicción teórica de cargas con un error relativo bajo. Sin embargo, las máquinas de vector soporte (SVM) ha presentado problemas de precisión con la predicción de las cargas. Debido a la buena precisión de las redes neuronales (ANN), hemos desarrollado esta tecnología con múltiples salidas y en una geometría tridimensional de un fémur real, obteniendo resultados similares. Además, se ha realizado un análisis de sensibilidad con diferentes entradas y diferentes número de casos. Finalmente, se ha estudiado el coste computacional del proceso de entrenamiento.

Siguiendo la metodología propuesta en el Capítulo 5, se ha estudiado a cinco casos clínicos reales en el Capítulo6. Para ello, se ha presentado un metodología capaz de predecir las fuerzas que una tibia de cinco paciente diferentes, está soportando. Estos datos han sido obtenidos utilizando la geometría específica y

la distribución de la densidad ósea generada por un TAC. Posteriormente, se ha obtenido las cargas mediante la introducción de la densidades y los volumenes de ciertas regiones de interés (ROI) del TAC en nuestro modelo predictivo. Las cargas predichas se han comparado con las cargas obtenidas a partir del análisis de la marcha del paciente. La comparación entre las fuerzas predichas y las de la marcha ha demostrado la buena predicción, especialmente en la fuerza vertical (fuerza principal). Sin embargo, las fuerzas resultantes de las direcciones horizontal (Fx y Fz) no se predijeron con mucha exactitud. Los resultados son muy prometedores y podrían ser trasladados a la práctica clínica

I.5 Conclusiones

En resumen, las principales conclusiones de esta tesis se agrupan y se pueden resumir de la siguiente manera:

- *Modelos de remodelación ósea*

  - Los modelos de remodelación ósea presentan importantes limitaciones numéricas.
  - El estímulo homeostático de referencia es uno de los principales parámetros clave que controlan la distribución ósea y no puede mantenerse constante.
  - Cambiando el estímulo homeostático de referencia acorde con la historia de carga, se consigue mejorar la estabilidad de la distribución de la densidad en los modelos de remodelación ósea.
  - Hay una fuerte dependencia de las condiciones iniciales en los modelos de remodelación ósea.
  - La relación entre el nivel micro (tejido) y el nivel macro (órgano) no es clara. Existen múltiples relaciones en la literatura y es necesario desarrollar un método capaz de afrontar todas variables (Colloca et al., 2014).
  - Un cambio de multiescala adecuado permite mejorar la estabilidad en la distribución de la densidad ósea tanto en términos a nivel micro como a nivel macro, y en consecuencia, permite obtener las soluciones independientes de las condiciones iniciales.
  - En los modelos modificados de multiescala para la geometría 2D se ha obtenido poco cortical. Este fenómeno puede ser justificado por la baja carga aplicada en la simulación numérica. Por el contrario, en el

caso 3D, el cortical es ligeramente inferior a los modelos originales pero conseguiendo resultados más similares a las radiografías.

- *Técnicas matemáticos para estimar las cargas*

  - La predicción de las cargas en el fémur ha sido lograda mediante la integración de dos metodologías de ingeniería complementarias: algoritmos de remodelación ósea a través del modelado por elementos finitos (FE) y el problema de remodelación ósea inversa a través de diferentes técnicas matemáticas.
  - Las técnicas de aprendizaje automático son una técnica precisa para resolver el problema inverso remodelación ósea.
  - Las redes neuronales artificiales (ANN) y la regresión lineal representan unas poderosas herramientas para predecir las condiciones de carga en el fémur.
  - La relación entre la distribución de la densidad y de las cargas es casi lineal.
  - Las máquinas de vector soporte (SVM) presenta peores resultados debido a la linealidad de los datos.
  - Las redes neuronales artificiales (ANN) presentan múltiples opciones para obtener el resultado como con salidas individuales o múltiples.
  - El número de datos para el entrenamiento influye en el coste computacional, y no implica la optimización del problema.

- *Cargas musculoesqueléticas de paciente específico de la tibia*

  - Hay una clara relación entre los valores de densidad, los valores de fuerza de paciente específico y la geometría concreta del paciente.
  - Los modelos de remodelación ósea predicen adecuadamente la distribución de la densidad en relación con la escala de grises proveniente del TAC.
  - Es posible obtener la carga en un paciente con técnicas no invasivas.
  - La metodología presentada en este trabajo abre una nueva estrategia para la creación sistemática de modelos de paciente específico, facilitando su aplicación clínica.

I.6 Contribuciones originales

Hasta donde sabemos, algunos aspectos de esta tesis son completamente novedosos y las aportaciones originales más importantes son las siguientes:

- Una formulación para los modelos de remodelación de hueso que asegura la estabilidad de los resultados numéricos correspondientes a una distribución espacial de la densidad aparente y en consecuencia, garantiza la convergencia del modelo. En esta formulación, el algoritmo adapta el estímulo homeostático de referencia de acuerdo a las cargas soportadas.

- Un análisis teórico se ha realizado para demostrar la convergencia lineal del algoritmo de la remodelación ósea incorporando que el estímulo homeostático de referencia no es constante.

- Formulación y desarrollo de un novedoso modelo de remodelado óseo basado en la adaptación de la escala a nivel órgano y a nivel tejido. Esta novedosa relación considera que el estímulo homeostático de referencia depende de la densidad aparente, y la energía de tejido se mantiene constante durante todo el proceso, mejorando así, la independencia de las condiciones iniciales.

- Una metodología para obtener las cargas que soporta el hueso a través de tres enfoques numéricos: redes neuronales artificiales (ANN), máquinas de vectores de soporte (SVM) y regresión lineal (LR). Para ello, es necesario combinar multiples modelos de remodelación ósea que son los datos iniciales para la metodología.

- Una metodología que combina los modelos de remodelación ósea, redes neuronales artificiales y análisis de imágenes médicas es capaz de predecir las cargas de paciente específico en la tibia.

I.6.1 Publicaciones en revistas

Las publicaciones en revistas internacionales realizadas durante el período de la tesis se enumeran a continuación:

1. **N. Garijo**, J. Martínez, J. M. García-Aznar, M.A. Pérez. Computational evaluation of different numerical tools for the prediction of proximal femur loads from bone morphology. *Comput. Methods Appl. Mech. Engrg.* 268, 437-450, 2014. (Capítulo 5).

2. **N. Garijo**, J.R. Fernández, M.A. Pérez, J.M. García-Aznar. Numerical stability and convergence analysis of bone remodeling model. *Comput. Methods Appl. Mech. Engrg.* 271 253-268, 2014. (Capítulo 3).

3. **N. Garijo**, N. Verdonschot, J.M. García-Aznar, M.A. Pérez. Subject-Specific musculoskeletal loading of the tibia: Computational load estimation. *Bone*. *(Enviado)* (Capítulo 6).

4. **N. Garijo**, M.A. Pérez, J.M. García-Aznar. A multiscale modeling approach based on the stability. *(En preparación)*.(Capítulo 4).

I.6.2 Contribuciones a congresos y conferencias

Las siguientes comunicaciones en congresos se han presentado durante el desarrollo de este Tesis:

1. **N. Garijo**, M. Remacha, A. Alberich-Bayarri, J.M. García-Aznar, M.A. Pérez. Patient-specific simulations of human bones: CT data and bone remodelling models. Presentación oral. *Materialise World Conference 2012*. LEUVEN (BÉLGICA). Abril 2012

2. **N. Garijo**, A. Alberich-Bayarri, M.A. Pérez. Patient-Specific simulation of the human radius. Presentación oral. 18^{th} *Congress of the European Society of Biomechanics (ESB)*. LISBON (PORTUGAL). Julio 2012

3. **N. Garijo**, J. Martínez, J.M. García-Aznar, M.A. Pérez. Different mathematical techniques to estimate femur loads. Presentación oral. *Second meeting of the Spanish National Chapter of the European Society of Biomechanics (CapESB-SP)*. SEVILLA (ESPAÑA). Octubre 2012

4. **N.Garijo**, M.J. Gómez-Benito, M. Remacha, M.A. Pérez, J.M. García-Aznar. CAD-BONE: analysis and design of our bones. Presentación oral. *Congress: Researchers' Night 2012*. ZARAGOZA (ESPAÑA). Septiembre 2012

5. **N. Garijo**, J. Martínez, J.M. García-Aznar, M.A. Pérez. Different numerical approaches for the prediction of proximal femur loads. Presentación oral. 19^{th} *Congress of the European Society of Biomechanics (ESB)*. PATRAS (GRECIA). Agosto 2013

6. **N. Garijo**, J. Martínez, J.M. García-Aznar, M.A. Pérez. Different numerical approaches for the prediction of proximal femur loads. Presentación oral. *V International Conference on Computational Bioengineering (ICCB)*. LEUVEN (BÉLGICA). Septiembre 2013

7. **N. Garijo**, S. Walscharts, M.A. Pérez, L. Vigneron, J.V. Sloten, G.H. van Lenthe, J.M. García-Aznar. Towards the creation of patient-specific bone

remodeling models. Presentación oral. *V International Conference on Computational Bioengineering (ICCB)*. LEUVEN (BÉLGICA). Septiembre 2013

8. **N. Garijo**, M.A. Pérez, J.M. García-Aznar. Bone remodeling simulations: challenges, problems and applications. Poster. 7^{th} *World Congress of Biomechanics (WCB)*. BOSTON (USA). Julio 2013

9. **N. Garijo**, A. Vahdati, G.H. van Lenthe, M.A. Pérez, J.M. García-Aznar. Numerical algorithms for Patient-specific predictions of proximal femoral loads. Presentación oral. 12^{th} *International Symposium on Computer Methods in Biomechanics and Biomedical Engineering (CMBBE)*. AMSTERDAM (PAÍSES BAJOS). Octubre 2014

10. **N. Garijo**, M.A. Pérez, J.M. García-Aznar. Stability of bone remodeling models. Presentación oral. 12^{th} *International Symposium on Computer Methods in Biomechanics and Biomedical Engineering (CMBBE)*. AMSTERDAM (PAÍSES BAJOS). Octubre 2014

11. **N. Garijo**, M.A. Pérez, J.M. García-Aznar. An efficient approach for the stability of bone remodeling models. Presentación oral. 21^{th} *Congress of the European Society of Biomechanics (ESB)*. PRAGUE (REPÚBLICA CHECA). Julio 2015

I.7 Líneas futuras de trabajo

La variedad de enfoques presentados en esta Tesis es sólo una pequeña contribución a la comprensión de la conducta adaptativa del hueso. Los resultados y conclusiones obtenidas a lo largo de este trabajo plantean nuevas preguntas y sugiere nuevas posibles líneas de investigación que necesitan ser exploradas. Las más importantes se describen a continuación:

- Análisis probabilístico de los modelos de remodelación ósea.

  Mejorar los modelos de remodelación de cambiando las variables "teóricas" como la zona muerta, para predecir más adecuadamente la densidad ósea, y comparar estas variables con valores experimentales.

- Remodelación ósea después de la implantación de una prótesis.

  Aplicar los modelos de remodelación ósea previamente mejorados, para estudiar y predecir la evolución de la densidad ósea después de la colocación de una prótesis. Los modelos previos presentan problemas para estudiar

como afecta la colocación de una prótesis a largo plazo. La metodología propuesta permite estudiar la densidad en el largo plazo, así como la pérdida de densidad en diferentes regiones. Esto puede ayudar a mejorar el diseño y el posicionamiento de las prótesis.

- Mejorar la metodología de las redes neuronales (ANN).

  Obtener una base de datos pacientes específicos para incrementar la aplicabilidad de la metodología de las redes neuronales basada en casos clínicos y que permitan mejorar la predicción.

  Mejorar la metodología que permite la retroalimentación con nuevos datos.

  Introducir nuevas variables en las técnicas de redes neuronales (ANN) como la edad, peso, sexo, ... para la obtención de una mejor predicción de la carga y aplicar esta metodología a otros huesos largos.

  Extrapolar el modelo, con fin de acelerar las simulaciones de remodelación ósea y obtener la predicción de carga en breve periodo de tiempo.

  Estudiar la anisotropía en el análisis de imagenes para mejorar la comparación con los resultados computacionales, y disminuir el error en la metodología de predicción.

CHAPTER 1

Introduction

During the daily activities, the bones of the skeleton, individually and collectively, are subjected to a variety of forces. The response of the bones to these forces is a function, to a large extent, of the mechanical properties of the bones. Of course, the type, magnitude, direction and point of application of the forces as well as, whether or not it is applied slowly, rapidly, repetitively, or for a long duration must also be considered. Additional variables should also be included, whether the bone is living or dead, embalmed or fresh, and the age, sex, race and species of animal from which the bone is obtained. The specific bone and part of the bone being studied, as well as its microscopic structure, influence its mechanical properties. Although other environmental variables such as moisture and temperature, also determine these bone properties.

1.1 Introduction

Bones are living organisms whose main function is to form the skeleton and therefore support and protect various organs of the body. Bones come in a variety of shapes and sizes, have a complex internal and external structure, are lightweight yet strong and hard, and perform multiple functions. Among the functions, bones have to bear the load weight of the body and the muscle forces that control their movements. In consequence, they are subjected to permanent and transient loads caused by daily activity or specific events such as impact in accidents. As a living material, bone is able to respond differently to these loads. In addition, when a bone fracture occurs, healing mechanisms are activated in order to recover its functionality. Conversely, in order to react to these specific events, bone is able to continuously maintain and adapt bone mass by an enduring process, termed as remodeling. Several mechanical and biochemical factors may regulate the final

bone remodeling response. In fact, bone remodeling is hypothesized to achieve several mechanical objectives: repair damage to reduce the risk of fracture and optimize stiffness and strength with minimum weight (Doblaré et al., 2004). For all these reasons, bone is a material not easy to model.

Additionally, patient-specific analysis of bone is considered an important tool for diagnosis and treatment of skeletal diseases and for clinical research aimed at understanding the etiology of skeletal diseases and the effects of different types of treatments on their progress (Zadpoor and Weinans, 2015). In the literature, there are research works that study how integration of several important components enable accurate and cost effective patient-specific bone analyses (Mohaghegh et al., 2014).

Therefore, in the following sections, a review of bone behavior is presented, modeling aspects of bone tissue mechanics are briefly introduced and the importance of patient-specific bone analyses and automation of modeling approaches are discussed. Finally, the main aim and outline of this thesis is presented.

1.2 Bone tissue mechanics

1.2.1 Bone and its internal structure

The bony skeleton is a remarkable organ that serves both a structural function-providing mobility, support, and protection for the body, and a reservoir function, as the storehouse for essential minerals. It is not a static organ, but is constantly changing to better carry out its functions. The architecture of the skeleton is remarkably adapted to provide adequate strength and mobility so that bones do not break when subjected to substantial impact, even the loads placed on bone during vigorous physical activity. The shape or structure of bone is at least as important as its mass in providing this strength.

The skeletal body have multiples of shapes and sizes (Figure 1.1). Although most of the time in this Thesis, we will refer to long bones, we can classify bones as according to their size in 5 types (Gray, 1918):

- Long bones are some of the longest bones in the body, such as the femur, humerus and tibia but there are also some of the smallest including the metacarpals, metatarsals and phalanges. The classification of a long bone includes having a body which is longer than its width, with growth plates (epiphysis) at either ends, having a hard outer surface of compact bone and a spongy inner known as cancellous bone containing bone marrow. Both ends of the bone are covered in hyaline cartilage to protect the bone and help shock absorption.

- Short bones are defined as being approximately as wide as they are long and have a primary function of providing support and stability with little movement. Examples of short bones are the carpals and tarsals, the wrist and foot bones. They consist of only a thin layer of compact, hard bone with cancellous bone on the inside along with relatively large amounts of bone marrow.

- Flat bones are as they sound, strong, flat plates of bone with the main function of providing protection to the bodies vital organs and being a base for muscular attachment. The classic example of a flat bone is the scapula (shoulder blade). The sternum (breast bone), cranium (skull), os coxae (hip bone) pelvis and ribs are also classified as flat bones. Anterior and posterior surfaces are formed of compact bone to provide strength for protection with the centre consisting of cancellous (spongy) bone and varying amounts of bone marrow. In adults, the highest number of red blood cells are formed in flat bones.

- Irregular bones are those in the body which do not fall into any other category, due to their non-uniform shape. Good examples of these are the vertebrae, sacrum and mandible (lower jaw). They primarily consist of cancellous bone, with a thin outer layer of compact bone.

- And finally, sesamoid bones are usually short or irregular bones, imbedded in a tendon. The most obvious example of this is the patella (knee cap) which sits within the patella or quadriceps tendon. Other sesamoid bones are the pisiform (smallest of the carpals) and the two small bones at the base of the first metatarsal. Sesamoid bones are usually presented in a tendon where it passes over a joint which serves to protect the tendon.

Bone has a complex hierarchical microstructure (Rho et al., 1998; Hellmich et al., 2004; Cowin and Cardoso, 2015) that can be considered at many dimensional scales (Figure 1.2). From a macroscopic point of view, bone tissue is nonhomogeneous, porous and anisotropic and can be classified into two types: compact and cancellous bone (Cowin and Doty, 2007).

Compact or cortical bone forms the outer layer of all bones (Figure 1.2). This type of bone is very dense and strong and therefore, it is more resistant to fracture. Its primary purpose is providing structural support to the body and its organs and tissues. Compact or cortical bone, is made up many by rod-like units called osteons or Haversian systems which run longitudinally within the bone. Haversian systems have a central Haversian canal which carries blood and lymphatic vessels and nerve branches. Cortical bone is denser with a porosity ranging between

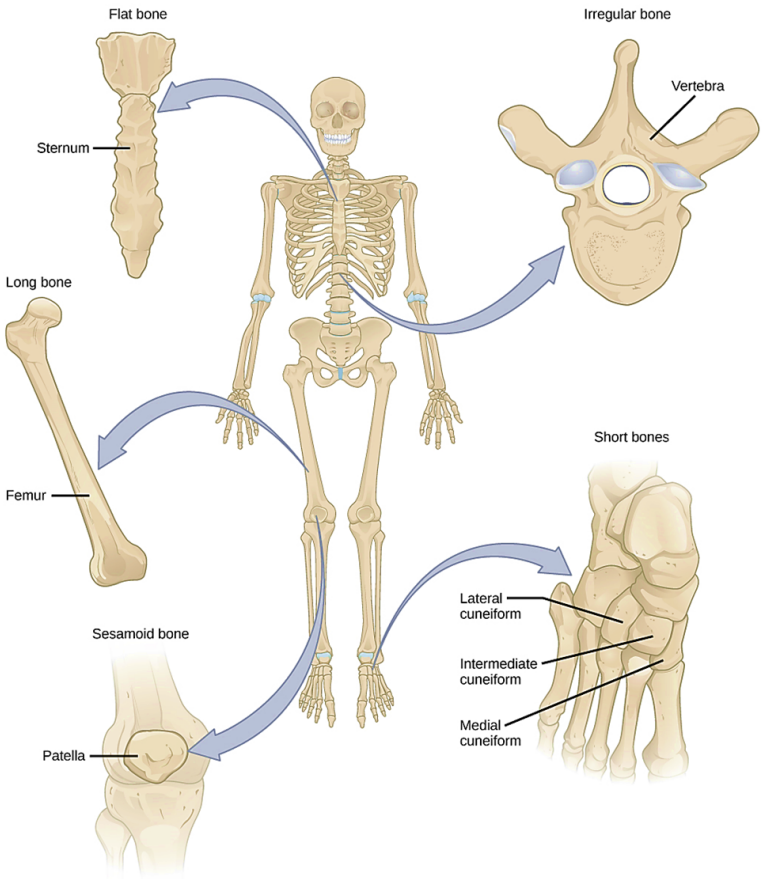

Figure 1.1: *Types of bones based on its size (Molnar and Gair, 2013)*

5 – 10% and is found primarily in the shaft of long bones and surrounding the trabecular bone forming the external shell of flat bones.

Cancellous is also known as spongy or trabecular bone because it resembles a sponge or honeycomb (Figure 1.2). Cancellous bone makes up about 20% of the typical adult human skeleton. Trabecular bone has a porosity ranging from 45 – 95% and is found in the end of long bones, in vertebrae and flat bones. The pores are interconnected and filled with marrow while the bone matrix has the form of plates and struts called trabeculae.

Bone strength depends upon both macro- and microarchitectural characteristics. The primary macroarchitectural components are bone length, diameter and cortical thickness. Additionally, the cross-sectional shape and distribution of bone mass within this cross-section are important (Martin, 1991). At the microarchitectural level, fiber along with trabecular spacing, connectivity, and alignment are the important components that determine bone strength (Turner et al., 1994).

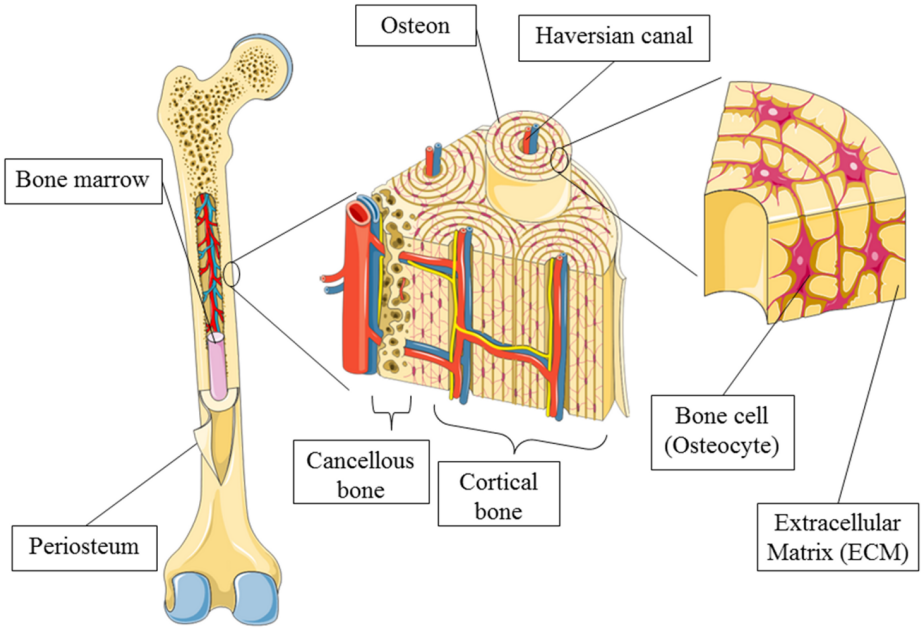

Figure 1.2: *Illustration of a long bone, depicting gross overview, and cellular distribution (taken from Bao et al. (2013)).*

1.2.2 Biology of bone remodeling

Bones are living tissues that are constantly changing. The regeneration or replacement of bone tissue is continuous in order to maintain stability, and this process is known as bone remodeling (Sheng et al., 2014). In general, the structure and bone mass are adapted to mechanical loads that they are supporting. In normal situations, this adaptive process ensures a good balance between bone mass and strength. About 10% of bone mass is being renewed every year. This process involves bone resorption, the removal of minerals and collagen fibers from bone (destruction of bone extracellular matrix), followed by bone deposition, the formation of bone matrix that subsequently becomes mineralized (Figure 1.4). Then, bone remodeling serves to adjust bone architecture to meet changing mechanical needs and it helps to repair microdamages in bone matrix preventing the accumulation of old bone (García-Aznar et al., 2005).

At the cellular level, bone remodeling occurs over several weeks and is performed by clusters of bone-resorbing osteoclasts and bone-forming osteoblasts arranged within temporary anatomical structures known as “basic multicellular units” (BMUs) (Figure 1.3). Traversing and encasing the BMU is a canopy of cells that creates a bone remodeling compartment (Hauge et al., 2001).

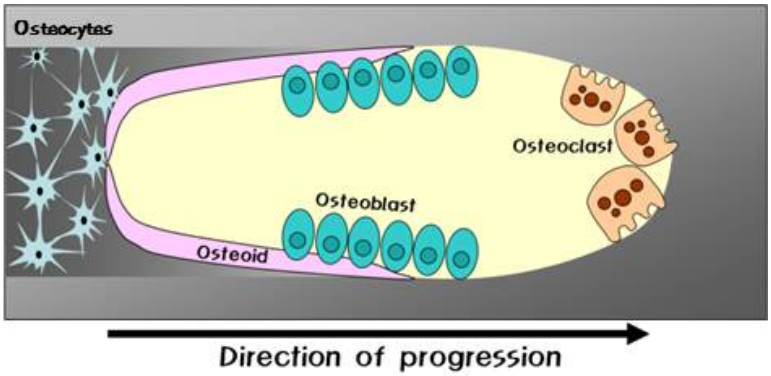

Figure 1.3: *Schematic diagram of basic multicellular unit (BMU). Histologically the BMU consists of 1) osteoclastic frontor osteogenic front, 2) reversal phase mononucleocytes, 3) osteoblastic layer. It is observed in the Haversian system of the cortical bone which is under the physiological loading such as the masticatory function. The osteoblasts are exclusively intraosseous Haversian system osteoblasts reacting to the load (Lee, 2011).*

An osteoclast is a type of bone cell that resorbs bone tissue and this function is critical in the maintenance and repair of compact bones. This cell is in front of the active BMU and the process is known as bone resorption.

In the process of bone formation, osteoblasts are cells with single nuclei that synthesize bone. However, these cells function in groups and all must be connected. Osteoblasts occupy the tail portion of the BMU and secrete and deposit unmineralized bone matrix known as osteoid and direct their formation and mineralization into mature lamellar bone.

Osteoclasts and osteoblasts are instrumental in controlling the amount of bone tissue (Figure 1.4): osteoblasts form bone, osteoclasts remove bone. And finally, osteocyte is a cell that lies within the matrix of fully formed bone. It occupies a small chamber called lacunae, which is contained in the calcified matrix of bone. Osteocytes derive from osteoblasts, and are essentially osteoblasts surrounded by the products they secreted. Therefore, osteocytes are the mechanosensory cells of bone and play a pivotal role in functional adaptation of bone.

This unique spatial and temporal arrangement of cells within the BMU is critical to bone remodeling, ensuring coordination of the distinct and sequential phases of this process: activation, resorption, reversal, formation, and termination, which are discussed below and illustrated schematically in Figure 1.4.

- **Activation Phase**

  The first stage of bone remodeling involves detection of an initiating remodeling signal. This signal can take several forms, e.g. direct mechanical strain on the bone that results in structural damage or hormone (e.g. estrogen or parathyroid hormone (PTH)) action on bone cells in response to more systemic changes in homeostasis. As a consequence, lining cells, increase their own surface expression of RANKL (Receptor Activator of Nuclear κ B Ligand), which in turn interacts with its receptor RANK (Receptor Activator of Nuclear κ B), expressed by pre-osteoclasts. RANKL/ RANK interaction triggers pre-osteoclasts fusion and differentiation toward multinucleated osteoclasts (Zaidi et al., 1989; Matsuo and Irie, 2008).

- **Resorption Phase**

  Once differentiated, osteoclasts polarize, adhere to the bone surface and begin to dissolve bone. This function requires two steps: i) acidification of the bone matrix to dissolve the inorganic component, and ii) release of lysosomial enzymes, both in charge for the degradation of the organic component of bone. Once accomplished their function, osteoclasts undergo to apoptosis. This is a physiological consequence needed to avoid an excessive bone resorption (Nielsen et al., 2007).

- **Reversal Phase**

  Following osteoclast-mediated resorption, the Howship lacunae remain covered with undigested demineralized collagen matrix (Everts et al., 2002). A mononuclear cell of undetermined lineage removes these collagen remnants and prepares the bone surface for subsequent osteoblast-mediated bone formation.

- **Formation Phase**

  Bone matrix resorption leads to the release of several growth factors herein stored, including bone morphogenetic proteins (BMPs), fibroblast growth factors (FGFs) and transforming growth factor β (TGFβ), which are likely responsible for the recruitment of the osteoblasts in the reabsorbed area (van Bezooijen et al., 2004). Once recruited, osteoblasts produce the new bone matrix, initially not calcified (osteoid) and then they promote its mineralization, thus completing the bone remodeling process. Unbalance between the resorption and formation phases mirrors an incorrect bone remodeling, which in turn affects the bone mass, eventually leading to a pathological condition.

- **Termination Phase or Mineralization**

  When an equal quantity of resorbed bone has been replaced, the remodeling cycle concludes (Tamma and Zallone, 2012). The termination signals that inform the remodeling machinery to cease work are largely unknown, although a role for osteocytes is emerging. The loss of sclerostin expression, which occurred to initiate osteoblastic bone formation, likely returns toward the end of the remodeling cycle. Following mineralization, mature osteoblasts undergo apoptosis, revert back to a bone-lining phenotype or become embedded in the mineralized matrix, and differentiate into osteocytes. The resting bone surface environment is reestablished and maintained until the next wave of remodeling is initiated.

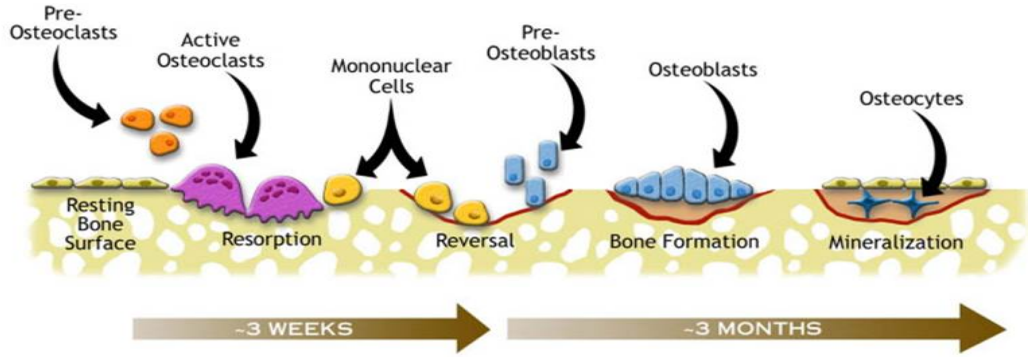

Figure 1.4: *Representation of the bone remodeling cycle (taken from Williams (2015)).*

The remodeling cycle occurs continuously at discrete sites throughout the skeleton in response to mechanical and metabolic influences. In order to achieve a balance in this process, it is important that the cellular components maintain a well-balanced relationship in spatial and temporal terms. Many studies have focused on developing models that reproduce this behavior. Next, we present a review of these models.

1.3 Review of state of the art of bone remodeling models

Historically, since 1638 it has been known that the mechanical loading has profound influences on bone tissue. The current concept is that the bone architecture is controlled by a local regulatory mechanism. In the 19th century, several

scientists attempted to relate bone trabecular morphology to its mechanical, load-bearing function. It was suggested that bone architecture was an answer to requirements of optimal stress transfer, pairing maximal strength to minimal weight, according to particular mathematical design rules. Using contemporary methods of analysis, stress transfer in bones was studied and compared with anatomical specimens, from which it was hypothesized that trabecular architecture is associated with stress trajectories. Others focused on the biological processes by which trabecular architectures are formed and on the question of how bone could maintain the relationship between external load and architecture in a variable functional environment.

The idea originates from Roux (1881), who proposed the principle of functional adaptation as a self-organizing process based on the tissues, which provides the capability of self-repair to bone. The change in form is known as Wolff's law, which appeared in the year 1892. The Law of Bone Remodeling (Wolff, 1982) is based on the observation that trabeculae tend to align with principal stress directions in many bones (long bones) (Figure 1.5). Wolff described the dependency of bone on applied loads and proposed that forces are somehow sensed by the bone which adapts its structure and morphology according to mechanical stimuli, acquiring the structure more resistant to this loading, with minimal mass. Within limits, mechanical stress is a particularly potent stimulus for bone cells and, in response to that, bone tissue has the ability to alter its strength. This way, the loading history of trabeculae influences the distribution of bone density and trabecular orientation (Figure 1.5). Thus, bone is a material with self-optimizing capabilities and able to control its mass and structure in direct relationship to its mechanical demands, ensuring that its mechanical integrity is maintained.

These concepts were captured by Frost (1960a,b), who assumes that local strains regulate bone mass. If strain levels exceed a mechanical 'set-point', new bone is formed (bone deposition), whereas, if strain levels are below this set-point bone is removed (bone resorption). This qualitative theory has motivated many authors and served as theoretical basis for several mathematical and computational theories that have been developed to study bone adaptation (Cowin and Hegedus, 1976; Huiskes et al., 1987; Beaupré et al., 1990; Weinans et al., 1992; Jacobs, 1994; Mullender et al., 1994).

With the advances in computing and the development of mathematical concepts associated with optimization of structures, it is possible to understand better the bone remodeling process, and to develop models that simulate the biomechanical behavior of the bone. These models may be classified into two main categories depending on the assumptions on which they are based: *phenomenological* and *mechanistic*.

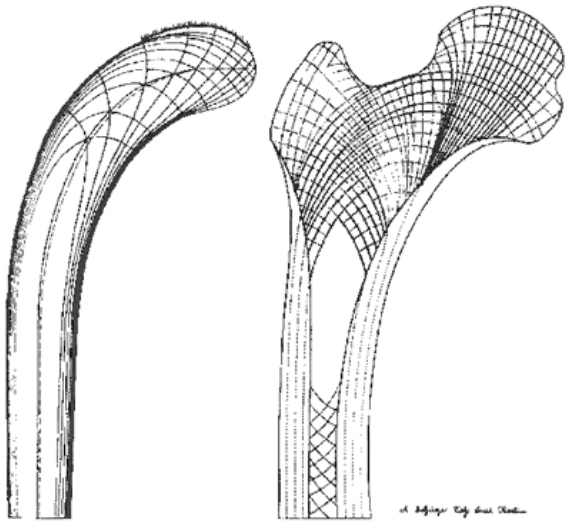

Figure 1.5: *On the left is the Culmann crane with principal stress trajectories indicated. On the right is the Meyer's sketch of the trabecular architecture in a section through the proximal end of the human femur (Wolff, 1982).*

Phenomenological models

Phenomenological models are able to predict bone remodeling through direct mathematical relationships between mechanical stimulus and bone response, following known experimental and clinical evidences, but no actual cell processes are considered, that is, the biological effects are not really considered in the model but its overall effect. Inside of the *phenomenological* models, we can find different theories and mathematical models. Some of the *phenomenological* models are based on achieving a homeostatic value for a certain mechanical stimulus. These models admit the existence of a certain mechanical stimulus that produces bone apposition or resorption such that, by this process, the stimulus tends to a certain uniform physiological level (homeostasis) in the whole tissue (Cowin and Hegedus, 1976; Carter, 1987; Huiskes et al., 1987; Beaupré et al., 1990; Jacobs, 1994; Fyhrie and Schaffler, 1995; Doblaré and García, 2001).

In the eighties, two *phenomenological* models have been developed which have the advantage of involving much fewer parameters than the theory of adaptive elasticity, one at Stanford University (Beaupré et al., 1990; Carter, 1987; Carter et al., 1989) and another at the University of Nijmegen (The Netherlands) (Huiskes et al., 1989, 1987; Weinans et al., 1992). The Nijmegen group chose the strain energy density (SED) per unit of bone volume for the remodeling stimulus while the Stanford group proposed a daily tissue-level stress stimulus (referred to as the Stanford model). Both models originally considered an isotropic structural material, neglecting the role of the structural orientation in the remodeling pro-

cess. Essentially, both models are equivalent predicting similar results (Jacobs, 1994).

Other *phenomenological* models (based either on these two original ones or on the adaptive elasticity theory) are based on damage repair, assuming that bone aims to optimize its strength and stiffness regulating the local damage generated by fatigue or creep (Prendergast and Taylor, 1994; Ramtani and Zidi, 2001; McNamara and Prendergast, 2007). Other numerical models coupled material density with orientation or anisotropy (Doblaré and García, 2002; Fernandes et al., 1999; Jacobs et al., 1997; Hambli et al., 2011).

Mechanistic models

Mechanistic models, are more complex since they try to characterize, understand and unravel the role of the mechanical environment into the biological mechanisms involved in bone remodeling. These models are interested not only in the prediction of the long-term behavior of bone under loading, but also in its rate of adaptation and the specific role of bone cells in each stage of the mechanosensation and adaptation processes.

While many of the earlier research questions aimed at a deeper understanding of the macroscopic mechanical properties, the scientific community has started to focus more and more on how these mechanical properties are determined by the underlying cellular processes. Some authors have proposed models of the interaction between osteoblasts and osteoclasts or osteocytes within the BMU (Smit and Burger, 2000; Hernandez et al., 2000, 2001; Huiskes et al., 2000; Hazelwood et al., 2001; Komarova et al., 2003; García-Aznar et al., 2005; Cox et al., 2011; Klika et al., 2014). And there is a recent model considering the interstitial fluid flow (Tsubota et al., 2009).

Other models focus at the microstructural scale (*mm* to μm) and describe the evolution of trabecular bone microarchitecture through resorption and formation events at the bone surface induced by the local mechanical state (Ruimerman et al., 2005; van Oers et al., 2008; Hellmich et al., 2004; Christen et al., 2012b,a; Pivonka and Komarova, 2010; Scheiner et al., 2015).

Patient-specific models

During last years there has been an increasing recognition towards the fact that biology or medicine problems require an analysis closer to the patient. For this reason some mathematical or theoretical models have recently emerged using parameters o geometries coming from real patients. Most of previous models, are based on generic geometries and arbitrary parameters, however, these models are not easy to compare with real data from patient (Kent and Hayward, 2007).

One of the advantages of using real data is creating patient specific models that describe the reaction of the organism in the daily life and so, we are able to characterize their behavior. Thanks to this technology, it is feasible to simulate the behavior of our bones. These patient-specific models may revolutionize the way clinicians diagnose and treat certain pathologies (Neal and Kerckhoffs, 2010). Then, specific models may be created for each subject, helping to develop specific preventive treatments.

For providing an overview of the importance of these techniques, it is worth noting that each year, the medical consultation related to bone treatments is increasing. For example, more than 300.000 hip fracture and more than 600.000 knee replacements are performed in the United States every year (Dettmer et al., 2015), and it is expected that this number will double in the coming decades. The growing trend of minimally invasive surgeries and increasing number of patients opting for active lifestyle are also fueling the growth of the specific orthopaedic procedures.

Nowadays, thanks to advances in science and technology with a simple tomography (CT), it is possible to obtain a three-dimensional reconstruction of bone and at the same time, to determine its bone density distribution. This allows to evaluate the quality of bone and additionally, to study its behavior under different physiological actions. This procedure allows developing patient-specific simulations. The main difference between patient-specific and generic models is that the specific geometry, material properties, and loading conditions of individual patients are used when creating patient-specific models (Poelert et al., 2012). Inside patient-specific models on bone, we may find different approaches that focus on obtaining specific data of the patient. For example, patient-specific musculoskeletal models enable the prediction of the influence of orthopedic surgery on musculoskeletal loading during gait (Asseln et al., 2014). Patient-specific, image-based models are required to accurately model hip contact and muscle forces. However, these models are not always combined with bone remodeling models for obtaining a full analysis of the patient. Bone remodeling models are normally used to design implants, analysing the influence on the bone adaptation response due to different factors (material stiffness, coating and ingrowth conditions, prosthesis shape design, loading conditions, different external fixation design concepts, time effects) (Sun et al., 2001; Caouette et al., 2015). These mechanobiological theories have been combined in order to simulate the process in idealized bone treatments. Each model includes different relevant contributions in their simulations. For that, the combination of both patient specific models, provides a high information for bone treatments.

1.4 Motivation, aim and scope of the Thesis

The main motivation of this Thesis is to develop bone remodeling models able to help in a clinical environment. There are several theoretical models that describe accurately the bone behavior, although, not all of them meet the demands. The challenge of remodeling models is to provide useful information for the researcher and, in consequence, for the treatments of the patient. For that, these new and promising techniques can provide useful information, as the quality of bone, their evolution, predict the risk of fracture. Therefore, we would like to advance towards a numerical methodology for bone modeling, helping to understand the bone behavior and creating a patient specific bone remodeling model. These methodologies may help in a clinical environment. It can give us information about which prosthesis will be more appropriate and which one will produce the best distribution of the loads in order to increase lifespan and reduce the likelihood of revision surgery. Then, all these features may provide a saving cost and a health improvement. Consequently, these methodologies may be helpful in virtual surgery and provide with information about the treatment and the evolution of the bone of a certain patient.

This PhD dissertation has been involved as part of the European project CAD-BONE: Patient-specific predictions for bone treatments (Marie Curie Industry-Academia Partnerships and Pathways / FP7-PEOPLE-2011-IAPP) whose main purpose is to perform a multidisciplinary research that will result in a technology that will radically improve the development of patient-specific computer models for the modelling of bone adaptation/healing after prosthesis implantation in musculoskeletal applications. The main aim of CAD-BONE is to demonstrate the feasibility of integrating patient specific modelling, musculoskeletal loading, and analysis of adaptive bone remodeling to simulate functional outcome of patient treatments (Figure 1.6) (http://cadbone.unizar.es/). Also, this research was involved in the National Project entitled “Design and development of a computational tool for the personalised risk fracture prediction in Osteoporotic patient” and supported by the Spanish Ministry of Economy and Competitiveness (DPI 2011-22413).

Therefore, the main objective of this Thesis is to study bone remodeling models, showing their challenges, the problematic that currently presents and their applicability in the clinical setting. In order to achieve this objective, a computational model that allows to predict the bone density distribution has been developed, improving previous models. The remodeling model has been used in the inverse process to obtain different tools that can predict the load that the bone is really supporting. Then, the final objective is to apply this methodology in clin-

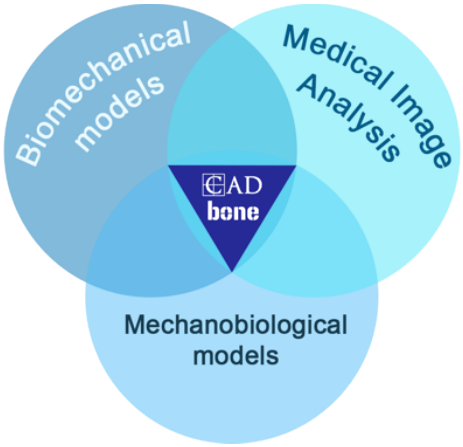

Figure 1.6: *Methodologies used in CADBONE (http://cadbone.unizar.es/).*

ical cases and the resulting information may help in future bone treatments. To achieve this goal, secondary objectives are defined as follows:

- Study different bone remodeling theories, their problematic and their limitations. For that, we develop a computational method able to simulate the evolution of density distribution in a patient-specific model. In particular, we modify the Stanford algorithm (Jacobs, 1994) and anisotropic bone remodeling model (Doblaré and García, 2002; Mengoni and Ponthot, 2015), based on the reference homeostatic stimulus which will be now dependent on the loading history that each point is supporting. We improve the stabilization of the numerical results corresponding to the spatial distribution of the apparent density and in consequence, the convergence of the algorithm. Also, we perform a theoretical analysis to demonstrate the linear convergence of the bone remodeling algorithm incorporating a non-constant reference homeostatic stimulus.

- Study the strong dependency of the initial condition on bone remodeling models and develop a methodology able to decrease this dependency. For that, we develop a computational method able to modified the relationship between the the micro and macro scale through the reference stimulus.

- Develop a methodology for obtaining the subject-specific loads that one bone supports. For that, we need to solve the inverse bone remodeling model. For this purpose, we develop, evaluate and compare three existing numerical approaches to estimate the musculoskeletal loads in the femur in order to accurately solve the inverse bone remodeling problem. Specifically, we focus on two different machine learning techniques (MLT): multilayer

percepton (MLP) as a representation of the artificial neural networks (ANN) and support vector machines (SVM), comparing their results with a classical technique: linear regression (LR).

- Prove the importance of bone remodeling models in a clinical case. For that, we apply all previously developed methodologies on five specific tibias from which we know their bone geometry and density distribution from CT grey data through an image-based analysis. We will predict their specific tibia loading conditions. Finally, to quantitatively evaluate the predictive capacity of this novel methodology, we compare these forces with those obtained for each patient from an individual-based gait analysis.

1.5 Outline of the Thesis

This Thesis is organized into seven Chapters as follows.

The main features of the bone remodeling model are presented in Chapter 2. A review of the bone remodeling models is provided and special emphasis is placed on phenomenological models as the Stanford model (Jacobs, 1994) and the anisotropic model (Doblaré and García, 2002) as well as in its formulation.

In Chapter 3, we present a novel bone remodeling model which considers that the reference equilibrium stimulus is dependent on the loading history. We also perform a theoretical analysis to demonstrate the linear convergence of the bone remodeling algorithm. And finally, a quantitative and qualitative evaluation of the model comparing with the original Stanford model (Jacobs, 1994) and Doblaré and García model (Mengoni and Ponthot, 2015) has been performed.

In addition, Chapter 4 follows with the limitations in bone remodeling models. For that, we evaluate the dependency of the initial condition and we present another novel modification of previous bone remodeling models that overcomes this problem.

Chapter 5 comprises a review of mathematical tools based on, MLT, such as ANN and SVM. These mathematical tools have been used for creating a methodology that allows estimating the loads that each specific bone supports. Furthermore, a comparison of the performance of these techniques (SVM and ANN) with the classical linear regression in order to solve the inverse problem, is provided. In addition, we explain all the methodologies for obtaining the data to perform the inverse methodology. This computational tool has been trained with the results obtained in the 2D and 3D model of a femur.

Then, in Chapter 6 we apply all previous methodologies in different clinical cases. For that, we select five patient-specific tibias in collaboration with the Orthopaedic Research Laboratory (ORL) in Nijmegen and Laboratory for Biome-

chanical Engineering of the University of Twente (Netherlands). From individual CT data, through current standard image analysis, we obtain their bone geometry and density distribution. FE models are constructed and they are used for obtaining the density distribution with multiple different loads through a bone remodeling model. Then, these data are used as inputs for the numerical tools. Finally, in order to validate the ANN performance for tibia loading predictions, we compare predicted subject-specific loads with the loads obtained from the patient-specific musculoskeletal model.

Finally, the main conclusions of this work, together with a brief summary of the original contributions presented along this thesis and the future work lines are collected in Chapter 7.

Additionally, at the beginning of the document, in aggrement with the University of Zaragoza guidelines to obtain the European PhD grade (art. 15 RD 99/2011), a Spanish summary of the Thesis is presented. This summary which reports the motivation, structure, objectives and methodology as well as the main conclusion, original contributions and future lines of this work.

CHAPTER 2

Bone remodeling models

At the end of the nineteenth century, Wolff (1982) proposed that bone morphology depends on applied loads and that the adaptation of bone to its mechanical environment could be described by mathematical rules (Figure 2.1). As a consequence, researchers developed progressively more sophisticated and complete mathematical and computational models to predict this behavior. This chapter describes the basic concepts of the computational models for bone remodeling used in this Thesis. These models are based on structural topology optimization and simulate bone adaptation process due to mechanical loading, i.e., they describe bone behavior in response to mechanical environment.

Many different empirical relationships have been described in the literature for bone material behavior. With the more simple ones, bone is modeled as isotropic. It is known, however, that bone can be highly anisotropic. Bone anisotropy is the macroscopic manifestation of the microstuctural orientation of trabeculae along a "grain direction" in which mechanical stiffness and strength are the greatest. This direction has been suggested to be correlated with the maximal strain/stress direction and gives trabecular bone anisotropy in general, or at least orthotropic symmetry (Zysset et al., 1998; Yang et al., 1998; Turner et al., 1990) and in some instances displaying transverse isotropy (Odgaard et al., 1997). The directionality of the trabeculae may be expressed through a geometric fabric tensor (Cowin, 1985). The main feature of this tensor is that its eigenvalues are all distinct for an orthotropic behavior, two of them are repeated when transversely isotropic and the three eigenvalues are the same when isotropic. The bone anisotropy is also a function of the apparent density. Cortical bone is loaded longitudinally along the diaphyseal axis compared with the radial or circumferential "transverse" directions. Comparatively smaller differences in modulus and strength have been reported between the radial and circumferential directions, indicating that human cortical bone may be treated as transversely isotropic. Then, we can define the bone as anisotropic.

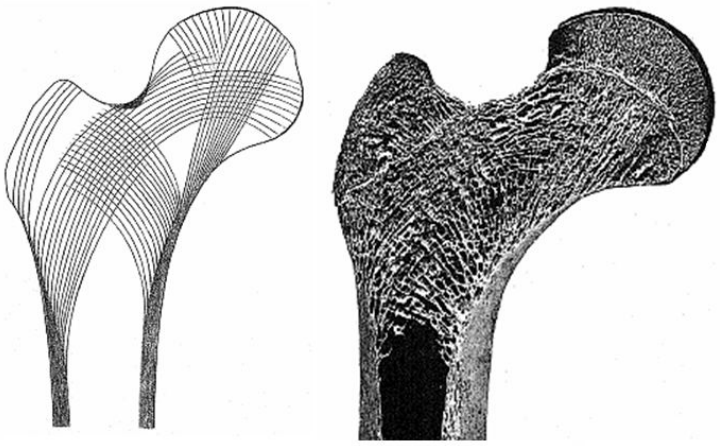

Figure 2.1: *Wolff's law (Wolff, 1982).*

As we have seen in Chapter 1, bone remodeling models can be classified into two main types: *phenomenological* and *mecanistic* models. In this Thesis, we are focused on phenomenological models due to the lowest computational cost in comparison with mechanobiological ones and given their good accuracy in the apparent bone density predictions (McNamara and Prendergast, 2007). In particular, we present two phenomenological bone remodeling models based on previous works developed at the Stanford University (Carter et al., 1989; Beaupré et al., 1990; Jacobs et al., 1995): One isotropic and another one with anisotropic behavior. An extension of these formulations will be presented in the following sections and some of their mathematical problems will be analysed.

2.1 Isotropic bone remodeling models: Stanford model

The Stanford theory of isotropic bone remodeling (Jacobs, 1994) is mainly based on the remodeling model proposed by Beaupré et al. (1990), in turn based on the models previously mentioned (Carter, 1987; Carter et al., 1989). This model is based on the idea that bone remodeling response is guided by a homeostatic regulator of the local mechanical microenvironment that the bone is actually supporting. The homeostatic mechanical stimulus (ψ) defines the equilibrium or dead zone where the bone response is null (Figure 2.2). However, if overload/disuse occurs and the mechanical stimulus is higher/lower than the equilibrium level, bone formation/resorption is promoted, respectively. Following, we describe the mechanical environment of this model.

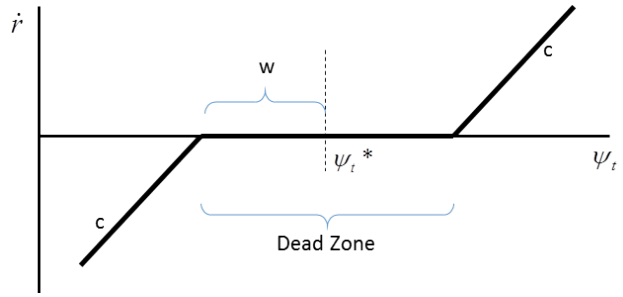

Figure 2.2: *Bone adaptation law: Bone resorption occurs in an underloading condition when the bone formation rate is negative. Formation of new bone tissue occurs in an overloading condition and a positive bone formation rate. Within a dead zone, a change of the bone remodeling stimulus does neither lead to formation nor to resorption of bone tissue.*

Mechanical problem

The bone is assumed as elastic (Figure 2.3) and the constitutive law is written as follows (see Weinans et al. (1992)),

$$\boldsymbol{\sigma} = \boldsymbol{\sigma}(\boldsymbol{u}) = 2\,\mu(\rho)\boldsymbol{\varepsilon}(\boldsymbol{u}) + \lambda(\rho)\mathrm{Div}\,(\boldsymbol{u})\mathcal{I} \quad \text{in} \quad \overline{\Omega} \times [0, T] \tag{2.1}$$

Here, $\mathcal{I}$ denotes the identity operator, Div represents the divergence operator and $\mu(\rho)$ and $\lambda(\rho)$ are Lame's coefficients of the material, assumed to depend on the apparent density of the bone denoted by ρ. These coefficients are related to Young's modulus $E(\rho)$ and Poisson's ratio $\kappa(\rho)$ through the relations:

$$\mu(\rho) = \frac{E(\rho)}{2(1 + \kappa(\rho))} \tag{2.2}$$

and

$$\lambda(\rho) = \frac{\kappa(\rho)E(\rho)}{1 - \kappa^2(\rho)} \tag{2.3}$$

if the plane stress hypothesis is assumed, or

$$\lambda(\rho) = \frac{\kappa(\rho)E(\rho)}{(1 + \kappa(\rho))(1 - 2\kappa(\rho))} \tag{2.4}$$

if the plane strain hypothesis is used or if the three-dimensional case is considered. Moreover, the Poisson's ratio is assumed to be independent of ρ, $\kappa(\rho) = \kappa$, and the following equation is used for Young's modulus depending on the apparent density:

$$E(\rho) = M\rho^{\gamma} \tag{2.5}$$

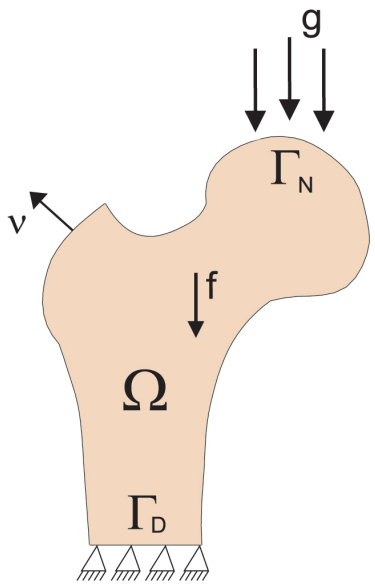

Figure 2.3: *Bone remodeling benchmark problem.*

where M and γ are positive constants which characterize the bone behavior.

According to Carter and Hayes (1977), the mechanical stimulus required to maintain bone homeostasis (which regulates the bone mass evolution) is identified with the so-called daily tissue stress level, ψ_t, a scalar quantity but generalized to include several load cases:

$$\psi_t = \left(\sum_{i=1}^{N} n_i \overline{\sigma}_{t_i}^m \right)^{1/m} \tag{2.6}$$

where N is the number of different load cases, n_i the average number of load cycles per time step for each load case i, m an experimental parameter (Whalen et al., 1988) and $\overline{\sigma}_{t_i}^m$ the so-called effective stress at the tissue level.

Beaupré et al. (1990) also established a relation between the stress at the continuum level $\overline{\sigma}$ and the one at the tissue level $\overline{\sigma}_{t_i}$ following a standard homogenisation procedure and supported by experimental data. With these two assumptions, ψ_t may be rewritten as a function of the stress at the continuum level as

$$\psi_t = \left(\sum_{i=1}^{N} n_i \left(\frac{\bar{\rho}}{\rho} \right)^2 \overline{\sigma}_i^m \right)^{1/m} \tag{2.7}$$

with ψ defined by

$$\psi = \left(\sum_{i=1}^{N} n_i \overline{\sigma}_i^m \right)^{1/m} \tag{2.8}$$

In this work, we assume, for the sake of simplicity in the analysis, that $N = 1$ and so

$$\psi = n^{1/m} \overline{\sigma} \tag{2.9}$$

where the effective stress is then calculated as

$$\overline{\sigma} = \sqrt{2E(\rho)U(\boldsymbol{\sigma}(\boldsymbol{u}), \boldsymbol{\varepsilon}(\boldsymbol{u}))} \tag{2.10}$$

Keeping in mind that the stimulus $U(\boldsymbol{\sigma}(\boldsymbol{u}), \boldsymbol{\varepsilon}(\boldsymbol{u}))$ is given by

$$U(\boldsymbol{\sigma}(\boldsymbol{u}), \boldsymbol{\varepsilon}(\boldsymbol{u})) = \frac{1}{2} \boldsymbol{\sigma}(\boldsymbol{u}) \, : \, \boldsymbol{\varepsilon}(\boldsymbol{u}) \tag{2.11}$$

by using the above constitutive law for the stress tensor we have

$$\psi = n^{1/m} \sqrt{E(\rho) \left(2\mu(\rho) \boldsymbol{\varepsilon}(\boldsymbol{u}) : \boldsymbol{\varepsilon}(\boldsymbol{u}) + \lambda(\rho) (\mathrm{Div}\,(\boldsymbol{u}))^2 \right)} \tag{2.12}$$

Therefore, it follows that

$$\psi = n^{1/m} \sqrt{E(\rho)^2 \left(\alpha \boldsymbol{\varepsilon}(\boldsymbol{u}) : \boldsymbol{\varepsilon}(\boldsymbol{u}) + \beta (\mathrm{Div}\,(\boldsymbol{u}))^2 \right)} \tag{2.13}$$

where $\alpha = \dfrac{1}{\frac{1}{\kappa} + \kappa}$ and $\beta = \dfrac{\kappa}{1 - \kappa^2}$ if the plane stress hypothesis is assumed or $\beta = \dfrac{\kappa}{(1 + \kappa)(1 - 2\kappa)}$ if the plane strain hypothesis is used or if the three-dimensional case is considered. We also recall that $E(\rho) = M\rho^\gamma$ for two given positive constants M and γ.

Now, we define the function $f : \mathbb{R} \to [c(-L + \omega), c(L - \omega)]$ as follows,

$$f(z) = \begin{cases} c(-L + \omega) & \text{if} \quad z \leq -L \\ c(z + \omega) & \text{if} \quad -L \leq z \leq -\omega \\ 0 & \text{if} \quad -\omega \leq z \leq \omega \\ c(z - \omega) & \text{if} \quad L \geq z \geq \omega \\ c(L - \omega) & \text{if} \quad z \geq L \end{cases} \tag{2.14}$$

where $L > 0$ is a truncation value needed for mathematical reasons and 2ω is the width of the dead zone (Figure 2.2). We note that, with this definition, this function f is a Lipschitz and bounded function. Moreover, c is assumed constant for the sake of simplicity but it does not necessarily have to be equal for the distinct

cases. It is an interval around the equilibrium stimulus, in which no remodeling takes place.

Therefore, we define the bone remodeling rate as $\dot{r}=f(\psi_t-\psi_t^*)$ (function (2.14)), being the difference between ψ_t and ψ_t^* the stimulus that regulates the bone remodeling responses, and ψ_t^* is the reference value of the tissue stress level of the equilibrium zone. This value was assumed constant in Beaupré et al. (1990).

After calculating the stimulus and the bone remodeling rate, the new bone apparent density can be updated (Figure 2.5). The evolution of the apparent density function is obtained from the following first-order ordinary differential equation (Jacobs et al., 1995),

$$\dot{\rho} = k\dot{r}S_v(\rho)\overline{\rho} \quad \text{in} \quad \Omega \times (0,T) \tag{2.15}$$

where the added or removed bone is assumed to be completely mineralized; that is, at maximum density $\overline{\rho}$. In the previous bone remodeling law (2.15), k is the ratio between the available surface for remodeling and the total internal surface ($k = 1$ - porosity null). $S_v(\rho)$ is the specific surface (internal surface per unit volume) that depends on the apparent density (Figure 2.4) and it can be approximated accurately enough by a fifth order polynomial of the apparent density given by Martin (1984):

$$S_v(\rho) = 0.02876\rho^5 - 0.10104\rho^4 + 0.13396\rho^3 - 0.09304\rho^2 + 0.03226\rho \tag{2.16}$$

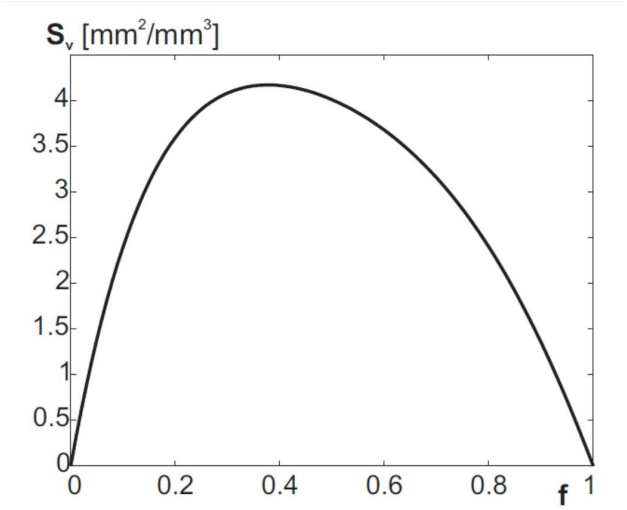

Figure 2.4: *Specific surface as function of porosity (Martin, 1984).*

In order to obtain a real apparent density we have to assume that this function is bounded as

$$\underline{\rho} \leq \rho \leq \overline{\rho} \tag{2.17}$$

where we recall that $\overline{\rho}$ is the maximal density of cortical bone and $\underline{\rho}$ represents the minimal density corresponding to the reabsorbed bone (Carter and Hayes, 1977).

Finally, the process is assumed quasistatic and therefore the inertia effects are neglected. Moreover, let ρ_0 and $(\psi_t^*)_0$ denote the initial apparent density function and the initial reference value of the tissue stress level.

2.2 Anisotropic bone remodeling model: Doblaré and García model

As we explained in the introduction, bone clearly behaves anisotropically. For that, a remodeling model has to be able to reproduce this evolution.

For isotropic remodeling models, it is then assumed that only the density is affected by remodeling. Mechanical parameters, such as Young's modulus, are only affected by the density. Anisotropic remodeling models also require to define the stiffness variation as a function of the remodeling rate. This anisotropic stiffness variation function needs to account for the tendency of bone to align its microstructure with the stress or strain principal directions. Therefore, the stiffness tensor principal directions need to align themselves with these directions as well.

The Stanford model was initially designed as an isotropic law for remodeling and later extended to an anisotropic one (Jacobs et al., 1997). The assumed stimulus responsible for remodeling is a stress-equivalent intensity at tissue level. The anisotropic extension of this model formulates the stiffness variation considering remodeling as an optimized process.

Doblaré and García (2002) proposed a damage-based remodeling model, damage is understood as a measure of bone tissue porosity and directional mass distribution, as suggested by Cowin (1986) for the fabric tensor. The undamaged state is the ideal situation of null porosity and perfectly isotropic. This model is able to predict the non-homogeneous and anisotropic bone mass distribution in a representative volume. The independent internal variables are those that define the internal microstructure of the bone, i.e. the apparent density and the "fabric tensor", which measure the bone mass distribution and the directionality of the microstructure, respectively. The "fabric tensor" is demonstrated to be aligned with the elasticity tensor, while using the principles of the internal variables theory drives to demonstrate that the material tends to align its principal directions of

anisotropy with the ones of the strain tensor, achieving a directional equilibrium when the stress is aligned with the "fabric tensor".

2.2.1 Mechanical problem

In this subsection (Doblaré and García, 2002) model for bone remodeling is presented. It is based on the anisotropic Stanford model (Jacobs et al., 1997) and it expresses the stiffness variation in a Continuum Damage Mechanics (CDM) framework.

Then, they define the damage tensor, **D**, used in a strain energy equivalence approach of CDM, by the expression:

$$\mathbf{D} = \mathbf{1} - \left(\frac{\rho}{\bar{\rho}}\right)^{\gamma/2} \sqrt{A}\hat{H} = 1 - H^2 \tag{2.18}$$

with ρ the apparent density, $\bar{\rho}$ the maximum density, γ is the experimental parameter which relates the elastic modulus and the apparent density and O an adjusting parameter that is obtained by particularizing the general anisotropic model to the isotropic case

$$O(\rho) = \frac{M(\rho)}{M(\bar{\rho})}\bar{\rho}^{\gamma(\rho)-\gamma(\bar{\rho})} \tag{2.19}$$

In addition, the expression of the effective stress tensor is defined as:

$$\widetilde{\sigma} = \mathbf{H}^{-1}\sigma\mathbf{H}^{-1} \tag{2.20}$$

The stimulus is identified with the variable thermodynamically (**Y**) associated with the damage tensor or, even better, to the remodeling tensor **H**.

However, in order to establish this stimulus, we have to define the mechanical variable (strain or stress) that externally "drives" the process. We have used the strain as the "external driving force", although exactly the same results can be obtained if stress is considered as earlier proposed by Wolff (1982). With this, the stimulus is defined as:

Resorption:

$$\mathbf{Y} = \frac{\partial\Psi(\varepsilon,\mathbf{H})}{\partial\mathbf{H}} = \frac{\partial\Psi}{\partial\sigma}\frac{\partial\sigma}{\partial\mathbf{H}}\bigg|_{\varepsilon=ct} \tag{2.21}$$

being Ψ the free energy function and where the constancy of ε in the evaluation of the partial derivative has been made explicit.

And, $\mathbf{Y}$ is immediately obtained in terms of the external independent variable (strain) and the internal variable (remodeling tensor) as

$$\mathbf{Y} = 2\left[2\mu(\rho)sym\left[(\mathbf{H}\varepsilon\mathbf{H})(\mathbf{H}\varepsilon)\right] + \lambda(\rho)tr(\mathbf{H}^2\varepsilon)sym[\mathbf{H}\varepsilon]\right] \tag{2.22}$$

with $\mu(\rho)$, $\lambda(\rho)$ the Lame's parameters of the ideal compact bone with null porosity.

At this stage, the stimulus is defined in the same manner than in equation (2.21) but now using the stress as the independent variable, we get

Formation:

$$\mathbf{Y}^{\sigma} = \frac{\partial\hat{\Psi}(\sigma,\mathbf{H})}{\partial\mathbf{H}} = \frac{\partial\hat{\Psi}}{\partial\varepsilon}\frac{\partial\varepsilon}{\partial\mathbf{H}}\bigg|_{\sigma=ct} \tag{2.23}$$

With this,

$$\mathbf{Y}^{\sigma} = (-2)\mathbf{H}^{-2}\left[\frac{1+\kappa}{E}sym\left[(\mathbf{H}^{-1}\sigma\mathbf{H}^{-1})(\mathbf{H}^{-1}\sigma)\right]\frac{\kappa}{E}tr(\mathbf{H}^{-2}\sigma)sym[\mathbf{H}^{-1}\sigma]\right] \tag{2.24}$$

For that, we finally obtain

$$\mathbf{Y} = -\mathbf{Y}^{\sigma} \tag{2.25}$$

leading, therefore, to the same model.

Damage evolution law

Doblaré and García proposed this criteria:

$$\boldsymbol{g}^{r} = \frac{\sqrt{2(1-\omega)}}{n^{1/m}\sqrt{B}\bar{\rho}^{(2-\gamma/8)}O^{1/8}27^{1/4}}(\mathbf{J}^{-1}:\mathbf{J}^{-1})^{1/4} - \frac{1}{(\Psi_t^{*}-w)\rho^{(16-5\gamma)/8}} \tag{2.26}$$

$$\boldsymbol{g}^{f} = \frac{n^{1/m}\sqrt{B}\bar{\rho}^{(2-\gamma/8)}O^{1/8}3^{1/4}}{\sqrt{2(1-\omega)}}(\mathbf{J}:\mathbf{J})^{1/4} - (\Psi_t^{*}+w)\rho^{(16-5\gamma)/8} \tag{2.27}$$

where $\mathbf{J}$ is a new tensor and a function of the stimulus that quantifies the relative influence of the spherical and deviatory parts of the stimulus in the damage criterion, defined as

$$\mathbf{J} = (1-\omega)tr(\mathbf{Y})\frac{1}{3}\mathbf{1} + \omega dev(\mathbf{Y}) = (1-2\omega)tr(Y)\frac{1}{3}\mathbf{1} + \omega(\mathbf{Y}) \tag{2.28}$$

with $\omega \in [0, 1]$ being a scalar parameter such that when $\omega = 0$ the model is solely dependent on the spherical component of the stimulus and, therefore, to a purely isotropic evolution model. For $\omega = 1$ the highest degree of anisotropy is achieved, which corresponds to $\mathbf{J} = dev(\mathbf{Y})^4$.

In this model, an associated damage evolution law is proposed, so this flow rule is presented as

$$\dot{H} = \mu^r \frac{\partial \boldsymbol{g}^r}{\partial Y} + \mu^f \frac{\partial \boldsymbol{g}^f}{\partial Y} \tag{2.29}$$

fulfilling the joined consistency condition $\mu^r, \mu^f \geq 0; g^f, g^r \leq 0$ and $\mu^r g^r = \mu^f g^f = 0$

Deriving the damage criteria (2.26 and 2.27), the evolution law for the remodeling tensor $\mathbf{H}$ is written as:

$$\dot{H}_{resorption} = \frac{3\gamma k \dot{r} S_v}{4tr(\mathbf{H}^{-1}\mathbf{J}\hat{\omega})} \frac{\bar{\rho}}{\rho} \mathbf{J}^{-3} \hat{\omega} \tag{2.30}$$

$$\dot{H}_{formation} = \frac{3\gamma k \dot{r} S_v}{4tr(\mathbf{H}^{-1}\mathbf{J}\hat{\omega})} \frac{\bar{\rho}}{\rho} \mathbf{J} \hat{\omega} \tag{2.31}$$

After that, the evolution of the remodeling law is proposed, being the criteria of bone remodeling multiplied by the remodeling velocity.

$$\dot{r} = \begin{cases} -c_r \frac{g^r}{\rho^{2-\gamma/2}} & \text{if} \quad g^r \geq 0 \quad g^f < 0 \\ c_f \frac{g^f}{\rho^{2-\gamma/2}} & \text{if} \quad g^r < 0 \quad g^f \geq 0 \\ 0 & \text{if} \quad g^r < 0 \quad g^f < 0 \end{cases} \tag{2.32}$$

where c_r and c_f are both expressed as a velocity per unit stress.

2.2.2 Correction of model by Mengoni and Ponthot

Doblaré and García's model presented a problem associated with the inconsistency in the dimensional analysis of the model in the equation (2.32). Following the approach of Mengoni and Ponthot (2015), g_r and g_f need to have identical dimensions so that the remodeling rate is expressed with the same units in the resorption or formation cases. The dimension of the remodeling criteria has the dimension of stress per day (MPa/day). However, if we observe the equations (2.27) and (2.26), the dimensions are different. g_f is stress^{-1} x $\rho^{-(16-5\gamma)/8}$ and g_r is stress^{-2} x $\rho^{(32-9\gamma)/8}$.

Then, the problem was found in Doblaré and García due to the fact that a dimensionless inconsistency emerged. For that, Mengoni and Ponthot proposed

a modification of g_r to obtain the same dimension than g_f. This enhancement of the resorption criterion also involves a change of the remodeling tensor evolution in the resorption case. Following the approach of Doblaré and García (2002), the evolution of the remodeling tensor $\mathbf{H}$ is inversely related to the strain energy density. For that, the new remodeling tensor in resorption case is (Mengoni and Ponthot, 2015):

$$\boldsymbol{g}^r = \frac{n^{1/m}\sqrt{B}\bar{\rho}^{(2-\gamma/8)}O^{1/8}3^{1/4}}{\sqrt{2(1-\omega)}}(\mathbf{J}:\mathbf{J})^{1/4} - (\Psi_t^* - w)\rho^{(16-5\gamma)/8} \tag{2.33}$$

where the formation criterion remains the same:

$$\boldsymbol{g}^f = \frac{n^{1/m}\sqrt{B}\bar{\rho}^{(2-\gamma/8)}O^{1/8}3^{1/4}}{\sqrt{2(1-\omega)}}(\mathbf{J}:\mathbf{J})^{1/4} - (\Psi_t^* + w)\rho^{(16-5\gamma)/8} \tag{2.34}$$

Following previous development and deriving the damage criteria, it finally gets an evolution law for the remodeling tensor:

$$\dot{H}_{resorption} = \frac{3\gamma k \dot{r} S_v}{4tr(\mathbf{H}^{-1}\mathbf{J}\hat{\omega})}\frac{\bar{\rho}}{\rho}\mathbf{J}\hat{\omega} \tag{2.35}$$

$$\dot{H}_{formation} = \frac{3\gamma k \dot{r} S_v}{4tr(\mathbf{H}^{-1}\mathbf{J}\hat{\omega})}\frac{\bar{\rho}}{\rho}\mathbf{J}\hat{\omega} \tag{2.36}$$

Finally, the second correction applied on Doblaré and García model is in the criteria of bone remodeling. Keeping the definition of the formation criterion as it is, Mengoni and Ponthot (2015) modified the remodeling rate in such a way that it was dimensionally consistent with respect to Equation 2.32. However, they proposed the criteria of bone remodeling g_r and g_f to be divided by $\rho^{(16-5\gamma)/8}$ instead of $\rho^{2-\gamma/2}$. Additional, g_r and g_f are the same although with different sign, keeping the same dimensions. Thanks to this strategy, the second part of resorption criterion is equal to the anisotropic law proposed by Jacobs et al. (1997). Therefore, the new equation of the evolution of the remodeling law is:

$$\dot{r} = \begin{cases} -c_r \frac{g^r}{\rho^{(16-5\gamma)/8}} & \text{if} \quad g^r \geq 0 \quad g^f < 0 \\ c_f \frac{g^f}{\rho^{(16-5\gamma)/8}} & \text{if} \quad g^r < 0 \quad g^f \geq 0 \\ 0 & \text{if} \quad g^r < 0 \quad g^f < 0 \end{cases} \tag{2.37}$$

where c_r and c_f are both expressed as a velocity per unit stress.

These modifications were defined by Mengoni and Ponthot (2015) where they proposed an enhancement of this resorption criterion, ensuring the dimensional correctness while keeping the physical properties of the original remodeling model. In their manuscript, we have found all details of these corrections as well as the analysis of the change of resorption criterion surface in the stress space for a 2D analysis.

2.3 Numerical implementation scheme

In this section, we briefly show the numerical scheme implemented (Figure 2.5). In the Stanford model, the isotropic material parameters E_n and κ_n and the apparent density ρ_n are passed in from time step n for every integration point. After calculating the stimulus and the porosity, the remodeling rate and surface density can be evaluated, yielding the new density. The new density ρ_{n+1} defines the new material parameters E_{n+1} and κ_{n+1} which are passed back to the global program. Figure 2.5 shows the block diagram of the Stanford algorithm with its implicit structure. Similar block diagram would be for the anisotropic model, although it is not here shown.

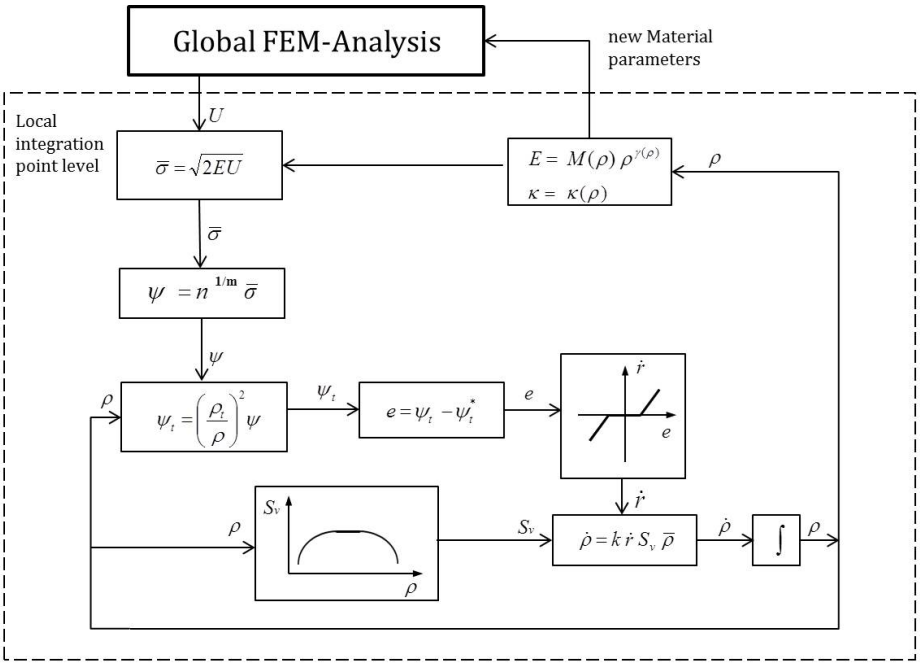

Figure 2.5: *A block diagram of Stanford model (Jacobs, 1994).*

The following parameter values have been used in the simulations of this thesis (see Table 2.1) (Weinans et al., 1992; Jacobs et al., 1995; Fernández et al., 2010, 2012a).

Reference stimulus:	$(\psi_t^*)_0$ = 50 MPa	Initial density:	$\rho_0 = 0.5\ g/cm^3$
Minimal density:	$\underline{\rho} = 0.05\ g/cm^3$	Maximal density:	$\overline{\rho} = 2.021\ g/cm^3$
Cycles per day:	$\overline{n}$ = 10000	Remodeling velocity:	c = 0.02
Time step size:	Δt = 1 day	Weighting exponent:	$m = 4$
M = 2014 ($\rho \leq 1.2$)	$\gamma = 2.5$ ($\rho \leq 1.2$)	M = 1763 ($\rho > 1.2$)	$\gamma = 3.2$ ($\rho > 1.2$)
Poisson's ratio:	$\kappa = 0.32$ ($\rho > 1.2$)	$\kappa = 0.2$ ($\rho \leq 1.2$)	
Constant of mechanical stimulus:	a = 0.01	A = 0.039	
Half-width of the lazy zone:	w = 12.5%		

Table 2.1: Values used for the parameters in the bone remodeling simulations.

2.3.1 2D FE model

A classical benchmark problem corresponding to a two-dimensional FE model of the proximal femur (see Figure 2.6) is used in this work to test the stability and convergence of the Stanford model, Doblaré and García model and its correction. The FE model is composed of 1700 bilinear quadrilateral elements and 1822 nodes. For the connection between the two cortical layers of the diaphysis, an additional plate is used joining both layers as proposed by other authors (Beaupré et al., 1990; Bergmann et al., 2001). This lateral plate varies in thickness and resembles the gradual increment in thickness in the cortical layer from the metaphysis to the diaphysis (see Figure 2.6). Moreover, the lateral plate remodeling capacities are constrained, and its properties are considered constant in time. Finally, it is assumed that the only connection to the cortical layers is produced at the lateral nodes.

The lower part of the femur is restrained along the vertical direction at all nodes and along the vertical and horizontal directions at only one node, to avoid rigid body movements. Three simultaneous (consecutive in the model application) load cases and their corresponding reactions on the greater trochanter are considered in order to simulate the walking movement (Figure 2.7): time when the foot touches the floor (case 1) and the other two alternative moments of abduction (case 2) and adduction (case 3) (Jacobs et al., 1997). The loads correspond to the reaction force on the femoral head and the abductor muscle force (Figure 2.6 for the walking process). The load values are detailed in Table 2.2 (Jacobs et al., 1995). The simulation for the bone remodeling problem starts from an arbitrary initial situation (uniform density $\rho_0 = 0.5\ gr/cm^3$ and isotropic behavior), and applying the previously described load sequence, changes in the bone apparent density distribution are computed until 300 days.

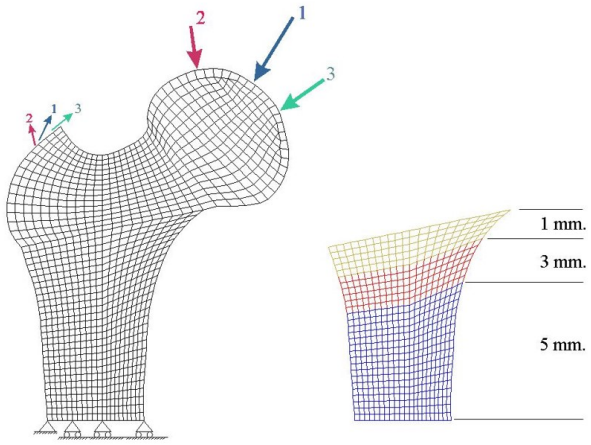

Figure 2.6: *2D FE mesh of the femur.*

Mean value and orientation of the forces for the three load cases considered. Angles refer to the vertical direction					
Case	Cycles/day	Load value at the head		Reaction force at the abductor muscle	
		Magnitude (N)	Angle (°)	Magnitude(N)	Angle (°)
1	6000	2317	24	703	28
2	2000	1158	-5	351	-8
3	2000	1548	56	468	35

Table 2.2: Loading conditions considered for the walking movement (Carter, 1987).

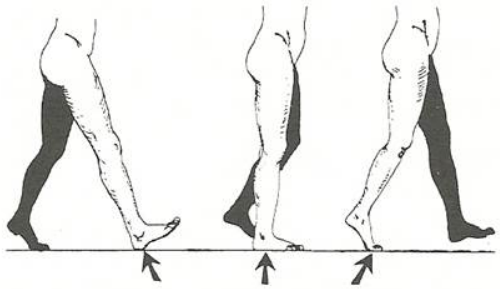

Figure 2.7: *Load cases during walking (Schafer et al., 1995).*

2.4 Numerical results

In this section, we present the bone density predictions obtained by Stanford model, Doblaré and García model and its correction (Mengoni and Ponthot, 2015). Small diferences were predicted between the Stanford model (Figure 2.8a) and

Doblaré and García model (Figure 2.8b). Doblaré and García improves the prediction of the load bearing regions of the femoral head and great trochanter. Besides of the numerical inconsistency of Doblaré and García model, the result of the final density (300 increments) shows small differences with respect to its correction (Mengoni and Ponthot, 2015). In Figure 2.8 (b-c), we observed the bone density distribution for both models where there is only a slight difference in the resorption area.

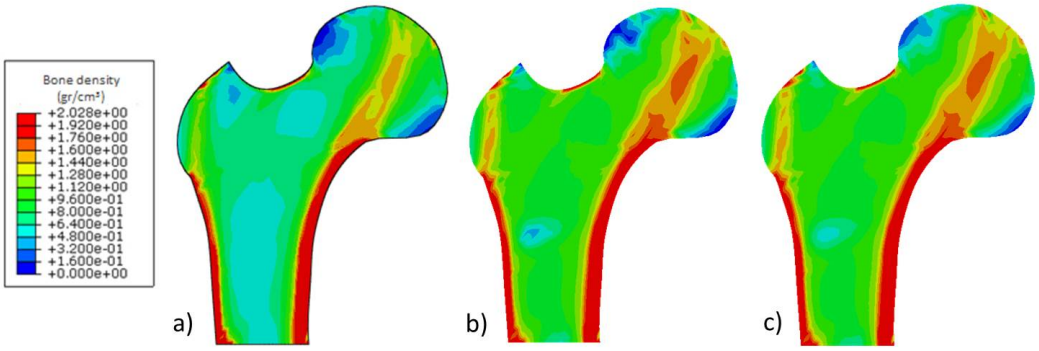

Figure 2.8: *Bone density distribution after 300 days with a) Stanford model, b) Doblaré and García model and b) its correction (Mengoni and Ponthot, 2015).*

2.5 Summary of the presented models

As explained before, phenomenological remodeling models are based on the definition of three characteristics: the density rate function ($\dot{\rho}$ function of $\dot{r}$), the remodeling rate function ($\dot{r}$ function of ψ_t and ψ_t^*), and the stimulus definition (ψ and its homeostatic level ψ_t^*).

These models are coupled to a constitutive law for the bone matrix and both models reproduce the bone density distribution. However, Doblaré and García anisotropic model presented two inconsistencies in its formulation that leads to numerical irregularities (Mengoni and Ponthot, 2015). For that, we have explained the model and its correction. Specifically, the correction presents a remodeling criterion in resorption (g^r) that differs significantly to the one presented in the original Doblaré and García model. Indeed, it can be easily shown that the criteria in resorption and in formation have opposite dimensions as it clearly appears in their isotropic formulation. Mengoni and Ponthot (2015) also modified the parameter that divided the evolution of the remodeling law. Finally, with all of these changes, a new evolution of the remodeling law has been obtained.

Standford and Doblaré and García models have been used in this Thesis. From now as when we named Doblaré and García model, we refer to the correction proposed by Mengoni and Ponthot (2015). Stanford and Doblaré and García model present some limitations and problems that will be analyzed into following Chapters.

CHAPTER 3

Numerical stability and convergence analysis of bone remodeling models

3.1 Introduction

Bone remodeling is the mechanism that regulates the relationship between bone morphology and its external mechanical loads. It is based on the fact that the "living bone is continuously adapting itself to external stimuli". The ability of the models presented in this Thesis to predict bone remodeling is of great importance because this process has an enormous effect on the overall behavior and health of the entire body. During the last years, some works with mathematical issues of these models (Cowin and Doty, 2007) as the existence and uniqueness of their solutions have been studied under some quite strong assumptions (Fernández et al., 2008, 2012b).

In this Chapter, we show the limitations of the Stanford bone remodeling theory (Jacobs, 1994) and the anisotropic extension of the Stanford model proposed by Doblaré and García (2002). And we propose a novel assumption modifying the Stanford bone remodeling model (Beaupré et al., 1990), specifically the reference homeostatic stimulus which will be now dependent on the loading history that each point is supporting. Other authors (Schriefer et al., 2005; Vahdati and Rouhi, 2009) have also used a non-constant homeostatic stimulus in bone remodeling simulations known as the cellular accommodation theory. In fact, in this Thesis we also hypothesize that this modification will directly affect the stabilization of the numerical results corresponding to the spatial distribution of the apparent density. In addition, we also perform a theoretical analysis to demonstrate the linear convergence of the bone remodeling algorithm. Specifically, for the Stanford bone remodeling theory (Beaupré et al., 1990), we incorporate a non-constant reference homeostatic stimulus.

3.2 Some problems of bone remodeling models

All these models are robust tools that provide us with important information from the bone. However, if we are interested in studying patient-specific characteristics or the behavior of a prosthesis in the long term, we could have difficulties with these models because they present numerical instabilities and dependence of the initial conditions.

These models normally use a reference homeostatic mechanical stimulus that defines the equilibrium or dead zone (Huiskes et al., 1987; Carter, 1987), where the bone response is null. However, if overload/disuse occurs and the mechanical stimulus is higher/lower than the equilibrium level, bone formation/resorption is promoted. Different kinds of mechanical variables are used to define this reference homeostatic stimulus, such as strain (Frost, 1990; Fernandes et al., 1999), strain energy density (Huiskes et al., 1987; Weinans et al., 1992; Kaczmarczyk and Pearce, 2011) or effective stress (Beaupré et al., 1990; Doblaré and García, 2002).

All these models assumed that this reference homeostatic stimulus was constant, at least when characterized for specific zones in bones. Thus, for example, Carter and Beaupré (2001) considered an equilibrium effective stress stimulus of 50 MPa/day for the femur, 62.5 MPa/day for the femoral periosteal, around 42 MPa/day for the rooster ulna bone and 60 MPa/day for the human tibia (Figure 3.1).

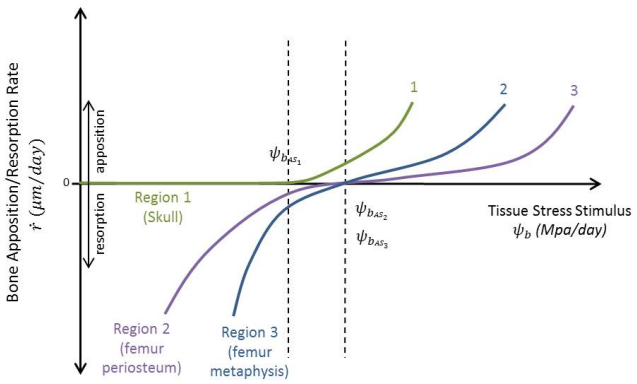

Figure 3.1: *Hypothetical curves for three bone regions showing the rate of surface remodeling as a function of the tissue level stress stimulus (Beaupré et al., 1990).*

One of the main contributions of this Chapter is to modify this assumption, hypothesizing that this reference homeostatic stimulus is not constant, but is locally dependent on the loading history that each local point is effectively supporting. As a direct consequence of this assumption, we will demonstrate that the nu-

merical instabilities that all these algorithms normally present (Fernández et al., 2010) are directly solved, clearly improving the final results. Several numerical techniques have been proposed in order to stabilize these results: extrapolation from gauss points to nodes (Jacobs et al., 1995), Cosserat's theory (Madeo et al., 2012), gradient elasticity (Gitman et al., 2010) and diffusion of the apparent density (Fernández et al., 2012a). However, even if the results have been improved, the numerical problems still persist.

Figure 3.2: *Radiography of the real density in the femur with permission from Jacobs et al. (1997).*

In fact, independently of the bone remodeling theory implemented, strong bone density discontinuities and instabilities are normally presented. For instance, the numerical results of the typical bone remodeling benchmark problem using the bone remodeling theory (Beaupré et al., 1990; Jacobs et al., 1995), known as the Stanford remodeling model are represented in Figure 3.3. As we can see, after 300 load increments the bone density distribution (Figure 3.3a) is very similar to the actual distribution (Figure 3.2). However, after 1000 and 3000 load increments, the bone density distribution clearly presents spatial instabilities.

Therefore, in this thesis, we have modified the Stanford bone remodeling model (Beaupré et al., 1990), specifically the reference homeostatic stimulus which will now be dependent on the loading history that each point is supporting. In addition, we perform a theoretical analysis to demonstrate the linear convergence of the bone remodeling algorithm. Specifically, for the Stanford bone remodeling theory (Beaupré et al., 1990), we incorporate a non-constant reference homeostatic stimulus. After the theoretical analysis did in the isotropic model, this novel modification has been applied in a FE analysis in the following models: isotropic Stanford model (Section 2.1) and anisotropic Doblaré and García model (Section 2.2).

Therefore, we define the bone remodeling rate as $\dot{r} = f(\psi_t - \psi_t^*)$ (function (2.14)), being the difference between ψ_t and ψ_t^* the stimulus that regulates the bone remodeling responses, and ψ_t^* is the reference value of the tissue stress level

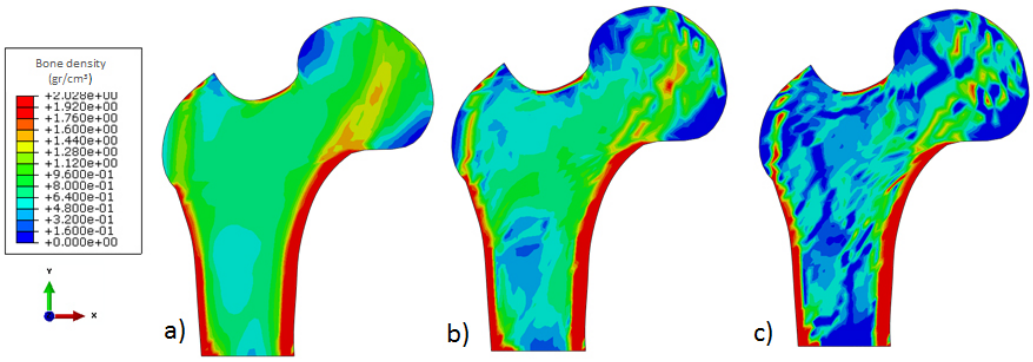

Figure 3.3: *Results of a simulation with the Stanford isotropic model in 2D (Beaupré et al., 1990) for the distribution of the bone density after a) 300, b) 1000 and c) 3000 days.*

of the equilibrium zone. This value was assumed constant in Beaupré et al. (1990), but we propose here that this reference value is adapted to the loading history in relation with the bone remodeling rate. Schriefer et al. (2005) and Vahdati and Rouhi (2009) used a similar mathematical law to consider the effect of cellular accommodation in trabecular bone. In this thesis, this reference value is directly related to the surface remodeling rate ($\dot{r}$), using the following ordinary differential equation:

$$\dot{\psi}_t^* = \psi_t^* A \dot{r} e^{a|\dot{r}|} \tag{3.1}$$

where a and A are constants that regulate the adaptivity of the reference stimulus. We note that the adaptation of the reference value allows higher accuracy in the bone remodeling area and greater stability in the process to be obtained.

Introducing this equation in the previously model explained (Stanford model - Section 2.1) allows to solve the mechanical problem. This part has been done in collaboration with Dr. J.R. Fernández (University of Vigo) (Garijo et al., 2014a). We have not developed the demonstration for the Doblaré and García model, because it is very similar and Doblaré and García model is based on the Stanford model. Then, we can say if one fulfills the stability, the other also.

3.3 Numerical analysis of the convergence

3.3.1 Variational problems

First of all, we describe the variational problem in the mechanical environment for the mathematical analysis.

Let $\mathbb{S}^d$ be the space of second order symmetric tensors on $\mathbb{R}^d$, or equivalently, the space of symmetric matrices of order d, and let : be its inner product and $|\cdot|$ its norm.

Let $\Omega \subset \mathbb{R}^d$, $d = 1, 2, 3$, be an open bounded domain and $\Gamma = \partial\Omega$ its boundary, assumed to be Lipschitz continuous and divided into two disjoint parts Γ_D and Γ_N. We denote by $\boldsymbol{x} = (x_i)_{i=1}^d$ a generic point of $\overline{\Omega} = \Omega \cup \Gamma$, and for $\boldsymbol{x} \in \Gamma$, let $\boldsymbol{\nu}(\boldsymbol{x}) = (\nu_i(\boldsymbol{x}))_{i=1}^d$ be the outward unit normal vector to Γ at point $\boldsymbol{x}$ (see Figure 3.4).

The body occupies a set $\overline{\Omega}$ which is being acted upon by a volume force of density $\boldsymbol{f}$, it is clamped on Γ_D and surface tractions with density $\boldsymbol{g}$ act on Γ_N. Finally, we denote by $[0, T]$, $T > 0$, the time interval of interest.

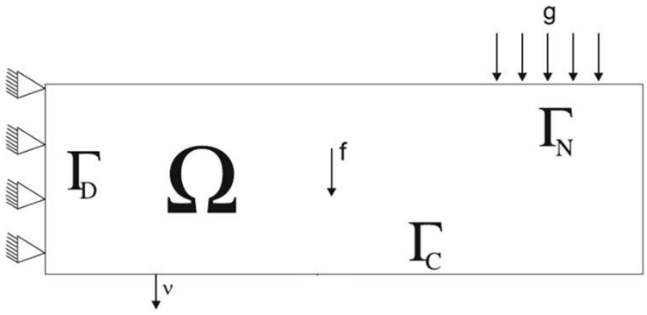

Figure 3.4: *Bone remodeling benchmark problem*

Let $\boldsymbol{u} = (u_i)_{i=1}^d$, $\boldsymbol{\sigma} = (\sigma_{ij})_{i,j=1}^d$ and $\boldsymbol{\varepsilon}(\boldsymbol{u})$ denote the displacement field, the stress field and the linearized strain tensor, respectively. As usual, we recall that $\boldsymbol{\varepsilon}(\boldsymbol{u}) = (\varepsilon_{ij}(\boldsymbol{u}))_{i,j=1}^d$ is given by

$$\varepsilon_{ij}(\boldsymbol{u}) = \frac{1}{2}\left(\frac{\partial u_i}{\partial x_j} + \frac{\partial u_j}{\partial x_i}\right), \quad i, j = 1, \ldots, d \tag{3.2}$$

The bone is assumed elastic and the constitutive law is written as follows (see Weinans et al. (1992)),

$$\boldsymbol{\sigma} = \boldsymbol{\sigma}(\boldsymbol{u}) = 2\,\mu(\rho)\boldsymbol{\varepsilon}(\boldsymbol{u}) + \lambda(\rho)\mathrm{Div}\,(\boldsymbol{u})\mathcal{I} \quad \text{in} \quad \overline{\Omega} \times [0, T] \tag{3.3}$$

Here, $\mathcal{I}$ denotes the identity operator in $\mathbb{S}^d$, Div represents the divergence operator and $\mu(\rho)$ and $\lambda(\rho)$ are Lame's coefficients of the material, assumed to depend on the density of the bone denoted by ρ.

Problem P. *Find the displacement field* $\boldsymbol{u} : \overline{\Omega} \times [0, T] \to \mathbb{R}^d$*, the reference value of the tissue stress level* $\psi_t^* : \overline{\Omega} \times [0, T] \to \mathbb{R}$ *and the density function* $\rho : \overline{\Omega} \times [0, T] \to [\underline{\rho}, \overline{\rho}]$ *such that* $\rho(0) = \rho_0$*,* $\psi_t^* = (\psi_t^*)_0$ *and,*

$$\dot{\rho} = kf(\psi_t - \psi_t^*)S_\nu(\rho)\overline{\rho} \quad in \quad \Omega \times (0,T) \tag{3.4}$$
$$-\mathrm{Div}\,\boldsymbol{\sigma}(\boldsymbol{u}) = \boldsymbol{f} \quad in \quad \Omega \times (0,T) \tag{3.5}$$
$$\dot{\psi_t^*} = \psi_t^* Af(\psi_t - \psi_t^*)e^{af(\psi_t - \psi_t^*)} \quad in \quad \Omega \times (0,T) \tag{3.6}$$
$$\boldsymbol{u} = \boldsymbol{0} \quad on \quad \Gamma_D \times (0,T) \tag{3.7}$$
$$\boldsymbol{\sigma\nu} = \boldsymbol{g} \quad on \quad \Gamma_N \times (0,T) \tag{3.8}$$

where Lame's coefficients $\lambda(\rho)$ and $\mu(\rho)$ were defined above and the stress field $\boldsymbol{\sigma}(\boldsymbol{u}) : \overline{\Omega} \times [0,T] \to \mathbb{S}^d$ is given by

$$\boldsymbol{\sigma}(\boldsymbol{u}) = 2\,\mu(\rho)\boldsymbol{\varepsilon}(\boldsymbol{u}) + \lambda(\rho)\mathrm{Div}\,(\boldsymbol{u})\mathcal{I} \quad in \quad \overline{\Omega} \times [0,T]. \tag{3.9}$$

Moreover, the mechanical stimulus ψ_t is defined as

$$\psi_t = n^{1/m}\sqrt{E(\rho)^2\left(\alpha\boldsymbol{\varepsilon}(\boldsymbol{u}) : \boldsymbol{\varepsilon}(\boldsymbol{u}) + \beta(\mathrm{Div}\,(\boldsymbol{u}))^2\right)} \tag{3.10}$$

We obtain now a variational formulation of the mechanical Problem P. Denoting by $Y = L^2(\Omega)$ and $H = [L^2(\Omega)]^d$, we define the following variational spaces equipped with the product norms derived from usual norms in Sobolev spaces:

$$\begin{aligned} V &= \{\boldsymbol{v} = (v_i)_{i=1}^d \in [H^1(\Omega)]^d \;;\; \boldsymbol{v} = \boldsymbol{0} \quad \text{on} \quad \Gamma_D\} \\ Q &= \{\boldsymbol{\tau} = (\tau_{ij})_{i,j=1}^d \in [L^2(\Omega)]^{d\times d} \;;\; \tau_{ij} = \tau_{ji}, \quad 1 \le i,j \le d\} \end{aligned} \tag{3.11}$$

We make the following assumptions on the problem data:

(i) The density forces have regularity:

$$\boldsymbol{f} \in C([0,T];[C(\overline{\Omega})]^d), \quad \boldsymbol{g} \in C([0,T];[C(\overline{\Gamma_N})]^d) \tag{3.12}$$

(ii) The initial density ρ_0 satisfies the following conditions:

$$\rho_0 \in C(\overline{\Omega}), \quad \underline{\rho} \le \rho_0(\boldsymbol{x}) \le \overline{\rho} \quad \text{for all} \quad \boldsymbol{x} \in \overline{\Omega} \tag{3.13}$$

(iii) The initial reference value of the tissue stress level $(\psi_t^*)_0$ satisfies the following condition:

$$(\psi_t^*)_0 \in Y \tag{3.14}$$

In order to simplify the writing, for every $\rho \in \nu L^\infty(\Omega)$, we define the bilinear form $c(\rho;\cdot,\cdot) : V \times V \to \mathbb{R}$ given by

$$c(\rho;\boldsymbol{u},\boldsymbol{v}) = \int_\Omega [2\mu(\rho)\boldsymbol{\varepsilon}(\boldsymbol{u}) \,:\, \boldsymbol{\varepsilon}(\boldsymbol{v}) + \lambda(\rho)\mathrm{Tr}(\boldsymbol{\varepsilon}(\boldsymbol{u}))\mathrm{Tr}(\boldsymbol{\varepsilon}(\boldsymbol{v}))]\, d\boldsymbol{x}, \quad \forall \boldsymbol{u},\boldsymbol{v} \in V \tag{3.15}$$

where Tr denotes the trace operator given as $\mathrm{Tr}(\boldsymbol{\tau}) = \sum_{i=1}^{d} \tau_{ii}$ for all $\boldsymbol{\tau} = (\tau_{ij})_{i,j=1}^{d}$, and we introduce the linear form $L : V \to \mathbb{R}$ and the function $\Phi : Y \times Y \to Y$ as follows,

$$\begin{aligned} L(\boldsymbol{v}) &= \int_\Omega \boldsymbol{f}\cdot\boldsymbol{v}\, d\boldsymbol{x} + \int_{\Gamma_N} \boldsymbol{g}\cdot\boldsymbol{v}\, d\Gamma, \quad \forall \boldsymbol{v} \in V, \\ \Phi(\rho, \psi_t - \psi_t^*) &= kf(\psi_t - \psi_t^*)S_\nu(\rho)\overline{\rho}. \end{aligned} \tag{3.16}$$

Now, proceeding as in Fernández et al. (2010), we give an equivalent expression for equation (3.4), incorporating the restriction $\underline{\rho} \le \rho \le \overline{\rho}$. Thus, we write it in the following form:

$$\dot{\rho} - kf(\psi_t - \psi_t^*)S_\nu(\rho)\overline{\rho} + \partial I_{[\underline{\rho},\overline{\rho}]}(\rho) \ni 0 \tag{3.17}$$

where $\partial I_{[\underline{\rho},\overline{\rho}]}$ denotes the subdifferential of the indicator function $I_{[\underline{\rho},\overline{\rho}]}$ of the interval $[\underline{\rho},\overline{\rho}]$.

Finally, let us define the convex set of admissible density functions,

$$K = \{\xi \in Y \,;\, \underline{\rho} \le \xi \le \overline{\rho},\ \text{a.e. in } \Omega\} \tag{3.18}$$

Applying Green's formula, we derive the following variational formulation of the mechanical Problem P.

Problem VP. *Find a displacement field $\boldsymbol{u} : [0,T] \to V$, a reference value of the tissue stress level $\psi_t^* : [0,T] \to Y$ and a density function $\rho : [0,T] \to K$ such that $\rho(0) = \rho_0$, $\psi_t^* = (\psi_t^*)_0$ and for a.e. $t \in (0,T)$,*

$$c(\rho(t);\boldsymbol{u}(t),\boldsymbol{v}) = L(\boldsymbol{v}), \quad \forall \boldsymbol{v} \in V \tag{3.19}$$

$$(\dot{\rho}(t), \xi - \rho(t))_Y \ge (\Phi(\rho(t), \psi_t - \psi_t^*), \xi - \rho(t))_Y, \quad \forall \xi \in K \tag{3.20}$$

$$\dot{\psi}_t^* = \psi_t^* A f(\psi_t - \psi_t^*) e^{af(\psi_t - \psi_t^*)} \tag{3.21}$$

where the function Φ is given in (3.16), the mechanical stimulus ψ_t is defined by (3.10) and the stress field $\boldsymbol{\sigma}(\boldsymbol{u}(t))$ is obtained from (3.9).

The existence of a unique weak solution to Problem VP still remains an open problem. Even if we have observed some similarities between this problem and

the damage problems considered, for instance, in Campo et al. (2007) or Campo et al. (2006), the techniques developed there can no be used here because there is not diffusion of the bone remodeling.

3.3.2 Numerical analysis of a fully discrete scheme

In this section, we introduce fully discrete approximations of the variational problem VP. The discretization is done in two steps. First, the spatial variable is approximated using three finite element spaces $V^h \subset V$, $Q^h \subset Q$ and $B^h \subset Y$, which are defined as

$$
\begin{aligned}
V^h &= \{\boldsymbol{w}^h \in [C(\overline{\Omega})]^d \ ; \ \boldsymbol{w}^h_{|_T} \in [P_1(T)]^d, \ T \in \mathcal{T}^h, \quad \boldsymbol{w}^h = \boldsymbol{0} \text{ on } \Gamma_D\} \\
Q^h &= \{\boldsymbol{\tau}^h \in [L^2(\Omega)]^{d\times d} \ ; \ \boldsymbol{\tau}^h_{|_T} \in [P_0(T)]^{d\times d}, \ T \in \mathcal{T}^h\} \\
B^h &= \{\xi^h \in Y \ ; \ \xi^h_{|_T} \in P_0(T), \quad T \in \mathcal{T}^h\}
\end{aligned}
$$

Here, we assume that Ω is a polyhedral domain, we denote by $\mathcal{T}^h$ a triangulation of $\overline{\Omega}$ compatible with the partition of the boundary $\Gamma = \partial\Omega$ into Γ_D and Γ_N, and we represent by $P_q(T)$, $q = 0 - 1$, the space of polynomials of global degree less or equal to q in T. Moreover, as usual $h > 0$ denotes the spatial discretization parameter. Finally, we define the discrete convex set of admissible density functions as $K^h = K \cap B^h$; that is,

$$
K^h = \{\xi^h \in B^h \, ; \, \underline{\rho} \leq \xi^h \leq \overline{\rho} \quad \text{in} \quad \Omega\} \tag{3.22}
$$

Secondly, the time derivatives are discretized by using a uniform partition of the time interval $[0, T]$, denoted by $0 = t_0 < t_1 < \ldots < t_N = T$, and let k be the time step size, $k = T/N$. Moreover, for a continuous function $g(t)$ we denote $g_n = g(t_n)$.

Using the explicit Euler scheme, the fully discrete approximation of Problem VP is the following.

Problem VP^{hk}. *Find a discrete displacement field $\boldsymbol{u}^{hk} = \{\boldsymbol{u}^{hk}_n\}_{n=0}^N \subset V^h$, a discrete reference value of the tissue stress level $(\psi^*_t)^{hk} = \{(\psi^*_t)^{hk}_n\}_{n=0}^N \subset B^h$ and a*

discrete density function $\rho^{hk} = \{\rho_n^{hk}\}_{n=0}^N \subset K^h$ *such that for all* $\boldsymbol{v}^h \in V^h$ *and* $\xi^h \in K^h$,

$$c(\rho_n^{hk}; \boldsymbol{u}_n^{hk}, \boldsymbol{v}^h) = L(\boldsymbol{v}^h), \quad n = 0, 1, \ldots, N \tag{3.23}$$

$$\left(\frac{\rho_n^{hk} - \rho_{n-1}^{hk}}{k}, \xi^h - \rho_n^{hk}\right)_Y \geq \left(\Phi(\rho_{n-1}^{hk}, (\psi_t)_{n-1}^{hk} - (\psi_t^*)_{n-1}^{hk}), \xi^h - \rho_n^{hk}\right)_Y, \quad n = 1, 2, \ldots, N \tag{3.24}$$

$$\frac{(\psi_t^*)_n^{hk} - (\psi_t^*)_{n-1}^{hk}}{k} = (\psi_t^*)_{n-1}^{hk} A f((\psi_t)_{n-1}^{hk} - (\psi_t^*)_{n-1}^{hk}) e^{af((\psi_t)_{n-1}^{hk} - (\psi_t^*)_{n-1}^{hk})}, \; n = 1, 2, \ldots, N \tag{3.25}$$

where ρ_0^{hk} and $(\psi_t^*)_0^{hk}$ denote appropriate approximations of the initial conditions ρ_0 and $(\psi_t^*)_0$, respectively, and the discrete mechanical stimulus field $(\psi_t)^{hk} = \{(\psi_t)_n^{hk}\}_{n=0}^N \subset B^h$ and the discrete stress field $\boldsymbol{\sigma}_n^{hk} = (\boldsymbol{\sigma}_n^{hk})_{n=0}^N \subset Q^h$ are given by, for all $n = 0, 1, \ldots, N$,

$$(\psi_t)_n^{hk} = n^{1/m} \sqrt{E(\rho_n^{hk})^2 \left(\alpha \boldsymbol{\varepsilon}(\boldsymbol{u}_n^{hk}) : \boldsymbol{\varepsilon}(\boldsymbol{u}_n^{hk}) + \beta (\mathrm{Div}\,(\boldsymbol{u}_n^{hk}))^2\right)} \tag{3.26}$$

$$\boldsymbol{\sigma}_n^{hk} = 2\,\mu(\rho_n^{hk}) \boldsymbol{\varepsilon}(\boldsymbol{u}_n^{hk}) + \lambda(\rho_n^{hk}) \mathrm{Div}\,(\boldsymbol{u}_n^{hk}) \mathcal{I} \tag{3.27}$$

A unique solution existence to this discrete problem is easily obtained applying classical results on elliptic linear variational inequalities (Glowinski, 1984).

In this section, our aim is to obtain an error estimate of the numerical errors $\|\boldsymbol{u}_n - \boldsymbol{u}_n^{hk}\|_V$, $\|(\psi_t)_n - (\psi_t)_n^{hk}\|_Y$, $\|(\psi_t^*)_n - (\psi_t^*)_n^{hk}\|_Y$ and $\|\rho_n - \rho_n^{hk}\|_Y$. Therefore, we assume that Problem VP has a unique solution with the following regularity:

$$\begin{aligned} &\boldsymbol{u} \in C^1([0,T]; V) \cap C([0,T]; [W^{1,\infty}(\overline{\Omega})]^d), \quad \rho \in C^1([0,T]; Y) \\ &\psi_t^* \in C^1([0,T]; Y), \quad \psi_t \in C([0,T]; Y) \end{aligned} \tag{3.28}$$

We have the following result which provides a priori error estimates.

Theorem 3.3.1 *Assume that Problem VP has a unique solution* $(\boldsymbol{u}, \psi_t, \psi_t^*, \rho)$ *with regularity (3.28) and denote by* $(\boldsymbol{u}^{hk}, (\psi_t)^{hk}, (\psi_t^*)^{hk}, \rho^{hk})$ *the solution to Problem VP*^{hk}. *Then, there exists a positive constant* $C > 0$, *independent of the discretization parameters* h *and* k *but depending on the continuous solution* $(\boldsymbol{u}, \psi_t, \psi_t^*, \rho)$ *and the data of the problem, such that, for all* $\{\boldsymbol{v}_n^h\}_{n=0}^N \subset V^h$, $\{z_n^h\}_{n=0}^N \subset B^h$ *and*

$\{\xi_n^h\}_{n=0}^N \subset K^h$,

$$\begin{aligned}
&\max_{0\le n\le N}\|\boldsymbol{u}_n-\boldsymbol{u}_n^{hk}\|_V^2+\max_{0\le n\le N}\|\rho_n-\rho_n^{hk}\|_Y^2+\max_{0\le n\le N}\|(\psi_t)_n-(\psi_t)_n^{hk}\|_Y^2\\
&\qquad\qquad+\max_{0\le n\le N}\|(\psi_t^*)_n-(\psi_t^*)_n^{hk}\|_Y^2\\
&\le C\max_{0\le n\le N}\|\boldsymbol{u}_n-\boldsymbol{v}_n^h\|_V^2+Ck\sum_{j=1}^{N}\|\rho_j-\xi_j^h\|_Y^2+C\max_{1\le n\le N}\|\rho_n-\xi_n^h\|_Y^2\\
&\quad+\frac{C}{k}\sum_{j=1}^{N-1}\|\rho_j-\xi_j^h-(\rho_{j+1}-\xi_{j+1}^h)\|_Y^2+C\|\rho_0-\rho_0^h\|_Y^2+C\|\boldsymbol{u}_0-\boldsymbol{u}_0^h\|_V^2\\
&\quad+Ck\sum_{j=1}^{N}\Big\{\|\rho_j-\xi_j^h\|_Y^2+\|\Phi_j-\frac{\rho_j-\rho_{j-1}}{k}\|_Y\|\rho_j-\xi_j^h\|_Y\\
&\quad+\|\frac{\rho_j-\rho_{j-1}}{k}-\dot\rho_j\|_Y^2\Big\}+Ck^2+C\Big(\max_{0\le n\le N}\|(\psi_t^*)_n-z_n^h\|_Y^2\\
&\quad+\|(\psi_t^*)_0-(\psi_t^*)_0^{hk}\|_Y^2+\|(\psi_t^*)_1-z_1^h\|_Y^2\\
&\quad+\frac{1}{k}\sum_{j=1}^{N-1}\|(\psi_t^*)_j-z_j^h-((\psi_t^*)_{j+1}-z_{j+1}^h)\|_Y^2\Big)\\
&\quad+Ck\sum_{j=1}^{N}\Big\{\|(\dot\psi_t^*)_j-\frac{(\psi_t^*)_j-(\psi_t^*)_{j-1}}{k}\|_Y^2+\|(\psi_t^*)_j-z_j^h\|_Y^2\Big\}
\end{aligned}\tag{3.29}$$

Proof. The first step is to obtain some error estimates of the displacement fields proceeding as in Fernández et al. (2010). Then, we subtract variational equation (3.19) at time $t = t_n$ for $\boldsymbol{v} = \boldsymbol{v}^h \in V^h$ and variational equation (3.23), and we find that

$$c(\rho_n;\boldsymbol{u}_n,\boldsymbol{v}^h)-c(\rho_n^{hk};\boldsymbol{u}_n^{hk},\boldsymbol{v}^h)=0,\quad\forall\boldsymbol{v}^h\in V^h\tag{3.30}$$

Therefore,

$$\begin{aligned}
&c(\rho_n;\boldsymbol{u}_n,\boldsymbol{u}_n-\boldsymbol{u}_n^{hk})-c(\rho_n^{hk};\boldsymbol{u}_n^{hk},\boldsymbol{u}_n-\boldsymbol{u}_n^{hk})\\
&\qquad=c(\rho_n;\boldsymbol{u}_n,\boldsymbol{u}_n-\boldsymbol{v}^h)-c(\rho_n^{hk};\boldsymbol{u}_n^{hk},\boldsymbol{u}_n-\boldsymbol{v}^h),\quad\forall\boldsymbol{v}^h\in V^h
\end{aligned}\tag{3.31}$$

Since $\rho_n^{hk}\in K^h$, we have $\rho_n^{hk}\ge\underline{\rho}>0$ and we get

$$\begin{aligned}
&c(\rho_n;\boldsymbol{u}_n,\boldsymbol{u}_n-\boldsymbol{u}_n^{hk})-c(\rho_n^{hk};\boldsymbol{u}_n^{hk},\boldsymbol{u}_n-\boldsymbol{u}_n^{hk})\\
&\qquad=c(\rho_n^{hk};\boldsymbol{u}_n-\boldsymbol{u}_n^{hk},\boldsymbol{u}_n-\boldsymbol{u}_n^{hk})\\
&\qquad\quad+c(\rho_n;\boldsymbol{u}_n,\boldsymbol{u}_n-\boldsymbol{u}_n^{hk})-c(\rho_n^{hk};\boldsymbol{u}_n,\boldsymbol{u}_n-\boldsymbol{u}_n^{hk}),\\
&c(\rho_n;\boldsymbol{u}_n,\boldsymbol{u}_n-\boldsymbol{v}^h)-c(\rho_n^{hk};\boldsymbol{u}_n^{hk},\boldsymbol{u}_n-\boldsymbol{v}^h)\\
&\qquad=c(\rho_n^{hk};\boldsymbol{u}_n-\boldsymbol{u}_n^{hk},\boldsymbol{u}_n-\boldsymbol{v}^h)\\
&\qquad\quad+c(\rho_n;\boldsymbol{u}_n,\boldsymbol{u}_n-\boldsymbol{v}^h)-c(\rho_n^{hk};\boldsymbol{u}_n,\boldsymbol{u}_n-\boldsymbol{v}^h),\\
&c(\rho_n^{hk};\boldsymbol{u}_n-\boldsymbol{u}_n^{hk},\boldsymbol{u}_n-\boldsymbol{u}_n^{hk})\ge\alpha\|\boldsymbol{u}_n-\boldsymbol{u}_n^{hk}\|_V^2
\end{aligned}\tag{3.32}$$

Keeping in mind the regularity $\boldsymbol{u} \in C([0,T];[W^{1,\infty}(\overline{\Omega})]^{d\times d})$ and that $\rho_n, \rho_n^{hk} \in [\underline{\rho}, \overline{\rho}]$, it follows that

$$\begin{aligned} &c(\rho_n;\boldsymbol{u}_n,\boldsymbol{u}_n-\boldsymbol{u}_n^{hk})-c(\rho_n^{hk};\boldsymbol{u}_n,\boldsymbol{u}_n-\boldsymbol{u}_n^{hk})\le C\|\rho_n-\rho_n^{hk}\|_Y\|\boldsymbol{u}_n-\boldsymbol{u}_n^{hk}\|_V,\\ &c(\rho_n;\boldsymbol{u}_n,\boldsymbol{u}_n-\boldsymbol{v}^h)-c(\rho_n^{hk};\boldsymbol{u}_n^{hk},\boldsymbol{u}_n-\boldsymbol{v}^h)\\ &\qquad\le C\|\boldsymbol{u}_n-\boldsymbol{u}_n^{hk}\|_V\|\boldsymbol{u}_n-\boldsymbol{v}^h\|_V+C\|\rho_n-\rho_n^{hk}\|_Y\|\boldsymbol{u}_n-\boldsymbol{v}^h\|_V \end{aligned} \tag{3.33}$$

Hence, using Cauchy's inequality

$$pq\le\epsilon p^2+\frac{1}{4\epsilon}q^2,\quad p,q,\epsilon\in\mathbb{R},\ \epsilon>0 \tag{3.34}$$

we obtain the following estimate for the displacement fields,

$$\|\boldsymbol{u}_n-\boldsymbol{u}_n^{hk}\|_V^2\le C(\|\boldsymbol{u}_n-\boldsymbol{v}^h\|_V^2+\|\rho_n-\rho_n^{hk}\|_Y^2),\quad \forall\boldsymbol{v}^h\in V^h \tag{3.35}$$

Now, we get an error estimate on the reference value of the tissue stress level. Subtracting equation (3.21) at time $t=t_n$ and equation (3.25) and multiplying by a test function $z^h\in B^h$, we have

$$\begin{aligned} &\left(\dot{\psi}_t^*-\frac{(\psi_t^*)_n^{hk}-(\psi_t^*)_{n-1}^{hk}}{k},z^h\right)_Y-\Big(\psi_t^*Af(\psi_t-\psi_t^*)e^{af(\psi_t-\psi_t^*)}\\ &\qquad-(\psi_t^*)_{n-1}^{hk}Af((\psi_t)_{n-1}^{hk}-(\psi_t^*)_{n-1}^{hk})e^{af((\psi_t)_{n-1}^{hk}-(\psi_t^*)_{n-1}^{hk})},z^h\Big)_Y=0 \end{aligned} \tag{3.36}$$

Therefore, for all $z^h\in B^h$ it follows that

$$\begin{aligned} &\left(\dot{\psi}_t^*-\frac{(\psi_t^*)_n^{hk}-(\psi_t^*)_{n-1}^{hk}}{k},(\psi_t^*)_n-(\psi_t^*)_n^{hk}\right)_Y-\Big(\psi_t^*Af(\psi_t-\psi_t^*)e^{af(\psi_t-\psi_t^*)}\\ &\qquad-(\psi_t^*)_{n-1}^{hk}Af((\psi_t)_{n-1}^{hk}-(\psi_t^*)_{n-1}^{hk})e^{af((\psi_t)_{n-1}^{hk}-(\psi_t^*)_{n-1}^{hk})},(\psi_t^*)_n-(\psi_t^*)_n^{hk}\Big)_Y\\ =\ &\left(\dot{\psi}_t^*-\frac{(\psi_t^*)_n^{hk}-(\psi_t^*)_{n-1}^{hk}}{k},(\psi_t^*)_n-z^h\right)_Y-\Big(\psi_t^*Af(\psi_t-\psi_t^*)e^{af(\psi_t-\psi_t^*)}\\ &\qquad-(\psi_t^*)_{n-1}^{hk}Af((\psi_t)_{n-1}^{hk}-(\psi_t^*)_{n-1}^{hk})e^{af((\psi_t)_{n-1}^{hk}-(\psi_t^*)_{n-1}^{hk})},(\psi_t^*)_n-z^h\Big)_Y \end{aligned} \tag{3.37}$$

Taking into account that

$$\begin{aligned} &|\Big(\psi_t^*Af(\psi_t-\psi_t^*)e^{af(\psi_t-\psi_t^*)}-(\psi_t^*)_{n-1}^{hk}Af((\psi_t)_{n-1}^{hk}-(\psi_t^*)_{n-1}^{hk})\\ &\qquad e^{af((\psi_t)_{n-1}^{hk}-(\psi_t^*)_{n-1}^{hk})},z\Big)_Y|\\ &\quad\le C\|(\psi_t^*)_n-(\psi_t^*)_{n-1}^{hk}\|_Y\|z\|_Y+C\|(\psi_t)_n-(\psi_t)_{n-1}^{hk}\|_Y\|z\|_Y \end{aligned} \tag{3.38}$$

using several times inequality (3.34) we have

$$\begin{aligned}\left(\frac{(\psi_t^*)_n-(\psi_t^*)_{n-1}}{k}-\frac{(\psi_t^*)_n^{hk}-(\psi_t^*)_{n-1}^{hk}}{k},(\psi_t^*)_n-(\psi_t^*)_n^{hk}\right)_Y\\ \leq\left(\frac{(\psi_t^*)_n-(\psi_t^*)_{n-1}}{k}-\frac{(\psi_t^*)_n^{hk}-(\psi_t^*)_{n-1}^{hk}}{k},(\psi_t^*)_n-z^h\right)_Y\\ +C\Big(\|(\psi_t^*)_n-(\psi_t^*)_{n-1}^{hk}\|_Y^2+\|\dot{\psi}_t^*-\frac{(\psi_t^*)_n-(\psi_t^*)_{n-1}}{k}\|_Y^2\\ +\|(\psi_t)_n-(\psi_t)_{n-1}^{hk}\|_Y^2+\|(\psi_t^*)_n-z^h\|_Y^2\Big),\quad\forall z^h\in B^h\end{aligned}\tag{3.39}$$

Keeping in mind that

$$\begin{aligned}\left(\frac{(\psi_t^*)_n-(\psi_t^*)_{n-1}}{k}-\frac{(\psi_t^*)_n^{hk}-(\psi_t^*)_{n-1}^{hk}}{k},(\psi_t^*)_n-(\psi_t^*)_n^{hk}\right)_Y\\ \geq\frac{1}{2k}\left(\|(\psi_t^*)_n-(\psi_t^*)_n^{hk}\|_Y^2-\|(\psi_t^*)_{n-1}-(\psi_t^*)_{n-1}^{hk}\|_Y^2\right)\end{aligned}\tag{3.40}$$

by induction we find that

$$\begin{aligned}\|(\psi_t^*)_n-(\psi_t^*)_n^{hk}\|_Y^2\leq C\sum_{j=1}^{n}\left((\psi_t^*)_j-(\psi_t^*)_{j-1}-((\psi_t^*)_j^{hk}-(\psi_t^*)_{j-1}^{hk}),(\psi_t^*)_j-z_j^h\right)_Y\\ +Ck\sum_{j=1}^{N}\Big(\|(\psi_t^*)_j-(\psi_t^*)_{j-1}^{hk}\|_Y^2+\|\dot{\psi}_{t\,j}^*-\frac{(\psi_t^*)_j-(\psi_t^*)_{j-1}}{k}\|_Y^2\\ +\|(\psi_t)_j-(\psi_t)_{j-1}^{hk}\|_Y^2+\|(\psi_t^*)_j-z_j^h\|_Y^2\Big),\quad\forall\{z_j^h\}_{j=1}^n\subset B^h\end{aligned}\tag{3.41}$$

Next, let us obtain an error estimate for the density functions using some ideas introduced in Fernández et al. (2010). Employing the notations $\Phi_j=\Phi(\rho_j,(\psi_t)_j-(\psi_t^*)_j)$ and $\Phi_j^{hk}=\Phi(\rho_j^{hk},(\psi_t)_j^{hk}-(\psi_t^*)_j^{hk})$, rewriting the discrete variational inequality (3.24) in the form:

$$\begin{aligned}\left(\frac{\rho_n^{hk}-\rho_{n-1}^{hk}}{k},\rho_n-\rho_n^{hk}\right)_Y\\ \geq(\Phi_{n-1}^{hk},\xi^h-\rho_n^{hk})_Y+\left(\frac{\rho_n^{hk}-\rho_{n-1}^{hk}}{k},\rho_n-\xi^h\right)_Y,\quad\forall\xi^h\in K^h\end{aligned}\tag{3.42}$$

and taking variational inequality (3.20) at time $t = t_n$ and for $\xi = \rho_n^{hk} \in B^h \subset Y$, by subtracting the two inequalities with $\xi^h = \xi_n^h \in K^h$ and doing some easy algebraic manipulations we conclude that

$$\begin{aligned}\left(\frac{\rho_n-\rho_{n-1}}{k}-\frac{\rho_n^{hk}-\rho_{n-1}^{hk}}{k},\rho_n-\rho_n^{hk}\right)_Y \\ \leq \left(\Phi_n-\Phi_{n-1}^{hk},\xi_n^h-\rho_n^{hk}\right)_Y+(\Phi_n,\rho_n-\xi_n^h)_Y \\ +\left(\frac{\rho_n-\rho_{n-1}}{k}-\dot\rho_n,\rho_n-\rho_n^{hk}\right)_Y-\left(\frac{\rho_n-\rho_{n-1}}{k},\rho_n-\xi_n^h\right)_Y \\ +\left(\frac{\rho_n-\rho_{n-1}}{k}-\frac{\rho_n^{hk}-\rho_{n-1}^{hk}}{k},\rho_n-\xi_n^h\right)_Y\end{aligned} \tag{3.43}$$

Taking into account that

$$\left(\frac{\rho_n-\rho_{n-1}}{k}-\frac{\rho_n^{hk}-\rho_{n-1}^{hk}}{k},\rho_n-\rho_n^{hk}\right)_Y \geq \frac{1}{2k}\left(\|\rho_n-\rho_n^{hk}\|_Y^2-\|\rho_{n-1}-\rho_{n-1}^{hk}\|_Y^2\right) \tag{3.44}$$

applying several times inequality (3.34), we get, for $n = 1, 2, \ldots, N$,

$$\begin{aligned}\|\rho_n-\rho_n^{hk}\|_Y^2 \leq Ck\Big\{\|\Phi_n-\Phi_{n-1}^{hk}\|_Y^2+\|\rho_n-\xi_n^h\|_Y^2+\left\|\Phi_n-\frac{\rho_n-\rho_{n-1}}{k}\right\|_Y\|\rho_n-\xi_n^h\|_Y \\ +\|\rho_n-\rho_n^{hk}\|_Y^2+\left\|\frac{\rho_n-\rho_{n-1}}{k}-\dot\rho_n\right\|_Y^2\Big\}+\|\rho_{n-1}-\rho_{n-1}^{hk}\|_Y^2 \\ +C\left(\rho_n-\rho_{n-1}-(\rho_n^{hk}-\rho_{n-1}^{hk}),\rho_n-\xi_n^h\right)_Y \quad \forall \xi_n^h \in K^h\end{aligned} \tag{3.45}$$

and, by induction in n, we then obtain

$$\begin{aligned}\|\rho_n-\rho_n^{hk}\|_Y^2 \leq Ck\sum_{j=1}^{n}\Big\{\|\Phi_j-\Phi_{j-1}^{hk}\|_Y^2+\|\rho_j-\xi_j^h\|_Y^2+\left\|\Phi_j-\frac{\rho_j-\rho_{j-1}}{k}\right\|_Y\|\rho_j-\xi_j^h\|_Y \\ +\|\rho_j-\rho_j^{hk}\|_Y^2+\left\|\frac{\rho_j-\rho_{j-1}}{k}-\dot\rho_j\right\|_Y^2\Big\}+\|\rho_0-\rho_0^{hk}\|_Y^2 \\ +C\sum_{j=1}^{n}\left(\rho_j-\rho_{j-1}-(\rho_j^{hk}-\rho_{j-1}^{hk}),\rho_j-\xi_j^h\right)_Y \quad \forall\{\xi_j^h\}_{j=1}^n \subset K^h\end{aligned} \tag{3.46}$$

From the definition of Φ_j and Φ_j^{hk} (see also (3.16)), taking into account that ρ_n, $\rho_n^{hk} \in [\underline{\rho}, \overline{\rho}]$ and the Lipschitz behavior of function f we get

$$\|\Phi_j-\Phi_{j-1}^{hk}\|_Y^2 \leq C\left(\|\rho_j-\rho_{j-1}^{hk}\|_Y^2+\|(\psi_t)_j-(\psi_t)_{j-1}^{hk}\|_Y^2+\|(\psi_t^*)_j-(\psi_t^*)_{j-1}^{hk}\|_Y^2\right) \tag{3.47}$$

After some algebra and using several times inequality (3.34) we obtain the following relations:

$$\begin{aligned}
&\sum_{j=1}^{n}\Big(\rho_j-\rho_{j-1}-(\rho_j^{hk}-\rho_{j-1}^{hk}),\rho_j-\xi_j^h\Big)_Y\\
&\quad=(\rho_n-\rho_n^{hk},\rho_n-\xi_n^h)_Y+(\rho_0-\rho_0^{hk},\rho_1-\xi_1^h)_Y\\
&\qquad+\sum_{j=1}^{n-1}(\rho_j-\rho_j^{hk},\rho_j-\xi_j^h-(\rho_{j+1}-\xi_{j+1}^h))_Y\\
&\quad\le\epsilon\|\rho_n-\rho_n^{hk}\|_Y^2+C\Big(\|\rho_n-\xi_n^h\|_Y^2+\|\rho_0-\rho_0^{hk}\|_Y^2+\|\rho_1-\xi_1^h\|_Y^2\\
&\qquad+k\sum_{j=1}^{n}\|\rho_j-\rho_j^{hk}\|_Y^2+\frac{1}{k}\sum_{j=1}^{n-1}\|\rho_j-\xi_j^h-(\rho_{j+1}-\xi_{j+1}^h)\|_Y^2\Big)
\end{aligned}\tag{3.48}$$

$$\begin{aligned}
&\sum_{j=1}^{n}\Big((\psi_t^*)_j-(\psi_t^*)_{j-1}-((\psi_t^*)_j^{hk}-(\psi_t^*)_{j-1}^{hk}),(\psi_t^*)_j-z_j^h\Big)_Y\\
&\quad=((\psi_t^*)_n-(\psi_t^*)_n^{hk},(\psi_t^*)_n-z_n^h)_Y+((\psi_t^*)_0-(\psi_t^*)_0^{hk},(\psi_t^*)_1-z_1^h)_Y\\
&\qquad+\sum_{j=1}^{n-1}((\psi_t^*)_j-(\psi_t^*)_j^{hk},(\psi_t^*)_j-z_j^h-((\psi_t^*)_{j+1}-z_{j+1}^h))_Y\\
&\quad\le\epsilon\|(\psi_t^*)_n-(\psi_t^*)_n^{hk}\|_Y^2+C\Big(\|(\psi_t^*)_n-z_n^h\|_Y^2+\|(\psi_t^*)_0-(\psi_t^*)_0^{hk}\|_Y^2\\
&\qquad+\|(\psi_t^*)_1-z_1^h\|_Y^2+k\sum_{j=1}^{n}\|(\psi_t^*)_j-(\psi_t^*)_j^{hk}\|_Y^2\\
&\qquad+\frac{1}{k}\sum_{j=1}^{n-1}\|(\psi_t^*)_j-z_j^h-((\psi_t^*)_{j+1}-z_{j+1}^h)\|_Y^2\Big)
\end{aligned}\tag{3.49}$$

Thus, we have proved the following estimate for the density function,

$$\begin{aligned}
\|\rho_n-\rho_n^{hk}\|_Y^2\le Ck\sum_{j=1}^{n}\Big\{&\|\boldsymbol{u}_j-\boldsymbol{u}_j^{hk}\|_V^2+\|\rho_j-\rho_j^{hk}\|_Y^2+\|\rho_j-\xi_j^h\|_Y^2\\
&+\left\|\Phi_j-\frac{\rho_j-\rho_{j-1}}{k}\right\|_Y\|\rho_j-\xi_j^h\|_Y+\|\rho_j-\rho_{j-1}\|_Y^2\\
&+\|\boldsymbol{u}_j-\boldsymbol{u}_{j-1}\|_V^2+\left\|\frac{\rho_j-\rho_{j-1}}{k}-\dot\rho_j\right\|_Y^2\Big\}+C\|\rho_n-\xi_n^h\|_Y^2\\
&+\frac{C}{k}\sum_{j=1}^{n-1}\|\rho_j-\xi_j^h-(\rho_{j+1}-\xi_{j+1}^h)\|_Y^2+C\|\rho_1-\xi_1^h\|_Y^2\\
&+C\|\rho_0-\rho_0^{hk}\|_Y^2+C\|\boldsymbol{u}_0-\boldsymbol{u}_0^{hk}\|_V^2\quad\forall\{\xi_j^h\}_{j=1}^n\subset K^h
\end{aligned}\tag{3.50}$$

and the following estimate for the reference value of the tissue stress level,

$$\begin{aligned}\|(\psi_t^*)_n - (\psi_t^*)_n^{hk}\|_Y^2 \le C\Big(&\|(\psi_t^*)_n - z_n^h\|_Y^2 + \|(\psi_t^*)_0 - (\psi_t^*)_0^{hk}\|_Y^2 + \|(\psi_t^*)_1 - z_1^h\|_Y^2 \\ &+k\sum_{j=1}^{n}\|(\psi_t^*)_j - (\psi_t^*)_j^{hk}\|_Y^2 + \frac{1}{k}\sum_{j=1}^{n-1}\|(\psi_t^*)_j - z_j^h - ((\psi_t^*)_{j+1} - z_{j+1}^h)\|_Y^2\Big) \\ &+Ck\sum_{j=1}^{N}\Big(\|(\psi_t^*)_j - (\psi_t^*)_{j-1}^{hk}\|_Y^2 + \|\dot{\psi}_{t\,j}^* - \frac{(\psi_t^*)_j - (\psi_t^*)_{j-1}}{k}\|_Y^2 \\ &+\|(\psi_t)_j - (\psi_t)_{j-1}^{hk}\|_Y^2 + \|(\psi_t^*)_j - z_j^h\|_Y^2\Big), \quad \forall\{z_j^h\}_{j=1}^n \subset B^h \end{aligned} \tag{3.51}$$

Finally, we obtain some estimates of the mechanical stimulus field. Therefore, subtracting equation (3.10) at time $t = t_n$ and equation (3.26), we find that

$$\begin{aligned}\|(\psi_t)_n - (\psi_t)_n^{hk}\|_Y \le\ & C\|\sqrt{E(\rho_n)^2\left(\alpha\boldsymbol{\varepsilon}(\boldsymbol{u}_n) : \boldsymbol{\varepsilon}(\boldsymbol{u}_n) + \beta(\mathrm{Div}\,(\boldsymbol{u}_n))^2\right)} \\ &- \sqrt{E(\rho_n^{hk})^2\left(\alpha\boldsymbol{\varepsilon}(\boldsymbol{u}_n^{hk}) : \boldsymbol{\varepsilon}(\boldsymbol{u}_n^{hk}) + \beta(\mathrm{Div}\,(\boldsymbol{u}_n^{hk}))^2\right)}\|_Y \\ \le\ & C\|\rho_n - \rho_n^{hk}\|_Y + C\|\sqrt{\boldsymbol{\varepsilon}(\boldsymbol{u}_n) : \boldsymbol{\varepsilon}(\boldsymbol{u}_n) - \boldsymbol{\varepsilon}(\boldsymbol{u}_n^{hk}) : \boldsymbol{\varepsilon}(\boldsymbol{u}_n^{hk})}\|_Y \\ &+C\|\sqrt{(\mathrm{Div}\,(\boldsymbol{u}_n))^2 - (\mathrm{Div}\,(\boldsymbol{u}_n^{hk}))^2}\|_Y \end{aligned} \tag{3.52}$$

where we used the fact that $\rho_n^{hk} \le \overline{\rho}$.

Then, after easy algebraic manipulations, it follows that

$$\|(\psi_t)_n - (\psi_t)_n^{hk}\|_Y \le C\|\rho_n - \rho_n^{hk}\|_Y + C\|\boldsymbol{u}_n - \boldsymbol{u}_n^{hk}\|_V \tag{3.53}$$

From estimates (3.35), (3.50), (3.51) and (3.53), we obtain the following estimates for the numerical errors:

$$\begin{aligned}&\|\boldsymbol{u}_n - \boldsymbol{u}_n^{hk}\|_V^2 + \|\rho_n - \rho_n^{hk}\|_Y^2 + \|(\psi_t)_n - (\psi_t)_n^{hk}\|_Y^2 + \|(\psi_t^*)_n - (\psi_t^*)_n^{hk}\|_Y^2 \\ &\le C\|\boldsymbol{u}_n - \boldsymbol{v}_n^h\|_V^2 + Ck\sum_{j=1}^{n}\Big\{\|\rho_n - \psi_n^h\|_Y^2 + \frac{C}{k}\sum_{j=1}^{n}\|\rho_j - \xi_j^h - (\rho_{j+1} - \xi_{j+1}^h\|_Y^2 \\ &+C\|\rho_1 - \xi_1^h\|_Y^2 + C\|\rho_0 - \rho_0^h\|_Y^2 + C\|\boldsymbol{u}_0 - \boldsymbol{u}_0^h\|_V^2 + Ck\sum_{j=1}^{n}\Big\{\|\boldsymbol{u}_j - \boldsymbol{u}_j^{hk}\|_V^2 \\ &+\|\rho_j - \rho_j^{hk}\|_Y^2 + \|\rho_j - \xi_j^h\|_Y^2 + \|\Phi_j - \frac{\rho_j - \rho_{j-1}}{k}\|_Y\|\rho_j - \xi_j^h\|_Y \\ &+\|\rho_j - \rho_{j-1}\|_Y + \|\boldsymbol{u}_j - \boldsymbol{u}_{j-1}\|_V^2 + \|\frac{\rho_j - \rho_{j-1}}{k} - \dot{\rho}_j\|_Y^2\Big\} + C\Big(\|(\psi_t^*)_n - z_n^h\|_Y^2 \\ &+\|(\psi_t^*)_0 - (\psi_t^*)_0^{hk}\|_Y^2 + \|(\psi_t^*)_1 - z_1^h\|_Y^2 + k\sum_{j=1}^{n}\|(\psi_t^*)_j - (\psi_t^*)_j^{hk}\|_Y^2 \\ &+\frac{1}{k}\|(\psi_t^*)_j - z_j^h - ((\psi_t^*)_{j+1} - z_{j+1}^h)\|_Y^2 + Ck\sum_{j=1}^{N}\Big(\|(\psi_t^*)_j - (\psi_t^*)_{j-1}^{hk}\|_Y^2 \\ &+\|(\dot{\psi}_t^*)_j - \frac{(\psi_t^*)_j - (\psi_t^*)_{j-1}}{k}\|_Y^2 + \|(\psi_t)_j - (\psi_t)_{j-1}^{hk}\|_Y^2 + \|(\psi_t^*)_j - z_j^h\|_Y^2\Big) \end{aligned} \tag{3.54}$$

Keeping in mind the regularities $\boldsymbol{u} \in C^1([0,T];V)$, $\psi_t^* \in C^1([0,T];Y)$ and $\rho \in C^1([0,T];Y)$ it is easy to prove that

$$k\sum_{j=1}^{n}\left\{\|\rho_j-\rho_{j-1}\|_Y^2+\|(\psi_t^*)_j-(\psi_t^*)_{j-1}\|_Y^2+\|\boldsymbol{u}_j-\boldsymbol{u}_{j-1}\|_V^2\right\}\leq Ck^2 \tag{3.55}$$

Finally, using a discrete version of Gronwall's lemma (Campo et al., 2007), combining the previous estimates Theorem 3.1 holds.

We notice that estimates (3.29) are the basis for the analysis of the convergence rate of the algorithm. For instance, if we assume the following additional regularity for the continuous solution:

$$\begin{array}{l}\boldsymbol{u}\in L^\infty(0,T;[H^2(\Omega)]^d),\\ \rho\in H^2(0,T;Y)\cap H^1(0,T;H^1(\Omega))\cap C([0,T];H^2(\Omega)),\\ \psi_t^*\in H^2(0,T;Y)\cap H^1(0,T;H^1(\Omega))\end{array} \tag{3.56}$$

we obtain the linear convergence of the algorithm that we state in the following corollary.

Corollary 3.3.2 *Let the assumptions of Theorem 3.3.1 hold. Define the discrete initial condition for the density function as follows,*

$$\rho_0^{hk}=\mathcal{P}^h\rho_0 \tag{3.57}$$

where $\mathcal{P}^h$ is the $L^2(\Omega)$-projection operator onto B^h. Under the additional regularity conditions (3.56) the algorithm is linearly convergent; that is, there exists a positive constant $C>0$, independent of the discretization parameters h and k, such that

$$\begin{array}{c}\max\limits_{0\leq n\leq N}\|\boldsymbol{u}_n-\boldsymbol{u}_n^{hk}\|_V+\max\limits_{0\leq n\leq N}\|\rho_n-\rho_n^{hk}\|_Y+\max\limits_{0\leq n\leq N}\|(\psi_t)_n-(\psi_t)_n^{hk}\|_Y\\ +\max\limits_{0\leq n\leq N}\|(\psi_t^*)_n-(\psi_t^*)_n^{hk}\|_Y\leq C(h+k)\end{array} \tag{3.58}$$

The proof of the above corollary is obtained by using well-known results on the approximations by finite elements and the projection operator $\mathcal{P}^h$ (see, e.g., Clement (1975)), and some arguments already introduced in Barboteu et al. (2005).

3.4 Numerical implementation scheme

This novel modification model has been implemented in a FE model, through a subroutine UMAT in Abaqus. Figure 3.5 shows the block diagram of this algorithm with its implicit structure. Then, we describe different examples used to show the behavior of the solution. In particular, we used a 2D and 3D femur model. Although, the methodology has been explained for the isotropic model of Jacobs (1994), the new assumption has been also implemented for the anisotropic model of Doblaré and García (2002). As the process is the same, we omit this explanation, although, we show results for both models.

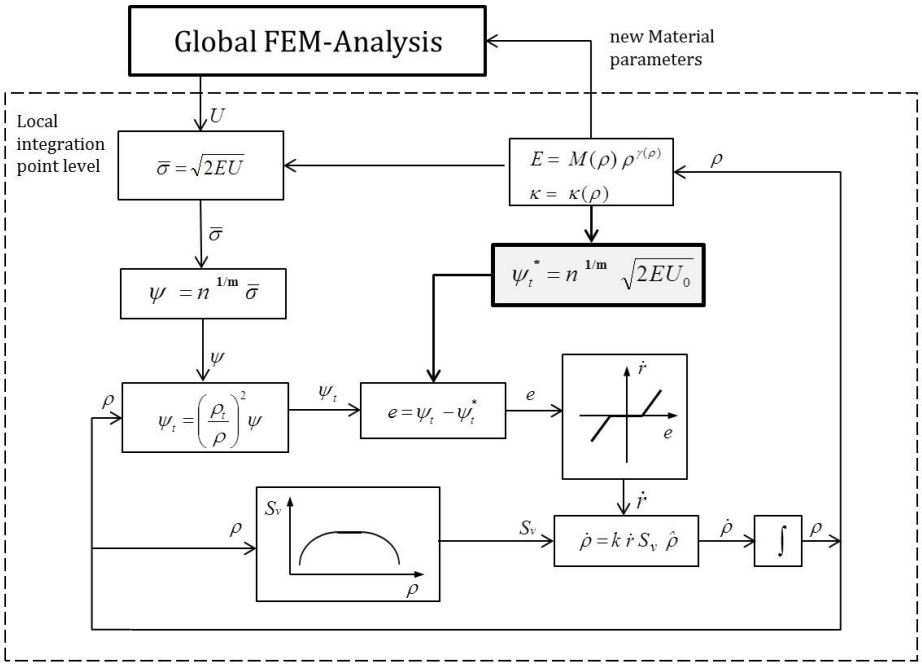

Figure 3.5: *A block diagram of the algorithm for the modified model.*

3.4.1 2D Benchmark FE model and its numerical results

We started with the demonstration of the algorithm on a simple benchmark problem. We propose a simple benchmark with four elements and we restricted the node displacements perpendicular to the plane for the left and bottom limits (Figure 3.6). We began with the uniform initial density ($\rho_0 = 0.5 g/cm^3$) and we applied compression forces. In all the analyses we kept the same parameters that we had used in the bone remodeling algorithm (see Table 2.1). Then, we study

the temporal density evolution in the Stanford model and in our modified bone remodeling model. We apply three different loads (low, medium and high) to obtain a different density distribution.

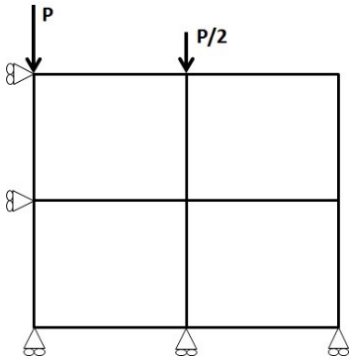

Figure 3.6: *A simple benchmark problem*

In Figures 3.7, 3.8 and 3.9, we can see that in classical Stanford model, the density changes as time goes on, until it reaches the minimum and maximum possible values of density (the density tends to go to extremes) (Figures 3.7, 3.8 and 3.9 - a, b, and c). However in our model, the density changes during the first days and, as the number of days is increased, the density remains constant and with a value consistent with the force applied (Figures 3.7, 3.8, 3.9 - d, e, and f).

Finally, we applied the modification of the model on a single quadrilateral element. We began with the same initial density ($\rho_0 = 0.5 g/cm^3$) and we applied compression forces. In all the analyses, we kept the same parameters.

In Figure 3.10, we show the evolution of the density and the mechanical stimulus (Figure 3.11) for different loads, and we can conclude that for higher loads the model increases the density (formation) and for a lower load, the density decreases (resorption). In this modified model, we observe the stability of the bone density evolution as a direct response to mechanical changes.

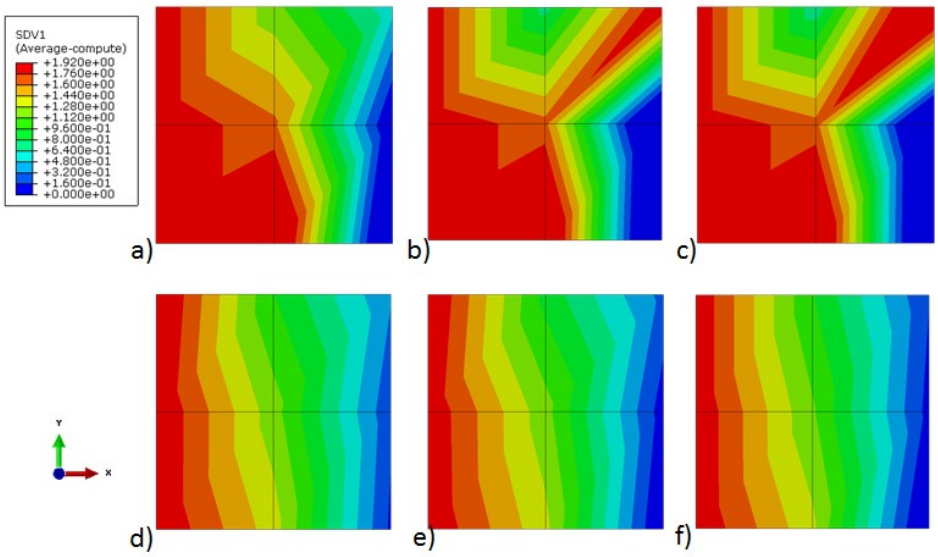

Figure 3.7: *Evolution of the density distribution resulting from the Stanford remodeling model for (a) 300, (b) 1000 and (c) 3000 days; and the modified model for (d) 300,(e) 1000 and (f) 3000 days with high load.*

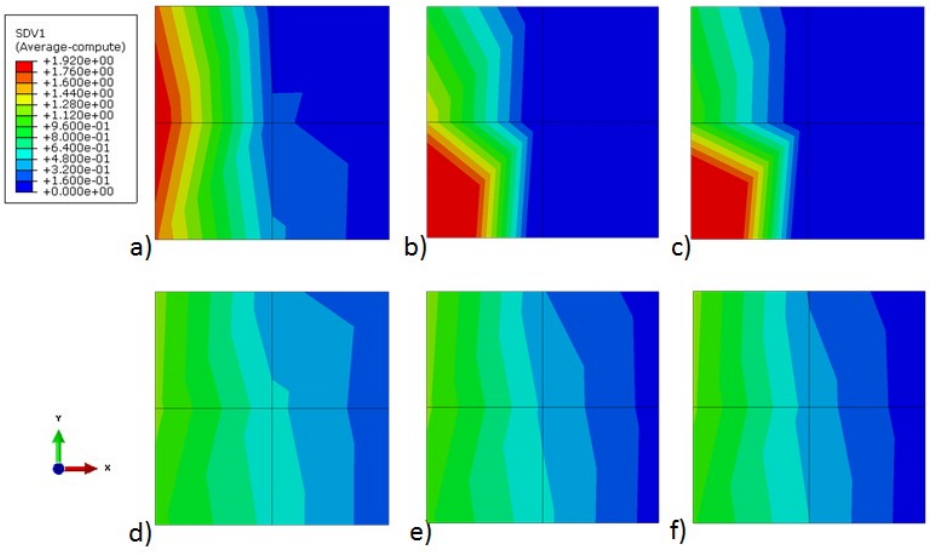

Figure 3.8: *Evolution of the density distribution resulting from the Stanford remodeling model for (a) 300, (b) 1000 and (c) 3000 days; and the modified model for (d) 300,(e) 1000 and (f) 3000 days with medium load.*

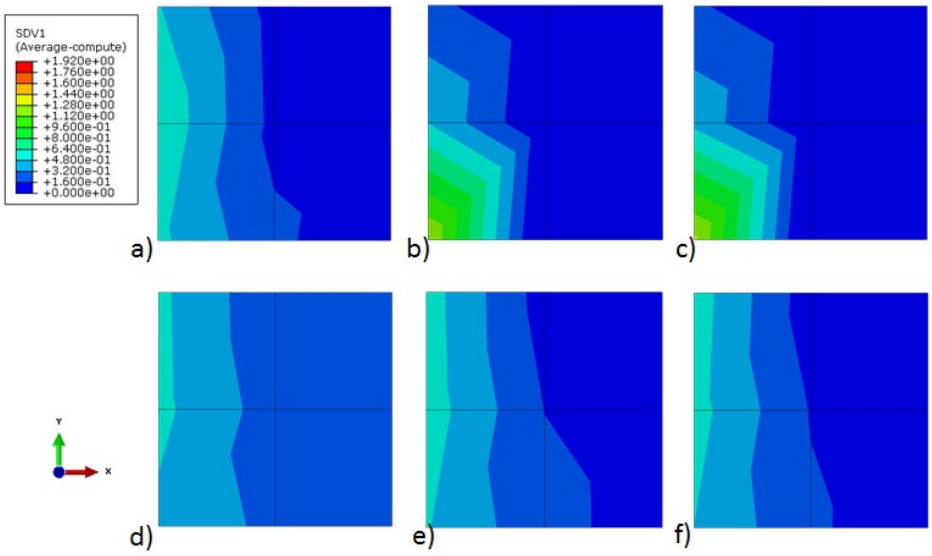

Figure 3.9: *Evolution of the density distribution resulting from the Stanford remodeling model for (a) 300, (b) 1000 and (c) 3000 days; and the modified model for (d) 300, (e) 1000 and (f) 3000 days with low load.*

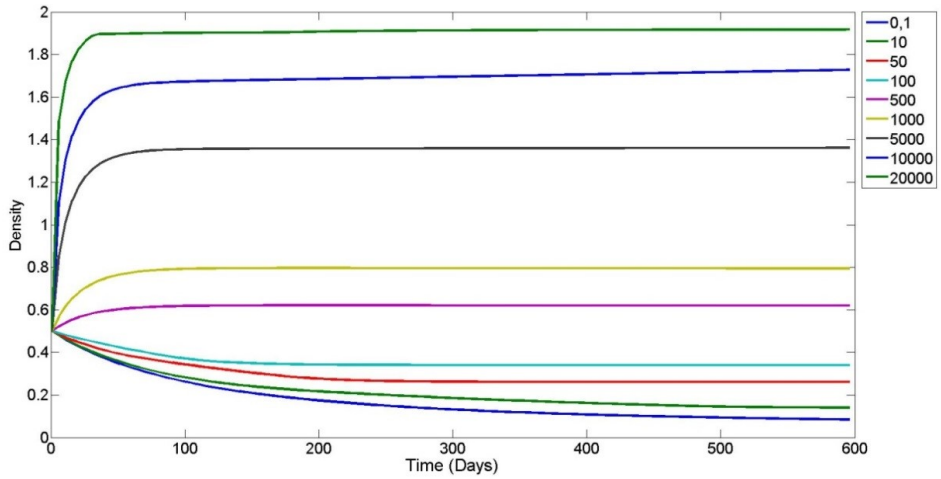

Figure 3.10: *Temporal evolution of the bone density with different loads (N) on a single element with the modified Stanford model.*

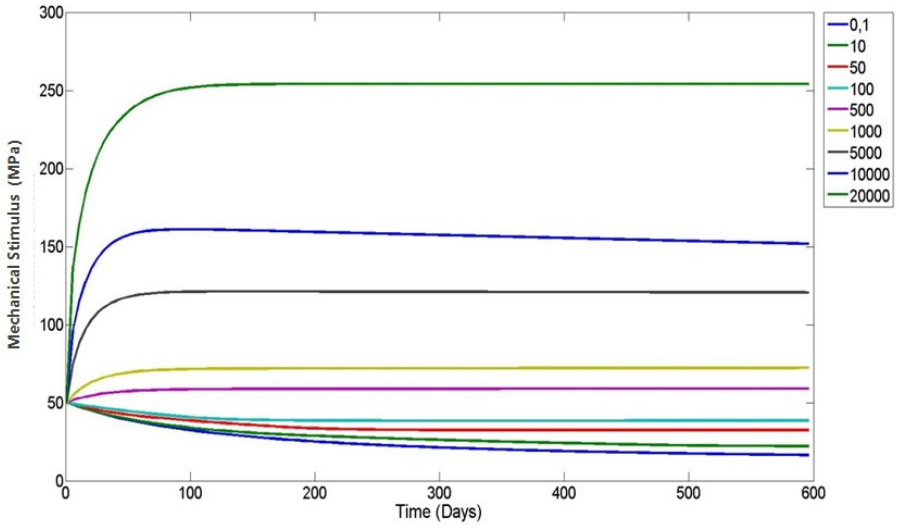

Figure 3.11: *Temporal evolution of the mechanical stimulus with different loads (N) on one single element with the modified Stanford model.*

3.4.2 2D numerical results

Our modification of the Stanford remodeling model is applied to the previously explained 2D FE model of the femur in Section 2.3.1 (Figure 2.6). Figure 3.12a shows the bone density distribution obtained. We can observe how the model is able to predict different regional areas such as the great trochanter, load line, the cortical bone and the medular canal. It has been compared with the real bone density from the radiograph (Figure 3.2). As can be observed the general trend of the bone density prediction agrees with the radiograph morphology. The radiograph shows an increasingly thicker cortical structure as you move down the shaft. The model does not show this, because it is a 2D model. This result is clearly improved with the 3D simulation of the problem (Section 3.4.3).

In Figure 3.12b, we observe the final distribution of the mechanical stimulus. We can also notice that the areas with more bone density correspond to areas with a higher stimulus. Moreover, a higher mechanical stimulus appears to shift the equilibrium towards bone formation whilst a lower one promotes bone resorption.

The parameters of the mechanical stimulus (equation (3.1)) were adjusted through a sensitivity study. It was observed that increasing the parameter values (a and A)(Figures 3.13b and 3.13d), the bone density distribution does not accurately reproduce the bone density distribution of a healthy bone (less cortical). However, if the parameter A decreases, the model does not converge (Figure 3.13c). If a is reduced, almost no differences are observed (Figure 3.13e).

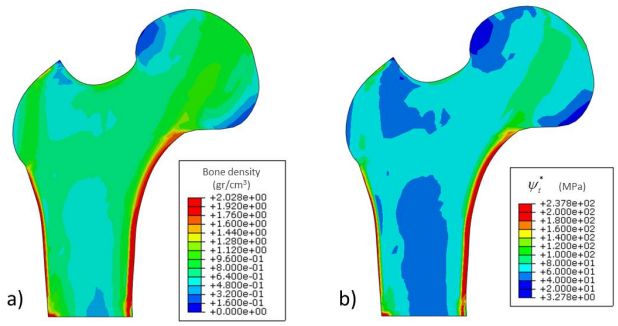

Figure 3.12: *a) The density distribution* (gr/cm^3) *of our bone remodeling simulation after 3000 days, b) Mechanical stimulus distribution of our modified bone remodeling simulation after 3000 days.*

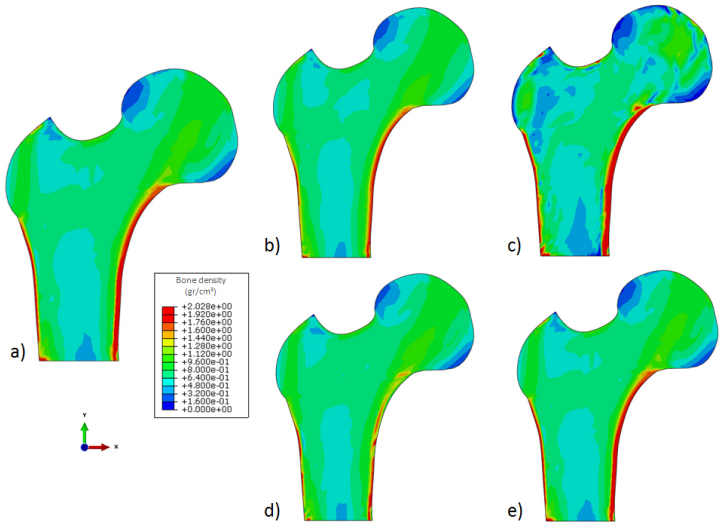

Figure 3.13: *Sensitivity study on the mechanical stimulus parameters (a and A - Eq.3.1) after 3000 days: a) a=0.01, A=0.039 (reference values); b) a=0.01, A=0.05; c) a=0.01, A=0.025; d) a=0.1, A=0.039; e) a=0.001, A=0.039.*

In this work, a qualitative comparison has also been performed with our modification of the Stanford's model. As outlined by Jacobs et al. (1995), the number of load cases applied significantly affects the computational results. The Stanford model obtains the best results in a certain number of days (T=300 days) (Figure 3.14a). At this point of increments of analyses the result contains the basic structural elements such as the cortex, medullary canal, and a qualitative distribution of the trabecular density. Unfortunately, the results become less accurate as time goes on, and the predicted structure generated after 1000 and 3000 days is almost unrealistic (Figures 3.14b and 3.14c, respectively). There is no numerical sta-

bility of the model. The modification proposed in this Thesis shows a stabilized bone density distribution as time goes on (Figures 3.14d to 3.14f) although with a loss of thickness of the cortical. The model needs more computational time to stabilize, but once stabilization is achieved, it remains almost unchanged. Similar results where obtained applying this modification to the anisotropic model of Doblaré and García (Figure 3.15).

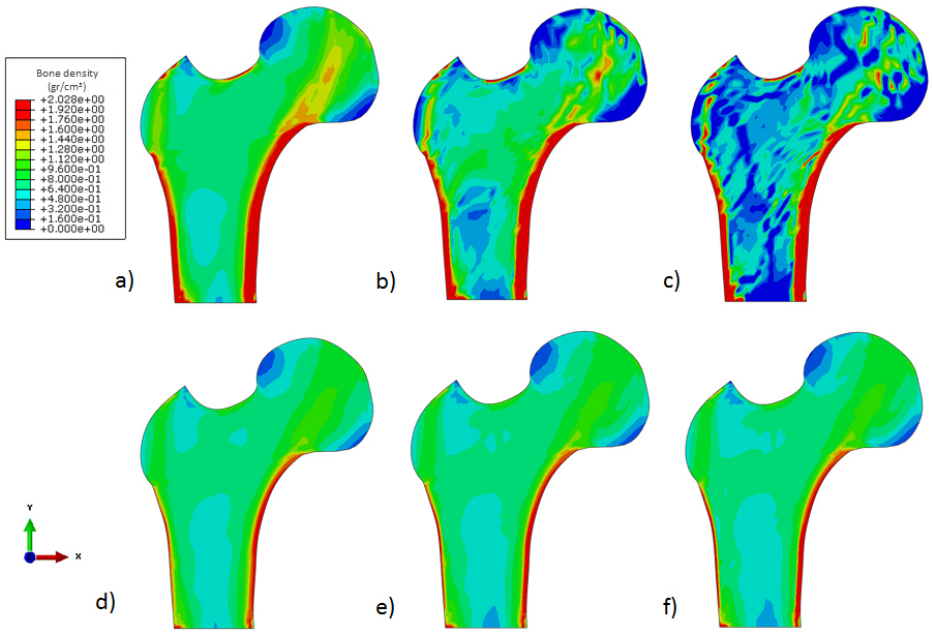

Figure 3.14: *The density distribution resulting from a bone remodeling simulation carried out using the Stanford's remodeling model (Beaupré et al., 1990) for (a) 300, (b) 1000 and (c) 3000 days; and the modified model with adaptive reference stimulus for (d) 300,(e) 1000 and (f) 3000 days.*

On the other hand, a quantitative comparison has also been performed. The surface remodeling rate ($\dot{r}$) has been analysed at all the model integration points. Their position in the dead zone, resorption or formation area has been quantified and represented in Figure 3.16 as time increases. The integration points located in the dead zone are considered in equilibrium. For this reason, it is important that all the integration points remain in this dead zone at the end of the simulation. In fact, a non-equilibrium situation is achieved with the Stanford remodeling model (Figure 3.16a). The integration points at the dead zone and resorption area continue increasing and reducing, respectively, as the simulation evolves, whereas with our modification of the Stanford remodeling model (Figure 3.16b) convergence and equilibrium are achieved. Nevertheless, we have to remark that there are integration points where bone formation or resorption occur. This effect is due

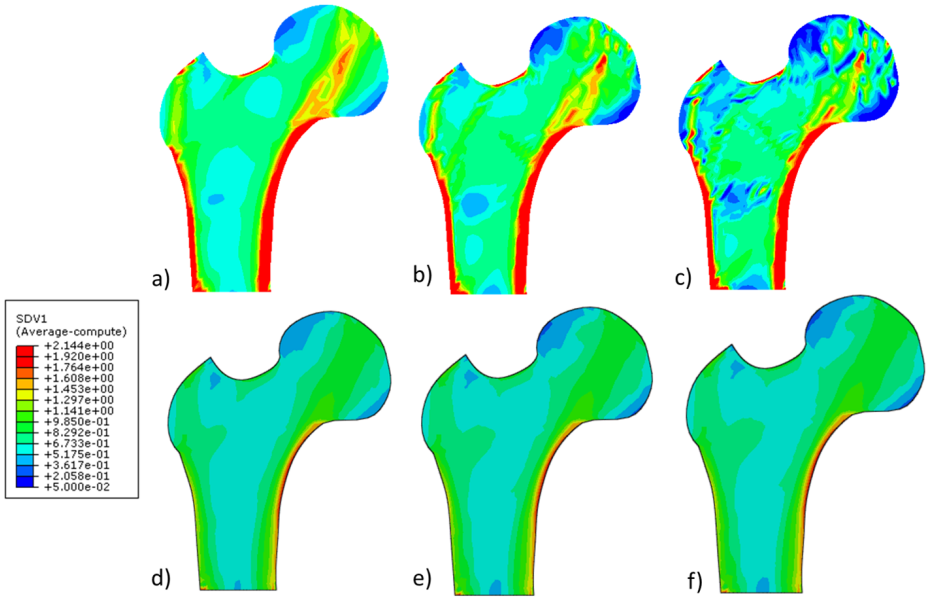

Figure 3.15: *The density distribution resulting from a bone remodeling simulation carried out using the anisotropic remodeling model (Doblaré and García, 2002) for (a) 300, (b) 1000 and (c) 3000 days; and the anisotropic model with adaptive reference stimulus for (d) 300,(e) 1000 and (f) 3000 days.*

to the fact that we are considering three different loadings on the bone, implying that mechanical demands change in certain regions due to these changes in the load. If only one loading case is used, all the integration points are inside the dead zone.

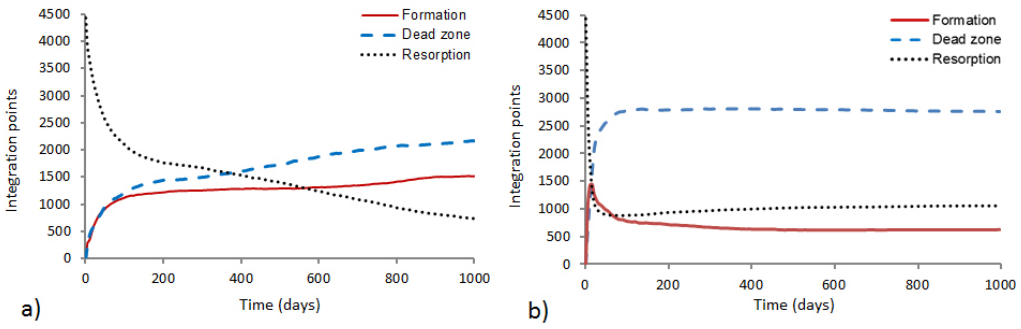

Figure 3.16: *Temporal evolution of the number of points in the dead zone, in the resorption and in the formation regions: a) the Stanford remodeling model and b) the modified Stanford bone remodeling model.*

3.4.3 3D FE model and its numerical results

3D FE model.

The bone remodeling models have also been applied to a 3D FE model of the femur. In this case, we used a whole femur with 32536 elements and 13590 nodes (Figure 3.17). The loading conditions are detailed in Table 3.1 (Carter, 1987). The angle projection is with respect to the frontal plane and sagittal plane. The femur has also been constrained distally. The same methodology as in the 2D case has been applied.

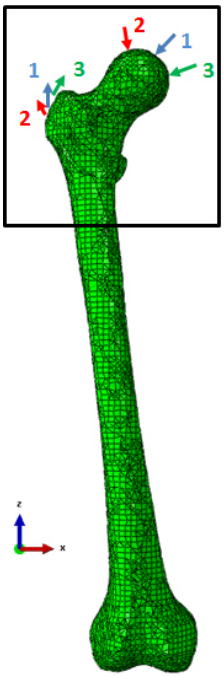

Figure 3.17: *3D FE mesh of the femur.*

3D numerical results.

The original Stanford model and the modified bone remodeling model have been tested and their results are shown in Figure 3.18. In this 3D model, we observe similar results to those obtained with the 2D model. The Stanford model provides the best results in 300 days (Figure 3.18a) but after this number of days the computed solution becomes less accurate (Figure 3.18b and c). However, the modification shows a stabilized bone density distribution as time goes on. Therefore, our modified model (where equilibrium is adapted) achieves convergence (Figure 3.18 d, e and f). Similar result were obtained using modified Doblaré and

Mean value and orientation of the forces for the three load cases.							
	Hip-Joint force			Abductor force			
Load Case	Module (N)	FP (°)	SP (°)	Module (N)	FP (°)	SP (°)	Cycles/day
1	2316	24	6	703	28	15	6000
2	1158	-15	-35	351	-8	9	2000
3	1548	56	-20	468	35	16	2000

Table 3.1: Loading conditions considered for the $3D$ problem for the walking movement (Carter, 1987): FP (°) (frontal plane) and SP (°) (sagittal plane). Cycles/day are the number of cycle considered for each load case when the bone remodelling simulation is considered.

García model (Figure 3.19). The stability was achieved, moreover, the cortical thickness was lower than the one obtained with the original Doblaré and García model (Doblaré and García, 2002).

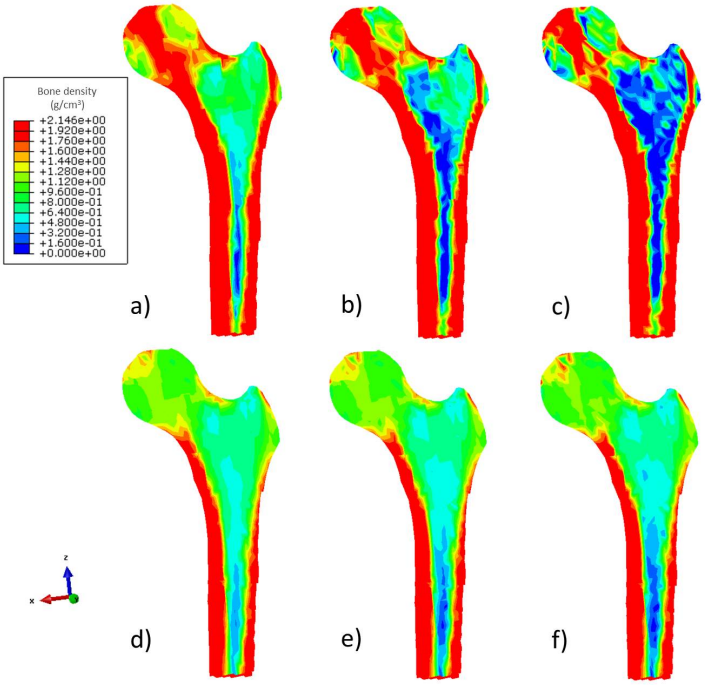

Figure 3.18: *The density distribution resulting from a 3D bone remodeling simulation carried out using the Stanford bone remodeling model for (a) 300, (b) 1000 and (c) 3000 days; and the modified model with adaptive reference stimulus for (d) 300,(e) 1000 and (f) 3000 days*

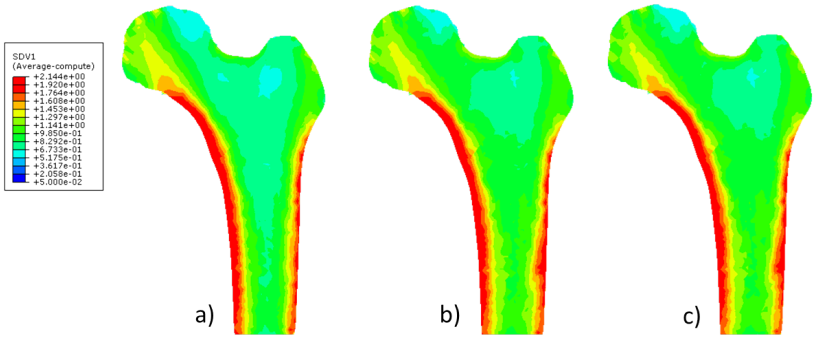

Figure 3.19: *The density distribution resulting from a 3D bone remodeling simulation carried out using the modified Doblaré and García bone remodeling model for (a) 300, (b) 1000 and (c) 3000 days.*

3.5 Conclusions

In this Chapter, we have studied different bone remodeling models and how we can improve then. Firstly, we have studied the convergence/stability of the previously developed bone remodeling theory known as the Stanford model (Jacobs et al., 1995). To improve the stability of this algorithm, a modification of the Stanford model has been proposed which consists of the reference homeostatic stimulus being locally dependent on the loading history that each local point is supporting (Figure 3.12b).

Firstly, we have introduced fully discrete approximations by using the finite element method and the explicit Euler scheme to approximate the spatial variable and to discretize the time derivatives, respectively. Then, we have proved some a priori error estimates (Theorem 3.3.1) from which the linear convergence of the algorithm is deduced under some additional regularity conditions. Secondly, numerical analysis of 2D and 3D FE-based bone remodeling simulations has been presented. These results clearly show a great improvement in the stability of the solution with the modification proposed for the Stanford model. Finally, we introduced the equation (3.1) in the anisotropic model and a full analysis in 2D and 3D FE-based bone remodeling has been performed.

In addition, we have to keep in mind that this novel adaptation of the reference (mechanostat) equilibrium mechanical stimulus improves not only the algorithm stability, but also the biophysical adaptation of the result. In fact, we propose that the reference equilibrium mechanical stimulus is not a constant, but a value dependent on the loading history that this point has supported. Although other authors have also proposed an accommodation of the reference equilibrium me-

chanical stimulus (Schriefer et al., 2005; Vahdati and Rouhi, 2009), none of them have carried out a numerical analysis of its convergence and stability. Different equations have been tested for the temporal accommodation law of the reference equilibrium stimulus, but the exponential function (equation (3.1)) has been considered the most suitable because it controls the velocity of remodeling as well as the reference mechanical stimulus. A sensitivity analysis on the parameters of equation (3.1) has also been carried out. Although other authors have performed a sensitivity analysis on the rest of the model parameters (Beaupré et al., 1990; Jacobs et al., 1995; Doblaré and García, 2002), it would be very interesting in the future to perform a probabilistic FE analysis of the role of all these parameters (Pal et al., 2007, 2008).

The previous works of Jacobs et al. (1995, 1997) show encouraging results for the prediction of the bone density. However, their model does not predict invariant density patterns along the time. It undergoes an important change of density after obtaining the ideal distribution, which yields to a non-real distribution (Figure 3.3). Therefore, these bone remodeling models are difficult to used for the observation of bone adaptation to changes in applied loads and, furthermore, aligning its internal structure along the time. Figure 3.14 shows a stabilized bone density distribution as time goes on. The same result can be approximated in Figure 3.16b which shows the quantitative stability of the resorption or formation values. The Stanford model and its derivatives (anisotropic model) predicted an adequate pattern density at 300 days but after this time period a deterioration of density began, leading to a non-realistic distribution.

Finally, it is important to keep in mind that in the literature there are many algorithms for modeling bone remodeling (Huiskes et al., 1987; Carter, 1987; Frost, 1990; Weinans et al., 1992). Most of them are based on the mechanostat theory, defining a reference equilibrium stimulus and a dead zone. Therefore, the updated law here proposed for the reference equilibrium stimulus could be applied to all of them.

CHAPTER 4

Some additional problems of bone remodeling models

4.1 Introduction

Several mathematical models have been proposed in an attempt to elucidate the features of bone adaptation at the different scales. Though at the organ, tissue and cell level, these models mainly exist in isolation (Webster and Müller, 2011). By integrating numerical equations into finite element models, it was shown that the load-driven bone remodeling algorithm based on mechanosensory theory can explain many features of bone adaptation at the tissue and cell-level (Ruimerman et al., 2005), e.g. the formation of load-adapted microstructures, as well as the loss of bone mass and microstructural integrity after disuse or increased osteoclast activity (Scheiner et al., 2013). The precise mechano-biological pathways of load induced bone metabolism are not really known. Hence, the bone remodeling theories are partly based on assumptions.

For that we need a multi-scale framework that can translate structural changes at the tissue-level to changes in bone density at the organ level. By using an analytical formulation of the bone remodeling equation integrated with multiscale micromechanical models that use generalized structural models at each level of organization (Fritsch and Hellmich, 2007), such multi-step homogenization schemes can provide a very flexible framework to derive mechanical properties at any level. By integrating such models with bone remodeling equations, it will be possible to predict bone remodeling at these different levels in an efficient manner. Following this idea, Colloca et al. (2014), presented a multiscale analytical model developed for the simulation of bone remodeling where they related the effects of structural changes at the nanometer level to changes in bone density at higher levels. Such an analytical formulation includes the feedback from the osteoclast-osteoblast activ-

ity and includes the influences from mechanical stimuli and surface area available for remodeling. Recently, a complete study of the mechano-chemical coupling has been carried out within the generic framework that sheds a light on the distinction in the effects of static and dynamic stimuli (Klika and Grmela, 2013). Klika et al. (2014) developed a bone adaptation model based on mechanical formulation of bone tissue response but incorporating biochemical control mechanisms. This chemo-mechanical coupling achieves the equilibrium in bone when it is in a dynamic equilibrium where resorption balances deposition. All these mechanobiological models present a better adaptation of the different scales.

In phenomenological models the link between scales is not clear. Although there are different assumptions, we believe that there is a relationship with the input data. Most of previous mathematical models (Chapter 2) have been focused on describing the mechanical properties of bone using numerical approaches with "arbitrary" initial conditions without a wide analysis of the behavior of density distribution by changing these initial conditions.

In this chapter, we continue to study some problems of bone remodeling models because, as we demonstrate before, most of the bone remodeling models present several restrictions and limitations. For that, we study their strong dependence on the initial conditions. We consider that a model should achieve the same solution with independence of the initial conditions. As it was shown in the previous chapter, the reference stimulus depends on the load history, and therefore, it is related to the density. This assumption shows the dependence of the reference stimulus and the density. Therefore, their initial values should be related. In this chapter, we show that the relationship between the stimulus and the density occurs when there is a scale change. Therefore, in this Chapter, we revisit the remodeling models, present the dependency of the initial condition and we describe a new strategy for overcoming the limitation of the initial conditions by relating the micro and macro scale through the reference stimulus.

4.2 Some additional problems of bone remodeling models

Most bone remodeling models start the simulation with an arbitrary initial condition that have not been obtained from experimental cases and it has been selected because it is the most suitable for their models. For example, the Stanford model (Jacobs et al., 1995) initial density was 0.5 gr/cm^3, however Weinans et al. (1992) began the algorithm for the simulation with 0.6 gr/cm^3. But if we study these initial conditions, there is a strong dependence on these initial values. Figure 4.1 shows different density distributions in the Stanford model starting with different

initial densities. After 300 days, we observe that the density distribution is clearly different in all cases and we do not achieve the same result.

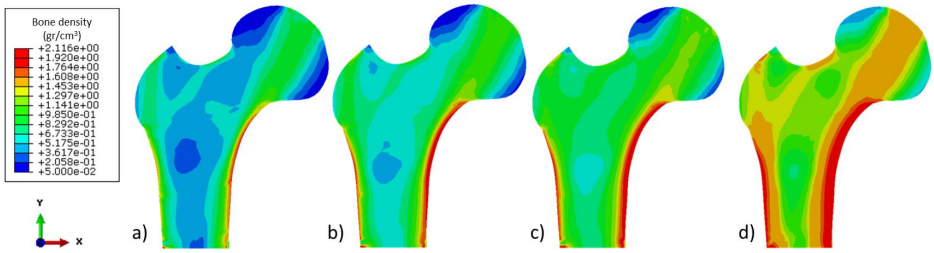

Figure 4.1: *Density distribution in 2D Stanford model after 300 days starting with different initial densities (0.2, 0.5, 0.8 and 1.0 gr/cm^3), respectively.*

In Figure 4.2, we quantitatively show the value of the final density in all the integration points at the end of the analysis starting with different initial conditions. We can see that increasing or decreasing the initial densities, the initial densities result also in changes of the final density distribution. In addition, a strong dependence on the initial density is observed and the majority of the values remain in the dead zone with the same initial density and do not move towards the convergence.

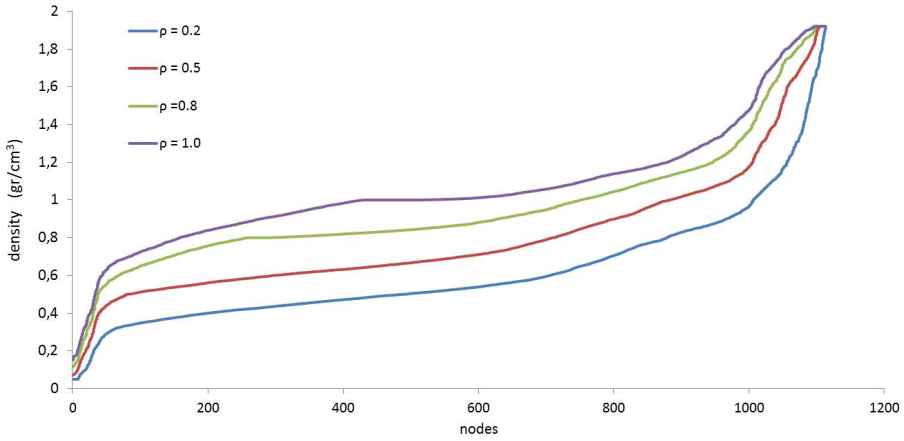

Figure 4.2: *Density after 300 days in all nodes of the 2D Stanford model starting with different initial densities (0.2, 0.5, 0.8 and 1.0 gr/cm^3).*

These variations may not be presented if we aim to study a specific case or to analyse the effect of a prosthesis implantation in the long term. We should find a model able to achieve the final density distribution without dependency on the initial densities selected. For that, we follow the idea that the reference homeostatic stimulus depends on the density (Chapter 3). For this reason, we hypothesize that

this relationship will directly affect to the initial conditions. Then, we propose a new equation to avoid this dependency.

4.2.1 Methodology

Following the methodology developed by isotropic Stanford remodeling model (Beaupré et al., 1990; Jacobs et al., 1995), the mechanical stimulus can be identified as,

$$\psi = n^{1/m}\overline{\sigma} \tag{4.1}$$

where the effective stress is then calculated as

$$\overline{\sigma} = \sqrt{2E(\rho)U(\boldsymbol{\sigma}(\boldsymbol{u}), \boldsymbol{\varepsilon}(\boldsymbol{u}))} \tag{4.2}$$

Therefore, it follows that

$$\psi = n^{1/m}\sqrt{2E(\rho)U(\boldsymbol{\sigma}(\boldsymbol{u}), \boldsymbol{\varepsilon}(\boldsymbol{u}))} \tag{4.3}$$

In order to use this stimulus into a finite element code, distinction between tissue level and apparent or continuum level has to be made following a similar approach to the one shown in the Stanford model. To distinguish between values between tissue and macroscopic scale, the subscript t denotes tissue level. Obviously, stress averaged over a continuum cannot be the same as it really appears in the microstructure. The relation between the tissue-level stress stimulus and the continuum-level one is given, from theoretical considerations as

$$\psi_t = \left(\frac{\bar{\rho}}{\rho}\right)^2 \psi \tag{4.4}$$

Therefore,

$$\psi_t = n^{1/m}\sqrt{2E(\rho)U_t} \tag{4.5}$$

In bone remodeling models, the remodeling error used in the bone remodeling law is obtained as the difference between ψ_t and ψ_t^*, where ψ_t is the stimulus that regulates the bone remodeling responses, and ψ_t^* is the reference value of the tissue stress level of the equilibrium zone.

$$e = \psi_t - \psi_t^* \tag{4.6}$$

However, this reference stimulus is not constant as we conclude in Chapter 3, changing with bone conditions. For that, we consider that the reference stimulus behaves the same as the stress stimulus. Then, the equation that describes their

behavior is the same that the tissue-level stimulus (equation 4.7) where we assume that the effective tissue-level energy (U_t) is constant and its value is 0.035 MPa.

The value of the effective tissue-level energy has been obtained from previous equation (equation 4.7) and the initial values for the simulation in the Stanford model (Jacobs, 1994) (Table 2.1). We consider $\rho_0 = 0.5\ gr/cm^3$ and $\psi_0 = 50$ Mpa. Then, the effective energy U_t is constant and its value is U_t= 0.035 Mpa.

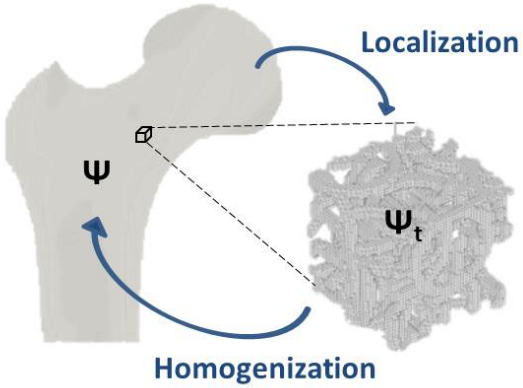

Figure 4.3: *Representation of the transition between macroscopic model of the femur and its microstructure.*

Finally, the reference homeostatic mechanical stimulus can be defined as:

$$\psi_t^* = n^{1/m}\sqrt{2E(\rho)U_t} \tag{4.7}$$

Therefore, the relationship between the tissue-level and the continuum level is (Figure 4.3):

$$\psi_t = F(\rho)\psi \tag{4.8}$$

where $F(\rho)$ is the relationship between the equilibrium tissue level and the remodeling process when we have cortical bone, we assume that if $\rho = \bar{\rho}$, then $F(\bar{\rho} = 1$. Then, equilibrium stimulus at tissue level is defined as

$$\psi_t = F(\rho)n^{1/m}\overline{\sigma} \tag{4.9}$$

$$\psi_t = F(\rho)n^{1/m}\sqrt{2E(\rho)U} \tag{4.10}$$

We conclude that

$$\dot{r} = f\left[n^{1/m}\sqrt{2E}\left(F(\rho)\sqrt{U} - \sqrt{U_t}\right)\right] \tag{4.11}$$

where f is a function following the equation 2.14.

Therefore, we define the bone remodeling rate as $\dot{r} = f(\psi_t - \psi_t^*)$, as function of the difference between ψ_t and ψ_t^*. Adding this expression in the above equations, we write:

$$\dot{r} = f\left[n^{1/m}\sqrt{2E}\left((F(\rho)\sqrt{U} - \sqrt{U_t}\right)\right] \tag{4.12}$$

This equation has been included in previous models (Section 2.1). In Figure 4.4, we briefly show the numerical scheme implemented.

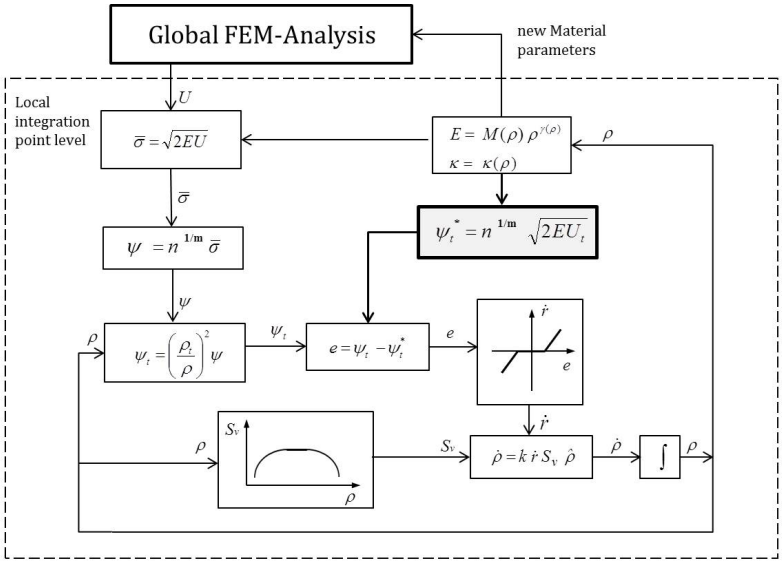

Figure 4.4: *A block diagram of the algorithm for the modified model.*

4.2.2 Numerical results for finite element simulations

This novel methodology has been incorporated in the classical benchmark problem corresponding to a two-dimensional FE model of the proximal femur, as explained in the Section 2.3.1. The simulation of the bone remodeling problem starts from an arbitrary initial situation (uniform density and their corresponding initial reference stimulus). We simulate different cases until convergence changing the initial conditions (ρ_0) for studying the independence on the initial values.

A qualitative comparison has also been performed with our modification of the Stanford's model. The classical Stanford model, presents different density distribution changing the initial bone density (Figure 4.5 a, b, c and d). However, in Figure 4.5 (e, f, g and h), the modification shows a similar bone density distribution for different initial bone densities. It is noticeable that the case with low initial bone density predicts low density distribution in the long term and viceversa, the case with high initial bone density, generates a high final bone density

distribution. Therefore, our modified model can be considered independent of the initial parameters. In addition, the modified model achieves convergence and the equilibrium in the long term.

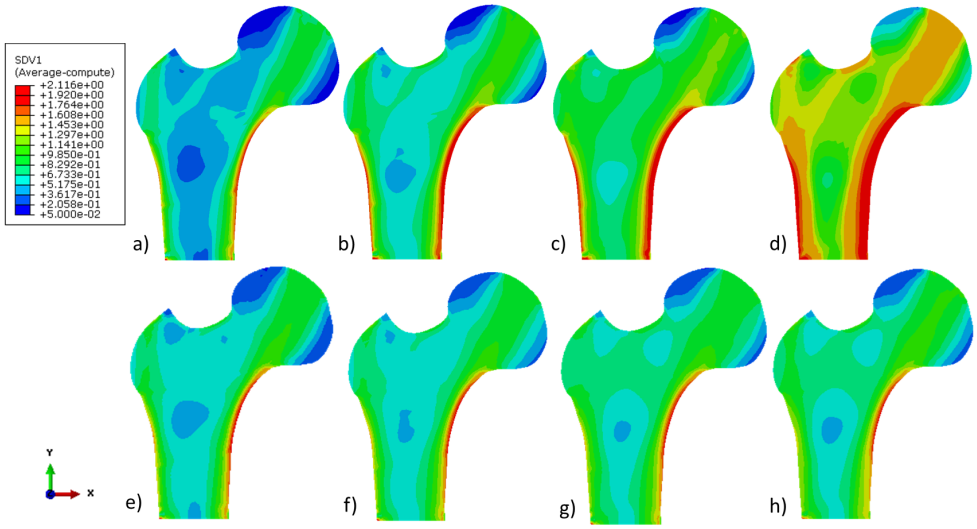

Figure 4.5: *The density distribution resulting from a bone remodeling simulation carried out using the Stanford model (Beaupré et al., 1990) for initial density after 300 days of analysis: a) 0.2, b) 0.5, c) 0.8 and d) 1.5 gr/cm^3; and using the modified model with adaptive reference stimulus for initial density: e) 0.2, f) 0.5, g) 0.8 and h) 1.5 gr/cm^3.*

Also, a quantitative comparison has been also performed. Figure 4.6 shows the final density values in all the points of the 2D FE model. We observe that the final density in all the points is the same independently of the initial bone density value. Similar quantitative results are obtained in the 3D model (Figure 4.7).

Finally, applying the same methodology as in the Stanford's model to the 3D FE model and the Doblaré and García remodeling model, we obtain same conclusion. These results are shown in Figures 4.8, 4.9 and 4.10.

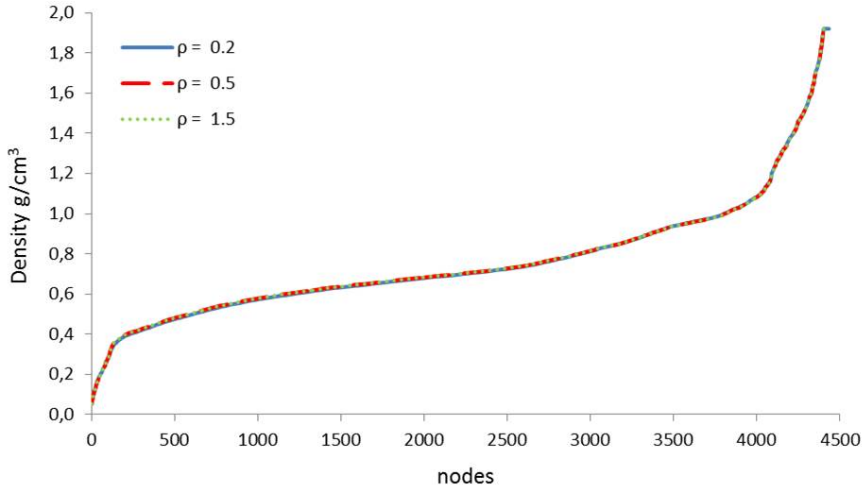

Figure 4.6: *Density after the stability in all nodes of the 2D FE model with the modified Stanford remodeling model starting with different initial density values (0.2, 0.5 and 1.5 gr/cm^3).*

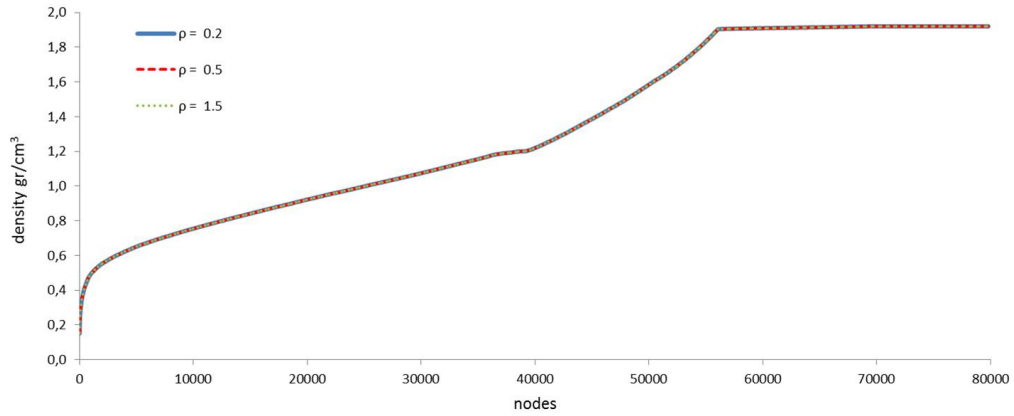

Figure 4.7: *Density after the stability in all nodes of the 3D FE model with the modified Stanford remodeling model starting with different initial density values (0.2, 0.5 and 1.5 gr/cm^3).*

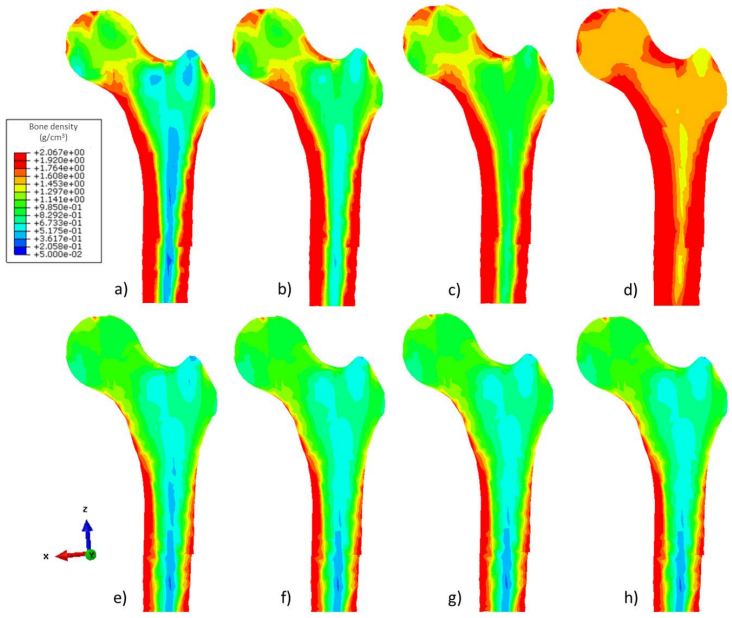

Figure 4.8: *3D density distribution resulting from a bone remodeling simulation carried out using the Stanford model (Jacobs, 1994) for initial density: a) 0.2, b) 0.5, c) 0.8 and d) 1.5 gr/cm^3; and using the modified Stanford model with adaptive reference stimulus for initial density: e) 0.2, f) 0.5, g) 0.8 and h) 1.5 gr/cm^3.*

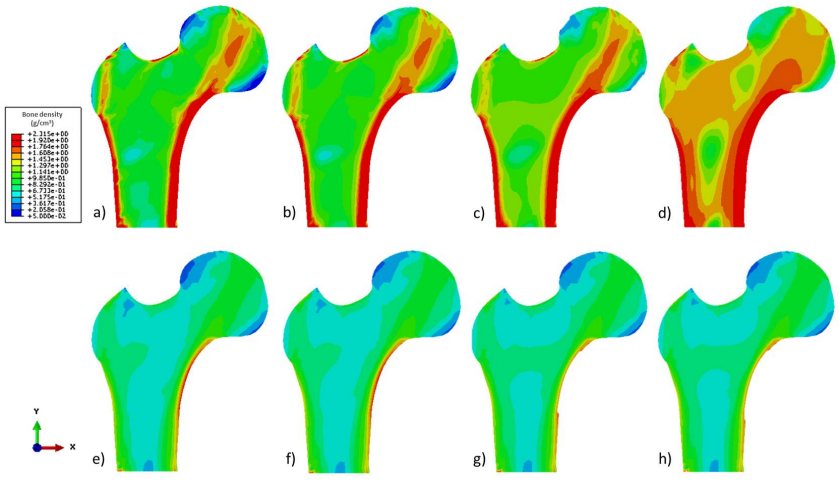

Figure 4.9: *The density distribution resulting from a bone remodeling simulation carried out using the Doblaré and García model (Doblaré and García, 2002) for initial density after 300 days of analysis: a) 0.2, b) 0.5, c) 0.8 and d) 1.5 gr/cm^3; and using the modified Doblaré and García model with adaptive reference stimulus for initial density: e) 0.2, f) 0.5, g) 0.8 and h) 1.5 gr/cm^3.*

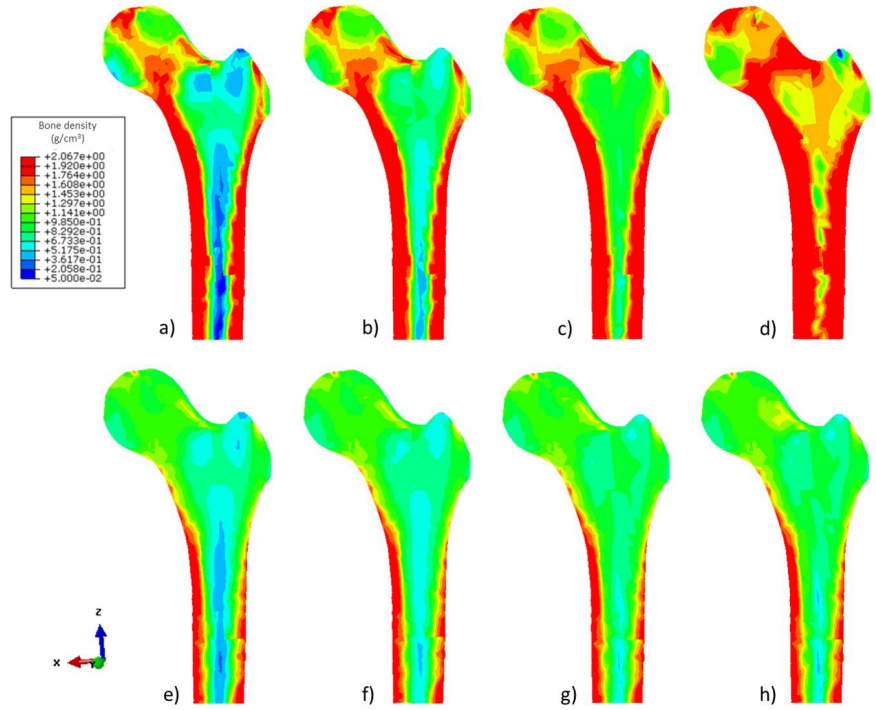

Figure 4.10: *3D density distribution resulting from a bone remodeling simulation carried out using the Doblaré and García model (Doblaré and García, 2002) for initial density after 300 days of analysis: a) 0.2, b) 0.5, c) 0.8, and d) 1.5 gr/cm^3; and using the modified Doblaré and García model with adaptive reference stimulus for initial density: e) 0.2, f) 0.5, g) 0.8 and h) 1.5 gr/cm^3.*

4.3 Conclusions

Previous works on bone remodeling (Jacobs et al., 1995; Doblaré and García, 2002) showed encouraging results for the prediction of the bone density. However, these models used a remodeling law that predicts the density with only an arbitrary value as an initial condition and a constant reference stimulus. However, if we apply several modifications to these values, the final result may change (Figure 4.1).

In this Chapter, we present a novel assumption for the bone remodeling law where the reference homeostatic stimulus changes according to the density (ρ). And accordingly, the effective energy remains constant. This assumption is similar to the one proposed by Weinans et al. (1992) who considered the energy between the density remaining unchanged during the process, however this model was not able to achieve the convergence. Our proposed methodology shows the qualitative

stability of the resorption or formation values with independence of the initial parameters of the simulation and providing accurate bone density distribution.

Our methodology shows accurate results in all cases (isotropic and anisotropic models - 2D and 3D geometry) where the density distribution is independent of the initial conditions. However, the simulation predicts a decrease of density in one region, more specifically, in the cortical part (Figures 4.5 and 4.9 - e, f, g and h). If we compare our simulation with radiography, cortical thickness is rather lower and also, lower than Stanford results (Figure 4.1b). In the 3D cases (Figures 4.8 and 4.10), the loss of bone density is lower. However, we also observed, a significant difference with previous cases.

Nevertheless, we consider that the improvement achieved in the modified model is relevant. We believe that these problems could be overcome by adjusting the reference parameters in order to improve the final result. For example, the value of the dead zone is a theoretical value that it was admitted to justify a certain stability in the previous models (Jacobs et al., 1995). In our model, the stability is included in the configuration with other equations, so we can consider reducing or even eliminating the dead zone. Figure 4.11 shows the density distribution where we can see the results when the dead zone is reduced in different widths (a 25% -original, a 20% a 10% and 6%). Introducing this modification a wider cortical area is predicted (Figure 4.11d).

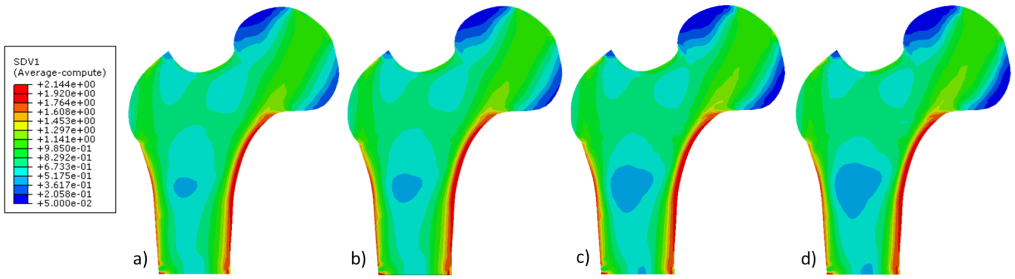

Figure 4.11: *The density distribution resulting from a bone remodeling simulation (Stanford model) carried out using the different width of the dead zone: half-widht a) 12.5 b) 10 c) 5 and d) 3%.*

Other parameters that can improve our methodology is the modification of the reference effective energy, because this value has been obtained from the theoretical parameters used in other models, but that not correspond to one actual experimental value. Therefore, we can conclude that the model here proposed is a step forward to continue improving bone remodeling models.

CHAPTER 5

Different numerical approaches to solve the inverse bone remodeling model

One of the most challenging difficulties in creating patient-specific models is the determination of the specific loads that each bone is really supporting. Real information related to specific patients, such as bone geometry and bone density distribution, can be used to determine patient loads as was pointed by Vahdati et al. (2014). In this Chapter, a theoretical methodology to estimate patient-specific loads from bone geometry and grey-scale is here presented. We compare different numerical approaches, such as, linear regression, artificial neural networks with individual or multiple outputs and support vector machines. This methodology has been theoretically applied to a 2D and 3D finite element model of the proximal femur. Then, it is shown that the proposed method is capable of predicting the loading that induces a specific bone density distribution.

5.1 Introduction

Computer science has been widely adopted by modern medicine and advances in technologies and computers have enabled to become a vital tool in conventional clinical practice. Nowadays, the medical information in hospitals become larger and larger, which causes great difficulties in extracting useful information for decision support, specially when traditional manual data analysis has become inefficient and methods for computer based analysis are indispensable (Baxt, 1995). Therefore, there is a need to introduce more efficient and effective computational methods in medical analysis for decision support to help clinicians. The idea is to build decision support tools based on numerical methods that store and use knowl-

edge from sources such as experienced clinicians, statistical analysis or computer simulations, and after that, these tools gather knowledge automatically, and use optimization methods to return appropriate answers to queries or accurate predictions on future data (Mitchell et al., 1997; Lavrac et al., 2000). There are many different methods, however, Machine Learning Techniques (MLT) have shown to be quite useful for this automation process (Langley and Simon, 1995). These techniques are based on the ability to learn from examples, which is an important facet of intelligence that has been an especially fertile area of study in the last decade (Carbonell, 1983).

Some of the techniques applied in the Machine Learning Techniques (MLT), are the Artificial Neuronal Network (ANN) and the Support Vector Machine (SVM). Artificial neural networks are mathematical models inspired by biological neural networks which consists of an interconnected group of artificial neurons, where it processes information using a connectionist approach to computation (McCulloch and Pitts, 1990; Gurney, 1997). Additionally, the multilayer perceptron (MLP), as a representation of the ANN, is a feed-forward network characterized by its layered structure where each layer consists of a set of perceptron neurons and its training algorithm (Bishop, 1995). The SVM (Vapnik, 1982) constructs a hyperplane or set of hyperplanes in a high or infinite dimensional space. A good separation is achieved by the hyperplane that has the largest distance to the nearest training data point of any class (so called functional margin), since in general the larger the margin the lower the generalization error of the classifier or regressor. Whereas the original problem may be stated in a finite dimensional space, it often happens that the sets to discriminate are not linearly separable in that space. For this reason, it was proposed that the original finite dimensional space can be mapped into a much higher dimensional space, presumably making the separation easier in that space. To keep the computational load reasonable, the mappings used by SVM schemes are designed to ensure that dot products may be computed easily in terms of the variables in the original space, by defining them in terms of a kernel function selected to suit the problem. More details about the MLT are described in the Appendix A.

Initially in this Chapter, an introduction about the theory of Machine Learning Techniques (MLT) and, in particular, about the Artificial Neuronal Network (ANN) and the Support Vector Machine (SVM) algorithms as well as the classical linear regression is exposed. MLT have been previously used by researchers to solve different classification and regression engineering problems. Although, these techniques are being increasingly used in the field of medicine.

In this Thesis, we will introduce this methodology in the bone, particularly in the determination of the forces acting on the bone. As mentioned in Chapter 2, bone tissue undergoes permanent changes in response to different signals such as external loads, hormonal influence, nutrition, etc. In particular, this process of mi-

crostructural change is due to the relationship between bone structure and applied loads. Many theories and mathematical models have been developed to analyze the evolution of bone microstructure and its mechanical properties depending on a certain loading pattern: (Huiskes et al., 1987; Beaupré et al., 1990; Doblaré and García, 2001; Prendergast and Taylor, 1994; Monnier and Trabucho, 1998). Previous bone remodeling models (Chapter 2) have normally been implemented in finite element (FE) models, and these have proved to be very useful tools for predicting the response of bone after prosthesis implantation (Doblaré and García, 2001; Folgado et al., 2008; Pérez et al., 2010; Caouette et al., 2012; Christen et al., 2012a; Webster et al., 2012; Fernández et al., 2010). However, these models have been developed for general purposes. Nowadays, the development of patient-specific models is becoming increasingly important (Galibarov et al., 2010). This importance lies in determining the specific loads that have caused the patient's bone density distribution in order to use these loads in a patient-specific study.

Knowledge of the internal loads acting on the human body during daily life movements has a wide range of applications, from clinical assessment of motor control patterns to prosthesis design and preclinical testing and as an input for finite element models predicting bone adaptation. External forces are generally measurable directly through force plates or load cells, while muscle forces and joint reaction forces remain unknown. In the last decade, in vivo joint contact forces acting at the hip have been recorded by instrumented prostheses, but the results are available only for a relatively small set of patients. On the other hand, direct muscle force measurement is not possible in humans as it is considered too invasive.

The problem of determining the specific loads, formulated in such a way, represents an inverse approach to the common bone remodeling analysis as is usually described in the literature, in which the apparent density distribution is estimated by fixing the loads.

This inverse problem has been previously solved by various authors using different numerical approaches for different applications. In fact, Fischer et al. (1995) developed an optimization procedure that adjusted the magnitude of each basic load to achieve the desired bone density. This approach was applied to the proximal femur in 2D for determining the loads using quantitative computed tomography (QCT) data (Fischer et al., 1998, 1999). Later, the approach was applied to the forearm (Fischer et al., 2003) and to the femur for different animals (Bona et al., 2003). Bona et al. (2006) proposed a contact algorithm for density-based load estimation and used the method to distinguish between different modes of locomotion of animals. More recently, Christen et al. (2012a) also developed a bone loading estimation algorithm to predict loading conditions by means of calculating the loading history that produces the most uniform strain energy density on the bone tissue. These previous approaches were based on iterative load pre-

diction techniques which involved significant computational cost. However, there are other numerical strategies that require less computational time. Indeed, many researchers have been trying to solve different inverse problems in biomechanics by developing controllers which employ intelligent computing methods such as artificial neural networks (ANN), neural-fuzzy (NF) networks, support vector regression (SVR), genetic algorithms or wavelet networks (Goulermas et al., 2005; Liu et al., 2009; Favre et al., 2012; Cilla et al., 2012; Behrens et al., 2009). Hambli's studies (Hambli, 2011b,a; Hambli et al., 2011) used a multiscale methodology for bone remodeling simulation using coupled finite element and ANN analysis. Nevertheless, Campoli et al. (2012) were the first to use the ANN approach for femur load prediction from the bone density distribution. They combined a wavelet decomposition technique with an artificial neuronal network for estimating the loading parameters of the femur. Although their results are very promising, they can be improved by analyzing the effect of each variable on the ANN performance. Zadpoor et al. (2013) also used ANN for prediction of tissue adaptation loads from a given density distribution of trabecular bone in a 2D example.

5.2 Methodology

We propose a hybrid methodology based on solving two problems and comparing their solutions: the bone remodeling problem (Section 5.2.1) and the inverse bone remodeling problem (Section 5.2.2) (Figure 5.1).

On the one hand, the bone remodeling problem is solved using the bone remodeling model previously developed by Jacobs (1994) (Chapter 2). Different loading conditions taking into account inter- and intra-individual variations are simulated in order to obtain their corresponding bone density distributions (Section 5.2.1).

On the other hand, the inverse bone remodeling problem is solved using three mathematical techniques (LR, ANN and SVM) (Section 5.2.2). The input data for these techniques are the solution of bone density distributions obtained from solving multiple direct bone remodeling problems. The way the input data have been selected is presented in Section 5.2.2. As a result of solving the inverse methodology, the proximal femur loading is estimated (magnitude of the force, its angle and its position) (Figure 5.1). These three loading values are the output data of the proposed methodology. All the FE simulations have been performed in Abaqus v6.11.

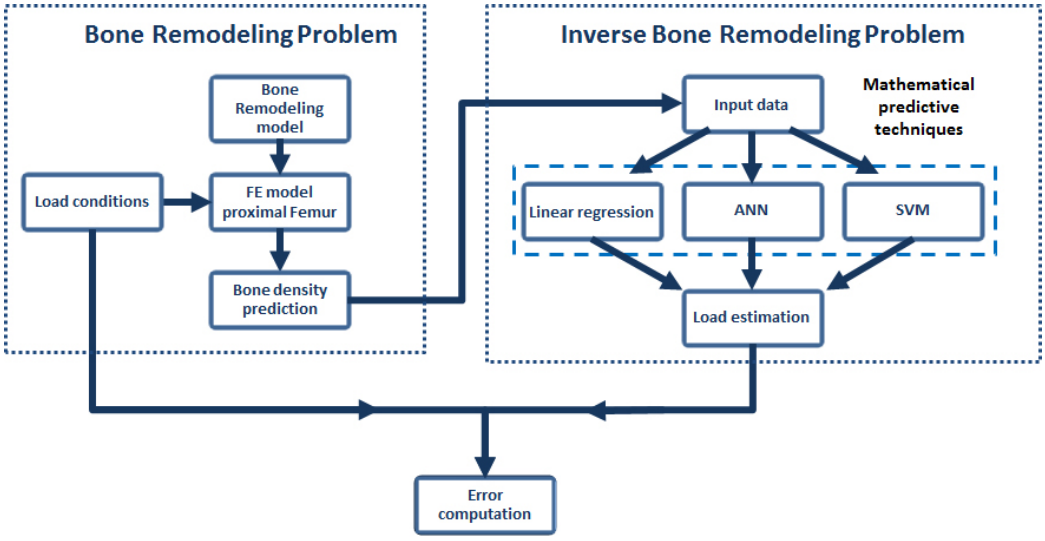

Figure 5.1: *Flow diagram of the computational approach.*

5.2.1 Definition of the bone remodeling problem

Bone remodeling model

In this Chapter, we use one of the most reknowned internal bone remodeling models: the Stanford bone remodeling theory (Section 2.1)(Beaupré et al., 1990). In fact, the bone density is used as an internal variable to quantify the adaptative evolution of the microstructure that defines the mechanical behavior of the bone. So, this model assumes that a certain level of mechanical stimulus is required to maintain bone homeostasis and regulate bone mass evolution (Chapter 2). A theoretical 2D FE model of the proximal femur (see Figure 5.2) is initially used in this chapter (Beaupré et al., 1990). This 2D FE model has been explained in 2.3.1.

The lower part of the femur is restrained along the vertical direction at all nodes and along the vertical and horizontal directions at only one node, to avoid rigid body movements (Figure 5.2).

Loading conditions

Following the same scheme as Jacobs (1994), we considered the remodeling behavior under the action of three simultaneous load cases (consecutive in the application to the model) that characterise the global load time history for walking activity. Walking is the most frequent activity that a patient performs (Morlock et al., 2001). Each load case was composed of a set of loads acting on the femoral head plus the reaction forces induced by these loads in the abductor muscle (see Table 5.1)(Figure 5.2). The first load represents the moment when the foot touches the

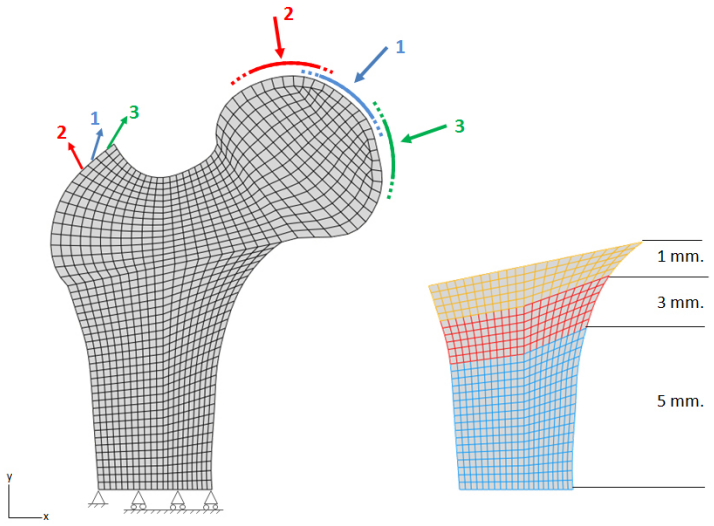

Figure 5.2: *2D FE model of the proximal femur with the boundary and loading conditions applied (Beaupré et al., 1990). Three cyclically applied load cases were selected to characterize a typical loading history for walking activity and the possible variation of the area of application. Each load case represents: 1- the foot touching the floor, 2- moment of abduction, 3 - moment of adduction.*

floor when walking, while the other two represent the two alternative moments of abduction and adduction (Huiskes et al., 1987; Jacobs, 1994; Carter, 1987). Load application is assumed to be sequential, acting in blocks of 10000 direct cycles but with different frequencies for each one.

The simulation for the bone remodeling problem starts from an arbitrary initial situation (uniform density ρ=0.5 gr/cm^3 and isotropic behavior) and, applying a previous load sequence, changes in the bone density distribution are computed until convergence. During the simulation, the internal bone structure (density and mechanical properties) adapts itself to the mechanical stimulus (see Chapter 2). After 300 increments, the bone exhibits a heterogeneous distribution of the density and Young modulus (Beaupré et al., 1990; Doblaré and García, 2001; Jacobs, 1994).

In fact, real loads present inter- and intra-individual variations during the most common activities (Bergmann et al., 2001; Heller et al., 2001). These variations are estimated by a mean of 15% for the force magnitude and 5% for the angle/orientation (Bergmann et al., 2001; Heller et al., 2001; Bitsakos et al., 2005). The position of the load application is also varied (see Table 5.1 and Figure 5.2) (Bergmann et al., 2001). For this reason, different load cases are considered taking into account previous physiological ranges of variation. The variation for each

parameter is indicated in Table 5.1 and each variation represents one bone remodeling problem. The force corresponding to the time when the foot touches the floor (case 1) is assumed to be predominant (higher force magnitude than the other load cases) and the other load cases (case 2 and 3 - Figure 5.2) are assumed to be correlative to case 1. Therefore, the variation of each parameter is considered with respect to its value for load case 1, and the other load values are varied within the same ratio. Summarizing, 1000 combinations of loading parameters have been simulated (Table 5.1). Therefore, a total of 1000 bone remodeling problems have been initially solved.

Mean value and orientation of the forces for the three load cases considered. Angles refer to the vertical direction

Case	Cycles/day	Load value at the head		Reaction force at the abductor muscle	
		Magnitude (N)	Angle (°)	Magnitude(N)	Angle (°)
1	6000	2317	24	703	28
2	2000	1158	-5	351	-8
3	2000	1548	56	468	35

Range of variation of the loading parameters.

Parameter	Variability	Variations for each parameter
Force Magnitude	±15 %	20
Angle	±5 %	10
Position	Indicated in figure 5.2	5

Table 5.1: Assumed load condition and its range of variation.

5.2.2 Definition of the inverse bone remodeling problem

The inverse remodeling problem aims to predict the musculoskeletal loads (output data - loading parameters: the force magnitude, its angle and its position) on the femur that have resulted for a specific measured bone density distribution (input data). In the following subsections, we define the input and output data of the inverse bone remodeling problem and then, we briefly present the mathematical methods that are used in our comparative study.

Input and output data of the inverse bone remodeling problem

The input data for the mathematical techniques is the bone density distribution at the proximal femur obtained from the previous 1000 direct bone remodeling problems (Section 5.2.1) where load parameters are changed: the load magnitude, its angle and its position. Initially, the inputs may be the density values of all the elements of the FE model (1700 inputs). This is inappropriate for the development of this methodology. Therefore, the number of inputs has to be reduced. Campoli et al. (2012) used the wavelet decomposition technique in order to reduce the

input data. In the present work, we present a different approach computing mean and standard deviation of the bone density distribution predicted in the previous 1000 bone remodeling problems (Section 5.2.1)(Figure 5.3). From the standard deviation contour (Figures 5.3b and 5.3c), the points with high standard deviation throughout the geometry are selected to be the input data. From the points with high standard deviation, 24 were seleted as the most representative ones from the cortical layer along the diaphysis, great trochanter, the load line at the femoral neck and the femoral head (Figure 5.3b).

As previously indicated, the output data of the proposed methodology are the load parameters: force magnitude, angle and position.

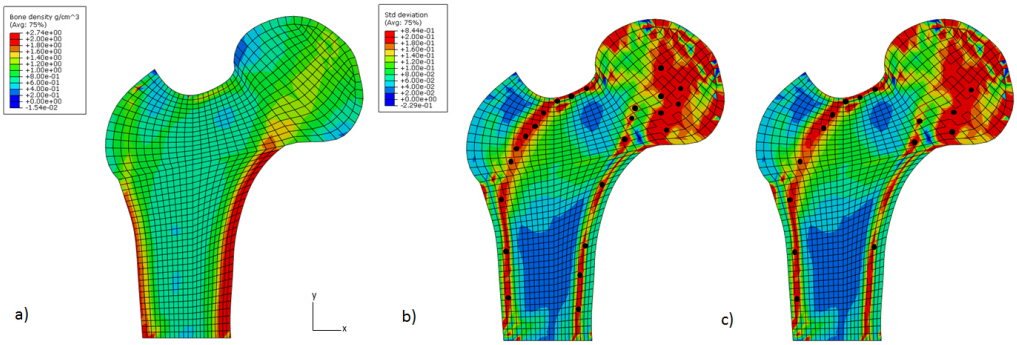

Figure 5.3: *Bone density distribution computed from the variation assumed for the loading conditions: a) mean bone density; b) standard deviation with 24 points assumed as inputs for the machine learning techniques; c) standard deviation with 15 points assumed as inputs for the machine learning techniques.*

Mathematical techniques

Linear Regression

Linear regression is an approach to model the relationship among variables. The linear relationship among variables comes to be determined through several constant parameters. These coefficients are obtained by the classical method, minimizing the mean square error obtained in the data fitting (Wilkinson and Reinsch, 1971).

Artificial Neural Network (ANN)

In our work, the back-propagation algorithm is used for training the ANN and only one hidden layer (Figure 5.4). The sigmoid-type and the linear function have been selected for the hidden layer and the output layer, respectively, among all the

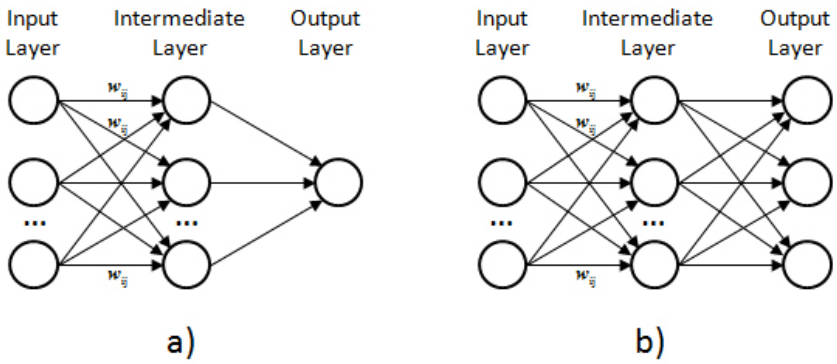

Figure 5.4: *Schematic diagram of the architecture of a typical artificial neuronal network: a) One neuron in the output layer b) Multiple neurons in the output layer.*

possible transfer functions (Bishop, 1995) (A.1.1). The network receives inputs from neurons in the input layer, and the output of the network is given by the neurons in an output layer (Figure 5.4). In this work, two different architectures of the ANN have been tested: one neuron in the output layer, therefore one ANN has been run for each output variable (Figure 5.4a); and multiple neurons in the output layer, i.e., a single ANN with three output variables (Figure 5.4b). The effect of the number of neurons in the hidden layer has been also analysed to optimize the technique.

Linear regression and the different ANN performance tested have been implemented in Matlab 7.10.0.

Support Vector Machines (SVM)

In this work, we focus on the regression problem (Figure 5.5) (A.1.3). A kernel function is used. Therefore, a gaussian kernel function has been selected. The solution, which can be obtained from the dual problem, is a linear combination of a subset of sample points denominated support vectors.

The SVM model has been implemented using Matlab and SVM libraries (Chang and Lin, 2011). The learning algorithm that we used is a linear kernel function for regression analysis.

5.2.3 Training and testing process: criteria of comparison following 10-fold cross validation technique.

For evaluating and comparing learning algorithms, we used 10-Fold Cross validation. Cross-validation is a model validation technique for assessing how the results of a statistical analysis are generalized to an independent data set. In this

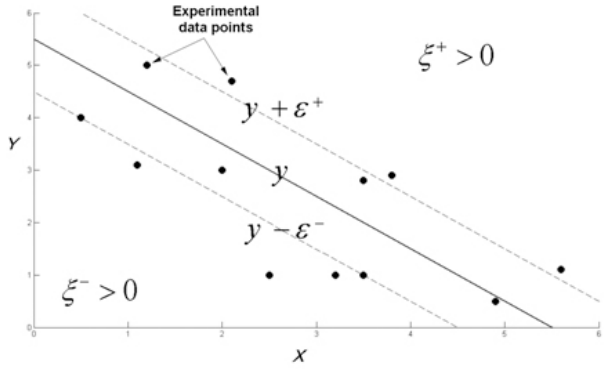

Figure 5.5: *Schematic diagram of the architecture of a typical Support Vector Machine (SVM) (Sayad, 2010).*

thesis, we used 10-Fold Cross validation by dividing randomly the data into two segments: one to learn or train the model (90% of the data) and another one (10% of the data) to validate or test the model. This process has been done 10 times (10-Fold Cross), changing the segments for validation or testing in each process (Figure 5.6) . The advantage of using a 10-Fold Cross validation is that all the data are eventually used for training, and testing and the final error is independent of the selected data in each model (Stone, 1974; Fushiki, 2011). Training data set is used to adjust the weights on the neural network and the testing data set is used only for validating the final solution in order to confirm the actual predictive power of the network (Twomey and Smith, 1997). This process has been used for the three mathematical approaches.

So as to predict the accuracy of these mathematical approaches, the absolute of relative error (RE) and the correlation coefficient (RSQ) have been used. The RE has been multiplied by 100 to get percents.

$$RE = abs(\frac{\hat{\theta} - \theta}{\theta}) \tag{5.1}$$

$$RSQ = \frac{\sigma_{\hat{\theta}\theta}}{\sigma_{\hat{\theta}}\sigma_{\theta}} \tag{5.2}$$

where $\hat{\theta}$ is the predicted data, θ is the real data, $\sigma_{\hat{\theta}\theta}$ is the covariance and $\sigma_{\hat{\theta}}$ and σ_{θ} are the standard deviations.

The results of relative error are calculated based on the training and the testing sets of the mean 10 Fold-cross. The training data are used to generate the model, so the corresponding error value set indicates if the model has been well trained, while the test data are used to validate it. The corresponding error indicates if the model is appropriate to solve the problem.

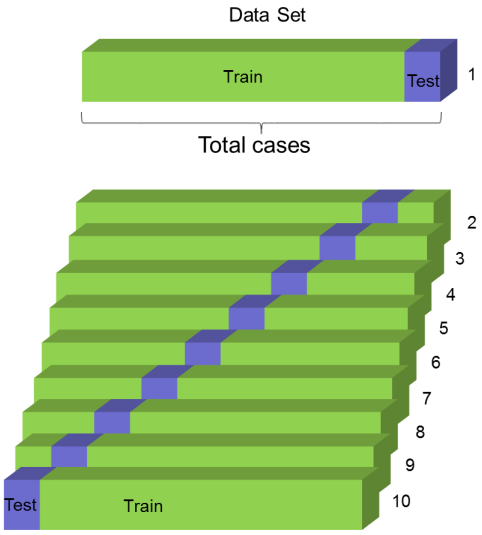

Figure 5.6: *Illustration of a k-fold cross validation with k = 10. The green boxes correspond to the training data and the purple ones to the data that will be used for testing.*

5.3 Results

5.3.1 Performance of the three mathematical approaches

In order to compare the results obtained by the three predictive mathematical approaches, each method has been initially applied to predict each output parameter (force magnitude, angle and position) independently. In other words, each method has been applied three times to obtain each of the three outputs, because some methods do not allow multiple outputs. Table 5.2 shows the mean relative error results obtained by the three methods applied independently for each output and the total error which has been computed summing up previous independent cases. The RE during training is lower than during testing (ANN and SVM). For all the methods, the RE computed for the force magnitude is lower than that corresponding to the angle and force position. When estimating the total RE, the ANN gives the lowest RE value (lower than 1%). Using linear regression and SVM, the total training RE is 1.26% and 15.2%, respectively.

The correlation coefficient between the vector containing the actual loading parameters and the vector containing predicted loading parameters is greater than 0.999 for all the test data set, indicating the excellent ability of the linear regression and ANN in the prediction of the load outputs (see Table 5.2).

The absolute of relative error (RE)% and the correlation coefficient (RSQ).				
		Linear Regression	ANN (15 neurons)	SVM
Force Magnitude	RE Training	0.09727 %	0.00107 %	9.199 %
	RE Testing	0.10533 %	0.00273 %	0.932 %
	RSQ Testing	0.99977	0.99999	0.976
Force Angle	RE Training	0.25842 %	0.00257 %	6.001 %
	RE Testing	0.55726 %	0.00522 %	1.441 %
	RSQ Testing	0.99718	0.99999	0.947
Force Position	RE Training	0.61120 %	0.00255 %	0.007 %
	RE Testing	0.60468 %	0.00508 %	0.002 %
	RSQ Testing	0.99988	0.99999	0.998
Total	RE Training	0.96689 %	0.0062 %	15.207 %
	RE Testing	1.26727 %	0.0130 %	2.375 %
	RSQ Testing	0.998943	0.99999	0.974

Table 5.2: The absolute of relative error (RE) and the correlation coefficient (RSQ) of the learning techniques analysed.

In Figure 5.7, the horizontal axis shows the different neurons used in the hidden layer during training while the vertical axis shows the error produced by the ANN performance with individual outputs (one neuron in the output layer -Figure 5.4a). It can be observed that the RE estimated for both the training and testing are quite low and that the RE of the training decreases as the number of neurons increases. However, from 15 neurons the testing error increases when more neurons are used in the hidden layer. This result means that there is an ANN over-training when increasing the number of neurons in the hidden layer.

The computational costs of the methods studied are very different. With linear regression, the calculation time is a few minutes for all cases. For the ANN, the computation training time is 53 minutes for 5 neurons in the hidden layer, 1 hour and 50 minutes for 10 neurons in the hidden layer, and the rest of the cases tend to grow exponentially (once the optimal parameters have been chosen by 10-fold cross validation and depending on the stopping criterion used). Therefore,the relationship between computational cost and relative error result, is very well in linear regression. The validation process time is negligible and provides an immediate estimated response. Each FE analysis takes 10 minutes. The 1000 FE cases and the mathematical techniques have been run in a computational cluster of 1535 cores and 3.5 Tb of the RAM.

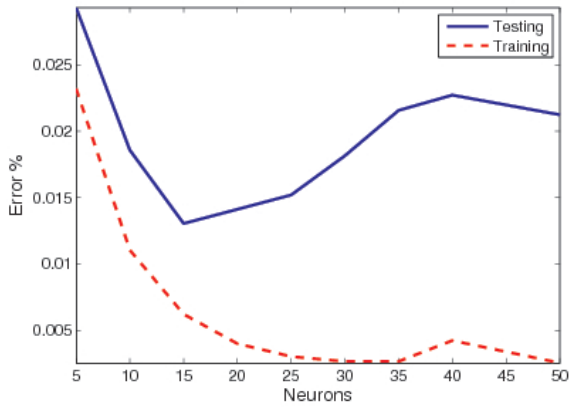

Figure 5.7: *Evolution of the absolute relative error (RE) depending on the number of neurons in the hidden layers during ANN training and testing with individual outputs.*

5.3.2 Performance of the ANN with multiple outputs

The ANN technique can be constructed to obtain multiple outputs following the architecture shown in Figure 5.4b (in our case three neurons in the output layer corresponding to the three output variables) (Section 5.2.2). Therefore, we have compared the performance of the ANN with individual outputs (one neuron in the output layer- Section 5.3.1 and Figure 5.4a) and multiple outputs (three neurons in the output layer - Figure 5.4b) (see Table 5.3).

The absolute of relative error (RE)%.		
	ANN individual output	ANN multiple outputs
	15 neurons	
RE Training	0.00621 %	1.1048 %
RE Testing	0.01304 %	1.1804 %
RSQ Testing	0.99999	0.99999
	40 neurons	
RE Training	0.00422 %	0.1197 %
RE Testing	0.02271 %	0.1553 %
RSQ Testing	0.99999	0.99999

Table 5.3: Comparison of the absolute of relative error (RE) and the correlation coefficient (RSQ) between the ANN with individual outputs and multiple outputs (3) with 15 neurons and 40 neurons in the hidden layer.

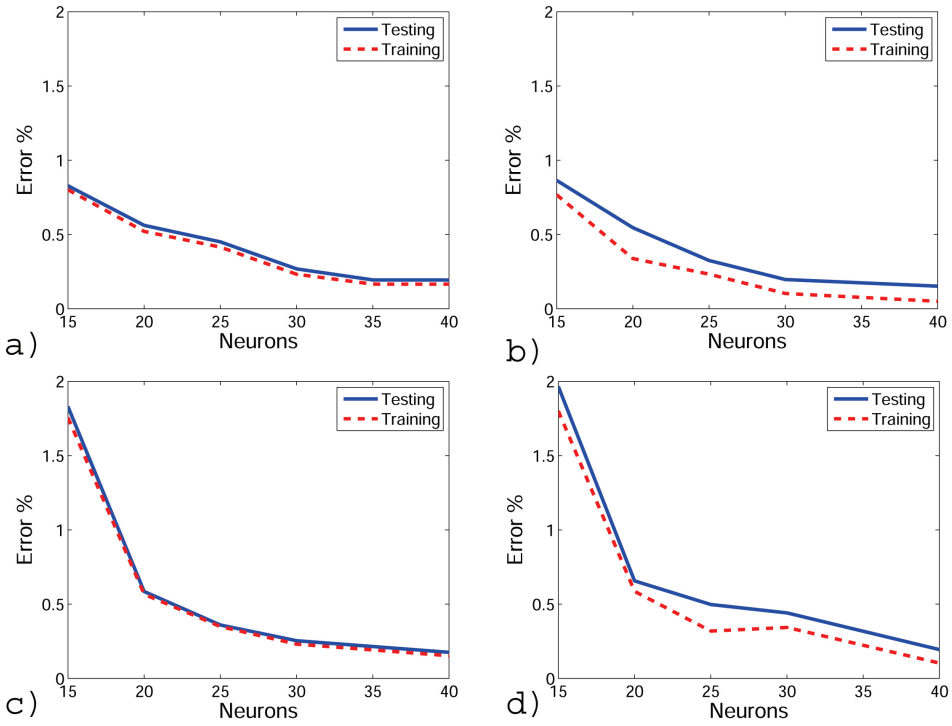

Figure 5.8: *Evolution of the absolute relative error (RE) depending on the number of neurons in the hidden layers during ANN training and testing with multiple outputs using (a) 1000 cases with 24 inputs; (b) 500 cases with 24 inputs; (c) 1000 cases with 15 inputs; (d) 500 cases with 15 inputs.*

The absolute of relative error (RE)% and the Standard deviation (σ)		
	RE	σ
Training	0.1197 %	0.022 %
Testing	0.1553 %	0.041 %

Table 5.4: The absolute of relative error (RE) and the Standard deviation (σ) for the ANN with multiple outputs and 40 neurons in the hidden layer.

The REs estimated for both training and testing considering the ANN with multiple outputs are relatively higher than considering the ANN with individual outputs (Table 5.3). Although, the ANN with individual outputs generates over-training (Figure 5.7). When multiple outputs are considered (Figure 5.8a) the REs is reduced as the number of neurons of the hidden layer is increased. Both training and testing RE are of the same order. No over-training is predicted when multi-

ple outputs are considered (Figure 5.8a). Table 5.4 shows the standard deviation computed for the ANN with multiple outputs with 40 neurons in the hidden layer. This deviation presents lower values, this fact indicates that the data points tend to be very close to the mean.

5.3.3 Validation of the ANN with multiple outputs

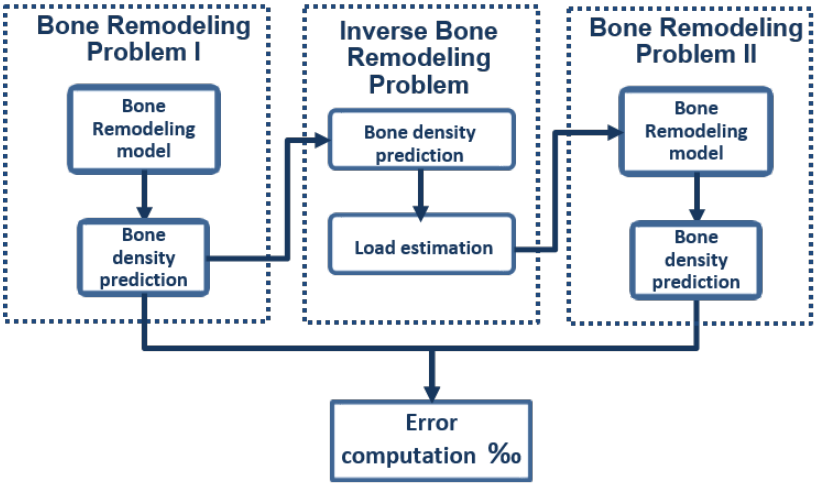

Figure 5.9: *Scheme of the ANN validation comparing the densities.*

In order to validate the ANN performance for femur loading prediction, one loading case not previously used for the training nor the testing has been chosen, i.e., none of the 1000 bone remodeling problems initially solved (Section 5.2.1). This new load case (force magnitude value, angle and position) is applied to the 2D FE model of the femur, so a new bone remodeling problem is solved until convergence is achieved. The bone density values of the 24 representative points (Section 5.2.2) are incorporated into the ANN as its input data and the three outputs are predicted using 40 neurons in the hidden layer. For the validation, these outputs are again incorporated into the 2D FE model of the femur and the bone density distribution is predicted (Figure 5.9). The error between both bone density distributions have been computed and represented (maximum error ‰) in Figure 5.10a. It is observed that the error is less than 1% at all points and there are small differences in the head of the femur and in the greater trochanter. The same process has been carried out choosing a load case out of the range of the variations studied (Table 5.1). It is observed that the error is higher than in the other case but it remains sufficiently low (less than 10% at all points) (Figure 5.10b).

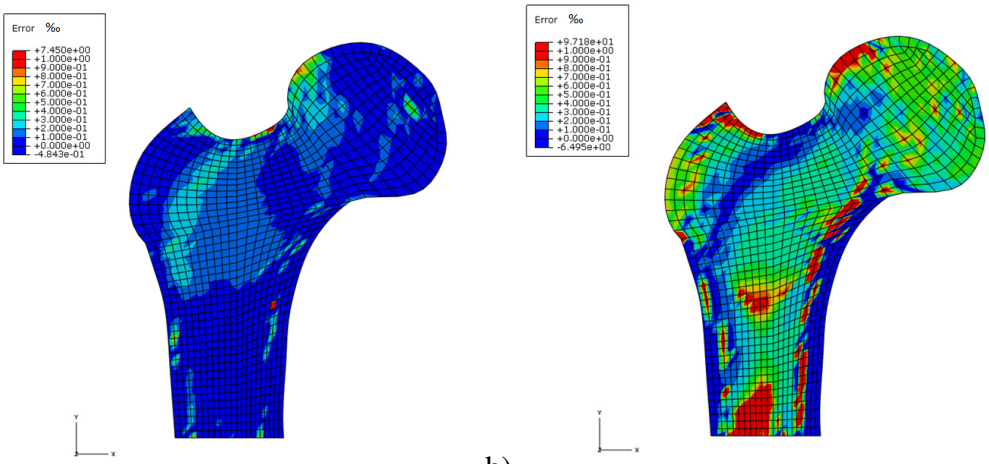

a) b)

Figure 5.10: *Error ‰ at bone density distribution computed between: a) the load from ANN and the predictions of the bone remodeling model; b) the load outside limits from ANN and the predictions of the bone remodeling model.*

5.3.4 Optimization of the ANN with multiple outputs

In order to optimize or simplify the problem and therefore reduce the time of training and testing, we consider that it is necessary to reduce the number of cases employed and the number of input data (at present 1000 cases and 24 inputs, respectively).

The effect of using 500 cases instead of 1000 has been analysed (each case corresponds to one variation of the loading parameters). The same range of variation for the loading parameters has been used. We have only increased the relative distance between cases. We also use a 10-Fold cross validation dividing randomly the 500 cases into two segments (90% of the data for training and 10% for testing). Reducing the number of cases reduced the training and testing errors mainly when few neurons in the hidden layer of the ANN were used (Figures 5.8a vs 5.8b). When the number of neurons increased (i.e. 40), the differences related with the number of cases used were smaller, although the training error was still smaller with 500 cases (0.05055%) than with 1000 cases (0.11978%).

We have also analysed the effect of reducing the number of inputs. It is known that in the ANN, the weight of each neuron of the input layer corresponds to the weight of each variable or attributable input. Hence, the weight of each input has been studied in the original ANN (1000 cases and 24 inputs) in order to identify which neurons had less influence and may be removed (Figure 5.3c). Reducing the number of inputs (15 inputs) increased the training and testing errors when few

neurons were used in the hidden layer (Figure 5.8c and 5.8d). When the number of neurons increased, there were almost no differences using 24 or 15 inputs.

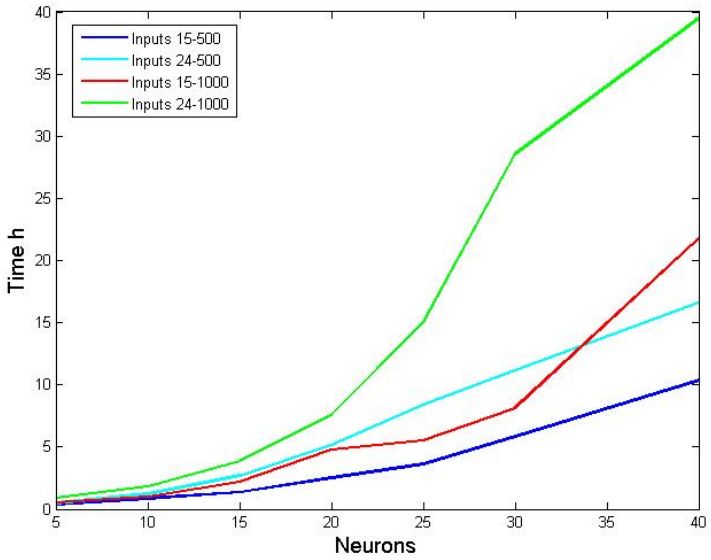

Figure 5.11: *Computational time using different number of cases and inputs as the number of neurons in the hidden layer increased.*

Finally, the main advantage of decreasing the number of cases and inputs is to reduce the computational cost. In Figure 5.11, the difference in computational cost depending on the number of cases and inputs is shown. A high number of cases/inputs implies a higher computational cost. We can observe that with 1000 cases and 24 inputs (40 neurons) in the hidden layer, we obtained a computational cost of 28.5 hours and the test RE is around 0.16%. However, if we reduce the number of cases (500), the error is equal but the computational cost is reduced to more than half (from 28.5h to 11.2 h). We obtained similar results when decreasing the number of inputs. The computational time with 15 inputs and 500 cases has been decreased at 5.8h, although the error undergoes a slight increase (0.19%). It is also noticeable that the reduction in the number of inputs is much more important than the reduction in the number of cases in terms of consuming time.

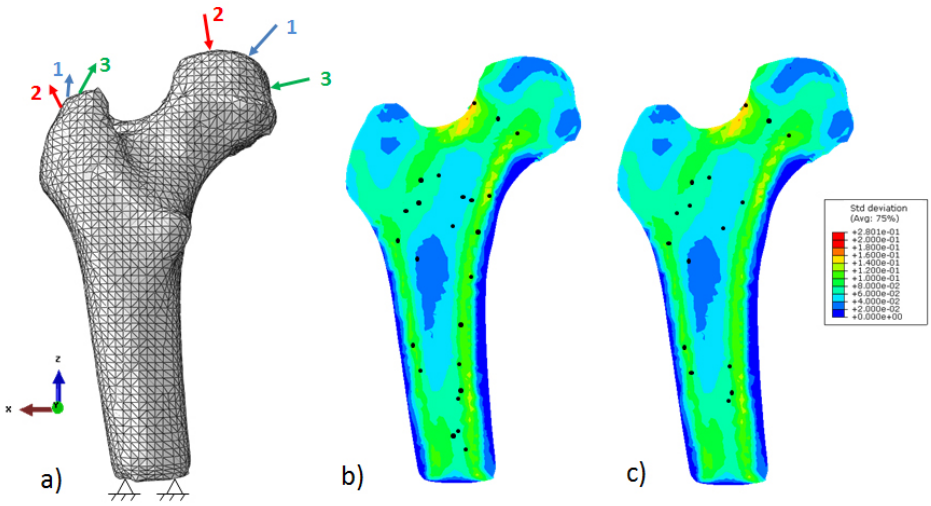

Figure 5.12: *(a) 3D FE model of the proximal femur with the boundary and loading conditions; (b) Standard deviation of the bone density distribution computed from the variation assumed for the loading conditions with 24 points and (c) 15 points assumed as inputs for the ANN.*

5.3.5 Application of the ANN with multiple outputs to a 3D case.

This methodology based on the ANN with multiple outputs has been extrapolated to a 3D real case in order to demostrate the potentiality of this tecnique in a situation closer to reality. For this purpose, we have used a specific CT-scanned 3D proximal femur, which give us the neccesary inputs for our algorithms in order to numerically estimate the femur loads. A real proximal femur has been scanned and the images have been automatically segmented using Mimics v15.0 (Materialise, Leuven, Belgium). At the end of this process the 3D FE model has been constructed and it is composed of 74460 tetrahedral elements (Figure 5.12). In this 3D example, in order to simplify the problem complexity the output data of the ANN (loading parameters) has been focused on the force magnitude and its angle. Therefore, the loading conditions (Table 5.1) are exactly the same than in the 2D case, but extrapolating the load values to the 3D problem. The femur has been also constrained distally. The number of the inputs has been selected as shown in Sections 5.2.2 and 24 and 15 (through the weight of each input) bone density values have been chosen as inputs of the ANN with multiple outputs (Figure 5.12). The algorithm has been trained with the same structure as in the 2D case (see Section 5.2.2) and in Figure 5.13 we can see the predicted results from the computational analysis.

The results derived from 3D models are very similar to the ones obtained with a 2D model. Using few neurons at the hidden layer, the RE is higher than in the 2D case, but as the number of neurons at the hidden layer increased (i.e. 40), the differences related with the number of cases used were smaller. For example, with 500 cases, 15 inputs and 40 neurons in the hidden layer, the RE is 0.16% while for the 2D case is 0.19% of the testing relative error.

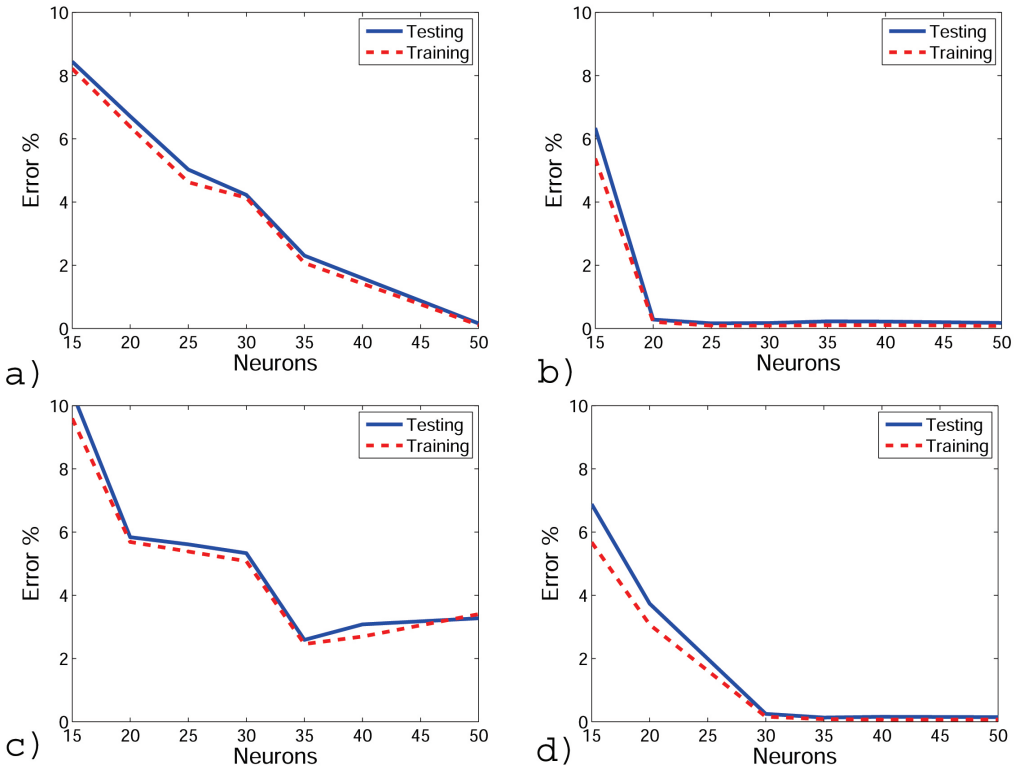

Figure 5.13: *Evolution of the absolute relative error (RE) depending on the number of neurons in the hidden layers in 3D model during ANN training and testing with multiple outputs using (a) 1000 cases with 24 inputs; (b) 500 cases with 24 inputs; (c) 1000 cases with 15 inputs; (d) 500 cases with 15 inputs.*

5.4 Conclusions

There is an increasing need to create a methodology to predict musculoskeletal loads for patient-specific models (Fluit et al., 2014). This information will be of considerable value in patient-specific musculoskeletal treatments, especially if it can be obtained easily and in a short time. Currently, there is no estab-

lished methodology for the prediction of musculoskeletal loads, although initial attempts have been described in previous works (Christen et al., 2012a). One way to overcome this limitation is the implementation of the inverse problem, which can provide the necessary information from known data (the bone density distribution through computational tomography data-CT or Dual-energy X-ray absorptiometry-DEXA). The main disadvantage of techniques for solving the inverse problem is that the computational time is very high (Fischer et al., 2003; Bona et al., 2006).

In this Chapter, we have applied three different mathematical techniques for predicting the load history. These techniques provide an extensive database which allows us to obtain a specific load case in short time. The three methods achieved this goal, but not with the same results. In all cases, it has been observed that the correlation coefficient (RSQ) is very close to 1. The high accuracy in this set indicates that the model has been well trained (see Tables 5.2, 5.3 and 5.4). On the one hand, the mean REs for training and testing in the three methods are small (Table 5.2). ANN and linear regression demonstrate a good load prediction with a RE lower than 1% for both training and testing methods. On the other hand, the RE shows that the SVM presents accuracy problems with the prediction of the load (Table 5.2). SVM computes REs at around 15.2% and we consider this as a poor approach. The reason is that the bone remodeling problem is quite linear, as the linear regression demonstrates. The SVM technique was implemented to compare its accuracy with that of the linear regression technique. It was concluded that a lower degree of accuracy was achieved with the SVM. Therefore, it is not an adequate tool for the bone remodeling algorithm here presented. However, one of the main features of the SVM is its high capacity to be updated during the training process (Cos et al., 2010; Butt et al., 2013) and it may present a great potential with other non-linear bone remodeling theories and for other applications (Kunkle et al., 2013).

If we compare the error estimated for each output, the force magnitude produces a lower error than the angle and position. This occurs because more related data have been used for the training.

ANN has been also applied following the scheme represented in Figure 5.4b. The results obtained with multiple outputs are similar to those computed for individual outputs (Tables 5.2 and 5.3). The difference between both ANN approaches is that when using multiple outputs we need to train with more neurons to obtain the same error, and this increases the training time. This is not a problem because the execution time is almost the same. It can be even lower because the ANN with multiple outputs only uses a single ANN for the same result instead of three independent ANNs. In both cases, the error is lower than 0.1% for the best training result. Another advantage of using multiple outputs is that there is no overtraining (Figure 5.8a vs. Figure 5.7-individual outputs). Finally, the results obtained with

different inputs and cases are very similar. It has been observed that the error is high when fewer cases and inputs are used, but increasing the cases and inputs exponentially increases the computation time. Therefore, for a high number of neurons in hidden layer, the optimized ANN procedure uses less cases and less inputs (500-15) because it computes similar results in test error than using a high number of cases and inputs, but the computational time decreases significantly. The ANN methodology with multiple outputs has been applied to a real 3D problem, where we have obtained errors around 0.16% for the best training result (40 neurons in the hidden layer, 500 cases and 15 inputs), as shown in Figure 5.13, which justifies the potential use of the proposed methodology.

We have to keep in mind that in this Chapter it is not possible to quantify the degree of accuracy achieved by this approach to solve a real inverse bone remodeling problem, due to the lack of patient-specific real data, measured for one specific bone geometry. However, we have proposed here a quantitative comparison of different ANN-based approaches from a theoretical point of view, presenting an optimization procedure to improve the accuracy of our approach. In fact, we study a theoretical bone remodeling example, showing that the optimization of the ANN is adequate. And, then it has been extrapolated to a 3D real geometry obtaining similar conclusions. In spite of considering simplified single 2D and 3D geometries for modeling the bone, this simplification does not reduce the importance and generality of the obtained results. The 3D model used corresponds to a real proximal femur. We have not been able to check the validity of the theoretical methodology proposed, because its corresponding loading conditions were unknown. But the results computed for the testing procedure indicate that the methodology proposed will work with real data. One of the advantages of these mathematical techniques (ANN, for example) is its feedback capacity (Franco and Cannas, 2000; Ferrante et al., 2004). Although, we have not been able to analyze this capacity, this technique would allow to work with real data subjects with different bone shape, weight, height, age, gender, etc. Actually, it is going to be presented in Chapter 6.

Another limitation of our study is that the density values considered as input data come from a theoretical remodeling analysis and not from a real CT. Nevertheless, we have also assumed that the algorithm used for bone remodeling has sufficient potential to obtain a representative distribution of the apparent density in function of different loads (Pérez et al., 2010). However, other bone remodeling algorithms could also be used, such as those described by Huiskes et al. (1987), Prendergast and Taylor (1994), Caouette et al. (2012) and Webster et al. (2012).

Mean and standard deviations of the bone density distribution were computed for the range of variation of loading. The points with a high standard deviation on the bone density in all representative areas (24 points) were initially considered as input data. If the subject changes (weight, height, age) the real loads will be

updated, but the most determinants points will be approximately the same ones. If this study is extrapolated to a real femur with CT-data available, this will allow us to obtain the density of the inputs from the Hounsfield Units (HU) (grey level from the images). But there will be also a lack of accuracy on the load, because the CT data used to come from clinical sources (with or without calibration phantom). Then, a relationship between the bone density and HU needs to be considered (Morgan et al., 2003; Peng et al., 2006; Taddei et al., 2004). These relationships are also a potential source of error in modulus data (Taddei et al., 2004). Directly related with this issue is that adding noise to the bone density images will provide results a little closer to a real application. In fact, when image acquisition is performed, a certain degree of background noise is present. Therefore, it becomes necessary to pre-filter the images (Gavgani and Dogrusoz, 2012; Wang et al., 2013) before the grey scale level is computed and methodology here proposed can be applied.

A further limitation of the present model is related to the load values considered. Only abductor muscle and hip joint contact forces were taken into account (Bergmann et al., 2001; Heller et al., 2001). It was assumed that the force corresponding to the moment when the foot touches the floor (case 1 - see Figure 5.2) was predominant and the other load values were estimated as correlative to case 1. Despite this limitation, a wide range of variation for the loading conditions was considered (Bergmann et al., 2001; Heller et al., 2001; Bitsakos et al., 2005).

In order to conclude, femur loading prediction has been achieved by the integration of two complementary engineering methodologies: bone remodeling algorithms through finite element (FE) modeling and the inverse bone remodeling problem through different mathematical techniques. A quantitative comparison of the bone density distribution for different cases with the ANN method and predicted by the bone remodeling model was also performed. In conclusion, ANN and linear regression represent powerful tools to predict femur loading conditions. ANN appears to be the most accurate technique when using multiple outputs. This technique needs a higher computation training time than using individual outputs but, despite this, it provides a more immediate response.

CHAPTER 6

Application of bone remodeling models for bone load estimation

The systematic development of patient-specific computer models for the analysis of personalized treatments is currently a reality. In fact, many advances have been recently developed to create virtual Finite Element-based models which recreate with accuracy patient-specific geometry and material properties from techniques based on quantitative image analysis. However, to determine the patient-specific forces, we need a full gait analysis in combination with a musculoskeletal model. In this Chapter, we originally determine the patient-specific forces from the tomographies used to evaluate bone material properties in five patient tibias. Actually, we combine those images with bone remodeling simulations (Chapter 2) and artificial neuronal networks (Chapter 5). The methodology here proposed is able to predict the tibia loading conditions.

6.1 Introduction

There is currently a general trend in healthcare for personalized medicine that includes use of imaging techniques, genetic analyses, and extensive biomarker evaluation to determine dedicated diagnosis or treatment protocols that differ for each specific-patient. Such protocols appreciate the differences with respect to e.g. shape morphology, genetics, and overall physiology of each individual in a much more extensive manner. The biomechanics are interested in mechanical functioning of bodies, e.g. the shape and morphology of bone on the one hand and the structural performance related to its mechanical function on the other hand. The relationship between form and function is of primary importance since such types of biomechanical analysis could help us to understand the evolutionary

biomechanics of species as well as to study biological tissues with the structural and mechanical aspects as their major function.

Development of better techniques for diagnosis and treatment of skeletal diseases requires application of bone analysis techniques to specific patients. To do patient-specific bone analysis, one needs additional information pertaining to individual patients so as to personalize the biomechanical models of bone behavior, improve the sensitivity and specificity of the obtained analytical results, and provide the patients with personalized health care (Cowin and Doty, 2007). That is why patient-specific bone analysis often starts from a set of images that are meant to provide the additional information needed for personalization of biomechanical models.

Images alone are, however, not enough for providing all the information that is required for patient-specific analysis of bones. At least two other types of information are needed, namely functional data and material properties. Functional data including the kinematics of patient's movements and the external forces exerted to the patient body during those movements (kinetic data) is needed to determine the internal musculoskeletal loads experienced by bones including joint reaction forces and muscle forces (Carbone et al., 2015). As for the material properties of bones, empirical relationships between bone density values measured using imaging modalities and elastic properties of bones are often used for obtaining patient-specific material properties (Campoli et al., 2014). However, the empirical relationships are not available for all bones and maybe drastically different from one patient to another.

6.1.1 Patient specific modeling

Patient-specific modeling is the development of computational models of human pathophysiology that are individualized to patient-specific data (Poelert et al., 2012). Patient-specific modeling is gaining more attention from research groups around the world because of its potential to improve diagnosis, optimize clinical treatment by predicting outcomes of therapies and surgical interventions, and inform the design of surgical training platforms. Most current medical diagnostic practices lead to rough estimates of outcomes for a particular treatment plan (Kent and Hayward, 2007), and treatments and their outcomes usually find their basis in the results of clinical trials. However, these results might not apply directly to individual patients because they are based on averages. If patient-specific bone analysis is going to be used in clinical settings, it needs to satisfy two criteria. First, it should provide clear added value for clinical diagnosis and treatment above that of currently available clinical tools. Second, it should be time and cost-effective. The first criterion relates to the accuracy of the analyses whereas these to their cost-effectiveness.

Patient-specific models are becoming increasingly important by the clinical demand of specifics treatments (Neal and Kerckhoffs, 2010). Thanks to advances in different technologies (computed tomography (CT), magnetic resonance imaging (MRI), gait analysis) have enabled the creation of more patient-specific models (Lekadir et al., 2015). However, direct subject-specific estimation of bone loads by means of in vivo imaging remains challenging (Zadpoor and Weinans, 2015).

The combination of patient-specific joint and muscle force-based models with consistent bone geometry into finite element-based models are a very important advance for creating specific working models that allow to perform predictive analysis of personalized treatments. Vahdati et al. (2014) combined gait analysis and a subject-specific musculoskeletal model with subject-specific bone geometry in a computational bone remodeling methodology to predict bone density distribution. The results confirmed that the predicted bone density distribution in the proximal femur is drastically influenced by the inclusion of subject-specific loadings. González-Carbonell et al. (2015) used the patient-specific geometry and material properties to study the tibial torsion using CT. Also, Carey et al. (2014) created subject-specific FE models of the tibiofemoral joint using dynamic stereoradiography data and kinematic analysis. Although these aforementioned models provide full information on bone properties, several difficulties arise for their application in clinics due to the amount of data.

6.1.2 Musculoskeletal models

Musculoskeletal models have been useful tools for virtual orthopedic surgery. Inverse dynamics techniques are used in gait analysis to calculate the net joint torques that the musculoskeletal system (Ambrósio and Kecskeméthy, 2007) produces during human locomotion. Musculoskeletal models are mathematical methods providing an approach to muscle and joint loading for analyses in vivo. In a musculoskeletal model the morphology of muscles, joints and bones is numerically represented with a set of anatomical parameters in order to investigate and quantify musculoskeletal interaction. In its simplest form with the inverse dynamic approach, the motion of segments and external forces are inputs for the model. Generally in gait analysis, these inputs are collected using a motion analysis system (e.g. Vicon, Optotrak) which measures 3D position of markers on bony landmarks on body segments. Force plates mounted in the floor of the lab collect ground reaction force during foot contact. With a linked segment model defining position and axes of the joints and inertial properties of the segments (Hinrichs, 1985; Koopman et al., 1995), torques with respect to the joints can be calculated. Subsequently, when muscles are defined in the model, muscle force can be determined given the moment arm of the muscle lines. If the number of muscles is

more than mechanically necessary, an optimization is required to share the determined joint torque over the defined muscle elements. In most cases, muscle force is optimized by minimizing a force related objective function, such as the sum of muscle forces or (squared) muscle stresses (Erdemir et al., 2007; Tsirakos et al., 1997). To determine the most optimal combination of muscle forces, a muscle force is imposed between physiological boundaries (typically zero and maximal force per muscle). Inverse muscle models, defining contraction and excitation dynamics, are used to estimate the required neural input for a given muscle force.

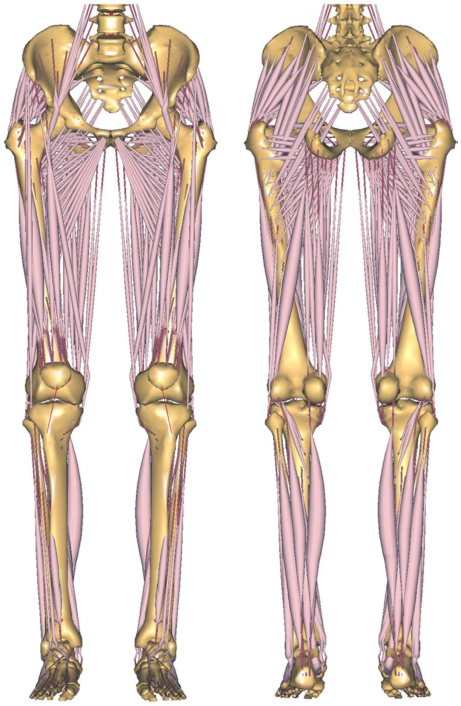

Figure 6.1: *Musculoskeletal models (TLEM 2.0) implemented in the Any Body Modeling System. The obtained model consisted of 12 body segments (head-arms-trunk, pelvis, and right and left femur, patella, tibia, talus and foot), 11 joints (L5S1 and left and right hip, knee, patello femoral, talocrural and subtalar) and 21 DOFs (Fluit et al., 2014).*

Several musculoskeletal models have been developed to study for example gait, jumping or cycling (Zajac, 1989; Pandy, 2001). Most models reviewed by Zajac (1989) and Pandy (2001) are simple 2D models that can be used to gain insight in the principles of control of movement and the role of its components. Several anatomical studies have been published containing information on the modeling parameters for the lower extremity, containing for example muscle at-

tachments sites (Brand et al., 1982) or muscle parameters (Wickiewicz et al., 1983; Spoor et al., 1991; Friederich and Brand, 1990). Unfortunately, none of these sets are complete which implies that when constructing a complete musculoskeletal model different data sets have to be combined or missing parameters have to be estimated. In recent decades, multiple methods have been developed to improve the performance of musculoskeletal patient-specific models (Fluit et al., 2012, 2014) (Figure 6.1). Carbone et al. (2012) showed errors in the estimated position of muscle attachment sites that affected muscle force predictions. Subsequently, Carbone et al. (2015) combined morphing of bone surface, with muscle volumes and functional optimization of muscle-tendon architecture for creating a musculoskeletal geometry dataset. This part, is linked with muscle-tendon attachment sites and lines-of-action (Pellikaan et al., 2014), or muscle volumes (Carbone et al., 2012), showing that subject-specific models resulted in more reliable outcome, while conventional anthropometric scaling laws were inadequate and caused unrealistic muscle activity predictions.

Musculoskeletal models that have been developed and are currently on the market are not easily accessible for surgeons because they are not user-friendly and do not present the data in a "clinically relevant" way. Most of these methodologies are not easy to prove the clinical benefits due to the complex process involved and their large computational cost. In addition, the estimation of the musculoskeletal loads requires information about the movements of an individual patient. So, these complex models not are applicable to patients. It is worth remarking that it is very difficult to measure loads in vivo, using non-invasive procedures. Hence, these models have the status of a research tool, but are not used by surgeons in their daily practice. To facilitate the use of these models, a more clinic oriented approach is therefore required.

6.1.3 Load estimation

Several studies have tried to estimate loads solving the inverse problem without using musculoskeletal models and using different numerical approaches. In fact, Fischer et al. (1995) developed an optimization procedure that adjusted the magnitude of each basic load in 2D to achieve the desired bone density. Bona et al. (2006) proposed a contact algorithm for density-based load estimation and used the method to distinguish between different modes of locomotion of animals. More recently, Christen et al. (2012a) also developed a bone loading estimation algorithm to predict loading conditions by means of calculating the loading history that produces the most uniform strain energy density on the bone tissue. Campoli et al. (2012) were the first to use the Artificial Neuronal Network (ANN) approach for femur load prediction from the bone density distribution. They combined a wavelet decomposition technique with an ANN for estimating the loading

parameters of the femur. Zadpoor et al. (2013) also used ANN for prediction of tissue adaptation loads from a given density distribution of trabecular bone in a 2D example of the femur. Garijo et al. (2014b), as was shown in Chapter 5, presented a methodology where the specific load that the bone is really supporting was predicted through different mathematical techniques by utilizing the bone density distribution of the patient. They used a single femur where they predicted the loading conditions that induces a specific bone density distribution with a good accuracy in ANN.

6.2 Methodology

Therefore in, this chapter we present a general methodology in order to determine the forces that a subject-specific tibia is supporting from CT grey data through an image-based analysis. In order to determine the loads that a subject-specific tibia is supporting, a computational-based approach is defined, which combines different numerical tools widely used in bone image analysis and bone mechanics. For that, we relate the methodology previously developed in Chapter 2. We used the bone remodeling model (Section 2.2- Anisotropic model) for the prediction of the density and then, we used this data for training our Artificial Neuronal Network (ANN) (Chapter 5).

For that, the proposed methodology is presented as follows. First, we describe this computer approach to determine the patient-specific forces. Next, we present the method of how we are going to validate this novel methodology. So, we present the final patient-specific cases that are studied. Finally, to quantitatively evaluate the predictive capacity of this novel methodology, we compare these forces with those obtained for each patient from an individual-based gait analysis and subsequent musculoskeletal subject specific force prediction.

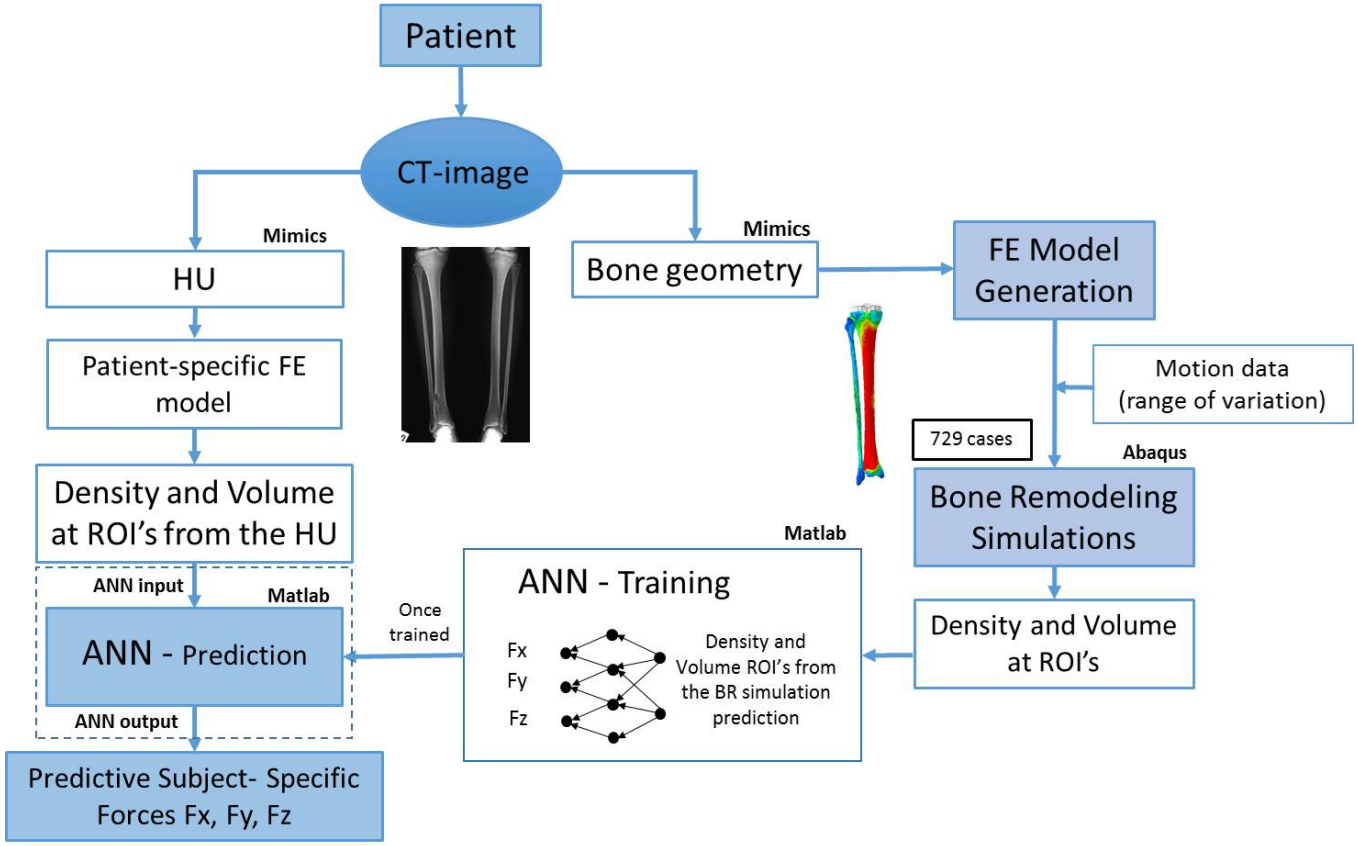

Figure 6.2: *Schematic flow chart of steps involved in subject-specific predictions of tibia loading.*

6.3 Computational-based methodology for estimating patient-specific loads

To apply this methodology (see Figure 6.2), we require the patient-specific bone geometry and its bone apparent density, which can be obtained from individual CT data (Hounsfield Units - HU) through current standard image analysis (Bitsakos et al., 2005). Therefore, from this analysis, we are able to construct a patient-specific FE model that replicates the main characteristics of the bone: its geometry and heterogeneous material properties (Figure 6.2-left).

This FE model is going to be used for intensive bone remodeling simulations (Doblaré and García, 2001) (see Chapter 2) with multiple different load cases that come from inter- and intra-subject variability (Motion data - Figure 6.2-right). From the multiple simulations, we obtained different bone density patterns for each load conditions. Then, we selected the apparent density and volume at different regions of interest (ROIs) defined for the tibia in all the analyses. Actually, these data (ROIs from remodeling) and their corresponding loads (from the motion database) have been used for training the Artificial Neural Network (ANN) (see Chapter 5 and Appendix A.1.1). Through multiple iterations, the ANN is trained obtaining a correlation between ROIs and forces (Figure 6.2).

After training the ANN (Figure 6.2- bottom left), we introduce the density and volumes values at the ROI regions from the subject-specific CT data (HU) as input data in the ANN. And, the ANN will predict the subject-specific forces (output value)(Figure 6.2).

6.4 Validation of the model by means of gait analysis.

In order to validate the ANN performance for tibia loading prediction, we compare previous ANN-based predicted loads (section 6.3) with the loads obtained from the patient-specific musculoskeletal model (see Figure 6.3) and the 3D gait measurements. 3D gait analysis, regarding kinematics and ground reaction forces of subjects were obtained from the Twente Lower Extremity Model (TLEM 2.0) data set (Figure 6.1). TLEM 2.0 is a new comprehensive data set of the musculoskeletal geometry of the lower extremity which is based in medical imaging data (Carbone et al., 2015).

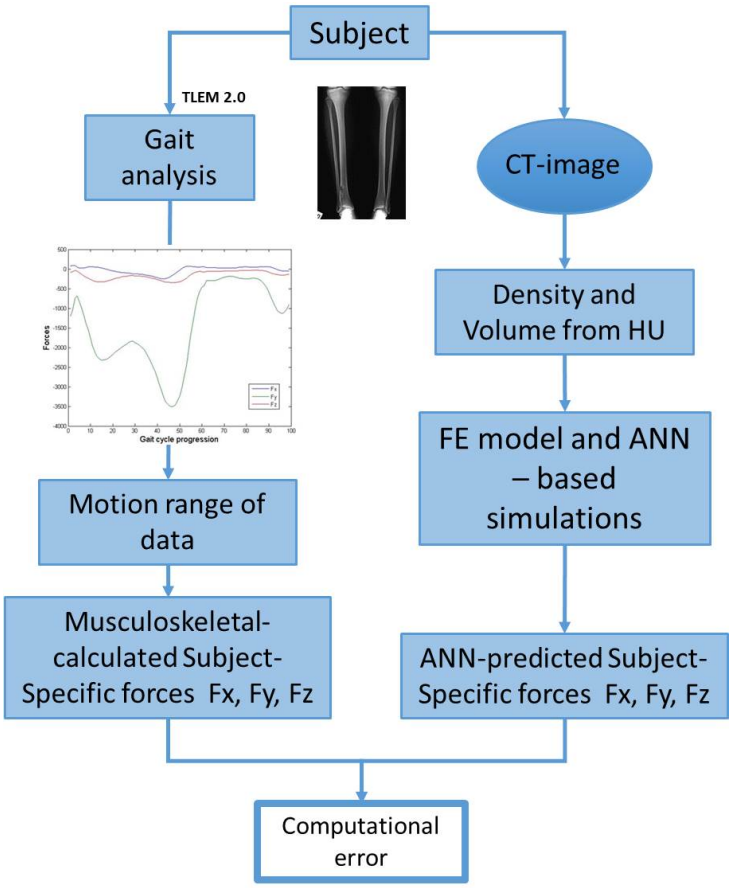

Figure 6.3: *Schematic flow in subject-specific predictions of tibia loading.*

6.5 Subject-specific data.

Previous computational-based model has been tested with five healthy subjects. They had no history of major injury, and had not undergone orthopedic surgery on the lower limb. We specifically chose them in order to include a wide variety of subjects in terms of age (23-61 years), gender (two men, three women) and weight (58 kg to 90.4 kg) (Table 6.1). The procedures developed in this study were approved by the ethical committee of the region Arnhem-Nijmegen (Netherlands). A written informed consent was obtained for each subject.

6.5.1 Subject-specific geometry.

In order to model the subject-specific geometry, full computational tomography (CT) scans of every subject left leg region were obtained (Kolk et al., 2014) (Figure 6.4). The CT images were imported to Mimics® 17.0 (Materialise, Leuven,

Subject	Age	Sex	Weight	HU max	HU min	Elements (N° FE)
Subject 1	23	Male	83.1	1603.14	-72.03	41510
Subject 2	26	Male	90.4	1568.1	-87.55	77270
Subject 3	27	Female	58.0	1858.8	-92.21	77777
Subject 4	23	Female	77.6	1579.52	-65.30	71739
Subject 5	61	Female	70.7	1836.93	-77.60	30504

Table 6.1: Subject-specific data used in the study.

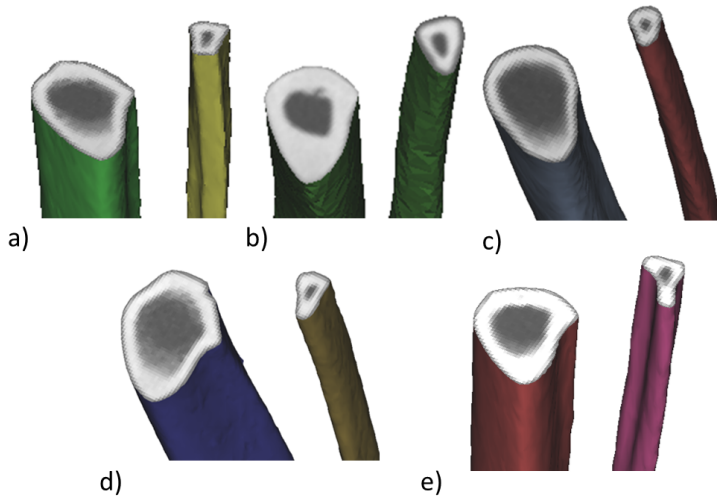

Figure 6.4: *Cutting view of the tibia and fibula with the grey scale (CT images): a) Subject 1, b) Subject 2, c) Subject 3, d) Subject 4 and e) Subject 5.*

Belgium). We performed a semiautomatic segmentation of left tibia and fibula and their corresponding 3D geometrical reconstruction of each bone. Afterwards, a union area was created between tibia and fibula that simulates the cartilage between both bones. The FE meshes were generated by 3-matic® (Materialise, Leuven, Belgium) through a semi-automatic meshing procedure.

Every tibia mesh was built by means of tetrahedral elements of size 3 mm approximately (see Table 6.1 and Figure 6.5a). The used element size is inside the asympotic region of convergence and represents a good trade-off between numerical accuracy and computational cost.

Subsequently, we defined the anatomical landmarks and joint centers for every patient. Then, the origin of local reference frame coincides with the midpoint between the medial (MM) and lateral malleoli (LM) (Figure 6.5b). The axis Y is the line connecting the midpoint between the tips of the medial (MM) and lateral

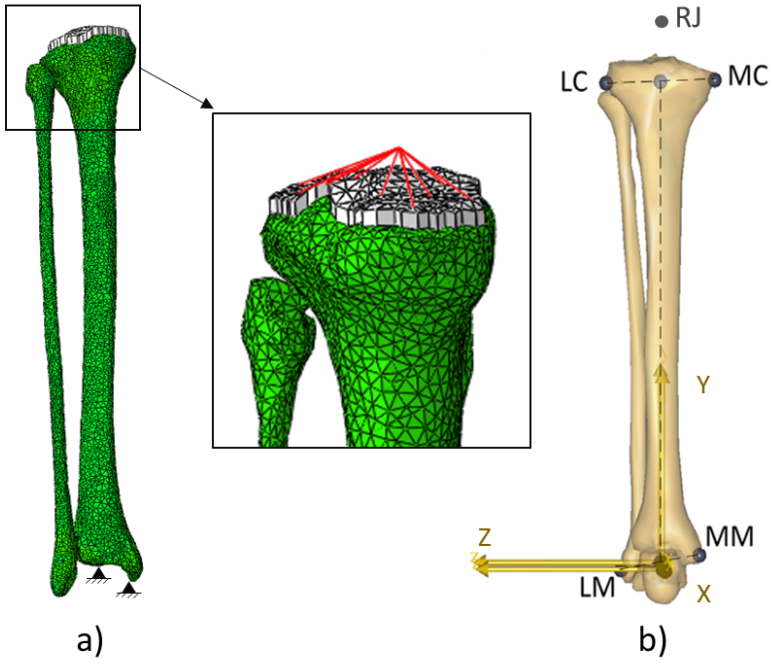

Figure 6.5: *a) FE model and zoom in proximal condyles where the load is applied. b) Local coordinate frames of tibia and talus segments (MC: most medial point of the medial condyle of the tibia, LC: most lateral point of the lateral condyle of the tibia, MM: medial malleolus, LM: lateral malleolus) and rotation center joint (RJ).*

malleoli (LM), and the midpoint between the most medial point on the border of the medial tibial condyle (MC) and the most lateral point on the border of the lateral tibia condyle (LC). The axis Z is the line lying in the plane defined by the tips of the medial (MM) and lateral femoral malleoli (LM) and the midpoint between the most medial point on the border of the medial tibial condyle (MC) and the most lateral point on the border of the lateral tibia condyle (LC), perpendicular to the Y- axis, pointing to the right (see Figure 6.5b). And finally, axis-X is the line perpendicular to both Y and Z-axis. In order to localize the knee rotation center, the positions of the skin markers were identified. The rotation center of the tibia-fibula joint (RJ) was approximated based on a cylindrical fit through the femoral condyles and the trajectory of the tibia-fibula with respect to the femur given by the musculoskeletal model (Carbone et al., 2012; Pellikaan et al., 2014) (see Figure 6.5b).

The load characteristics (Section 6.5.3) will be expressed relative to this local reference frame and will be applied through rigid beams that connect the rotation

of joint (RJ) with a surface over the proximal tibial condyles. Bilinear quadrilateral elements were created in the surface of the proximal condyles in order to apply loading conditions uniformly distributed in the knee joint (Figure 6.5a). This process was repeated for every subject.

Therefore, the beams and the layer of elements over the proximal tibia condyles were assumed as rigid. For the cartilage elements (joint between tibia and fibula), Young's modulus was assumed as 10.0 MPa and Poisson's ratio as 0.45 (Jin and Lewis, 2004).

For the bone remodeling simulation (Section 6.3- Chapter 2), each tibia was initially assigned a uniform bone density of 0.5 g/cm^3 and was fixed distally during the whole analysis. Changes in the bone density distribution are computed until 400 days (see Chapter 2 - Doblaré and García (2001)).

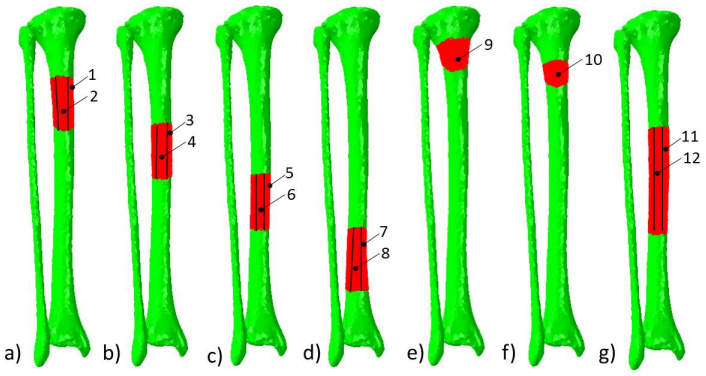

Figure 6.6: *Definition of the inputs for the ANN based on the following ROI's: a-d) Diaphysis (4 proportionality parts where separated the cortical and trabecular bone), e) Metaphysis (upper), f) Metaphysis (lower) and c) Central diaphysis (cortical and trabecular bone volume).*

In the tibia FE model, we have selected seven regions-of-interest (ROIs) to study the average apparent density in these areas (Figure 6.6 a-g). The diaphysis has been divided in four proportional parts (Figure 6.6 a-d). In each part, we have separated the cortical ($\rho \geq 1.2\ gr/cm^3$) and the trabecular bone ($\rho < 1.2\ gr/cm^3$) using the image grey level or Hounsfield Unit (HU) density values; so here, we have eight (Figure 6.6 1-8) average density values in these four ROI's. We have also divided the proximal metaphysis in two volumes, upper and lower, two additional inputs (9-10), where we compute their average density (Figure 6.6e-f). Therefore, we have ten inputs data that are the average bone density distribution within the ROI's. Additionally, we selected the central area of the diaphysis (Figure 6.6g) and we computed the volume of cortical (11) and trabecular bone (12) as

two additional inputs. So finally, we have twelve inputs for the ANN (see Chapter 5).

6.5.2 Subject-specific density

For computing the density from the HU values, the FE meshes were imported into Mimics® 17.0 again and different material properties were assigned to relate the bone mineral density with the HU. In the literature, different relationships between bone apparent density and HU can be found for the different bone types, mainly of the lower extremities (Peng et al., 2006). In the present study, we have used a linear relationship as proposed by Bitsakos et al. (2005).

From every subject CT data (see Table 6.1 and Figure 6.4), the HU maximum (HUmax) and minimum (HUmin) values were obtained and were correlated with 1.92 gr/cm^3 and 0.5 gr/cm^3 bone density values, respectively. These values were introduced in eq. 6.1, so the bone density value at every point is computed as:

$$\rho_i = 0.5 + \frac{1.92 - 0.5}{HU_{max} - HU_{min}}(HU_i - HU_{min}) \tag{6.1}$$

6.5.3 Subject-specific musculoskeletal loads

Every subject experiments different gait trials using the TLEM 2.0 (Carbone et al., 2015). Musculoskeletal loads were used to define the load patterns that are applied to the tibia. We assumed that the knee joint force is the one that predominantly defines the bone density distribution of the tibia and all forces are expressed in the local reference frame of tibia and fibula (Section 6.5.1). From subject-specific musculoskeletal load data, we evaluate the knee joint forces in X, Y and Z axis for all the subjects involved, computing maximum forces values (see Figure 6.7). Table 6.2 shows the maximum force in each direction for each subject.

Simulation loads

For the bone remodeling simulations, we also assumed that the maximum force X, Y and Z are consecutively applied to simulate tibia loading. These three consecutive loading cases were applied (Fy, Fx and Fz) acting in blocks of 10000 direct cycles but with different frequency for each one (6000, 2000 and 2000, respectively) (Doblaré and García, 2001). The first load (Fy) represents the moment when the foot touches the floor during walking, while the other two represent the two alternative movement of the tibia. The first load is assumed to be the predominant (high frequency) (see Chapter 2). These loads have been applied through the position of the rotation of knee joint (RJ) (Section 6.5.1).

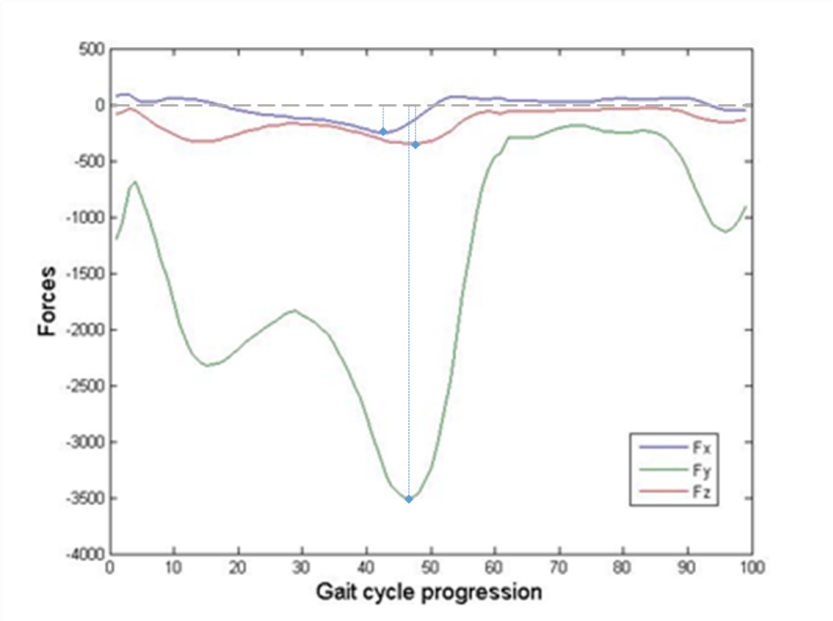

Figure 6.7: *Forces Fx, Fy and Fz of the Knee joint during the gait cycles. Maximum forces values at X, Y, and Z direction are applied as loading conditions for the tibia bone remodeling simulations.*

To represent the majority of real cases, different loading conditions taking into account inter-individual variations were simulated in order to obtain their corresponding bone density distributions for the ANN training. Given that we do not have a motion database with full information of many subjects, we used as motion data the information provided by the subjects studied in the work (Kolk et al., 2014; Fluit et al., 2014). For that, we consider the two subjects with higher difference on the in maximum loads (Table 6.2) of our musculoskeletal model and we calculate the mean of all forces. For the range of variation, we estimated a range of variation of 35% of this mean force calculated for representing the majority of population.

Finally, nine variations of each force value (Fx, Fy and Fz) are considered within the 35% range of variation. When one force value is varied, the rest remain constant. Summarizing, 729 (9x9x9) combinations of loading parameters have been simulated for every subject. Therefore, a total of 729 bone remodeling problems have been initially solved for each subject (see Figure 6.2) in order to train every subject-specific ANN. Summarizing, the ANN training has been performed with the 12 ROIs value of each of the 729 bone remodeling problems and their corresponding arbitrary loads.

	Subject 1	Subject 2	Subject 3	Subject 4	Subject 5
Fx	156.68	153.61	117.98	126.06	156.79
Fy	-2171.38	-2859.93	-2013.05	-1983.66	-3245.17
Fz	-391.04	-318.85	-369.78	-314.42	-263.59

Table 6.2: Maximum force of load cases from the gait cycle of the five subjects.

All the FE simulations have been performed in Abaqus v6.14. and they have been run in a computational cluster of 224 cores and 576 Gb of the RAM.

6.5.4 Performance of the ANN - based simulations

In order to predict the accuracy of this technique, the absolute of relative error (RE) and the correlation coefficient (RSQ) have been computed as well as in Chapter 5, through the following expressions:

$$RE = abs(\frac{\hat{\theta} - \theta}{\theta}) \tag{6.2}$$

$$RSQ = \frac{\sigma_{\hat{\theta}\theta}}{\sigma_{\hat{\theta}}\sigma_{\theta}} \tag{6.3}$$

where $\hat{\theta}$ is the predicted data, θ is the real data, $\sigma_{\hat{\theta}\theta}$ is the covariance and $\sigma_{\hat{\theta}}$ and σ_{θ} are the standard deviations.

The results of the relative error are calculated based on the training and the testing sets of the mean 10 fold-cross (see Chapter 5). The training data allows to generate the model, so the corresponding error value set indicates if the model has been well trained, while the test data are used to validate it. The corresponding error indicates if the model is appropriate to solve the problem.

6.6 Results

6.6.1 Quantitative performance of the ANN - based simulations

The performance of the ANN needs to be checked in order to determine its suitability for the present problem. Table 6.3 shows the mean error results obtained for each case. The RE computed during training and testing are lower than 1%. And the RSQ error is very close to 1. This means that the ANN is well trained and the force estimation is accurate.

The absolute of relative error (RE) % and the correlation coefficient (RSQ).						
		Subject 1	Subject 2	Subject 3	Subject 4	Subject 5
Force X	RE Train	0.082 %	0.127 %	0.053 %	0.04 %	0.158 %
	RE Test	0.061 %	0.043 %	0.019 %	0.018 %	0.035 %
	RSQ	0.999	0.999	0.999	0.999	0.998
Force Y	RE Train	0.006 %	0.011 %	0.004 %	0.002 %	0.004 %
	RE Test	0.040 %	0.002 %	0.001 %	0.001 %	0.001 %
	RSQ	0.999	0.999	0.999	0.999	0.999
Force Z	RE Train	0.060 %	0.035 %	0.031 %	0.020 %	0.065 %
	RE Test	0.040 %	0.015 %	0.010 %	0.008 %	0.015 %
	RSQ	0.999	0.999	0.999	0.999	0.999

Table 6.3: Comparison of the relative error (RE) and the correlation coefficient (RSQ) in all subjects.

6.6.2 Quantitative comparison of personalized forces between gait measurements and ANN-based analysis

In order to validate our methodology, we compare the forces predicted by the ANN (Section 6.3) with the forces obtained from the corresponding subject gait analysis (Table 6.2 and Section 6.4). We have computed the relative error between the predicted forces (predicted data) from the ANN and the gait analysis forces (real data).

We observe in Table 6.4 that force Y (force in the vertical direction of the tibia) is accurately predicted in all the cases. Values of this force are considerably higher than the others (Fx and Fz) (see Figure 6.3). Therefore, as forces in Y are higher, it is more difficult to estimate forces in X and Z direction, causing larger error in those directions. Additionally, Fx and Fz are very small values. Therefore, relative error could be very high, due to a very small Fx or Fz value. However, if we compute the force error through its total force, the error is lower than 6%, which clearly indicates a good prediction.

In order to evaluate the predictive capacity of this methodology for each individual patient, we compute the relative error when patient-specific inputs were interchanged between patients and introduced in another ANN based-patient model. We compared the predicted force module with the corresponding patient gait analysis data.

In all the cases, except for case 1, the error is minimum when we compare the predictive forces with each patient-specific forces, clearly showing that each patient presents a realistic pattern of the forces. However, in the case 1, the error is very similar for all the force conditions (except case 2 and 5), clearly indicating

The absolute of relative error (RE)%.					
		Force X	Force Y	Force Z	Total Force
Subject 1	Gait	156.68	-2171.38	-391.04	2211.87
	ANN	188.80	-2014.78	-493.84	2083.00
	Error%	20.50	7.21	26.29	5.83
Subject 2	Gait	153.61	-2859.93	-318.85	2881.75
	ANN	201.82	-2780.65	-443.23	2822.97
	Error%	31.38	2.77	39.01	2.04
Subject 3	Gait	117.98	-2013.05	-369.78	2050.13
	ANN	78.24	-1934.15	-652.23	2042.66
	Error%	33.69	3.92	76.38	0.36
Subject 4	Gait	126.06	-1983.66	-314.42	2012.38
	ANN	321.71	-1905.91	-125.16	1936.92
	Error%	155.20	3.92	60.19	3.75
Subject 5	Gait	156.79	-3245.17	-263.59	3259.63
	ANN	252.34	-3198.52	-283.63	3220.97
	Error%	60.94	1.44	7.61	1.19

Table 6.4: Relative error (RE) between forces from Gait and ANN predictive for all subject.

that in this patient is more difficult to estimate the personalized forces in comparison with other subjects.

The absolute of relative error (RE)%.											
Gait Analysis		Subject 1 - ANN		Subject 2 - ANN		Subject 3 - ANN		Subject 4 - ANN		Subject 5 - ANN	
Subject	Force	Force	Error%	Force	Error%	Force	Error%	Force	Error%	Force	Error%
Subject1	2211.87	2083.00	**5.83**	2752.39	24.44	2046.59	7.47	1949.07	11.88	2628.76	18.85
Subject2	2881.75	2216.73	23.08	2822.97	**2.04**	2124.59	26.27	1979.41	31.35	2549.75	11.52
Subject3	2050.13	2219.48	8.26	2752.00	34.24	2042.66	**0.36**	2251.94	9.84	2586.34	26.15
Subject4	2012.38	2083.50	3.53	2605.03	29.45	2024.60	0.61	1936.92	**3.75**	2689.32	33.64
Subject5	3259.63	2640.34	19.00	3344.09	2.59	3228.00	0.97	2865.94	12.08	3220.97	**1.19**

Table 6.5: Relative error (RE) between forces from Gait and ANN predictive for all subjects.

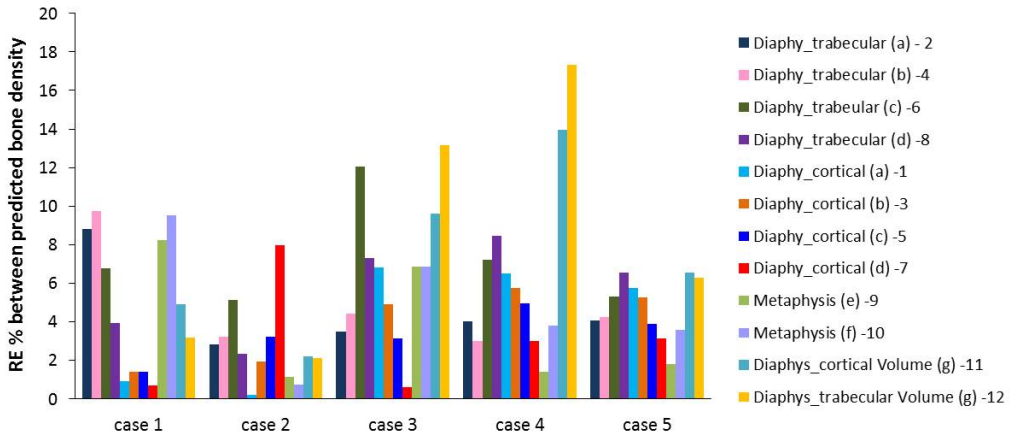

Figure 6.8: *Differences between predicted bone density from the force of ANN (predicted data) and density from force of the Gait analysis (real data) for 12 ROIs.*

6.6.3 Quantitative comparison of the density distribution in the tibia.

Finally, the predictive forces estimated from the ANN - based analysis are again incorporated into the personalized FE model of the tibia in order to compute the bone density distribution by means of direct bone remodeling simulations (See Chapter 2). In parallel, we introduced the force from the corresponding gait analysis in the FE model to obtain the bone density distribution.

The relative errors between the 12 inputs values (Figure 6.5) have been computed and represented (maximum error %) in Figure 6.8. It is observed that the error is low in all ROI's areas.

In most cases, the relative error is higher in the trabecular ROI regions than in the cortical ones (Figure 6.8). This fact occurs because we compute the relative error dividing by the current density, that in the case of trabecular bone is very low.

6.7 Conclusions

There is an increasing need to create a systematic methodology to predict personalised musculoskeletal loads for patient-specific models. This information will be of considerable value in patient-specific musculoskeletal treatments (as orthopedic surgery), especially if it can be obtained easily and in a short time. Currently, the patient-specific forces are obtained through the development of the corresponding

dynamical musculoskeletal model. Therefore, we need to perform an extensive subject gait analysis. These models are very accurate and very complete, providing information of all muscles (position, load values, etc) during the walking cycle (Fluit et al., 2012, 2014), however it is not easy to apply in the clinic. In addition, sometimes, the subject cannot move, so he/she is not able to perform the actions needed for the gait analysis.

In this Chapter, we present a methodology able to predict the forces that a subject-specific tibia is supporting from CT data. It is possible to obtain the specific geometry and the density for our methodology with a simple CT data, and it is not necessary to add any special requirement for the patient. Therefore, this methodology can be easily applied in the clinics. Our methodology has been tested in five patients obtaining good results. The comparison with gait analysis proves the good accuracy of our model (errors relative to the total force are less 6 %). However, the force results in the horizontal directions (Fx and Fz) are not very accurate. If absolute error would be computed, the error would be much lower. The reason is that we use a simplified model for the bone remodeling and we only considered the knee contact force acting on the tibia. This is one limitation of our methodology although its influence is reduced on the global result, where the density distribution is accurately predicted. On the other hand, we need to suppress the muscle, assuming that they are less influential for the later patient clinical treatments.

Additionally, from the musculoskeletel model, we have observed that Fx and Fy forces values are not very high and their variability during the walking cycle is really small (Fx=137.3 ±15% and Fz=327.3 ±19.5%), respectively. However, the Fx and Fz values predicted with our methodology presented a higher variability (Fx =200 ±61% and Fz=388.7 ±67.8%). This fact indicated that Fx and Fz forces values are highly influenced by the presence of the other muscles forces because their value is relative smaller than Fy force value. The vertical force (Fy) is considerably higher, so its consequences on bone remodeling is less affected by the presence of other muscle forces and the accuracy on its prediction is so high. According to Vahdati et al. (2014) the prediction of the density distribution in patients depends on the subject-specific loading condition, although they used all the forces. However, we can clearly demonstrate the relationships between the density values and the subject-specific force values. If we compare every subject-specific CT image (Figure 6.4), we clearly observe that case 2 and case 5 present more cortical area than the other cases. This fact is in agreement with the value of every subject force, cases 2 and 5 present a high value of gait forces (Table 6.2).

Another limitation is the high number of relationships between CT numbers (HU) and bone properties (Pérez et al., 2010). Some of these relationships, may not be very precise and introduce errors in the predictions. This limitation could be solved if the CT scan is performed using a validated phantom. An accurate

estimation of bone density would improve the accuracy of the subject-specific finite element model (Schileo et al., 2008), and consequently the prediction of the patient-specific loads. Additionally, bone properties extracted from the CT scans cannot include bone anisotropy, although the bone remodeling simulations take into account this actual anisotropy. For future works, the consideration of more complex image analysis algorithms (Bitsakos et al., 2005) that allow to determine bone anisotropic properties will provide additional information that would improve the accuracy of the force prediction.

Finally, the last limitation of this methodology is its high computational cost, because we need to run multiple bone remodeling simulations and we need to train the ANN to obtain a very accurate result. However, it is possible to use the ANN trained model of a similar patient, to obtain a faster prediction. Additionally, we could use extrapolation methods in order to accelerate the bone remodeling simulations (Mohaghegh et al., 2014). In our opinion, the methodology presented in this work opens a new strategy for the systematic creation of patient-specific models, facilitating the methodology for its clinical application.

CHAPTER 7

Conclusions and Future work

This chapter summarizes the work accomplished throughout the previous chapters, recapitulating the main conclusions and highlighting the original contributions of this Thesis. Finally, several open future lines are proposed.

7.1 Summary

The main objective of this Thesis has been the study of the bone behavior during the remodeling process through computational models, taken into account their problematic, more relevant challenges and applications. With this purpose, a computational methodology has been developed that is able to evaluate the bone density of an specific patient and predict the loads that this bone is supporting.

Firstly, we have studied two classical bone remodeling models, one isotropic (Stanford model) and another anisotropic (Doblaré and García model). In both cases, we have presented a full mathematical analysis showing their predictions. Afterward, we have showed some mathematical problems of the anisotropic model and we have presented an extension of the previous law with improvements in the reabsorption process (Mengoni and Ponthot, 2015).

Subsequently, in Chapter 3 and 4, we have justified that the current bone remodeling models present some numerical limitations. Many researchers have tried to find the most appropriate mathematical laws to describe bone behavior, without either getting a complete analysis. In this Thesis, we have proposed two novel assumptions that improve the remodeling models. Actually, in Chapter 3, we have modified the Stanford (Jacobs, 1994)and anisotropic bone remodeling model (Doblaré and García, 2002), based on the reference homeostatic stimulus, which now depends on the loading history that each point is supporting. For that, we have considered that the reference stimulus is not constant and changed

with the apparent density. This modification improves the stabilization of the numerical results corresponding to the spatial distribution of the apparent density and, in consequence, the convergence of the algorithm. This algorithm has been tested in 2D and 3D models, where we demonstrate that the density achieves a spatio-temporal equilibrium. Also, we have performed a mathematical analysis to demonstrate the linear convergence of the isotropic bone remodeling algorithm, incorporating previous assumption, where the reference homeostatic stimulus is non-constant. Finally, in the results, we have clearly showed that this modification improves both bone remodeling models.

Another modification has been proposed in Chapter 4, in which we have studied the strong dependency of the initial condition on bone remodeling models and we have developed a method capable of decreasing this dependency. For that, we have changed the relationship between the organ level and tissue level through the new equation where the reference homeostatic stimulus changes according to the density and the tissue effective energy remains unchanging. This modification improves the uniqueness of the solution, independently of the initial conditions selected and clearly helps in its numerical stability.

Furthermore, we have showed some applications of these models and how these models can be applied to a specific subject. First, we have developed a general methodology for obtaining the loads that bone supports. For this purpose, we have applied three different mathematical techniques for loads prediction: Artificial Neuronal Network (ANN), Support Vector Machine (SVM) and linear regression. These techniques allow us to obtain a specific load case in short time after the training. For that, the three mathematical models have solved the inverse process through a high amount of data obtained with different bone remodeling models. After an iterative process, ANN and linear regression have demonstrated a good theoretical load prediction with a low relative error. However, the SVM has presented accuracy problems with the prediction of the load. Due to the good accuracy of ANN, we have developed this technology with multiple outputs and a real 3D femur geometry obtaining similar results. Also, it has been performed a sensitive analysis with different inputs and number of cases and finally, we have studied the computational cost of the training process.

Following the methodology proposed in Chapter 5, we have applied it in five real clinical cases in Chapter 6. For that, we have presented a process able to predict the forces that a subject-specific tibia is supporting. These data have been obtained using the specific geometry and the bone density distribution generated by simple CT data. Subsequently, we have obtained the load by entering the density and volume at certain ROIs from the CT in our predictive model. The predicted load has been compared with the loads from the subject gait analysis. The comparison between the predicted and gait forces has proved the good accuracy,

especially in predicting the vertical force (main force). However, the force that results in the horizontal directions (Fx and Fz) were not such accurately predicted.

7.2 Conclusions

Summarizing, the main conclusions of this Thesis are grouped and they can be summarized as follows:

- *Bone remodeling models*
  - Bone remodeling models present some numerical limitations that can affect to the interpretation of the results.
  - Reference homeostatic stimulus is one of the main key parameters that controls the bone density distribution and we concluded that it cannot be remained constant.
  - Changing reference homeostatic stimulus according to the loading history, it achieves to improve the stability of the density distribution in bone remodeling simulations.
  - Bone remodeling simulations present a strong dependency of the initial conditions.
  - The relationship between the micro (tissue) and the macro (organ) level, is fundamental for the development of phenomenological bone remodeling models. There are multiple relationships in the literature and it is necessary to validate a method able to deal with all these variables (Colloca et al., 2014)
  - Adequate multiscale link between micro an macro scale allows to improve stability on bone density distribution and in consequence, allows to obtain the solutions with independence of the initial conditions
- *Mathematical approaches to estimate the loads*
  - The creation of numerical techniques that allows obtaining the load that each subject-specific bone supports without development of the gait experiment analysis of the patient is a very relevant application of bone remodeling simulations. The inverse bone remodeling model achieves this challenge obtaining the loads through the apparent density measured through CT image analysis.
  - Machine learning techniques are accurate techniques for solving the inverse bone remodeling problem.

  - ANN and linear regression represent powerful tools to predict femur loading conditions.
  - The relation between the density distribution and the loads is almost linear.
  - SVM presents worse results due to the linearity of the data.
  - ANN presents multiple options for obtaining the result as single or multiple outputs.
  - The amount of data used for the training influences on the computational cost, and is not involved in the optimization problem.

- *Subject-Specific musculoskeletal loading of the tibia*

  - There are clearly relationships between the density values, subject-specific force values and the corresponding geometry.
  - The bone remodeling model predicts accurate density distribution in relation with the HU.
  - It is possible to obtain the load in a patient with non-invasive techniques.
  - The methodology presented in this work opens a new strategy for the systematic creation of patient-specific models, facilitating the methodology for its clinical application.

7.3 Original contributions

To our knowledge, some aspects of this thesis are completely new and the foremost original contributions are the following:

- A formulation for bone remodeling models that ensures the stabilization of the numerical results corresponding to the spatial distribution of the apparent density and in consequence, ensuring the convergence of the model. In this formulation, the algorithm adapts the reference homeostatic stimulus according to the supported loads.

- A theoretical analysis has been performed to demonstrate the linear convergence of the bone remodeling algorithm incorporating a non-constant reference homeostatic stimulus.

- Formulation and development of a new bone remodeling model based on adaptation of organ and tissue levels. This novel relationship considers the reference homeostatic stimulus dependent on the apparent density and tissue energy remains constant during the whole process, improving the non-dependency on the initial conditions.

- A methodology for obtaining the loads that the bone supports through three numerical approaches: artificial neural networks (ANN), support vector machines (SVM) and linear regression (LR). For that, it is necessary to combine multiple bone remodeling analyses that is the input data-based for the methodology.

- A methodology that combines inverse bone remodeling models, artificial neuronal networks and medical image analysis is able to predict patient-specific loads in tibia.

7.3.1 Publications in peer-reviewed journals

The publications on international journals achieved during the Thesis period are listed below:

1. **N. Garijo**, J. Martínez, J. M. García-Aznar, M.A. Pérez. Computational evaluation of different numerical tools for the prediction of proximal femur loads from bone morphology. *Comput. Methods Appl. Mech. Engrg.* 268, 437-450, 2014. (Chapter 5).

2. **N. Garijo**, J.R. Fernández, M.A. Pérez, J.M. García-Aznar. Numerical stability and convergence analysis of bone remodeling model. *Comput. Methods Appl. Mech. Engrg.* 271 253-268, 2014. (Chapter 3).

3. **N. Garijo**, N. Verdonschot, J.M. García-Aznar, M.A. Pérez. Subject-Specific musculoskeletal loading of the tibia: Computational load estimation. *Bone. (Under review)* (Chapter 6).

4. **N. Garijo**, M.A. Pérez, J.M. García-Aznar. A multiscale modeling approach based on the stability. *(In preparation).*(Chapter 4).

7.3.2 Congress and conference contributions

The following communications have been presented during the development of this Thesis:

1. **N. Garijo**, M. Remacha, A. Alberich-Bayarri, J.M. García-Aznar, M.A. Pérez. Patient-specific simulations of human bones: CT data and bone remodelling models. Oral presentation. *Materialise World Conference 2012*. LEUVEN (BELGIUM). April 2012

2. **N. Garijo**, A. Alberich-Bayarri, M.A. Pérez. Patient-Specific simulation of the human radius. Oral presentation. 18^{th} *Congress of the European Society of Biomechanics (ESB)*. LISBON (PORTUGAL). July 2012

3. **N. Garijo**, J. Martínez, J.M. García-Aznar, M.A. Pérez. Different mathematical techniques to estimate femur loads. Oral presentation. *Second meeting of the Spanish National Chapter of the European Society of Biomechanics (CapESB-SP)*. SEVILLA (SPAIN). October 2012

4. **N.Garijo**, M.J. Gómez-Benito, M. Remacha, M.A. Pérez, J.M. García-Aznar. CAD-BONE: analysis and design of our bones. Oral presentation. *Congress: Researchers' Night 2012*. ZARAGOZA (SPAIN). September 2012

5. **N. Garijo**, J. Martínez, J.M. García-Aznar, M.A. Pérez. Different numerical approaches for the prediction of proximal femur loads. Oral presentation. 19^{th} *Congress of the European Society of Biomechanics (ESB)*. PATRAS (GREECE). August 2013

6. **N. Garijo**, J. Martínez, J.M. García-Aznar, M.A. Pérez. Different numerical approaches for the prediction of proximal femur loads. Oral presentation. *V International Conference on Computational Bioengineering (ICCB)*. LEUVEN (BELGIUM). September 2013

7. **N. Garijo**, S. Walscharts, M.A. Pérez, L. Vigneron, J.V. Sloten, G.H. van Lenthe, J.M. García-Aznar. Towards the creation of patient-specific bone remodeling models. Oral presentation. *V International Conference on Computational Bioengineering (ICCB)*. LEUVEN (BELGIUM). September 2013

8. **N. Garijo**, M.A. Pérez, J.M. García-Aznar. Bone remodeling simulations: challenges, problems and applications. Poster. 7^{th} *World Congress of Biomechanics (WCB)*. BOSTON (USA). July 2013

9. **N. Garijo**, A. Vahdati, G.H. van Lenthe, M.A. Pérez, J.M. García-Aznar. Numerical algorithms for Patient-specific predictions of proximal femoral loads. Oral presentation. 12^{th} *International Symposium on Computer Methods in Biomechanics and Biomedical Engineering (CMBBE)*. AMSTERDAM (NETHERLANDS). October 2014

10. **N. Garijo**, M.A. Pérez, J.M. García-Aznar. Stability of bone remodeling models. Oral presentation. 12^{th} *International Symposium on Computer Methods in Biomechanics and Biomedical Engineering (CMBBE)*. AMSTERDAM (NETHERLANDS). October 2014

11. **N. Garijo**, M.A. Pérez, J.M. García-Aznar. An efficient approach for the stability of bone remodeling models. Oral presentation. 21^{th} *Congress of the European Society of Biomechanics (ESB)*. PRAGUE (CZECH REPUBLIC). July 2015

7.4 Future lines of work

The variety of approaches presented in this Thesis is only a small contribution to the understanding of bone adaptive behavior. Results and conclusions obtained throughout this work raise new questions and suggest possible lines of research that need to be explored. The most important can be listed as follows:

- Probabilistic analysis of the bone remodeling model.

  Improve bone remodeling models changing the "theoretical" variables as dead zone, to reproduce more accurately the bone density. And compare these variables with experiments. Additionally, apply previously developed (Enns-Bray et al., 2014) probabilistic techniques that could help in the creation of more realistic bone remodeling models

- Bone remodeling after prosthesis implantation.

  Apply previous improved bone remodeling models to study and predict the bone density evolution after a prosthesis implantation. Previous models present some problems for studying the effect of a prosthesis implantation in the long term. The methodology proposed allow to study the density in the long-term, as well as the density loss in different regions. This can help to improve the design and positioning of the prosthesis.

- Improve the ANN methodology.

  Obtain a patient-specific database for increasing the ANN methodology based on clinical cases, that allow to improve the prediction.

  Improve the methodology allowing feedback with new data.

  Introduce new variables in the ANN techniques as age, weight, sex, ... for obtaining a best prediction of the load and apply this methodology in other long bones.

Extrapolate methods in order to accelerate the bone remodeling simulations and obtain the load prediction in short time.

Study the anisotropy from image analysis for improve the comparison with computational results and decrease the error value in the predictive methodology.

Appendix A

The learning paradigm

A.1 Machine Learning Techniques (MLT)

Machine learning is a type of artificial intelligence that provides computers with the ability to learn without being explicitly programmed. Machine learning focuses on the development of computer programs that can teach themselves to grow and change when exposed to new data (Michie et al., 1994). The main idea of the machine learning is that it is possible to gain knowledge starting from experience or data (i.e. a collection of objects) without understanding the internal mechanism that has generated such data. Knowledge gained through learning partly consists of descriptions of what we have already observed, and is partly obtained by making inferences from (past) data in order to predict (future) outcomes.

Machine learning tasks are typically classified into these broad categories, depending on the nature of the learning "signal" or "feedback" available to a learning system (Vapnik, 1998; Martínez et al., 2011):

- Supervised Learning: Input data is called training data and has a known label or result. A model is prepared through a training process where it is required to make predictions and is corrected when those predictions are wrong. The training process continues until the model achieves a desired level of accuracy on the training data. Example problems are classification and regression. Example algorithms include Logistic Regression and the Back Propagation Neural Network.

- Unsupervised Learning Algorithms: Input data is not labelled and does not have a known result. A model is prepared by deducing structures present in the input data. This may be used to extract general rules. It may be used through a mathematical process to systematically reduce redundancy, or it may be used to organize data by similarity. Example problems are

clustering, dimensionality reduction and association rule learning. Example algorithms include: the Apriori algorithm and k-Means.

- Semi-Supervised Learning: Input data is a mixture of labeled and unlabeled examples. There is a desired prediction problem but the model must learn the structures to organize the data as well as make predictions. Example problems are classification and regression. Example algorithms are extensions to other flexible methods that make assumptions about how to model the unlabeled data.

- Reinforcement: It attempts to learn from interaction, receiving feedback for its actions. Every action has some impact in the environment, and the environment provides feedback in the form of rewards or punishments that guides the learning algorithm.

Accordingly to the learning processes classification presented above, all the machine learning models presented in this Thesis are based on supervised learning algorithms. Because of this reason, the theory of two supervised learning algorithms, Artificial Neuronal Network (ANN) and Support Vector Machines (SVM) are presented here in detail.

A.1.1 Artificial Neural Network (ANN)

Artificial Neural Networks (ANNs) are mathematical models inspired by the structure and functional aspects of biological neural networks (McCulloch and Pitts, 1990). The human brain consists of around 10^{11} nerve cells called neurons (see Figure A.1). The neurons are interconnected at points called synapses. The complexity of the brain is due to the massive number of highly interconnected simple units working in parallel, with an individual neuron receiving input from up to 10000 others. Structurally the neuron can be divided in three major parts: the cell body (soma) where is the nucleus; the dentrites and the axon. The nucleus, where the main processes take place, can be treated as the computational center of a neuron. Axons are fibers acting as transmission lines that send activation to other neurons (output duct). And dentrites are the tree-like structure that receives the signal from surrounding neurons, where each line is connected to one neuron. One neuron can have many dendrites but only one axon. Connections between neurons are called synapses and their quantity in a human brain is greater than 10^{14}. A neuron receives electrical impulses through its dendrites and sends them to the next neurons using axon. An axon is split into many branches ending with synapses. Synapses change power of received signal before the next neuron will receive it (Figure A.1).

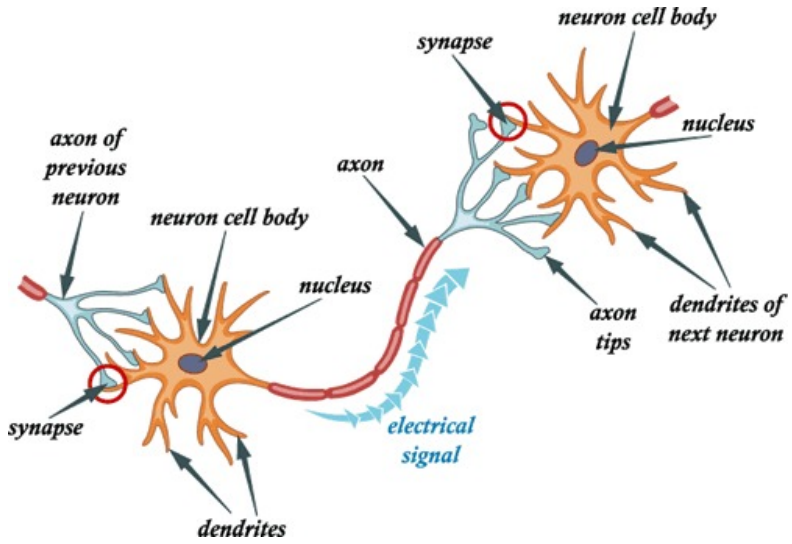

Figure A.1: *Model of a biological neuron. A signal is sent along the axon and through the synapse is transferred to dendrites of the other neuron (Carreon, 2012).*

Changing the strengths of synapse effects is assumed to be a crucial part of learning process and that property is exploited in models of a human brain in its artificial equivalent (Minsky and Papert, 1969; Bishop, 1995). However, the structure of an artificial neuron consists of two modules: summation module $\sum$ and activation module F. Roughly the summation module corresponds to biological nucleus. The algebra summation of weighted input signals is realized and the output signal is generated. Furthermore, output signal can be calculated using the following formula:

$$\varphi = \sum_{i=1}^{n} w_i x_i = \mathbf{w}^t \mathbf{x} \tag{A.1}$$

where $\mathbf{w}$ is the vector of weights (synapses equivalent), $\mathbf{x}$ the vector of input signals (dendrites equivalent), n the number of inputs. Signal φ is processed by the activation module F, which can be specified by different functions according to needs (Rumelhart et al., 1994).

Additionally, information capacity and processing ability of a single neuron is relatively small. However, it can be raised by the appropriate connection of many neurons. In 1958 the first ANN prototype, called perceptron, was developed by Rosenblatt (1958). It was used for alphanumerical character recognition. Although the perceptron initially seemed promising, the results were not satisfactory due to problems when characters were more complex or the scale was changed,

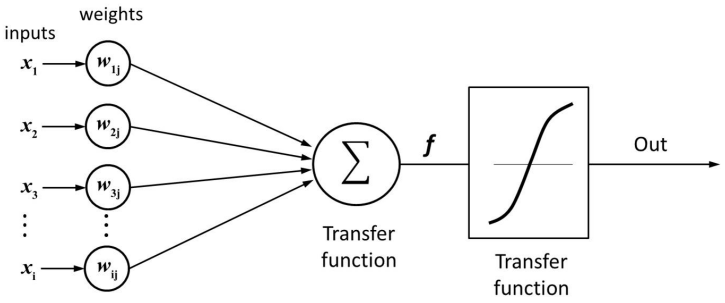

Figure A.2: *Model of an artificial neuron. In this neuron, the weighted sum of the inputs is transformed by the activation function to give the final output.*

however it can be considered successfully as the first system built, which simulated a neural network (Rosenblatt, 1958). An artificial network consists of simple processing units which communicate by sending signals to each other over a large number of weighted connections (Anthony and Bartlett, 1999).

Summarizing, an ANN model basically consists of two basic elements:

- A structure consisting in a set of basic units, called neurons, organized in different layers.
- A training algorithm for calibrating the network weights and other parameters as a function of deviations of the outputs provided by the network and the actual values.

Concerning this layered structure, its should be remarked that neurons in the multilayer ANN are grouped into three different types of layers: input, output, and hidden layer (see Figure A.3). There can be one or more hidden layers in the network but only one output and one input layer. The number of neurons in the input layer is specified by the number of data attributes. The number of output neurons corresponds to the type of answer of the network. The amount of hidden layers and their neurons is more difficult to determine (Minsky and Papert, 1969; Bishop, 1995). A network with one hidden layer suffices to solve most tasks. Each unit consists of the following neuronal components,

- A set of input connections, along with a set of weights that regulate the input signals intensity.
- The activation threshold, which is subtracted from the aggregation of the input signals transmitted.
- An activation function which focuses on the input signals.

- The output of the neuron as a function of the input signals, called transfer function.

This mentioned structure is often called the network architecture, being able to make a classification of the networks as a function of the number of networks layers, the interconnection degree of the structure or according to the character of the connections.

With regards to the architecture, two types of a multilayer ANNs can be distinguished: feed-forward and feed-back networks. In the feed-forward networks signal can move in one direction only and can not move between neurons in the same layer (see Figure A.3.a). Such networks can be used in the pattern recognition. Feed-back networks are more complicated, because a signal can be sent back to the input of the same layer with a changed value. Signals can move in these loops until the proper state is achieved. These networks are also called interactive or recurrent networks (see Figure A.3.b).

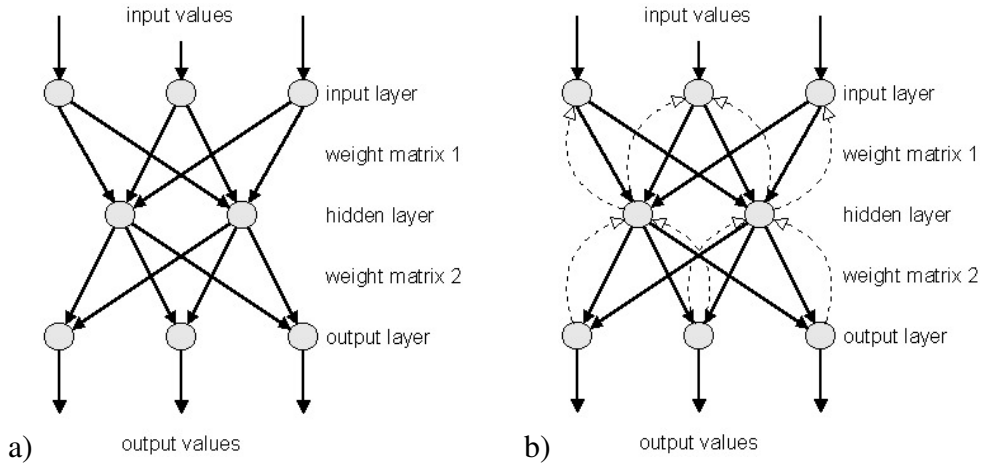

Figure A.3: *Multi-layer neural networks architecture: a) Feed-forward network: From the neurons in the input layer signals are propagated to the hidden layer and then finally to the output layer. b) Feed-back network: A signal can be returned to the same layer to adjust the proper state (Fröhlich, 1997).*

A.1.2 The Back-Propagation Algorithm

This basic supervised learning algorithm for multilayered feed-forward networks gives a recipe for changing the weights of the elements in neighbouring layers.

In order to train a neural network to perform some task, we must adjust the weights of each unit in such a way that the error between the desired output and the actual output is reduced. This process requires that the neural network compute

the error derivative of the weights (EW). In other words, it must calculate how the error changes as each weight is increased or decreased slightly. The back propagation algorithm is the most widely used method for determining the EW.

The back-propagation algorithm is easiest to understand if all the units in the network are linear. The algorithm computes each EW by first computing the EA, the rate at which the error changes as the activity level of a unit is changed. For output units, the EA is simply the difference between the actual and the desired output. To compute the EA for a hidden unit in the layer just before the output layer, we first identify all the weights between that hidden unit and the output units to which it is connected. We then multiply those weights by the EAs of those output units and add the products. This sum equals the EA for the chosen hidden unit. After calculating all the EAs in the hidden layer just before the output layer, we can compute in like fashion the EAs for other layers, moving from layer to layer in a direction opposite to the way activities propagate through the network. This is what gives back propagation its name. Once the EA has been computed for a unit, it is straight forward to compute the EW for each incoming connection of the unit. The EW is the product of the EA and the activity through the incoming connection.

However, as regards the training algorithm, it should be noted that one of the best-known learning algorithms is the back-propagation algorithm (Bishop, 1995). Backpropagation, an abbreviation for "backward propagation of error", is a common method of training artificial neural networks used in conjunction with an optimization method such as gradient descent. It was developed by Werbos (1974) and rediscovered independently by Parker (1985) and Rumelhart et al. (1986). The method calculates the gradient of a loss function with respect to all the weights in the network. The gradient is fed to the optimization method which in turn uses it to update the weights, in an attempt to minimize the loss function.

In outline, the algorithm is as follows:

- Initialization: the weights of the network are initialized to small random values.
- Forward pass: The inputs of each training pattern are presented to the network. The outputs are computed using the inputs and the current weights of the network. Certain statistics are kept from this computation, and used in the next phase. The target outputs from each training pattern are compared with the actual activation levels of the output units - the difference between the two is termed the error. Training may be pattern-by-pattern or epoch-by-epoch. With pattern-by-pattern training, the pattern error is provided directly to the backward pass. With epoch-by-epoch training, the pattern errors are summed across all training patterns, and the total error is provided to the backward pass.

- Backward pass: In this phase, the weights of the net are updated.

- Go back to step 2. Continue doing forward and backward passes until the stopping criterion is satisfied.

- Error backpropagation learning is often familiarly referred to just as back-prop.

The back propagation algorithm is an involved mathematical tool; however, execution of the training equations is based on iterative processes, and thus is easily implementable on a computer. Despite of the fact that back-propagation algorithm is an ill-conditioned optimization problem (Erikssont et al., 1998), thanks to specific way of the errors propagation, this algorithm has become one of the most effective learning algorithms (Minsky and Papert, 1969; Bishop, 1995).

Moreover, the activation and transfer functions can have many forms (Figure A.4). In the original work on perceptrons (McCulloch and Pitts, 1990; Rosenblatt, 1958) which generally had no hidden layers, the activation functions were a simple linear function and a threshold function. The functions can be classified into three:

- Linear (straight-line) functions are limited because the output is simply proportional to the input. Linear functions are not very useful. That was the problem in the earliest network models as noted in (Minsky and Papert, 1969). The transfer function could be something as simple as depending upon whether the result of the summation function is positive or negative. The network could output zero and one, one and minus one, or other numeric combinations.

- Another type of transfer function, the threshold or ramping function (Saturating linear transfer function), could mirror the input within a given range and still act as a hard limiter outside that range. It is a linear function that has been clipped to minimum and maximum values, making it non-linear (Figure A.4-Satlin and Satlins Transfer Function).

- Another option would be a sigmoid or S-shaped curve. That curve approaches a minimum and maximum value at the asymptotes. It is common for this curve to be called a sigmoid when it ranges between 0 and 1 (Figure A.4 - Log-Sigmoid Transfer Function), and a hyperbolic tangent when it ranges between -1 and 1 (Figure A.4 - Tan-Sigmoid Transfer Function). Mathematically, the exciting feature of these curves is that both the function and its derivatives are continuous. This option works fairly well and is often the transfer function of choice.

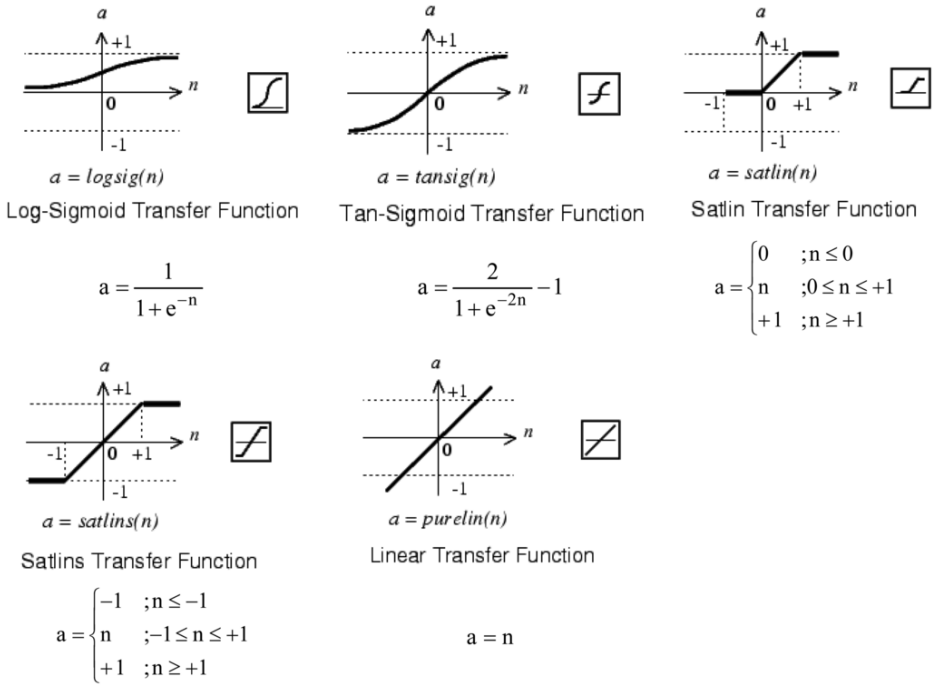

Figure A.4: *Activation and transfer type functions (Pérez-Suárez et al., 2013).*

This Thesis is focused on feed-forward network structures with specific activation functions and weights. The ANN mathematical model defined in Chapter c3 is based on this structure. Moreover, the back-propagation algorithm has been chosen to be implemented in this methodology proposed.

Within the feed-forward network structure, the network implements a function $f : \mathcal{X} \subset \mathbb{R}^n \rightarrow \mathcal{Y} \subset \mathbb{R}^k$ where n is the input space dimension and k is the output space dimension. The functions implemented by a network feed-forward can be formulated by the following general model

$$\begin{aligned} f(\mathbf{x}) = \varphi(\psi(\mathbf{x})) = (\varphi \circ \psi)(\mathbf{x}) \\ \psi\colon \mathcal{X} \subset \mathbb{R}^n \rightarrow \mathcal{U} \subset \mathbb{R}^m \\ \varphi\colon \mathcal{U} \subset \mathbb{R}^m \rightarrow \mathcal{Y} \subset \mathbb{R}^k \end{aligned} \tag{A.2}$$

where $\mathcal{U}$ is the hidden variables space with dimension m (number of neurons of this layer), and it is called feature space. And, based on the architecture defined above for the case of MLP (Bishop, 1995):

1. $\psi_j(\mathbf{x}) = \psi(\mathbf{w}_j^t \mathbf{x} + w_{j0})$ being ψ the hidden layer activation function, $w_j \in \mathbb{R}^n$ the parameter vector of the hidden layer and $w_{j0} \in \mathbb{R}$ its threshold value. The function ψ can be a sigmoid, a logistic or a hyperbolic tangent.

2. $\varphi_j(\mathbf{u}) = \varphi(\mathbf{c}_j^t\mathbf{u} + c_{j0})$ being φ the output layer activation function, $c_j \in \mathbb{R}^m$ the weights and $c_{j0} \in \mathbb{R}$ its threshold value. The activation function φ can be the identity function, threshold function or any bilateral function.

The process of training the ANN consists in changing the weights assigned to connections of neurons until the achieved result is satisfactory. ANN is considered to have learned when computed errors are minimized. For completeness, the steps which should be carried out in order to teach an ANN using feed-forward structure for each pattern in the learning set are described below (Mangan and Alon, 2003). The complex mathematical background of these techniques has been already described for many authors, however it has been here introduced for completeness Mitchell et al. (1997), Vidyasagar (1997), Anthony and Bartlett (1999).

1. Insert the learning vector $\mathbf{u}^{\mu_P}$ as an input to the network, being μ_P the index of actual learning patterns, $\mu_P = 1, ..., P$, and P the number of learning patterns.

2. Evaluate the output values $\mathbf{u}_j^{m\mu_P}$ of each element for all layers using the formula

$$u_j^{m\mu_P} = f(\varphi_j^{m\mu_P}) = f(\sum_{i=0}^{n_{m-1}} w_{ji}^m u_i^{(m-1)\mu_P}), \tag{A.3}$$

where m is the index of actual layer, $m = 1, ..., M$ and M the number of layers without including the input layer. j is the index of actual element, $j = 1, ..., n_m$ and n_m the number of elements or neurons in layer m. $\varphi_j^{\mu_P}$ is the weighted sum of input values for element j in layer μ_P, f the activation function, w_{ji}^m the weight between element j in layer m and element i in layer $m-1$ and $u_i^{(m-1)\mu_P}$ is the output of element i in layer $m-1$ for pattern μ_P.

3. Evaluate error values $\pi_j^{M\mu_P}$ for the output layer using the formula

$$\pi_j^{M\mu_P} = f'(\varphi_j^{M\mu_P})\pi_j^{\mu_P} = f'(\varphi_j^{M\mu_P})(\widehat{y}_j^{\mu_P} - y_j^{\mu_P}), \tag{A.4}$$

where $\pi_j^{M\mu_P}$ is learning error for element j for pattern μ_P, $\widehat{y}_j^{\mu_P}$ the expected network output value for element j for pattern μ_P and $y_j^{\mu_P}$ the actual network output value for element j for pattern μ_P,

4. Evaluate sum of squares errors ε_{μ_P} from

$$\varepsilon_{\mu_P} = \frac{1}{2}\sum_{j=1}^{n}(\pi_j^{\mu_P})^2. \tag{A.5}$$

5. Carry out the back propagation of output layer error $\pi_j^{M\mu_P}$ to all elements of hidden layers calculating their errors $\pi_j^{m\mu_P}$ from

$$\pi_j^{m\mu_P} = f'(\varphi_j^{m\mu_P}) \sum_{l=1}^{n_{m+1}} \pi_l^{(m+1)\mu_P} w_{lj}^{(m+1)}. \tag{A.6}$$

6. Update the weights of all elements between output and hidden layers and then between all hidden layers moving towards the input layer. Changes of the weights can be obtained from

$$\Delta_{\mu_P} w_{ji}^m = \eta \pi_l^{m\mu} u_i^{(m-1)\mu_P}, \tag{A.7}$$

where $\Delta_{\mu_P} w_{ji}^m$ is the change of given weight for pattern μ_P and η the proportion coefficient.

Above steps have to be repeated until satisfactory minimum of complete error function is achieved:

$$\varepsilon = \sum_{\mu_P=1}^{P} \varepsilon_{\mu_P} = \frac{1}{2} \sum_{\mu_P=1}^{P} \sum_{j=1}^{n} (\widetilde{y}_j^{\mu_P} - \varphi_j^{\mu_P})^2 \tag{A.8}$$

Every iteration of these instructions is called epoch. After the learning process is finished another set of patterns can be used to verify the knowledge of the ANN. For complicated networks and large sets of patterns the learning procedure can take a lot of time. Usually it is necessary to repeat the learning process many times with different coefficients selected by trial and error. Furthermore, there is a variety of optimization methods which can be used to accelerate the learning process such as the momentum technique (Moreira and Fiesler, 1995).

The advantages of neural networks are quite relevant, in particular a list of advantages might be made for feed-forward ANN (Tu, 1996):

- Feed forward neural networks have a fixed computation time.
- Computation speed is very high, as a result of the parallel structure.
- Fault tolerant, because of distributed nature of network knowledge.
- Learns general solutions of presented training data.
- Ability to generalize to situations not taught to network previously.
- Neural networks eliminate the need to develop an explicit model of a process.

- It does not use preprogrammed knowledge base.
- It suits to analyze complex patterns.
- It has no restrictive assumptions.
- It allows for qualitative data.
- It can handle noisy data and incomplete data, the solution will just be less precise. Besides, neural networks can model parts of a process that cannot be modeled or are unidentified.
- It can overcome autocorrelation.
- It is user-friendly, clear output, robust and flexible.

However, like any technique, ANNs have certain drawbacks as:

- It requires high quality data.
- The variables must be carefully selected a priori.
- There is a risk of overfitting.
- It requires a definition of architecture.
- It takes high computational cost.
- Neural networks errors vary, depending upon the architecture.
- It require lengthy training times.

A.1.3 Support Vector Machine (SVM)

Vapnik (1982) is considered the pioneer in introducing the concept of optimum separating hyperplane of a sample of data in a classification or regression problem, which is the core of the SVM. The SVM original algorithm was invented by Vapnik (1982), however the current standard approach (soft margin) was proposed by Vapnik (1995). The essence of SVM method is the construction of optimal hyperplane, which can separate data from opposite classes using the maximum margin. Margin is a distance between optimal hyperplane and a vector which lies closest to it (Boser et al., 1992; Vapnik, 1982, 1995, 1998).

Different historical facts could be highlighted in the development of SVM techniques:

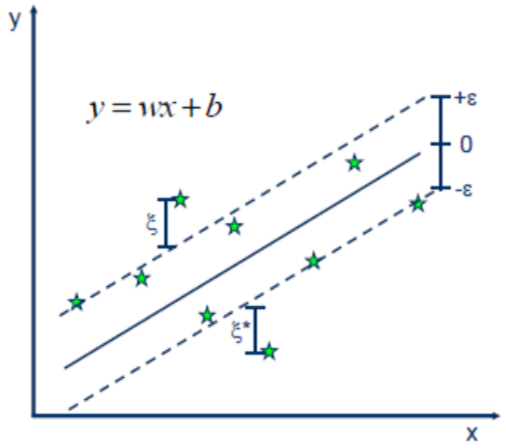

Figure A.5: *Schematic diagram of the architecture of a typical Support Vector Machine (SVM) (Sayad, 2010).*

1. The feature space generation from input space by the transformation $f : \mathcal{X} \subset \mathbb{R}^n \rightarrow \mathcal{Z} \subset \mathbb{R}^g$ with $g \geq n$ (can be ∞). By the reverse transformation, the linear boundaries of the separating hyperplanes in the feature space result in non-linear boundaries in the input space. This transformation is called "Kernel Trick" (Boser et al., 1992).

2. The appearance of soft-margin algorithm for problems where perfect separability is not reachable (problems with noise in the sample data).

3. The SVM generalization to regression problems by way of Vapnik's ε-insensitive loss function (Drucker et al., 1997).

An example of such hyperplane is illustrated in Figure A.5, where for a linearly separable set of 2D points which belong to one of two classes, a separating straight line is needed. In Figure A.5, there exists multiple lines that offer a solution for the problem. However, a line can be bad if it passes too close to the points because it will be noise sensitive and it will not generalize correctly. Therefore, the SVM should be able to find the line passing as far as possible from all points. Then, the operation of the SVM algorithm is based on finding the hyperplane that gives the largest minimum distance to the training examples. This distance receives the name of margin within theory of SVM. Therefore, the optimal separating hyperplane maximizes the margin of the training data.

Further, optimal hyperplane should satisfy

$$\frac{y_n f(x_n)}{\|\mathbf{w}\|} \leq \tau_m \tag{A.9}$$

where $\mathbf{w}$ is the normal vector to the hyperplane, τ_m is a margin and $f(\mathbf{x})$ is defined as:

$$f(\mathbf{x}) = \mathbf{w}^t\mathbf{x} + \beta_0 \tag{A.10}$$

where the parameter β_0 determines the offset of the hyperplane from the origin along the normal vector $\mathbf{w}$. And this function is not suitable for solving more complicated linearly non-separable problems.

Possibility of occurrence of the linearly non-separability in the input space is the main cause why the idea of SVM is not optimal for hyperplane construction in the input space but rather in high dimensional so called feature space ($\mathcal{Z}$). The feature space is usually defined as a non-linear product of base functions $\phi(\mathbf{x})$, defined in the input space. The solution can be expressed as a linear combination of the training vectors β_i. And, given a new point $\mathbf{x}_i$ to classify or regress, the solution is obtained by means of the inner product with the sample points $\mathbf{x}$. Thus, the function of the optimal hyperplane is now:

$$f(\mathbf{x}) = \sum_{i=1}^{n} \beta_i K(\mathbf{x}_i, \mathbf{x}) + \beta_0 \tag{A.11}$$

where $K(\mathbf{x}_i, \mathbf{x})$ is the inner product kernel of the base functions $\phi(\mathbf{x})$. Inner product may be defined as:

$$K(\mathbf{x}, \mathbf{x}') = \langle \phi(\mathbf{x}), \phi(\mathbf{x}') \rangle \tag{A.12}$$

We are now looking for solution in other space, but the problem is linearly separable, so it is more effective, even if the problem was linearly non-separable in the input space (see Figure A.6). It is known as Kernel trick (Boser et al., 1992).

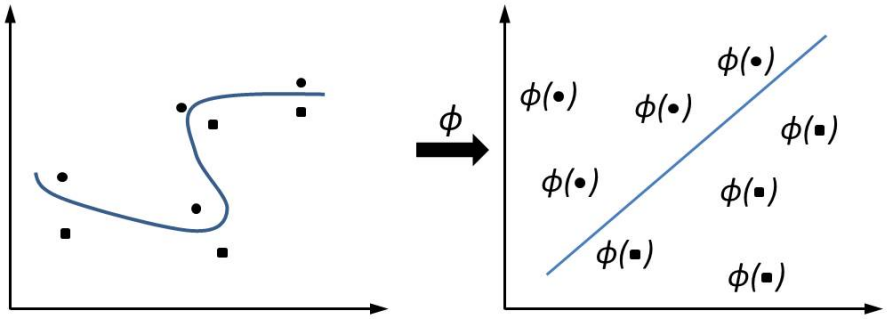

Figure A.6: *Transformation of input space into feature space.*

The kernel function can have many different forms. Some of the commonly used functions are: linear, polynomial or sigmoidal (see Figure A.4). Choosing the most appropriate kernel highly depends on the problem at hand, and fine tuning its parameters can easily become a tedious and cumbersome task. Automatic kernel selection is possible and is discussed in the works by Howley and Madden (2006). The choice of a Kernel depends on the specific problem which is going to be solved because it depends on what we are trying to model. The motivation behind the choice of a particular kernel can be very intuitive and straightforward depending on what kind of information we are expecting to extract about the data. Consequently, different elections of this kernel function will provide better or worse performance of the SVM. But generally, the linear and the polynomial kernel functions are used in problems without high nonlinearity, the radial basis functions allows picking out circles (or hyperspheres), and finally the sigmoid kernel functions are indicated for problems with high nonlinearity.

Therefore, the optimum hyperplane problem is obtained by means of the following constrained problem:

$$\begin{gathered} \max_{\mathbf{w},\beta_0} \left\{ \min_{i\in\{1:n\}} |\langle \mathbf{w}, \mathbf{x}\rangle + \beta_0| \right\} \\ \text{Subject to: } \|\mathbf{w}\| = 1 \end{gathered} \tag{A.13}$$

Or equivalently it can be also expressed as:

$$\begin{gathered} \min_{\mathbf{w},\beta_0} \frac{1}{2}\|\mathbf{w}\|^2 \\ \text{Subject to: } y_i(\langle \mathbf{w}, \mathbf{x}\rangle + \beta_0) \geq 1,\ i = 1, 2...n \end{gathered} \tag{A.14}$$

Then, this problem can now be solved by standard quadratic programming techniques and programs, and the Karush-Kuhn-Tucker condition are necessaries and sufficient (Vapnik, 1998).

And the solution, which can be obtained from the dual problem, is a linear combination of a subset of sample points denominated support vectors (SV) and it can be written as follows:

$$\begin{aligned} \mathbf{w} &= \sum_{i\in \text{sv}} \beta_i \phi(\mathbf{x_i}) \Rightarrow \\ f_{\mathbf{w},\beta_0}(\mathbf{x}) &= \sum_{i\in \text{sv}} \beta_i \langle \phi(\mathbf{x_i}), \phi(\mathbf{x})\rangle + \beta_0 = \sum_{i\in \text{sv}} \beta_i K(\mathbf{x}_i, \mathbf{x}) + \beta_0 \end{aligned} \tag{A.15}$$

Although SVM method is naturally adapted for separating or regretting data from two classes, it can be easily transformed into very useful tool for the classification of more than two classes.

Consequently, given a sample of data $\{(\mathbf{x}_i, y_i)\}_{i=1}^n$, the SVM regression problem (Drucker et al., 1997) can be formulated as follows:

$$\begin{min}_{\mathbf{w},\beta_0,\boldsymbol{\xi}} \frac{1}{2}\left\{\left\|\mathbf{w}^2\right\| + C\sum_{i=1}^{n}(\xi_i + \xi_i^{'})\right\}\end{min}$$
$$\left\{\begin{array}{c|c} \langle \mathbf{w}, \phi(\mathbf{x}_i)\rangle + \beta_0 - y_i \geq \epsilon + \xi_i & \\ y_i - (\langle \mathbf{w}, \phi(\mathbf{x}_i)\rangle + \beta_0) \geq \epsilon + \xi_i^{'} & i = 1, ..., n \\ \xi_i, \xi_i^{'} \geq 0 & \end{array}\right. \tag{A.16}$$

where $\xi_i, \xi_i^{'}$, are slack variables that ensure that the solution does not contain, within the band of radius ϵ, all the points $(\mathbf{x}_i, y_i)$ of the sample (thus avoiding possible outliers and overfitting), where C is the cost parameter and expresses the importance of the slack variables in each point, and where $\phi : \mathcal{X} \rightarrow \mathcal{Z}$ is a transformation of the input space into a new space $\mathcal{Z}$ usually of larger dimension, where we define an inner product by means of a positive definite function K (kernel).

Furthermore, it is possible to introduce the parameter ν_{SVM} in the SVM regression model (Nu-SVR) in order to control the number of support vectors determined (Schölkopf et al., 2000). Then, the SVM problem can be formulated as follows:

$$\begin{min}_{\mathbf{w},\beta_0,\boldsymbol{\xi}} \frac{1}{2}\left\{\left\|\mathbf{w}^2\right\| + C\left(\nu_{SVM}\epsilon + \frac{1}{n}\sum_{i=1}^{n}(\xi_i + \xi_i^{'})\right)\right\}\end{min}$$
$$\left\{\begin{array}{c|c} \langle \mathbf{w}, \phi(\mathbf{x}_i)\rangle + \beta_0 - y_i \geq \epsilon + \xi_i & \\ y_i - (\langle \mathbf{w}, \phi(\mathbf{x}_i)\rangle + \beta_0) \geq \epsilon + \xi_i^{'} & i = 1, ..., n \\ \xi_i, \xi_i^{'} \geq 0 & \end{array}\right. \tag{A.17}$$

where ν_{SVM} $(0 \leq \nu_{SVM} \leq 1)$ represents the upper bound on the function of margin errors in the training set and establishes the lower bound on the fraction of support vectors.

Obviously, all learning techniques have advantages and disadvantages, which are more or less important according to the data which are being analysed, and thus have a relative relevance. The advantages of the SVM technique could be summarized as follows:

- By introducing the kernel, SVM gain flexibility in the choice of the form of the threshold separating plane, which needs not be linear and even needs not have the same functional form for all data, since its function is non-parametric and operates locally.

- Because of the fact that the kernel implicitly contains a nonlinear transformation, no assumptions about the functional form of the transformation,

which makes data linearly separable, are necessary. Thus, the transformation occurs implicitly on a robust theoretical basis and human expertise judgement beforehand is not needed.

- SVM provide a good out of sample generalization.
- SVM deliver a unique solution, since the optimality problem is convex. This is an advantage compared to ANN, which have multiple solutions associated with local minimum, and for this reason may not be robust over different samples.
- SVM classifier or regressor depends only on the support vectors, and the classifier or regressor function is not influenced by the whole data set, as it is the case for many ANN systems.
- With the choice of an appropriate kernel and parameters, SVM are faster than ANN in training. SVM uses a subset of training points in the decision function called support vectors, so it is also memory efficient.
- Effective in high dimensional spaces.
- High computational efficiency.

In contrast, the main disadvantages of this technique are:

- A common disadvantage of non parametric techniques such as SVM is the lack of transparency of results. The parameters can not inform us of the importance of each independent variable since its dimension may be very high. In addition, high dimensionality of data can represent another limitation for SVM techniques.
- We need to select an appropriate kernel and its parameters. This is the same situation as that of ANN where we need to set the number of hidden units, initial values of weights, and so on.
- If the number of features is much greater than the number of samples, the method is likely to give poor performance.

Bibliography

Ambrósio, J. A., Kecskeméthy, A., 2007. Multibody dynamics of biomechanical models for human motion via optimization. Vol. 4. Springer Netherlands, pp. 245–272.

Anthony, M., Bartlett, P. L., 1999. Neural network learning: Theoretical foundation. Cambridge University Press.

Asseln, M., Al Hares, G., Eschweiler, J., Radermacher, K., 2014. Development of a patient-specific musculoskeletal model of the knee for clinical application and kinematic validation based on in-vivo measurements. J Bone Joint Surg Am 96-B (SUPP 16), 20.

Bao, C. L. M., Teo, E. Y., Chong, M. S., Liu, Y., Choolani, M., Chan, J. K., 2013. Regenerative Medicine and Tissue Engineering. ISBN.

Barboteu, M., Fernández, J., Hoarau-Mantel, T., 2005. A class of evolutionary variational inequalities with applications in viscoelasticity. Math Models Methods Appl Sci. 15(10), 1595–1617.

Baxt, W., 1995. Application of artificial neural networks to clinical medicine. The Lancet 346 (8983), 1135 – 1138.

Beaupré, G. S., Orr, T. E., Carter, D. R., 1990. An approach for time-dependent bone modeling and remodeling - theoretical development. J Orthop Res 8 (5), 651–661.

Behrens, B., Nolte, I., Wefstaedt, P., Stukenborg-Colsman, C., Bouguecha, A., 2009. Numerical investigations on the strain-adaptive bone remodelling in the periprosthetic femur: Influence of the boundary conditions. Biomed Eng Online 8 (7).

Bergmann, G., Deuretzbacher, G., Heller, M., Graichen, F., Rohlmann, A., Strauss, J., Duda, G. N., 2001. Hip contact forces and gait patterns from routine activities. J Biomech. 34 (7), 859–871.

Bishop, C., 1995. Neuronal networks and pattern recognition. Oxford University Press.

Bitsakos, C., Kerner, J., Fisher, I., Amis, A. A., 2005. The effect of muscle loading on the simulation of bone remodelling in the proximal femur. J Biomech. 38 (1), 133–139.

Bona, M. A., Martin, L. D., Fischer, K. J., 2003. Joint load estimation based on bone density and a contact model applied to the proximal femur of a chimp. Summer Bioengineering Conference, 25–29.

Bona, M. A., Martin, L. D., Fischer, K. J., 2006. Density-based load estimation using two-dimensional finite element models: a parametric study. Comput Methods Biomech Biomed Engin 9 (4), 221–9.

Boser, B. E., Guyon, I. M., Vapnik, V. N., 1992. A Training Algorithm for Optimal Margin Classifiers. ACM Press, Pittsburgh, PA, USA.

Brand, R., Crowninshield, R. D., Wittstock, C., Pedersen, D., Clark, C., van Krieken, F., 1982. A model of lower extremity muscular anatomy. ASME. J Biomech Eng. 104 (4), 304–310.

Butt, L., Zuccon, G., Nguyen, A., Bergheim, A., Grayson, N., 2013. Classification of cancer-related death certificates using machine learning. Australas Med J 8 (6), 292–299.

Campo, M., Fernández, J., Kuttler, K., Shillor, M., 2007. Quasistatic evolution of damage in an elastic body: numerical analysis and computational experiments. Appl Numer Math. 57 (9), 975–988.

Campo, M., Fernández, J., Kuttler, K., Shillor, M., no, J. V., 2006. Numerical analysis and simulations of a dynamic frictionless contact problem with damage. Comput Methods Appl Mech Engrg. 196, 476–488.

Campoli, G., Bolsterlee, B., van der Helm, F., Weinans, H., Zadpoor, A. A., 2014. Effects of densitometry, material mapping and load estimation uncertainties on the accuracy of patient-specific finite-element models of the scapula. J R Soc Interface. 11 (93), 20131146.

Campoli, G., Weinans, H., Zadpoor, A. A., 2012. Computational load estimation of the femur. J Mech Behav Biomed Mater. 10, 108–19.

Caouette, C., Bureau, M. N., Vendittoli, P. A., Lavigne, M., Nuno, N., 2012. Anisotropic bone remodeling of a biomimetic metal-on-metal hip resurfacing implant. Med Eng Phys 34 (5), 559–565.

Caouette, C., Bureau, M. N., Vendittoli, P. A., Lavigne, M., Nuno, N., 2015. Influence of the stem fixation scenario on load transfer in a hip resurfacing arthroplasty with a biomimetic stem. J Mech Behav Biomed Mater 45, 90–100.

Carbone, V., Fluit, R., Pellikaan, P., van der Krogt, M. M., Janssen, D., Damsgaard, M., Vigneron, L., Feilkas, T., Koopman, H. F. J. M., Verdonschot, N., 2015. TLEM 2.0 - a comprehensive musculoskeletal geometry dataset for subject-specific modeling of lower extremity. J Biomech 48 (5), 734–741.

Carbone, V., van der Krogt, M. M., Koopman, H. F. J. M., Verdonschot, N., 2012. Sensitivity of subject-specific models to errors in musculo-skeletal geometry. J Biomech 45 (14), 2476–2480.

Carbonell, J., 1983. Learning by analogy: Formulating and generalizing plans from past experience. In: Michalski, R., Carbonell, J., Mitchell, T. (Eds.), Machine Learning. Symbolic Computation. Springer Berlin Heidelberg, pp. 137–161.

Carey, R. E., Zheng, L., Aiyangar, A. K., Harner, C. D., Zhang, X., 2014. Subject-specific finite element modeling of the tibiofemoral joint based on CT, magnetic resonance imaging and dynamic stereo-radiography data in vivo. J Biomech Eng 136 (4), 041004–041004.

Carreon, L., 2012. Electrical signals in animals. Biological Sciences - University of Texas-Brownsville. StudyBlue.

Carter, D., 1987. Mechanical loading history and skeletal biology. J Biomech. 20, 1095–1109.

Carter, D., Hayes, W., 1977. The behavior of bone as a two-phase porous structure. J Bone Jt Surg. 59-A, 954–962.

Carter, D. R., Beaupré, G. S., 2001. Skeletal function and form: Mechanobiology of skeletal development, aging, and regeneration., 1st Edition. No. 1. Cambridge University Press, Cambridge.

Carter, D. R., Orr, T. E., Fyhrie, D. P., 1989. Relationships between loading history and femoral cancellous bone architecture. J Biomech 22 (3), 231–244.

Chang, C., Lin, C., 2011. Libsvm: A library for support vector machines. ACM TIST 2 (3-27), 1–27.

Christen, P., van Rietbergen, B., Lambers, F. M., Mueller, R., Ito, K., 2012a. Bone morphology allows estimation of loading history in a murine model of bone adaptation. Biomech Model Mechanobiol. 11 (3-4), 483–492.

Christen, P., van Rietbergen, B., Lambers, F. M., Mueller, R., Ito, K., 2012b. Bone morphology allows estimation of loading history in a murine model of bone adaptation. Biomech Model Mechanobiol 11 (3-4), 483–492.

Cilla, M., Martínez, J., Peña, E., Martínez, M. A., 2012. Machine learning techniques as a helpful tool toward determination of plaque vulnerability. IEEE Trans Biomed Eng. 59 (4), 1155–1161.

Clement, P., 1975. Approximation by finite element functions using local regularization. Rairo Anal Numer. 9R2, 77–84.

Colloca, M., Blanchard, R., Hellmich, C., Ito, K., van Rietbergen, B., 2014. A multiscale analytical approach for bone remodeling simulations: Linking scales from collagen to trabeculae. Bone 64, 303 – 313.

Cos, F., García, P., Martínez, J., Taboada, J., 2010. Analysis of lead times of metallic components in the aerospace industry through a supported vector machine model. Math Comput Model. 52, 1177–1184.

Cowin, S. C., 1985. The relationship between the elasticity tensor and the fabric tensor. J Mech Mater. 4 (2), 137 – 147.

Cowin, S. C., 1986. Wolffs law of trabecular architecture at remodeling equilibrium. J Biomech Eng-T Asme 108 (1), 83–88.

Cowin, S. C., Cardoso, L., 2015. Blood and interstitial flow in the hierarchical pore space architecture of bone tissue. J Biomech 48 (5), 842 – 854.

Cowin, S. C., Doty, S. B., 2007. Tissue Mechanics. Vol. 1. Springer-Verlag New York.

Cowin, S. C., Hegedus, D. H., 1976. Bone remodeling .1. theory of adaptive elasticity. J Elast 6 (3), 313–326.

Cox, L., van Rietbergen, B., van Donkelaar, C., Ito, K., 2011. Analysis of bone architecture sensitivity for changes in mechanical loading, cellular activity, mechanotransduction, and tissue properties. Biomech Model Mechanobiol 10 (5), 701–712.

Dettmer, M., Pourmoghaddam, A., Kreuzer, S. W., 2015. Comparison of patient-reported outcome from neck-preserving, short-stem arthroplasty and resurfacing arthroplasty in younger osteoarthritis patients. J Advances in Orthopedics (817689), 7.

Doblaré, M., García, J. M., 2001. Application of an anisotropic bone-remodelling model based on a damage-repair theory to the analysis of the proximal femur before and after total hip replacement. J Biomech 34 (9), 1157–1170.

Doblaré, M., García, J. M., 2002. Anisotropic bone remodelling model based on a continuum damage-repair theory. J Biomech 35 (1), 1–17.

Doblaré, M., García, J. M., Gómez, M. J., 2004. Modelling bone tissue fracture and healing: a review. Eng Fract Mech 71 (13-14), 1809–1840.

Drucker, H., Burges, C., Kaufman, L., Smola, A., Vapnik, V., 1997. Support Vector Regression Machines. MA: MIT Press, Cambridge.

Enns-Bray, W. S., Owoc, J. S., Nishiyama, K. K., Boyd, S. K., 2014. Mapping anisotropy of the proximal femur for enhanced image based finite element analysis. J Biomech 47 (13), 3272 – 3278.

Erdemir, A., McLean, S., Herzog, W., van den Bogert, A. J., 2007. Model-based estimation of muscle forces exerted during movements. Clin Biomech 22 (2), 131 – 154.

Erikssont, J., Gulliksson, M., Lindström, P., Wedin, P., 1998. Regularization tools for training large feed-forward neural networks using automatic differentiation. Optim Methods Softw. 10 (1), 49–69.

Everts, V., Delaissé, J. M., Korper, W., Jansen, D. C., Tigchelaar-Gutter, W., Saftig, P., Beertsen, W., 2002. The bone lining cell: Its role in cleaning howship's lacunae and initiating bone formation. J Bone Miner Res 17 (1), 77–90.

Favre, J., Hayoz, M., Erhart-Hledik, J. C., Andriacchi, T. P., 2012. A neural network model to predict knee adduction moment during walking based on ground reaction force and anthropometric measurements. J Biomech. 45 (4), 692–698.

Fernandes, P., Rodrigues, H., Jacobs, C., 1999. A model of bone adaptation using a global optimisation criterion based on the trajectorial theory of wolff. Comput Methods Biomech Biomed Engin. 2 (2), 125–138.

Fernández, J., Figueiredo, I., Martínez, R., 2008. A convergence result in the study of bone remodeling contact problems. J Math Anal Appl. 343 (2), 951 – 964.

Fernández, J. R., García-Aznar, J. M., Martínez, R., 2012a. Numerical analysis of a diffusive strain-adaptive bone remodelling theory. Int J Solids Struct 49 (15-16), 2085–2093.

Fernández, J. R., García-Aznar, J. M., Martínez, R., 2012b. Piezoelectricity could predict sites of formation/resorption in bone remodelling and modelling. J Theor Biol. 292, 86–92.

Fernández, J. R., García-Aznar, J. M., Martínez, R., no, J. M. V., 2010. Numerical analysis of a strain-adaptive bone remodelling problem. Comput Methods Appl Mech Engrg. (199), 1549–1557.

Ferrante, S., Pedrocchi, A., Ianno, M., Momi, E. D., Ferrarin, M., Ferrigno, G., 2004. Functional electrical stimulation controlled by artificial neural networks pilot experiments with simple movements are promising for rehabilitation applications. Funct Neurol 19 (4), 243–252.

Fischer, K., Bastidas, J., Pfaeffle, H., Towers, J., 2003. A method for estimating relative bone loads from CT data with application to the radius and the ulna. CMES-Comp Model Eng 4, 397–403.

Fischer, K., Jacobs, C., Levenston, M., Cody, D., Carter, D., 1998. Bone load estimation for the proximal femur using single energy quantitative CT data. Comput Methods Biomech Biomed Engin. (1), 233–245.

Fischer, K., Jacobs, C., Levenston, M., Cody, D., Carter, D., 1999. Proximal femoral density patterns are consistent with bicentric joint loads. Comput Methods Biomech Biomed Engin. (2), 271–283.

Fischer, K. J., Jacobs, C. R., Carter, D. R., 1995. Computational method for determination of bone and joint loads using bone density distributions. J Biomech. 28 (9), 1127–1135.

Fluit, R., Andersen, M. S., Kolk, S., Verdonschot, N., Koopman, H. F. J. M., 2014. Prediction of ground reaction forces and moments during various activities of daily living. J Biomech 47 (10), 2321–2329.

Fluit, R., van der Krogt, M. M., van der Kooij, H., Verdonschot, N., Koopman, H. F. J. M., 2012. A simple controller for the prediction of three-dimensional gait. J Biomech 45 (15), 2610–2617.

Folgado, J., Fernandes, P., Rodrigues, H., 2008. Computational study on bone remodeling and osseointegration for a hip replacement using a conservative femoral stem. Int J Comput Vis Biomech 1, 97–106.

Franco, L., Cannas, S. A., 2000. Generalization and selection of examples in feedforward neural networks. Neural Comput. 12 (10), 2405–2426.

Friederich, J. A., Brand, R. A., 1990. Muscle fiber architecture in the human lower limb. J Biomech. 23 (1), 91–95.

Fritsch, A., Hellmich, C., 2007. Universal microstructural patterns in cortical and trabecular, extracellular and extravascular bone materials: Micromechanics-based prediction of anisotropic elasticity. J Theor Biol. 244 (4), 597 – 620.

Fröhlich, J., 1997. Neural Net Components in an Object Oriented Class Structure. Fachhochschule Regensburg- Department of Computer Science.

Frost, H. M., 1960a. The Utah Paradigm of Skeletal Physiology. Vol. 1. ISMNI.

Frost, H. M., 1960b. The Utah Paradigm of Skeletal Physiology. Vol. 2. ISMNI.

Frost, H. M., 1990. Skeletal structural adaptations to mechanical usage (SATMU): 1. redefining wolff law - the bone modeling problem. Anat Rec. 226 (4), 403–413.

Fushiki, T., 2011. Estimation of prediction error by using k-fold cross-validation. Stat Comput 21 (1), 137–146.

Fyhrie, D. P., Schaffler, M. B., 1995. The adaptation of bone apparent density to applied load. J Biomech 28 (2), 135–146.

Galibarov, P. E., Prendergast, P. J., Lennon, A. B., 2010. A method to reconstruct patient-specific proximal femur surface models from planar pre-operative radiographs. Med Eng Phys. 32 (10), 1180–1188.

García-Aznar, J., Rueberg, T., Doblaré, M., 2005. A bone remodelling model coupling microdamage growth and repair by 3D BMU-activity. Biomech Model Mechanobiol 4 (2-3), 147–167.

Garijo, N., Fernández, J. R., Pérez, M. A., García-Aznar, J. M., 2014a. Numerical stability and convergence analysis of bone remodeling model. Comput Methods Appl Mech Eng 271, 253–268.

Garijo, N., Martínez, J., García-Aznar, J. M., Pérez, M. A., 2014b. Computational evaluation of different numerical tools for the prediction of proximal femur loads from bone morphology. Comput Methods Appl Mech Eng 268, 437–450.

Gavgani, A. M., Dogrusoz, Y. S., 2012. Noise reduction using anisotropic diffusion filter in inverse electrocardiology. Conf Proc IEEE Eng Med Biol Soc 2012, 5919–5922.

Gitman, I. M., Askes, H., Kuhl, E., Aifantis, E. C., 2010. Stress concentrations in fractured compact bone simulated with a special class of anisotropic gradient elasticity. Int J Solids Struct 47 (9), 1099–1107.

Glowinski, R., 1984. Numerical methods for nonlinear variational problems. Springer-Verlag, New York.

González-Carbonell, R. A., Ortiz-Prado, A., Jacobo-Armendáriz, V. H., Cisneros-Hidalgo, Y. A., Alpízar-Aguirre, A., 2015. 3D patient-specific model of the tibia from CT for orthopedic use. J Orthop 12 (1), 11–16.

Goulermas, J. Y., Howard, D., Nester, C. J., Jones, R. K., Ren, L., 2005. Regression techniques for the prediction of lower limb kinematics. J Biomech Eng-T ASME 127 (6), 1020–1024.

Gray, H., 1918. Anatomy of the human body. Philadelphia: Lea and Febiger.

Gurney, K., 1997. An Introduction to Neural Networks. Taylor & Francis, Inc., Bristol, PA, USA.

Hambli, R., 2011a. Apparent damage accumulation in cancellous bone using neural networks. J Mech Behav Biomed Mater. 4 (6), 868–878.

Hambli, R., 2011b. Numerical procedure for multiscale bone adaptation prediction based on neural networks and finite element simulation. Finite Elem Anal Des 47 (7), 835–842.

Hambli, R., Katerchi, H., Benhamou, C.-L., 2011. Multiscale methodology for bone remodelling simulation using coupled finite element and neural network computation. Biomech Model Mechanobiol. 10 (1), 133–145.

Hauge, E. M., Qvesel, D., Eriksen, E. F., Mosekilde, L., Melsen, F., 2001. Cancellous bone remodeling occurs in specialized compartments lined by cells expressing osteoblastic markers. J Bone Miner Res 16 (9), 1575–1582.

Hazelwood, S. J., Martin, R. B., Rashid, M. M., Rodrigo, J. J., 2001. A mechanistic model for internal bone remodeling exhibits different dynamic responses in disuse and overload. J Biomech 34 (3), 299 – 308.

Heller, M. O., Bergmann, G., Deuretzbacher, G., Claes, L., Haas, N. P., Duda, G. N., 2001. Influence of femoral anteversion on proximal femoral loading: measurement and simulation in four patients. Clin Biomech. 16 (8), 644–649.

Hellmich, C., Barthélémy, J.-F., Dormieux, L., 2004. Mineral-collagen interactions in elasticity of bone ultrastructure - a continuum micromechanics approach. Eur J Mech A Solids 23 (5), 783–810.

Hernandez, C., Beaupré, G., Carter, D., 2000. A model of mechanobiologic and metabolic influences on bone adaptation. J Rehabil Res Dev 37 (2), 235–44.

Hernandez, C., Beaupré, G., Keller, T., Carter, D., 2001. The influence of bone volume fraction and ash fraction on bone strength and modulus. Bone 29 (1), 74 – 78.

Hinrichs, R. N., 1985. Regression equations to predict segmental moments of inertia from anthropometric measurements: An extension of the data of chandler et al. (1975). J Biomech 18 (8), 621 – 624.

Howley, T., Madden, M. G., 2006. Artificial Neural Networks - ICANN 2006. Vol. 4132 of Lecture Notes in Computer Science. Springer Berlin Heidelberg.

Huiskes, R., Ruimerman, R., Van Lenthe, G. H., Janssen, J. D., 2000. Effects of mechanical forces on maintenance and adaptation of form in trabecular bone. Nature 405 (6787), 704–706.

Huiskes, R., Weinans, H., Dalstra, M., 1989. Adaptive bone remodeling and biomechanical design considerations for noncemented total hip arthroplasty. Orthopedics 12 (9), 1255–67.

Huiskes, R., Weinans, H., Grootenboer, H. J., Dalstra, M., Fudala, B., Slooff, T. J., 1987. Adaptive bone-remodeling theory applied to prosthetic-design analysis. J Biomech 20 (11-12), 1135–1150.

Jacobs, C., 1994. Numerical Simulation of Bone Adaptation to Mechanical Loading. Dissertation for the Degree of Doctor of Philosophy, Stanford University.

Jacobs, C. R., Levenston, M. E., Beaupré, G. S., Simo, J. C., Carter, D. R., 1995. Numerical instabilities in bone remodeling simulations - the advantages of a node-based finite-element approach. J Biomech 28 (4), 449–451.

Jacobs, C. R., Simo, J. C., Beaupré, G. S., Carter, D. R., 1997. Adaptive bone remodeling incorporating simultaneous density and anisotropy considerations. J Biomech 30 (6), 603–613.

Jin, H., Lewis, J. L., 2004. Determination of poisson's ratio of articular cartilage by indentation using different-sized indenters. J Biomech Eng 126 (2), 138–145.

Kaczmarczyk, L., Pearce, C. J., 2011. Efficient numerical analysis of bone remodelling. J Mech Behav Biomed Mater 4 (6), 858–867.

Kent, D., Hayward, R., 2007. Limitations of applying summary results of clinical trials to individual patients: The need for risk stratification. J Am Med Assoc. 298 (10), 1209–1212.

Klika, V., Grmela, M., Jan 2013. Coupling between chemical kinetics and mechanics that is both nonlinear and compatible with thermodynamics. Phys Rev E Stat Nonlin Soft Matter Phys 87 (1), 012141.

Klika, V., Pérez, M. A., García-Aznar, J. M., Maršík, F., Doblaré, M., 2014. A coupled mechano-biochemical model for bone adaptation. J Math Biol 69 (6-7), 1383–1429.

Kolk, S., Minten, M. J. M., van Bon, G. E. A., Rijnen, W. H., Geurts, A. C. H., Verdonschot, N., Weerdesteyn, V., 2014. Gait and gait-related activities of daily living after total hip arthroplasty: A systematic review. Clin Biomech 29 (6), 705–718.

Komarova, S. V., Smith, R. J., Dixon, S., Sims, S. M., Wahl, L. M., 2003. Mathematical model predicts a critical role for osteoclast autocrine regulation in the control of bone remodeling. Bone 33 (2), 206 – 215.

Koopman, B., Grootenboer, H. J., Jongh, H. J. D., 1995. An inverse dynamics model for the analysis, reconstruction and prediction of bipedal walking. J Biomech 28 (1), 1369–76.

Kunkle, B. W., Yoo, C., Roy, D., 2013. Reverse engineering of modified genes by bayesian network analysis defines molecular determinants critical to the development of glioblastoma. PLoS ONE 8 (5).

Langley, P., Simon, H. A., Nov. 1995. Applications of machine learning and rule induction. Commun. ACM 38 (11), 54–64.

Lavrac, N., Keravnou, E., Zupan, B., 2000. Intelligent data analysis in medicine. Encyclopedia of computer science and technology 42 (9), 113–157.

Lee, J. K., 2011. Bone Biology for Implant Dentistry in Atrophic Alveolar Ridge - Theory and Practice. Implant Dentistry - A Rapidly Evolving Practice.

Lekadir, K., Noble, C., Hazrati-Marangalou, J., Hoogendoorn, C., van Rietbergen, B., Taylor, Z. A., Frangi, A., 2015. Patient-specific biomechanical modeling of bone strength using statistically-derived fabric tensors. Ann Biomed Eng.In press (DOI: 10.1007/s10439-015-1432-2).

Liu, Y., Shih, S.-M., Tian, S.-L., Zhong, Y.-J., Li, L., 2009. Lower extremity joint torque predicted by using artificial neural network during vertical jump. J Biomech. 42 (7), 906–911.

Madeo, A., George, D., Lekszycki, T., Nierenberger, M., Remond, Y., 2012. A second gradient continuum model accounting for some effects of microstructure on reconstructed bone remodelling. Comptes Rendus Mecanique 340 (8), 575–589.

Mangan, S., Alon, U., 2003. Structure and function of the feed-forward loop network motif. Proceedings of the National Academy of Sciences 100 (21), 11980–11985.

Martin, R., 1991. Determinants of the mechanical properties of bones. J Biomech 24, 79 – 88.

Martin, R. B., 1984. Porosity and specific surface of bone. Vol. 10 of Biomedical Engineering. CRC Press, Ch. 3, pp. 179–222.

Martínez, J., Martínez, M., Matías, J. M., Taboada, J., 2011. Classifying slate tile quality using automated learning techniques. Math Comput Model. 10 (1016).

Matsuo, K., Irie, N., 2008. Osteoclast-osteoblast communication. Arch Biochem Biophys. 473 (2), 201 – 209.

McCulloch, W., Pitts, W., 1990. A logical calculus of the ideas immanent in nervous activity. Bull Math Biol 52 (99-115), 73–97.

McNamara, L. M., Prendergast, P. J., 2007. Bone remodelling algorithms incorporating both strain and microdamage stimuli. J Biomech 40 (6), 1381 – 1391.

Mengoni, M., Ponthot, J., 2015. An enhanced version of a bone-remodelling model based on the continuum damage mechanics theory. Comput Methods Biomech Biomed Engin. 18 (12), 1367–1376.

Michie, D., Spiegelhalter, D. J., Taylor, C. C., Campbell, J. (Eds.), 1994. Machine Learning, Neural and Statistical Classification. Ellis Horwood, Upper Saddle River, NJ, USA.

Minsky, M., Papert, S., 1969. Perceptrons. an introduction to computational geometry. Science 165 (3895), 780–782.

Mitchell, R. K., Agle, B. R., Wood, D. J., 1997. Toward a theory of stakeholder identification and salience: Defining the principle of who and what really counts. The Academy of Management Review 22 (4), 853–886.

Mohaghegh, K., Pérez, M. A., García-Aznar, J. M., 2014. Accelerating numerical simulations of strain-adaptive bone remodeling predictions. Comput Methods Appl Mech Eng 273, 255–272.

Molnar, C., Gair, J. (Eds.), 2013. Concepts of Biology. OpenStax College textbook.

Monnier, J., Trabucho, L., 1998. Existence and uniqueness of a solution to an adaptive elasticity model. Math Mech Solids 3 (2), 217–228.

Moreira, M., Fiesler, E., 1995. Neural networks with adaptive learning rate and momentum terms. Tech. rep., IDIAP Technical report - Institut Dalle Molle DÍntelligence Artificielle Perceptive.

Morgan, E. F., Bayraktar, H. H., Keaveny, T. M., 2003. Trabecular bone modulus-density relationships depend on anatomic site. J Biomech 36 (7), 897–904.

Morlock, M., E.Schneider, Bluhm, A., Vollmer, M., G. Bergmann, V. M., 2001. Duration and frequency of every day activities in total hip patients. J Biomech. 34, 873–81.

Mullender, M. G., Huiskes, R., Weinans, H., 1994. A physiological approach to the simulation of bone remodeling as a self-organizational control process. J Biomech 27 (11), 1389–1394.

Neal, M. L., Kerckhoffs, R., 2010. Current progress in patient-specific modeling. Brief Bioinform. 11 (1), 111–126.

Nielsen, R. H., Karsdal, M. A., Sørensen, M. G., Dziegiel, M. H., Henriksen, K., 2007. Dissolution of the inorganic phase of bone leading to release of calcium regulates osteoclast survival. Biochem Biophys Res Commun 360 (4), 834 – 839.

Odgaard, A., Kabel, J., van Rietbergen, B., Dalstra, M., Huiskes, R., 1997. Fabric and elastic principal directions of cancellous bone are closely related. J Biomech 30 (5), 487 – 495.

Pal, S., Haider, H., Laz, P. J., Knight, L. A., Rullkoetter, P. J., 2008. Probabilistic computational modeling of total knee replacement wear. Wear 264 (7-8).

Pal, S., Langenderfer, J., Stowe, J., Laz, P., Petrella, A., Rullkoetter, P., 2007. Probabilistic modeling of knee muscle moment arms: Effects of methods, origin-insertion, and kinematic variability. Ann Biomed Eng 35 (9), 1632–1642.

Pandy, M. G., 2001. Computer modeling and simulation of human movement. Annu Rev Biomed Eng. 3 (1), 245–273.

Parker, D. B., 1985. Learning-logic. Technical Report TR-47, Center for Comp. Research in Economics and Management Sci., MIT.

Pellikaan, P., van der Krogt, M. M., Carbone, V., Fluit, R., Vigneron, L. M., Deun, J. V., Verdonschot, N., Koopman, H. F. J. M., 2014. Evaluation of a morphing based method to estimate muscle attachment sites of the lower extremity. J Biomech 47 (5), 1144–1150.

Peng, L., Bai, J., Zeng, X. L., Zhou, Y. X., 2006. Comparison of isotropic and orthotropic material property assignments on femoral finite element models under two loading conditions. Med Eng Phys 28 (3), 227–233.

Pérez, M., García-Aznar, J., Doblaré, M., Seral, B., Seral, F., 2006. A comparative {FEA} of the debonding process in different concepts of cemented hip implants. Med Eng Phys. 28 (6), 525 – 533.

Pérez, M. A., Fornells, P., Doblaré, M., García-Aznar, J. M., 2010. Comparative analysis of bone remodelling models with respect to computerised tomography-based finite element models of bone. Comput Methods Biomech Biomed Engin 13 (1), 71–80.

Pérez-Suárez, S. T., Travieso-González, C. M., Alonso-Hernández, J. B., 2013. Design methodology of an equalizer for unipolar non return to zero binary signals in the presence of additive white gaussian noise using a time delay neural network on a field programmable gate array. Sensors 13 (12), 16829–16850.

Pivonka, P., Komarova, S. V., 2010. Mathematical modeling in bone biology From intracellular signaling to tissue mechanics. Bone 47 (2), 181 – 189.

Poelert, S., Valstar, E., Weinans, H., Zadpoor, A., 2012. Patient-specific finite element modeling of bones. Proc Inst Mech Eng H 227 (4), 464–478.

Prendergast, P. J., Taylor, D., 1994. Prediction of bone adaptation using damage accumulation. J Biomech 27 (8), 1067–1076.

Ramtani, S., Zidi, M., 2001. A theoretical model of the effect of continuum damage on a bone adaptation model. J Biomech 34 (4), 471–479.

Rho, J.-Y., Kuhn-Spearing, L., Zioupos, P., 1998. Mechanical properties and the hierarchical structure of bone. Med Eng Phys 20 (2), 92 – 102.

Rosenblatt, F., 1958. The perceptron: a probabilistic model for information storage and organization in the brain. Psychological review 65 (6), 386–408.

Roux, W., 1881. Der kampf der theile im organismus. Leipzig: Engelmann.

Ruimerman, R., Hilbers, P., van Rietbergen, B., Huiskes, R., 2005. A theoretical framework for strain-related trabecular bone maintenance and adaptation. J Biomech 38 (4), 931 – 941.

Rumelhart, D. E., Hinton, G. E., Williams, R. J., 1986. Parallel distributed processing: Explorations in the microstructure of cognition, vol. 1, 318–362.

Rumelhart, D. E., Widrow, B., Lehr, M. A., 1994. The basic ideas in neural networks. Commun. ACM 37 (3), 87–92.

Sayad, S., 2010. An Introduction to Data Mining. Free webinar.

Schafer, R. C., Johnson, G. C., Zolli, F., 1995. Basic principles of chiropractic : the neuroscience foundation of clinical practice. American Chiropractic Association - ACAPress.

Scheiner, S., Pivonka, P., Hellmich, C., 2013. Coupling systems biology with multiscale mechanics, for computer simulations of bone remodeling. Comput Methods Appl Mech Eng. 254, 181 – 196.

Scheiner, S., Pivonka, P., Hellmich, C., 2015. Poromicromechanics reveals that physiological bone strains induce osteocyte-stimulating lacunar pressure. Biomech Model MechanobiolIn Press.

Schileo, E., Dall'Ara, E., Taddei, F., Malandrino, A., Schotkamp, T., Baleani, M., Viceconti, M., 2008. An accurate estimation of bone density improves the accuracy of subject-specific finite element models. J Biomech 41 (11), 2483 – 2491.

Schölkopf, B., Smola, A. J., Williamson, R. C., Bartlett, P. L., 2000. New support vector algorithms. Neural computation 12 (5), 1207–1245.

Schriefer, J. L., Warden, S. J., Saxon, L. K., Robling, A. G., Turner, C. H., 2005. Cellular accommodation and the response of bone to mechanical loading. J Biomech 38 (9), 1838–1845.

Sheng, M. H. C., Lau, K. H. W., Baylink, D. J., 2014. Role of osteocyte-derived insulin-like growth factor i in developmental growth, modeling, remodeling, and regeneration of the bone. J Bone Metab. 21 (1), 41–54.

Smit, T. H., Burger, E. H., 2000. Is bmu-coupling a strain-regulated phenomenon? a finite element analysis. J Bone Miner Res 15 (2), 301–307.

Spoor, C. W., Van Leeuwen, J. L., Van Der Meulen, W. J., Huson, A., 1991. Active force-length relationship of human lower-leg muscles estimated from morphological data: a comparison of geometric muscle models. Eur J Morphol. 29, 137–60.

Stone, M., 1974. Cross-validatory choice and assessment of statistical predictions. J Roy Statist Soc Series B 36, 111–147.

Sun, L., Berndt, C. C., Gross, K. A., Kucuk, A., 2001. Material fundamentals and clinical performance of plasma-sprayed hydroxyapatite coatings: A review. J Biomed Mater Res 58 (5), 570–592.

Taddei, F., Pancanti, A., Viceconti, M., 2004. An improved method for the automatic mapping of computed tomography numbers onto finite element models. Med Eng Phys 26 (1), 61–69.

Tamma, R., Zallone, A., 2012. Osteoblast and osteoclast crosstalks: From oaf to ephrin. Inflamm Allergy Drug Targets 11 (3), 196–200.

Tsirakos, D., Baltzopoulos, V., Bartlett, R., 1997. Inverse optimization: functional and physiological considerations related to the force-sharing problem. Crit Rev Biomed Eng. 25, 371–407.

Tsubota, K., Suzuki, Y., Yamada, T., Hojo, M., Makinouchi, A., Adachi, T., 2009. Computer simulation of trabecular remodeling in human proximal femur using large-scale voxel fe models: Approach to understanding wolff's law. J Biomech 42 (8), 1088 – 1094.

Tu, J. V., 1996. Advantages and disadvantages of using artificial neural networks versus logistic regression for predicting medical outcomes. J Clin Epidemiol. 49 (11), 1225 – 1231.

Turner, C. H., Cowin, S. C., Rho, J. Y., Ashman, R. B., Rice, J. C., 1990. The fabric dependence of the orthotropic elastic constants of cancellous bone. J Biomech 23 (6), 549 – 561.

Turner, C. H., Forwood, M., Rho, J.-Y., Yoshikawa, T., 1994. Mechanical loading thresholds for lamellar and woven bone formation. J Bone Miner Res 9 (1), 87–97.

Twomey, J., Smith, A., 1997. Validation and Verification, in Artificial Neural Networks for Civil Engineers: Fundamentals and Applications. ASCE Press, New York.

Vahdati, A., Rouhi, G., 2009. A model for mechanical adaptation of trabecular bone incorporating cellular accommodation and effects of microdamage and disuse. Mech Res Commun 36 (3), 284–293.

Vahdati, A., Walscharts, S., Jonkers, I., García-Aznar, J. M., Sloten, J. V., van Lenthe, G. H., 2014. Role of subject-specific musculoskeletal loading on the prediction of bone density distribution in the proximal femur. J Mech Behav Biomed Mater 30 (0), 244–252.

van Bezooijen, R. L., Roelen, B. A., Visser, A., van der Wee-Pals, L., de Wilt, E., Karperien, M., Hamersma, H., Papapoulos, S. E., ten Dijke, P., Löwik, C. W., 2004. Sclerostin is an osteocyte-expressed negative regulator of bone formation, but not a classical bmp antagonist. J Exp Med 199, 805–814.

van Oers, R. F., Ruimerman, R., Tanck, E., Hilbers, P. A., Huiskes, R., 2008. A unified theory for osteonal and hemi-osteonal remodeling. Bone 42 (2), 250 – 259.

Vapnik, V., 1982. Estimation of dependences based on empirical data. Springer, New York.

Vapnik, V., 1998. Statistical learning theory. John Wiley, New York.

Vapnik, V. N., 1995. The Nature of Statistical Learning Theory. Springer-Verlag New York, Inc., New York, NY, USA.

Vidyasagar, M., 1997. A Theory of Learning and Generalization: With Applications to Neural Networks and Control Systems. Springer-Verlag New York, Inc., Secaucus, NJ, USA.

Wang, S., Liu, T., Chen, W., Spincemaille, P., Wisnieff, C., Tsiouris, A. J., Zhu, W., Pan, C., Zhao, L., Wang, Y., 2013. Noise effects in various quantitative susceptibility mapping methods. IEEE Trans Biomed Eng 60 (12), 3441–8.

Webster, D., Müller, R., 2011. In silico models of bone remodeling from macro to nano-from organ to cell. Wiley Interdiscip Rev Syst Biol Med. 3 (2), 241 – 251.

Webster, D., Wirth, A., van Lenthe, G. H., Muller, R., 2012. Experimental and finite element analysis of the mouse caudal vertebrae loading model: prediction of cortical and trabecular bone adaptation. Biomech Model Mechanobiol. 11 (1-2), 221–230.

Weinans, H., Huiskes, R., Grootenboer, H. J., 1992. The behavior of adaptive bone-remodeling simulation-models. J Biomech 25 (12), 1425–1441.

Werbos, P. J., 1974. Beyond Regression: New Tools for Prediction and Analysis in the Behavioral Sciences. PhD thesis, Harvard University.

Whalen, R. T., Carter, D. R., Steele, C. R., 1988. Influence of physical-activity on the regulation of bone-density. J Biomech 21 (10), 825–837.

Wickiewicz, T. L., Roy, R. R., Powell, P. L., Edgerton, V. R., 1983. Muscle architecture of the human lower limb. Clin Orthop Relat Res 179, 275–283.

Wilkinson, J., Reinsch, C., 1971. Linear Algebra. In: Handbook for Automatic Computation, Volume II. Vol. II. New York: Springer-Verlag.

Williams, S. J., 2015. Bisphosphonates and bone metabolism. BioMed Medicine and Life Sciences Scientific Journal 6 (3-1).

Wolff, J., 1982. Das gesetz der transformation der knochen. Hirschwald, Berlin.

Yang, G., Kabel, J., Van Rietbergen, B., Odgaard, A., Huiskes, R., Cown, S., 1998. The anisotropic hooke's law for cancellous bone and wood. J Elasticity 53 (2), 125–146.

Zadpoor, A. A., Campoli, G., Weinans, H., 2013. Neural network prediction of load from the morphology of trabecular bone. Appl Math Model 37 (7), 5260–5276.

Zadpoor, A. A., Weinans, H., 2015. Patient-specific bone modeling and analysis: The role of integration and automation in clinical adoption. J Biomech 48 (5), 750–760.

Zaidi, M., Datta, H. K., Patchell, A., Moonga, B., MacIntyre, I., 1989. Calcium-activated intracellular calcium elevation: A novel mechanism of osteoclast regulation. Biochem Biophys Res Commun 163 (3), 1461 – 1465.

Zajac, F. E., 1989. Muscle and tendon: properties, models, scaling, and application to biomechanics and motor control. Crit Rev Biomed Eng. 17 (4), 359–411.

Zysset, P., Goulet, R., Hollister, S., 1998. A global relationship between trabecular bone morphology and homogenized elastic properties. J Biomech Eng. 120 (5), 640–646.